

An Experimental Evaluation of the Instrumented Flux Synthesis Method

by
Jeffrey C. Hughes

Bachelor's of Science, Nuclear Engineering
University of Michigan, Ann Arbor, MI (1991)

Master's of Science, Nuclear Engineering
University of California, Berkeley, CA (1992)

Submitted to the Department of Nuclear Engineering
in partial fulfillment of the requirements for the degree of

DOCTOR OF PHILOSOPHY

at the

MASSACHUSETTS INSTITUTE OF TECHNOLOGY

September, 1995

© Massachusetts Institute of Technology, MCMXCV. All Rights Reserved

Signature of Author: _____ Date: July 24 1995
Department of Nuclear Engineering

Certified by: _____ Date: Jeff Hughes
Allan F. Henry, Thesis Advisor
Professor of Nuclear Engineering

Certified by: _____ Date: 27 July 95
Dr. John Bernard, Thesis Reader
MIT Nuclear Reactor Laboratory

Certified by: _____ Date: 9/5/95
David D. Lanning, Thesis Reader
Professor of Nuclear Engineering

Certified by: _____ Date: 7/24/95
Jeffrey Freidberg
Chairman, Department Committee on Graduate Students

MASSACHUSETTS INSTITUTE
OF TECHNOLOGY

APR 22 1996

Science

An Experimental Evaluation of the Instrumented Flux Synthesis Method

by

Jeffrey C. Hughes

Submitted to the Department of Nuclear Engineering on July 25, 1995, in partial fulfillment of the requirements for the degree of

DOCTOR OF PHILOSOPHY

ABSTRACT

Accurate knowledge of the neutron flux density distribution is required for safe design and operation of a nuclear reactor. One method of determining the flux density is flux synthesis which approximates the flux in the core by linear combinations of precomputed shape functions. In traditional flux synthesis, the unknown mixing coefficients are determined using a weighted residual method of solving the diffusion equation. In the instrumented synthesis method, the mixing coefficients are determined using count rates from neutron detectors in the core. In this way the mixing coefficients are linked to conditions in the reactor. Using the synthesized flux, kinetics parameters, notably reactivity, can be calculated in real time.

An experimental evaluation has been performed in the Massachusetts Institute of Technology Reactor, MITR-II. Detector measurements have been collected using fission chambers placed at the periphery of the core. The reactor was put into a number of various conditions, both static and transient, and data were collected using a digital acquisition system for later combination with shape functions. Transients included increasing power, decreasing power, and a reactor scram.

The shape functions were generated using Version 3.0 of the QUARTZ code, a quadratic nodal diffusion theory code in triangular-Z geometry. Supernodal analysis algorithms have been added to the original program, along with subroutines to guarantee diagonal dominance of the leakage matrix in the finite difference equations as well as proper determination of the adjoint flux. Supernodal analyses have been carried with discontinuity factors for either finite difference or quadratic current approximations in the coarse mesh. The agreement between coarse mesh and fine mesh in all cases is excellent, with finite difference coarse mesh solutions generally slightly better.

The synthesis method has been shown to accurately reflect the changes from an initial condition by combining representative flux shapes. It can be concluded that, with proper calibration of the measurement system and inclusion of representative flux shapes, the instrumented synthesis method will properly predict the flux in the core under a number of conditions.

Thesis Supervisor: Allan F. Henry

Title: Professor, Department of Nuclear Engineering

ACKNOWLEDGMENTS

I would like to first thank my advisor, Professor Allan Henry. It has been an honor and privilege to have worked with him during my course work and thesis research. His humor and willingness to help are appreciated as much as his knowledge, some of which I hope I have taken with me.

I would also like to thank my readers, Professor David Lanning and Dr. John Bernard. I am indebted to Professor Lanning not only for his insightful comments and direction on my thesis, but for the invaluable opportunities given to me to learn outside the classroom. Dr. Bernard's help with the experimental portion of the thesis and late night discussions of the results are deeply appreciated.

I would like to extend my thanks to the following people for their help with various portions of this research: Ed Lau, Tom Newton, the MIT Nuclear Reactor Operations Group, the Reactor Radiation Protection Office, Everett Redmond, Erik Iverson, and Rachel Morton.

Good luck - though you all don't need it - to Brett, Dave, Tanya, and the various and sundry residents of Hotel Lowell. Never a dull moment, to be sure. And to Jen and Paul, who always brought the mustard: thanks, guys.

To Jenna, the real doctor, who has seen me through classes, reports, exams, theses, hayrides, winery tours, holidays, and everything in between.

To my family, who have always been there and given me more support and opportunity than I could ever ask for.

This thesis is dedicated to them.

TABLE OF CONTENTS

ABSTRACT	2
ACKNOWLEDGMENTS	3
TABLE OF CONTENTS	4
LIST OF FIGURES	8
LIST OF TABLES	14
CHAPTER 1: INTRODUCTION	15
1.1 Background	15
1.2 Theoretical Methods	16
1.3 Empirical Methods	23
1.4 Instrumented Synthesis Method	23
1.5 Research Objectives	24
1.6 Thesis Organization	25
CHAPTER 2: THE INSTRUMENTED SYNTHESIS METHOD	27
2.1 Determining Neutron Flux	28
2.2 The Singular Value Decomposition Method	33
2.3 Orthogonalization of the Expansion Functions	35
2.4 Residual Vector and Expansion Functions	38
2.5 Characteristics of the Instrumented Synthesis Method	40
2.6 Instrumented Synthesis and Determining Reactivity	42
2.7 Conclusions from the Numerical Tests	47
2.8 Flow of the Experimental Evaluation	51

CHAPTER 3: THE QUARTZ CODE	54
3.1 Theory	54
3.2 Expressions for Current in Triangular Geometry	55
3.3 Supernodal Analysis in Triangular Geometry	70
3.4 Supernodal Results	79
3.5 Convergence of the Solution Methods	83
3.6 Corrections to the QUARTZ Code	92
3.7 Summary	94
CHAPTER 4: DESCRIPTION OF THE EXPERIMENT	95
4.1 Introduction	96
4.2 Previous Work	97
4.3 Description of the MITR-II	98
4.4 Description of the Data Acquisition	102
4.5 Description and Results of the Experiment	112
4.5.1 Description of Experiment	112
4.5.2 Results of Experiment	116
4.6 Summary	125
CHAPTER 5: MITR MODEL	126
5.1 Introduction	126
5.2 Motivation for a New Model	128
5.3 CITATION Model	130
5.3.1 Microscopic Cross Sections	131

5.3.2	U ²³⁵ and Fission Product Number Densities	133
5.3.3	Boundary Conditions	135
5.4	MCNP Model	138
5.5	Control Blades and Detector Positions	143
5.6	QUARTZ Model	149
5.6.1	Steps in QUARTZ Analysis	149
5.6.2	Static Results - Core #106	152
5.6.3	Static Results - Core #110	173
5.7	Application to the MITR Fuel Management Program	175
5.8	Summary	178
CHAPTER 6: EVALUATION OF THE EXPERIMENTS		180
6.1	Introduction	180
6.2	Determination of Detector Response and Evaluation of the Instrumented Synthesis	181
6.2.1	Determination of Detector Response	182
6.2.2	Evaluation of the Instrumented Synthesis	184
6.2.2.1	The Residual	184
6.2.2.2	Normalized Detector Readings	187
6.2.2.3	Reactivity	188
6.3	The Synthesis Code	189
6.4	Static Results	190
6.5	Transient Results	198
6.5.1	Discontinuous Synthesis	198

6.5.2	Insertion of Blade #3 - Cores #106 and #110	199
6.5.3	Insertion of Shim Blade #6 - Core #110	219
6.5.4	Withdrawal of Shim Blade #6 - Cores #106 and #110..	226
6.5.5	Shim Blade #1 Drop - Core #106	242
6.6	Summary	250
CHAPTER 7: CONCLUSION		252
7.1	Summary of Results	252
7.2	Conclusions	254
7.3	Recommendations for Future Research	255
REFERENCES		258
APPENDIX 1: SUPERNODAL TEST MODEL		261
APPENDIX 2: NUMBER DENSITIES		263
APPENDIX 3: QUARTZ MODEL OF MITR		267
APPENDIX 4: DECK AND PLOT CODE DESCRIPTIONS		278
APPENDIX 5: EXPERIMENTAL PROCEDURES		285

LIST OF FIGURES

2.1	Example of Flux Synthesis	41
2.2	Flowchart of Experimental Evaluation	52
3.1	Planar Coupling of Node I,J,K Through the Finite Difference Current Formulation	56
3.2	Planar Coupling of Node I,J,K Through the Finite Difference Current Formulation	63
3.3	Non-linear Iteration Method in QUARTZ	69
3.4	Fine Mesh Collapsing	73
3.5	Generation of Discontinuity Factors from a Quadratic Fine Mesh Solution	78
3.6	Power Convergence with No Change in Diffusion Coefficients	90
3.7	Power Convergence with Changing Diffusion Coefficients	91
4.1	MCNP Model of the MITR Core	97
4.2	Drawing of the MITR-II Fuel Element	99
4.3	MCNP Cross Section of MITR Core Tank	101
4.4	Schematic of Fission Chamber Operation	104
4.5	Schematic of Fission Chamber Placement in Guide Tube	107
4.6	Placement of Fission Chambers in Core	108
4.7	Connections to Fission Chamber and Ammeter	110
4.8	Schematic of Data Acquisition	112
4.9	Tilt Configuration #1	115
4.10	Tilt Configuration #2	115

4.11	Static Measurements at 50 kW, Core #106	117
4.12	Static Measurements at 50 kW, Core #110	118
4.13	Flux Measurements, Shim Blade #3 Insertion, Core #106	119
4.14	Flux Measurements, Shim Blade #3 Insertion, Core #110	121
4.15	Flux Measurements, Shim Blade #6 Withdrawal, Core #106	122
4.16	Flux Measurements, Shim Blade #6 Withdrawal, Core #110	123
4.17	Shim Blade #1 Dropped, Followed by Reactor Scram, Core #106...	124
5.1	DEplete Code Flow Chart	134
5.2	Schematic of CITATION Nodes Near the QUARTZ Boundary	136
5.3	Fine Mesh Model of an MITR-II Fuel Element	139
5.4	Homogenization Scheme #1 - Maintain Actual Geometry	140
5.5	Homogenization Scheme #2 - Change Geometry to Define Fewer Materials	141
5.6	Actual vs. QUARTZ Shim Blade Positions	145
5.7	Control Blade Geometry	147
5.8	Large Node Size in the MITR-II Model	151
5.9	Flux Tilts Using Flat Boundary Conditions	154
5.10	Flux Tilts Using Average Boundary Conditions	155
5.11	QUARTZ Model of Core #106, Plane #6 [6" to 8" from bottom of fuel] - Thermal Flux	158
5.12	QUARTZ Model of Core #106, Plane #8 [10" - 12" from bottom of fuel] - Thermal Flux	159
5.13	QUARTZ Model of Core #106, Plane #8 - Fast Flux	160
5.14	QUARTZ Model of Core #106, Tilt #1 Plane #7 - Thermal Flux.....	161

5.15	QUARTZ Model of Core #106, Tilt #2, Plane #7 - Thermal Flux....	162
5.16	Thermal Flux in Element A2 vs. Axial Position	165
5.17	Thermal Flux in Element B4 vs. Axial Position	166
5.18	Thermal Flux in Element C10 vs. Axial Position	167
5.19	Comparison of Tilted-to-Flat Measurements to QUARTZ Predictions, Core #106 at 10 kW, Vent Hole #1	168
5.20	Comparison of Tilted-to-Flat Measurements to QUARTZ Predictions, Core #106 at 10 kW, Vent Hole #3	170
5.21	Comparison of Tilted-to-Flat Measurements to QUARTZ Predictions with Unaveraged Boundary Conditions, Core #106 at 10 kW, Vent Hole #1	171
5.22	Current MITR Fuel Management Program	176
5.23	Possible Redesigned MITR Fuel Management Program	178
6.1	Node Collapsing at Detector Location	183
6.2	Relative Residual, Core #106 @ 50 kW Flat Shim Bank, One and Two Orthogonal Modes Retained	192
6.3	Mixing Coefficients, Core #106 @ 50 kW Flat Shim Bank One Mode Retained	193
6.4	Mixing Coefficients, Core #106 @ 50 kW Flat Shim Bank Two Modes Retained	194
6.5	Comparison of Power in Core #106 @ 50 kW One and Two Mode Synthesis	195
6.6	Comparison of Reactivity in Core #106 @ 50 kW One and Two Mode Synthesis	195
6.7	Power and Reactivity as Determined by Synthesis Shim Blade #3 Insertion - Core #106	200
6.8	Power and Reactivity as Determined by Synthesis Shim Blade #3 Insertion - Core #110	201

6.9	Power and Reactivity Determined by Synthesis with External Point Source Shim Blade #3 Insertion - Core #106	206
6.10	Power and Reactivity Determined by Synthesis with External Point Source Shim Blade #3 Insertion - Core #110	207
6.11	Relative Residual and Average Difference Between Synthesis Power and Normalized Detector Readings Shim Blade #3 Insertion - Core #106	209
6.12	Relative Residual and Average Difference Between Synthesis Power and Normalized Detector Readings Shim Blade #3 Insertion - Core #110	210
6.13	Differences Between Synthesis Power and Normalized Detector Readings Shim Blade #3 Insertion - Core #106	212
6.14	Differences Between Synthesis Power and Normalized Detector Readings Shim Blade #3 Insertion - Core #110	213
6.15	Comparison of Relative Residuals for Point Kinetics and Four Mode Synthesis Shim Blade #3 Insertion - Core #106	215
6.16	Comparison of Synthesis Power to QUARTZ Power Shim Blade #3 Insertion - Core #106	217
6.17	Comparison of Synthesis Reactivity to QUARTZ Reactivity Shim Blade #3 Insertion - Core #106	218
6.18	Power and Reactivity as Determined by Synthesis Shim Blade #6 Insertion - Core #110	221
6.19	Relative Residual and Average Difference Between Synthesis Power and Normalized Detector Readings Shim Blade #6 Insertion - Core #110	222
6.20	Mixing Coefficients over Time Shim Blade #6 Insertion - Core #110	224
6.21	Comparison of Relative Residuals for Point Kinetics and Four Mode Synthesis Shim Blade #6 Insertion - Core #110	225
6.22	Power and Reactivity as Determined by Synthesis Shim Blade #6 Withdrawal - Core #106	228

6.23	Relative Residual and Average Difference Between Synthesis Power and Normalized Detector Readings Shim Blade #6 Withdrawal - Core #106	230
6.24	Difference Between Synthesis Power and Normalized Detector Readings Shim Blade #6 Withdrawal - Core #106	231
6.25	Power and Reactivity as Determined by Synthesis Shim Blade #6 Withdrawal - Core #110	233
6.26	Relative Residual and Average Difference Between Synthesis Power and Normalized Detector Readings Shim Blade #6 Withdrawal - Core #110	234
6.27	Difference Between Synthesis Power and Normalized Detector Readings Shim Blade #6 Withdrawal - Core #110	235
6.28	Detector Readings from Each of Three Trials Shim Blade #6 Withdrawal - Core #110	236
6.29	Comparison of Relative Residuals for Point Kinetics and Four Mode Synthesis Shim Blade #6 Withdrawal - Core #110	237
6.30	Synthesis Power Compared to QUARTZ Prediction Shim Blade #6 Withdrawal - Core #106	239
6.31	Synthesis Reactivity Compared to QUARTZ Prediction Shim Blade #6 Withdrawal - Core #106	239
6.32	Residual for Filtered Detector Measurements Shim Blade #6 Withdrawal - Core #106	241
6.33	Power and Reactivity as Determined by Synthesis Shim Blade #1 Drop - Core #106	244
6.34	Relative Residual Retaining One and Two Modes Shim Blade #1 Drop - Core #106	245
6.35	Detector Measurements After Blade Drop Shim Blade #1 Drop - Core #106	246
6.36	Relative Residual After Blade Drop Shim Blade #1 Drop - Core #106	247

6.37	Difference Between Synthesis Power and Normalized Detector Readings, One and Two Modes Retained	
	Shim Blade #1 Drop - Core #106	249

LIST OF TABLES

4.1	Normalized Detector Responses	106
4.2	Measurements for Evaluation of the Instrumented Flux Synthesis Method	114
5.1	Microscopic Cross Sections Available from CITATION	132
5.2	CITATION Energy Group Structure	132
5.3	Delayed Neutron Data	133
5.4	QUARTZ Boundary Conditions Taken from CITATION ($\alpha_g=1.0$)..	138
5.5	Nominal Number Densities of Some MITR Materials	142
5.6	QUARTZ Model of Core #106 Static Conditions	153
5.7	Effects of Averaging Boundary Conditions on Tilted Eigenvalues....	155
5.8	Flux Shapes Generated for the Transient Measurements in Core #106	156
5.9	Other Flux Shapes Generated for Core #106	157
5.10	QUARTZ Model of Core #110 Static Conditions	174
5.11	Flux Shapes Generated for the Transient Measurements in Core #110	174
6.1	Comparison of Tilted-to-Flat Power Ratios	197
6.2	Shape Functions Shim Blade #3 Insertion - Core #106	199
6.3	Shape Functions Shim Blade #3 Insertion - Core #110	199
6.4	Shape Functions Shim Blade #6 Insertion - Core #110	220
6.5	Shape Functions Shim Blade #6 Withdrawal - Core #106	226
6.6	Shape Functions Shim Blade #6 Withdrawal - Core #110	226
6.7	Shape Functions Shim Blade #1 Dropped - Core #106	242

Chapter 1

Introduction

1.1 BACKGROUND

Knowledge of the power in a nuclear reactor core, and how it is distributed, is the foundation upon which safe operation of a nuclear power plant is built. There are numerous ways of acquiring this knowledge. For the purposes of this discussion, we can broadly group the methods into the theoretical and the empirical. The former attempt to solve governing equations to calculate the power in various regions of the reactor core. The latter use measurements taken directly from the core itself and infer power from those measurements. There is, of course, overlap in each method. For example, parameters in the governing equations are derived from measured data, introducing empirical data into

theoretical methods. Conversely, some theoretical description is required to translate a temperature measurement into a local power. The basic differences in the two methods are in the primary means in which power is determined. It is the goal of the instrumented synthesis method to take the best attributes of each method to provide an accurate way of determining the total reactor power and its spatial distribution in real time. We shall look at each of the two approaches separately before examining how they can be combined in the instrumented synthesis method.

1.2 THEORETICAL METHODS

We first take up the theoretical methods. The local power density in a reactor core is related directly to the angular neutron flux density, $\Psi(\underline{r}, E, \underline{\Omega}, t)$. This is defined as

$$\Psi(\underline{r}, E, \underline{\Omega}, t) = v(E) N(\underline{r}, E, \underline{\Omega}, t), \quad (1.1)$$

$v(E)$ = velocity of neutrons with energy E

$N(\underline{r}, E, \underline{\Omega}, t) dV dE d\Omega$ = the number of neutrons in volume dV about \underline{r} , energies

dE about E , traveling in directions $d\Omega$ about Ω

The angular flux density is directly related to the fission power produced at position \underline{r} and time t by the macroscopic fission cross section. In a region of volume V_n , the fission power is given by

$$\text{Power}(t) = K \cdot \int_{\Omega} d\Omega \int_{E=0}^{\infty} dE \int_{V_n} d\underline{r} \Psi(\underline{r}, E, \Omega, t) \Sigma_f(\underline{r}, E, t) \quad (1.2)$$

where

$\Sigma_f(\underline{r}, E, t)$ = macroscopic fission cross section [cm^{-1}]

K = a conversion factor [Watts/fission]

By determining the angular flux, we can determine both the total power and its spatial distribution. Hence knowledge of the angular neutron flux density is the most fundamental aspect of safe operation of a nuclear power plant. The governing equation for determining this quantity is the transport equation. It is in general, however, very difficult to solve.

Fortunately in most commercial nuclear power plants, we can assume a weak dependence of $N(\underline{r}, E, \underline{\Omega}, t)$ upon $\underline{\Omega}$. Under these circumstances it is sufficient to determine $\Phi(\underline{r}, E, t) = \int_{\Omega} d\Omega \Psi(\underline{r}, E, \underline{\Omega}, t)$, the scalar neutron flux density, a much more tractable problem.

In addition to the flux, it is necessary to know the concentration of delayed neutron precursors. The precursors are created as fission fragments. They emit neutrons after the fission event that created them, sometimes up to minutes later.

To determine the flux and precursor concentrations, the time-dependent, continuous energy balance and precursor equations must be solved:

$$\begin{aligned}
\frac{\partial}{\partial t} \left[\frac{1}{v(E)} \Phi(\underline{r}, E, t) \right] &= -\underline{\nabla} \cdot \underline{J}(\underline{r}, E, t) - \Sigma_t(\underline{r}, E, t) \Phi(\underline{r}, E, t) \\
&+ \chi_p(E) (1 - \beta) \int_0^\infty v \Sigma_f(r, E', t) \Phi(\underline{r}, E', t) dE' \\
&+ \int_0^\infty \Sigma_s(r, E' \rightarrow E, t) \Phi(\underline{r}, E', t) dE' \\
&+ \sum_{iprec=1}^{nprec} \chi_{iprec}(E) \lambda_{iprec} c_{iprec}(\underline{r}, t)
\end{aligned} \tag{1.3a}$$

$$\frac{\partial c_{iprec}(\underline{r}, t)}{\partial t} = \beta_{iprec} \int_0^\infty v \Sigma_f(r, E, t) \Phi(\underline{r}, E, t) dE - \lambda_{iprec} c_{iprec}(\underline{r}, t) \tag{1.3b}$$

where

$v(E)$ = velocity of neutrons with energy E . [cm/sec]

$\Phi(\underline{r}, E, t)$ = scalar flux density at time t of neutrons at position \underline{r} and energy E [neutrons/cm²-sec]

$\underline{J}(\underline{r}, E, t)$ = net current density at time t of neutrons at position \underline{r} and energy E [neutrons/cm²-sec]

$\Sigma_t(\underline{r}, E, t)$ = total macroscopic cross section [cm⁻¹]

$\chi_p(E)$ = prompt fission neutron spectrum at energy E

β_{iprec} = fraction of delayed neutrons from precursor group $iprec$.

β = total fraction of delayed neutrons, $\beta = \sum_{iprec=1}^{nprec} \beta_{iprec}$

$v \Sigma_f(\underline{r}, E, t)$ = average number of neutrons per fission, v , times the macroscopic fission cross section [cm⁻¹]

$\Sigma_s(\underline{r}, E' \rightarrow E, t)$ = macroscopic differential scattering cross section for neutrons of energy E' to a range about energy E . [cm⁻¹]

$\chi_{iprec}(E)$ = energy spectrum for delayed neutrons from precursor group $iprec$

λ_{iprec} = decay constant for precursor group $iprec$ [s^{-1}]

$c_{iprec}(\underline{r}, t)$ = concentration of precursors at time t at position \underline{r} .

Equations 1.3a and 1.3b are the “governing equations” referred to in Section 1.1.

If all the parameters were known exactly, they would provide a complete and wholly accurate description of the flux density, and therefore the power distribution, throughout the reactor.

To solve Equations 1.3 on a computer, some discretization must be used. The scalar flux is determined over energy ranges of width ΔE_g and spatial spans V_n comprising node n . By integrating Equations 1.3 over ΔE_g and V_n we obtain the nodal balance and precursor equations, given below.

$$\begin{aligned} \frac{d}{dt} \left[\frac{l}{v_g} \bar{\Phi}_g^n(t) \right] = & -\frac{l}{V_n} \sum_{p=1}^P A_p \bar{J}_g^n(p, t) \cdot \underline{n}_p - \Sigma_g^n(t) \bar{\Phi}_g^n(t) + \sum_{\substack{g'=1 \\ g' \neq g}}^G \Sigma_{gg'}^n(t) \bar{\Phi}_{g'}^n(t) \\ & + \chi_{pg}(1-\beta) \sum_{g'=1}^G v \Sigma_{fg'}^n(t) \bar{\Phi}_{g'}^n(t) + \sum_{iprec=1}^{nprec} \chi_{iprec,g} \lambda_{iprec} c_{iprec}^n \end{aligned} \quad (1.4a)$$

and

$$\frac{d}{dt} c_{iprec}^n(t) = \beta_{iprec} \sum_{g=1}^G v \Sigma_{fg}^n \bar{\Phi}_g^n - \lambda_{iprec} c_{iprec}^n \quad (1.4b)$$

where

$$v_g \equiv \frac{l}{\bar{\Phi}_g^n(t) V_n} \int dV \int_{\Delta E_g} dE \frac{l}{v(E)} \Phi(\underline{r}, E, t)$$

$$\bar{\Phi}_g^n(t) \equiv \frac{1}{V_n} \int_{V_n} dV \int_{\Delta E_g} dE \Phi(\underline{r}, E, t)$$

$$\Sigma_{t,g}^n \equiv \frac{1}{\bar{\Phi}_g^n(t) V_n} \int_{V_n} dV \int_{\Delta E_g} dE \Sigma_t(\underline{r}, E, t) \Phi(\underline{r}, E, t)$$

$$\chi_{pg} \equiv \int_{\Delta E_g} dE \chi_p(E)$$

$$v\Sigma_{f,g}^n \equiv \frac{1}{\bar{\Phi}_g^n(t) V_n} \int_{V_n} dV \int_{\Delta E_g} dE v\Sigma_f(\underline{r}, E, t) \Phi(\underline{r}, E, t)$$

$$\Sigma_{gg'}^n \equiv \frac{1}{\bar{\Phi}_g^n(t) V_n} \int_{V_n} dV \int_{\Delta E_g} dE \int_{\Delta E_{g'}} dE' \Sigma_s(\underline{r}, E' \rightarrow E, t) \Phi(\underline{r}, E', t)$$

$$\Sigma_g^n \equiv \Sigma_{t,g}^n - \Sigma_{gg}^n$$

$$\chi_{iprec,g} \equiv \int_{\Delta E_g} dE \chi_{iprec}(E)$$

$$c_{iprec}^n(t) \equiv \frac{1}{V_n} \int_{V_n} dV c_{iprec}(\underline{r}, t)$$

Note that the divergence theorem has been applied to the volume integral of the current.

A net surface-averaged current has been defined for node n , side p as

$$\bar{J}_g^n(p, t) \equiv \frac{1}{A_p} \int_{A_p} ds \int_{\Delta E_g} dE \underline{J}(\underline{r}, E, t) \quad (1.5)$$

\underline{n}_p in Eqn. 1.4a is the outward directed normal from surface p .

Note also that Equations 1.4 are equivalent to 1.3. If $\Phi(\underline{r}, E, t)$ were known exactly, the parameters defined in Eqn. 1.4 could be determined without approximation,

and the nodal flux $\overline{\Phi}_g^n(t)$ found by solving Eqn. 1.4 would indeed equal the continuous scalar flux, integrated over space and energy, found by Eqn. 1.3.

$$\overline{\Phi}_g^n(t) = \frac{1}{V_n} \int_{V_n} dV \int_{\Delta E_g} dE \Phi(\underline{r}, E, t) \quad (1.6)$$

Because $\Phi(\underline{r}, E, t)$ is not known in general, the homogenization process is not exact. The

$\overline{\Phi}_g^n(t)$ found by 1.4 will not be equivalent to $\frac{1}{V_n} \int_{V_n} dV \int_{\Delta E_g} dE \Phi(\underline{r}, E, t)$. The approximation

is worsened by the fact that the spatial variation of the cross sections may not be well known.

In addition to homogenizing over energy and space, there must be an additional approximation. At this point, there are $1+nprec$ equations, 1.4a and 1.4b, with

$1+nprec+P$ unknowns, $\underline{J}_g^n(p, t)$, $\overline{\Phi}_g^n(t)$, and $\overline{c}_{iprec}^n(t)$, where P is the number of faces on

a node. To relate the currents $\underline{J}_g^n(p, t)$ to the flux $\overline{\Phi}_g^n(t)$, the diffusion approximation

can be made. It is given by Fick's law, which for the continuous energy and space case is

$$\underline{J}(\underline{r}, E, t) \cong -D(\underline{r}, E) \underline{\nabla} \Phi(\underline{r}, E, t) \quad (1.7)$$

This equation states that the current is proportional to the gradient of the flux. The equation resulting from the use of this approximation is called the neutron diffusion equation.

Prior to the late 1970s, the solution of the neutron diffusion equation relied primarily on fine-mesh finite difference discretization of the spatial variable. A fine mesh creates a large number of spatial unknowns, raising the cost of such calculations. These shortcomings can be largely overcome with the use of modern nodal methods [K1,S2], which introduce quantities called discontinuity factors to correct not only for the Fick's Law approximation, but homogenization errors as well. As a result, these nodal methods can use larger nodes than traditional finite difference methods, generating solutions that are just as accurate but in much shorter times.

With the increasing speed of computers, it is possible that such nodal methods will be used to simulate reactor transients in real time with great accuracy. Such methods could provide input for automatic controllers, supplying reactor operators with knowledge of the flux, and therefore power, at every node in the core. With reconstruction techniques, even more detailed power distributions are possible. Thus it seems that nodal methods could meet the reactor physicist's goal: real time knowledge of the neutron flux in the reactor core. Using the detailed flux distribution, other quantities of interest in reactor control, notably reactivity, can be calculated.

There is, however, a crucial missing element: detailed knowledge of the cross sections. Cross sections vary considerably with a number of parameters. For example, temperature of the fuel greatly affects the capture of neutrons in resonances of U^{238} . Temperature of the moderator will change the energy spectrum of fission neutrons. Positions of control elements will affect absorption over homogenized regions. Long term effects such as fuel depletion and burnable absorber concentration introduce even more

uncertainties. Finally, in fast-acting reactor transients, there is little likelihood of complete knowledge of the system. There appears to be no practical way of directly determining cross sections in real time. Thus even if solving the time-dependent nodal equations in real time becomes possible, the data needed to solve them may not be available.

1.3 EMPIRICAL METHODS

Reactor operators use parameters that can be directly measured to infer the power distribution. Exit coolant temperatures can be used to determine total power output. Neutron flux can be measured at selected locations. But because precise knowledge of these parameters is known only at selected locations, safety margins must be employed to ensure safe operation of the plant. These safety margins may lessen the ability of the operators to optimize the performance of the plant. Additionally, though these methods may provide a rough picture of the power distribution, none can do so with sufficient detail to allow calculation of the kinetics parameters under all conditions.

1.4 INSTRUMENTED SYNTHESIS METHOD

Reactor operators have been left with two choices: a method that provides detailed knowledge of the neutron flux with no accurate way of coupling it to the physical system, or measurement of physical properties that provide incomplete knowledge of the neutron flux.

The instrumented synthesis method seeks to bridge the gap between these two choices. It uses measurable data in the form of detector count rates to combine pre-determined flux shapes into the one that best represents the physical system. The complete, detailed knowledge of the system provided by theoretical methods, in the form of the flux shapes, is coupled with direct knowledge of the physical system through detector readings.

1.5 RESEARCH OBJECTIVES

The instrumented synthesis method was originally developed and tested by Jacqmin using simulated reactor transients [J1]. The success of these numerical tests suggest that, if the fluxes can be accurately determined, even at only selected points in the reactor, a flux shape throughout the reactor can be accurately synthesized. The experimental evaluation will attempt to prove the applicability of the method to real systems by testing it in a functional nuclear reactor, the Massachusetts Institute of Technology Research Reactor, MITR-II.

A theoretical description of the MITR-II will be developed using a version of the QUARTZ code. QUARTZ, a nodal diffusion theory code in triangular-z geometry, will be modified to allow fine mesh results to be collapsed to coarse mesh results, generating discontinuity factors and flux weighted cross sections that allow the fine mesh result to be duplicated. This will provide the flux shapes to be used in the synthesis.

Flux measurements from the MITR-II will be taken under various static and transient conditions. The measurements will provide the experimental data used to combine the flux shapes into a single, synthesized flux. Power and reactivity will be derived from this flux, and can be compared to previously measured data or to data taken at the time of the experiment.

The goals will be to improve the capability of the QUARTZ code such that it becomes a suitable tool for analysis of the MITR-II. The QUARTZ code will then be used to generate flux shapes for use in the synthesis. Finally, the synthesis method will be applied to analysis of the MITR-II. The ultimate objective of the research is to demonstrate that the synthesis method is capable of reflecting changes in the amplitude and shape of the flux in the reactor, as well as accurately determine power and reactivity.

1.6 THESIS ORGANIZATION

The instrumented flux synthesis method will be described in Chapter 2. Some of the lessons to be taken from the previous numerical evaluations will be presented as well. The QUARTZ code is discussed in Chapter 3. The changes made to incorporate supernodal analyses as well as other corrections to the code are described here. The system used to take measurements from the reactor core is detailed in Chapter 4. Chapter 5 returns to the theoretical description of the core. The modified QUARTZ code will be the tool to analyze the core model. The flux shapes and measurements will be combined, and the

results presented in Chapter 6. Chapter 7 will discuss conclusions and recommendations for future research.

Chapter 2

The Instrumented Synthesis Method

The theory detailing the instrumented synthesis method is given in Robert Jacqmin's 1991 Ph.D. thesis, *A Semi-Experimental Nodal Synthesis Method for the On-Line Reconstruction of Three-Dimensional Neutron Flux Shapes and Reactivity* [J1]. More detail is devoted to the method there, and interested readers are urged to consult that work as a complete description of the method. A brief summary will be given here.

2.1 DETERMINING NEUTRON FLUX

We begin with the basic synthesis approximation that the neutron flux throughout the reactor can be constructed using a linear combination of precomputed expansion functions.

$$\Phi_g^n(t) \cong \sum_{k=1}^K \psi_g^{n,k} T^k(t) \quad (2.1)$$

where

$\psi_g^{n,k}$ = the value of expansion function k in node n and group g

$T^k(t)$ = the mixing coefficient for $\psi_g^{n,k}$

A total of K expansion functions will be used. In matrix form, with a total of G groups, N nodes, and K expansion functions

$$\underline{\Phi}(t) \cong \underline{\Psi} \underline{T}(t) \quad (2.2)$$

where

$\underline{\Phi}(t)$ = a $G \times N$ column vector of the fluxes in each node,

$$\left[\Phi_1^1, \Phi_2^1, \Phi_3^1, \dots, \Phi_G^1, \Phi_1^2, \Phi_2^2, \Phi_3^2, \dots, \Phi_G^N \right]^T \quad (2.3a)$$

$\underline{\Psi}$ = a $G \times N$ - by - K matrix (K column vectors of length $G \times N$). Each

column vector is an expansion function.

$\underline{T}(t)$ = a K-element column vector of mixing coefficients

$$\begin{bmatrix} \psi_1^{1,1} & \psi_1^{1,2} & \dots & \dots & \dots & \psi_1^{1,K} \\ \vdots & & & & & \\ \psi_G^{1,1} & & \dots & & & \\ \psi_1^{2,1} & & & \dots & & \\ \vdots & & & & \dots & \\ \psi_G^{N,1} & & & & & \psi_G^{N,K} \end{bmatrix} = [\underline{\psi}^1, \underline{\psi}^2, \dots, \underline{\psi}^K] = \underline{\Psi} \quad (2.3b)$$

where we have defined $\underline{\psi}^k$ as the G×N column vector representing the expansion functions.

The phrases “flux shapes” and “expansion functions” will be used interchangeably throughout the thesis. “Expansion function” denotes more of a mathematical description, but the functions are in reality solutions to the static nodal equation, i.e. flux shapes.

The usual method for employing the synthesis approximation is to substitute Eqn. 2.2 into the diffusion equation,

$$-\nabla \cdot D_g^n(t) \nabla \Phi_g^n(t) + \Sigma_g^n(t) \overline{\Phi}_g^n(t) = \sum_{\substack{g'=1 \\ g' \neq g}}^G \Sigma_{gg'}^n(t) \overline{\Phi}_{g'}^n(t) + \sum_{g'=1}^G v \Sigma_{fg'}^n(t) \Phi_{g'}^n(t) \quad (2.4)$$

where the previous definitions are used along with the diffusion coefficient $D_g^n(t)$.

Because the synthesis form is an approximation, the left and right sides will, in general, not be equal. Both sides are multiplied by a weight function and integrated (or summed) over energy and volume. The unknowns, instead of Φ_g^n , become the mixing coefficients

$T^k(t)$. The number of unknowns is reduced from G×N, approximately 20,000, to G×K, usually <20.

The instrumented synthesis method uses the synthesis approximation in another way. Assume that there exist J detectors in the reactor core. A detector generates a signal proportional to the number of neutrons impinging upon it. This can be expressed mathematically as

$$C^j(t) = \int_{V^j} d\mathbf{r} \int_{E_{min}^j}^{E_{max}^j} dE \Sigma^j(\mathbf{r}, E, t) \Phi(\mathbf{r}, E, t), j=1,2,\dots,J \quad (2.5)$$

or in discrete variables as

$$C^j(t) = \sum_{g=1}^G \sum_{n=1}^N V_n \Sigma_g^{n,j}(t) \Phi_g^n(t), j=1,2,\dots,J \quad (2.6)$$

The response of the j^{th} detector, $\Sigma_g^{n,j}(t)$, can be thought of loosely as a macroscopic cross section. In fact, were $\Sigma_g^n(t)$ to have units of cm^{-1} , the units of C^j in Eqn. 2.5 would be interactions/s. However, detectors will usually have responses of pulses/neutron or coulomb/s (amperes). As discussed in Chapter 4, the detectors used in this experimental evaluation are fission chambers lined with U^{235} . The U^{235} will absorb a neutron and fission, creating charged fission products. The charge is collected in the detector, and the signal sent to a measurement device. In our case, the final units of $\Sigma_g^{n,j}(t)$ are microamps/unit flux [$\mu\text{A}/\text{neutrons}\cdot\text{cm}^{-2}\cdot\text{s}^{-1}$]. Imbedded in this value are the macroscopic fission cross section for U^{235} , the efficiency of charge collection by the detector, and any amplification of the signal.

To illustrate the use of the synthesis approximation with detectors, we make the following additional definitions.

- $\underline{\Sigma}^j$ is a $G \times N$ element column vector representing the weights for detector j in each node for each group.

$$\underline{\Sigma}^j \equiv [V_1 \Sigma_1^{1,j}, V_1 \Sigma_2^{1,j}, \dots, V_1 \Sigma_G^{1,j}, V_2 \Sigma_1^{2,j}, \dots, V_N \Sigma_G^{N,j}]^T \quad (2.7a)$$

It should be noted that the responses $\Sigma_g^{n,j}$ for a particular detector j are given in every node. But, in general, the detectors have non-zero values for $\Sigma_g^{n,j}$ only for the nodes in which they reside. Thus the $\underline{\Sigma}^j$ vectors are composed largely of zeroes.

- $\underline{\underline{\Sigma}}$ is a $G \times N$ -by- J matrix whose columns are the weight vectors for each detector.

$$\underline{\underline{\Sigma}} \equiv [\underline{\Sigma}^1, \underline{\Sigma}^2, \dots, \underline{\Sigma}^J] \quad (2.7b)$$

- $\underline{C}(t)$ is a J -element column vector of detector measurements at time t .

$$\underline{C}(t) \equiv [C^1(t), C^2(t), \dots, C^J(t)]^T \quad (2.7c)$$

Using these definitions with those in Equations 2.3, we can write Eqn. 2.6 as

$$C^j(t) = \underline{\Sigma}^{(j)T} \underline{\Phi}(t) \quad (2.8)$$

or, more succinctly,

$$\underline{C}(t) = \underline{\underline{\Sigma}}^T \underline{\Phi}(t) \quad (2.9)$$

We have related the detector measurements from particular nodes to the scalar neutron flux in each node. If we substitute the synthesis approximation for flux, Eqn. 2.2, we arrive at

$$\underline{C}(t) \approx \underline{\underline{\Sigma}}^T \underline{\Psi} \underline{T}(t) = \underline{\underline{A}} \underline{T}(t) \quad (2.10)$$

where we have defined the J-by-K matrix $\underline{\underline{A}} \equiv \underline{\underline{\Sigma}}^T \underline{\underline{\Psi}}$. Thus the mixing coefficients contained in the K-element column vector $\underline{T}(t)$ are related to the J detector measurements contained in $\underline{C}(t)$. The detector measurements can be related more precisely to the mixing coefficients by introducing a reconstructed flux vector

$$\underline{\hat{\Phi}} \equiv \sum_{k=1}^K \underline{\Psi}^k T^k(t) = \underline{\underline{\Psi}} \underline{T}(t) \quad (2.11a)$$

and an error vector

$$\underline{\delta\Phi}(t) \equiv \underline{\hat{\Phi}}(t) - \underline{\Phi}(t) \quad (2.11b)$$

We now have

$$\underline{\underline{\Sigma}}^T \underline{\underline{\Psi}} \underline{T}(t) - \underline{\underline{\Sigma}}^T \underline{\delta\Phi}(t) = \underline{C}(t) \quad (2.12a)$$

or

$$\underline{\underline{A}} \underline{T}(t) + \underline{E}(t) = \underline{C}(t) \quad (2.12b)$$

where

$$\underline{\underline{A}} = \underline{\underline{\Sigma}}^T \underline{\underline{\Psi}} \quad (2.12c)$$

and

$$\underline{E}(t) \equiv -\underline{\underline{\Sigma}}^T \underline{\delta\Phi}(t) \quad (2.12d)$$

If the vector $\underline{E}(t)$, known as the residual vector, is small, we can legitimately write Eqn. 2.10 as a good approximation. To find the mixing coefficients, and therefore the reconstructed flux, we need only to invert the $\underline{\underline{A}}$ matrix.

$$\underline{T}(t) \equiv \underline{\underline{A}}^{-1} \underline{C}(t) \quad (2.13)$$

2.2 THE SINGULAR VALUE DECOMPOSITION METHOD

The last section has left us with an approximate method of determining the scalar flux for all nodes and energy groups in a reactor using detector measurements in combination with pre-computed expansion functions. Eqn. 2.13 is the relationship that we would like to achieve between the measurements and the mixing coefficients. There is, however, one remaining problem. The $\underline{\underline{A}}$ matrix is a J-by-K matrix, and is generally not square. It is not, therefore, directly invertible.

It is shown by Jacqmin [J1] that it is desirable to have $J \gg K$, in other words many more detectors than expansion functions. In such a condition, the system of equations is overdetermined, and no solution is available. However, such a system can always be solved in a least-squares sense. Such systems of equations arise in a number of mathematical and scientific applications, and there are many ways to solve them. Jacqmin discusses several, but settles upon the singular value decomposition method to “pseudo-invert” the $\underline{\underline{A}}$ matrix and solve the system in a least squares sense. This method is discussed in Strang’s book [S1] and other mathematics textbooks. It is briefly presented here to illuminate some important points in the synthesis method.

Any J-by-K, real matrix of rank R can be expressed as the product of three matrices:

$$\underline{\underline{A}} = \underline{\underline{U}} \begin{bmatrix} \underline{\underline{S}} & \underline{\underline{0}} \\ \underline{\underline{0}} & \underline{\underline{0}} \end{bmatrix} \underline{\underline{V}}^T \quad (2.14)$$

where

$\underline{\underline{U}} \equiv [\underline{u}_1, \underline{u}_2, \dots, \underline{u}_J]$ is a $J \times J$ orthogonal matrix,

$\underline{\underline{V}} \equiv [\underline{v}_1, \underline{v}_2, \dots, \underline{v}_K]$ is a $K \times K$ orthogonal matrix, and

$\underline{\underline{S}} \equiv \text{diag} [s_1, s_2, \dots, s_R]$ is $R \times R$ diagonal matrix.

The elements s_i are the singular values of $\underline{\underline{A}}$, defined as the square roots of the non-zero eigenvalues, s_i^2 , of $\underline{\underline{A}}^T \underline{\underline{A}}$ and $\underline{\underline{A}} \underline{\underline{A}}^T$. They are ordered such that $s_1 > s_2 > s_3 > \dots > s_R$.

Equation 2.14 is called *the singular value decomposition of $\underline{\underline{A}}$* . The decomposition can be expanded as

$$\underline{\underline{A}} = \sum_{i=1}^R s_i \underline{u}_i \underline{v}_i^T \quad (2.15)$$

An approximate solution is found to the system of equations $\underline{C}(t) = \underline{\underline{A}} \underline{T}(t)$ by taking the pseudo-inverse, also known as the Moore-Penrose generalized inverse, of $\underline{\underline{A}}$ [B1]. In expanded form, this is

$$\underline{\underline{A}}^* = \sum_{i=1}^R \frac{1}{s_i} \underline{v}_i \underline{u}_i^T \quad (2.16)$$

The least-squares solution is then

$$\underline{T}_{LS} = \underline{\underline{A}}^* \underline{C} \quad (2.17)$$

Once the mixing coefficients have been determined, the flux vector is reconstructed according to Eqn. 2.11a, where the mixing coefficient vector \underline{T} is replaced by the least-squares solution \underline{T}_{LS} .

$$\hat{\underline{\Phi}}(t) \equiv \sum_{k=1}^K \underline{\Psi}^k T_{LS}^k(t) = \underline{\Psi} \underline{T}_{LS}(t) \quad (2.18)$$

2.3 ORTHOGONALIZATION OF THE EXPANSION FUNCTIONS

There are a number of ways of solving overdetermined systems of equations. The singular value decomposition method, hereafter known as SVD, is one of the slower procedures [G1]. However, it does possess the ability to eliminate spurious modes from the solutions using the singular values obtained as a part of the decomposition. This will be helpful in the instrumented synthesis method.

As pointed out earlier, the singular values are the square roots of the non-zero eigenvalues of $\underline{\underline{A}}^T \underline{\underline{A}}$ and $\underline{\underline{A}} \underline{\underline{A}}^T$. When one or more of these eigenvalues are zero, $\underline{\underline{A}}^T \underline{\underline{A}}$ and $\underline{\underline{A}} \underline{\underline{A}}^T$ are singular, and $\underline{\underline{A}}$, $\underline{\underline{A}}^T$, $\underline{\underline{A}}^T \underline{\underline{A}}$ and $\underline{\underline{A}} \underline{\underline{A}}^T$ are all rank deficient. When the singular values are not zero, but small, $\underline{\underline{A}}^T \underline{\underline{A}}$ and $\underline{\underline{A}} \underline{\underline{A}}^T$ are said to be nearly singular and ill-conditioned. The degree of ill-conditioning is given by the condition number.

$$\sqrt{\frac{s_I^2}{s_R^2}} = \frac{s_I}{s_R} \equiv \kappa(\underline{\underline{A}}) \quad (2.19)$$

The danger in using such ill-conditioned matrices for solving systems of equations is that relatively insignificant modes of the solution may overcome more significant modes upon being multiplied by $1/s_R$. In the instrumented synthesis case, we can take the example of a count rate vector $\underline{\underline{C}}$ “pointing” primarily in the direction of $\underline{\underline{u}}_I$, with a small

component in the perpendicular direction \underline{u}_R . In the solution, however, it is possible that

$$\frac{1}{s_R} (\underline{u}_R^T \underline{C}) \underline{v}_R \text{ would dominate } \frac{1}{s_I} (\underline{u}_I^T \underline{C}) \underline{v}_I \text{ if } s_R \ll s_I.$$

The natural course of action would be to remove such modes where s_i is small before constructing the pseudo-inverse \underline{A}^* . By orthogonalizing the expansion functions, we can provide a physical justification for doing so.

The decomposition of \underline{A} is into two orthogonal bases, \underline{U} and \underline{V} . The orthogonality of \underline{V} allows us to cast the reconstructed flux vector as

$$\underline{\hat{\Phi}}(t) \equiv \sum_{k=1}^K \underline{\Psi}^k T_{LS}^k(t) = \underline{\Psi} \underline{T}_{LS}(t) = \underline{\Psi} \underline{V} \underline{V}^T \underline{T}_{LS}(t) = \underline{\Psi}' \underline{T}'_{LS}(t) = \sum_{i=1}^R \underline{\Psi}'^{(i)} T_{LS}'^{(i)}(t) \quad (2.20)$$

where the following definitions have been made

$$\underline{T}'_{LS}(t) \equiv \underline{V}^T \underline{T}_{LS}(t) \quad (2.21)$$

$$\underline{\Psi}' \equiv \underline{\Psi} \underline{V} \quad (2.22)$$

or equivalently

$$T_{LS}'^{(i)}(t) = \underline{v}_i^T \underline{T}_{LS}(t) = \sum_{k=1}^K v_i^{(k)} T_{LS}^{(k)}(t), \quad i = 1, 2, \dots, R \quad (2.23)$$

and

$$\underline{\Psi}'^{(i)} = \sum_{k=1}^K \underline{\Psi}^{(k)} v_i^{(k)}, \quad i = 1, 2, \dots, R \quad (2.24)$$

The linear combination of the initial expansion functions, $\underline{\psi}^{(k)}$, has been replaced by a linear combination of new expansion functions, $\underline{\psi}'^{(i)}$. These second expansion functions are themselves combinations of the original functions. There are K such functions, but only R of them are used in the synthesis.

From Eqns. 2.12c, 2.14, and 2.22,

$$\underline{\Sigma}^T \underline{\Psi}' = \underline{\Sigma}^T \underline{\Psi} \underline{V} = \underline{A} \underline{V} = \underline{U} \begin{bmatrix} \underline{S} & \underline{0} \\ \underline{0} & \underline{0} \end{bmatrix}, \quad (2.25)$$

or

$$\underline{\Sigma}^T \underline{\psi}'^{(i)} = \underline{A} \underline{v}_i = \begin{cases} s_i \underline{u}_i, & i = 1, 2, \dots, R \\ 0, & i = R+1, R+2, \dots, J \end{cases} \quad (2.26)$$

From the orthogonality of the \underline{u}_i 's, we may write

$$\underline{\psi}'^{(i)T} \underline{\Sigma} \underline{\Sigma}^T \underline{\psi}'^{(j)} = s_i^2 \delta_{ij}, \quad \begin{cases} i = 1, 2, \dots, R \\ j = 1, 2, \dots, R \end{cases} \quad (2.27)$$

We can draw two conclusions from Eqn. 2.27. First, the new expansion functions are orthogonal in a weighted sense. Second, the length of the vector $\underline{\Sigma}^T \underline{\psi}'^{(i)}$ is given by the singular value s_i .

$$\left\| \underline{\Sigma}^T \underline{\psi}'^{(i)} \right\| = s_i, \quad i = 1, 2, \dots, R \quad (2.28)$$

The ratio of the i^{th} mode to the fundamental mode is therefore given as

$$\frac{\left\| \underline{\Sigma}^T \underline{\psi}'^{(i)} \right\|}{\left\| \underline{\Sigma}^T \underline{\psi}'^{(1)} \right\|} = \frac{s_i}{s_1} \quad (2.29)$$

If the length of the vector is small, its contribution to the synthesis is also small. By comparing the ratio of singular values, the contribution of a particular mode $\underline{\psi}^{(i)}$ can be assessed. If the mode contributes little, it is removed from the synthesis by zeroing the singular s_i associated with it.

By orthogonalizing the expansion modes, we have given physical justification to the removal of particular linear combinations of expansion functions by zeroing the associated singular value. To automate this removal, a cutoff factor is employed. If s_i/s_1 falls below a given tolerance, the s_i is zeroed, and that particular combination of expansion modes is removed from the synthesis.

The selection of the tolerance is a typical example of give-and-take. The tolerance should be large enough to eliminate spurious modes that do not make significant contributions to the synthesis, but may “swamp” the solution upon pseudo-inversion of \underline{A} . On the other hand, if the tolerance is made too large important modes will be eliminated, resulting in large systematic errors in the reconstruction of the flux vector. The tolerance selection in the experimental validation will depend upon the accuracy of the flux shapes as well as the precision of the detectors.

2.4 THE RESIDUAL VECTOR AND EXPANSION FUNCTIONS

One drawback of the instrumented synthesis method, or indeed any synthesis method, is the lack of a theoretical bound upon the error in the reconstructed flux. There

are, however, methods of determining the success of the synthesis reconstruction. The residual vector serves as one measure.

$$\underline{E}_{LS} = \underline{C} - \underline{A}\underline{T}_{LS} \quad (2.30)$$

The relative residual is given as $\|\underline{E}_{LS}\|/\|\underline{C}\|$. The use of this quantity as an error estimate gives some insight into the selection of expansion functions, particular the number of expansion functions to be used.

It was stated earlier that for the synthesis method to work, it was desired to have $J \gg K$. The number of detectors should be much larger than the number of expansion functions. A quick glance at the equations should provide some insight to why this is true.

The least-squares approach was used because we have assumed $J > K$. This leaves us with an overdetermined system of equations with no *exact* solution. We could just as well have included more linearly independent expansion functions such that $K \geq J$, resulting in a uniquely- or under-determined system of equations. Even if the expansion functions, or any combination of them, were incapable of reproducing the actual flux shape, the residual vector would constantly be $\underline{0}$. There would be no “room” for a non-zero residual. By having $J > K$, $J-K$ extra degrees of freedom are introduced, to be used by the least-squares solution method to discriminate between appropriate expansion functions.

Basis functions which do not contribute to improving the fit significantly are given relatively small weights, \underline{T}_{LS}^k . Since the success of the synthesis method depends so much upon an appropriate choice of expansion functions, and since this choice may sometimes be a delicate one, it seems highly desirable to let the synthesis method operate in this selective, overdetermined mode. [J1]

Moreover, if $J \gg K$ it would be highly improbable for a small residual to be achieved without the reconstructed flux accurately depicting the actual flux in the core.

One of the significant differences between the computational and experimental evaluations of the synthesis method is the absence of a reference flux vector in the experimental evaluation. Were such a reference available, the natural course of action to validate the method would be to compare the reconstructed flux to the reference flux. The residual provides an alternate method to assess the synthesis. By comparing the reconstructed count rates, given by $\underline{\underline{A}}\underline{\underline{T}}_{LS}(t)$, to the actual count rate $\underline{C}(t)$, we have a real time measurement of the success of the synthesis.

The use of the residual addresses some of the fears that have typically been expressed concerning the use of synthesis methods. Namely, the lack of a theoretical bound for error and the concern for the choice of expansion functions. For a sufficiently well instrumented system, a small residual is a good indicator of an accurate synthesis, while a large residual is a certain indication that the synthesis has not been successful. The method does not, however, give any guidance into what to do if the synthesis fails.

2.5 CHARACTERISTICS OF THE INSTRUMENTED SYNTHESIS METHOD

In Chapter 1, mention was made of a desire to combine the best attributes of theoretical and empirical methods to form the basis of an automated control system. Now that the method has been presented, we can discuss how well those goals are achieved in the instrumented synthesis method.

First, the method frees itself from detailed knowledge of the cross sections as a precondition to transient analysis. The synthesis does not require that any particular expansion function represent the actual flux shape in the core. In general, none of the expansion functions will duplicate core conditions at any given time. The synthesis will succeed if a *combination* of expansion functions will accurately represent the physical flux. By combining different expansion functions in different amounts, the method is freed from having to track any number of various changes in the cross sections. The conditions of the core are relayed through the detector readings. *Feedback is reflected in the detector readings, not the expansion functions.*

This is not to say that expansion functions can be generated haphazardly with little regard for anticipated core conditions. Take the example given below.

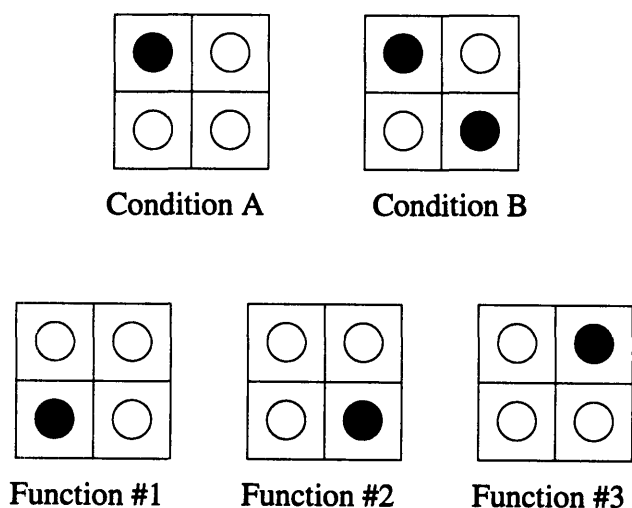


Figure 2.1. Example of Flux Synthesis

The two-by-two assemblies have slightly enriched fuel (white) and a control rod (black) in various positions. The expansion functions have been generated for fuel in three out of

four positions, with the control rod in the remaining position. However, neither the first nor the second actual condition is reflected in the expansion functions. But by combining the first and third expansion functions, the Condition #B could be synthesized. It is difficult to see how Condition #A could be synthesized from any combination of these functions. A flux shape should be generated for a condition close to Condition #A.

Similarly, feedback may be an important concern in the generation of flux shapes. A region filled with water will many times cause a peak in the thermal neutron flux. If the water is heated as the reactor power is increased, that peak may decrease from the lowering of the macroscopic scattering cross section. It may be important to have this change in the flux shape reflected in one of the expansion functions.

For the experimental evaluation, feedback effects were not accounted for in the generation of the shape functions. *The detectors, not the shape functions, reflect feedback in the core.* This ability to account for feedback in the final synthesis even if it is not taken into account in the expansion functions is one of the most attractive features of the instrumented flux synthesis method.

2.6 INSTRUMENTED SYNTHESIS AND DETERMINING REACTIVITY

The driving force for increasing or decreasing neutron population is the reactivity, $\rho(t)$. It is defined as

$$\rho(t) \equiv \frac{\langle W(\underline{r}, E) | M(t) - L(t) | S(\underline{r}, E, t) \rangle}{\langle W(\underline{r}, E) | M(t) | S(\underline{r}, E, t) \rangle} \quad (2.31)$$

where

$W(\underline{r}, E)$ = Weighting function

$S(\underline{r}, E, t)$ = Shape function

$M(t)$ = fission operator

$L(t)$ = loss operator

The $\langle \rangle$ symbol is Dirac notation, and represents the integral over all phase space,

$\int dV \int dE$. The shape function $S(\underline{r}, E, t)$ is related to the neutron flux through the amplitude function, $T(t)$.

$$T(t) \equiv \int_{\text{reactor}} dV \int dE W(\underline{r}, E) \frac{1}{v(E)} \Phi(\underline{r}, E, t) \quad (2.32)$$

$$S(\underline{r}, E, t) \equiv \frac{1}{T(t)} \Phi(\underline{r}, E, t) \quad (2.33)$$

By determining $\Phi(r, E, t)$, we can determine the reactivity.

But determining $\rho(t)$ by Eqn. 2.21 would require detailed knowledge of the cross sections. As discussed previously, this information is unlikely to be available during fast acting transients. An alternative method is inverse kinetics, described below.

Assuming G groups and N nodes, we can define an effective amplitude function,

$$\hat{T}_{eff}(t) \equiv \frac{1}{K_0} \sum_{g=1}^G \sum_{n=1}^N \Phi_{0,gn}^* \frac{1}{v_g} \hat{\Phi}_g^n(t) V_n, \quad (2.34)$$

where we have distinguished between the actual scalar flux for group g and node n ,

$\bar{\Phi}_g^n(t)$, and the measured flux for group g and node n , $\hat{\Phi}_g^n(t)$. We have also refined our

definition of the weighting function to be the adjoint flux, $\Phi_{0,gn}^*$. The “0” indicates that

the adjoint shape is unchanging, i.e. a single adjoint will be selected and used throughout

the duration of the transient. K_0 is an arbitrary constant. We further define the effective

delayed neutron fractions,

$$\hat{\beta}_{iprec,eff}(t) \equiv \frac{\sum_{g=1}^G \sum_{n=1}^N \Phi_{0,gn}^* \lambda_{iprec,gn} \beta_{iprec} \sum_{g'=1}^G \Sigma_{f,g'n}(t) \hat{\Phi}_{g'}^n(t) V_n}{\sum_{g=1}^G \sum_{n=1}^N \Phi_{0,gn}^* \lambda_{iprec,gn} \sum_{g'=1}^G \Sigma_{f,g'n}(t) \hat{\Phi}_{g'}^n(t) V_n}, \quad iprec = 1, nprec \quad (2.35)$$

and the prompt neutron lifetime,

$$\Lambda(t) \equiv \frac{\sum_{g=1}^G \sum_{n=1}^N \Phi_{0,g,n}^* \frac{1}{v_g^n} \hat{\Phi}_g^n(t) V_n}{\sum_{g=1}^G \sum_{n=1}^N \Phi_{0,g,n}^* \lambda_g^n \sum_{g'=1}^G \sum_{n'=1}^N \Sigma_{f,g'n}(t) \hat{\Phi}_{g'}^{n'}(t) V_{n'}}. \quad (2.36)$$

With the reconstructed fluxes $\hat{\Phi}_g^n(t)$ found by the synthesis, the delayed neutron fraction and the prompt neutron lifetime can be determined. The final definition is the as yet unknown effective neutron precursors

$$\hat{c}_{eff,iprec}(t) \equiv \frac{\sum_{g=1}^G \sum_{n=1}^N c_{iprec}^n(t) \Phi_{0,g,n}^* \lambda_{iprec,g}^n}{\sum_{g=1}^G \sum_{n=1}^N \Phi_{0,g,n}^* \frac{1}{v_g^n} \hat{\Phi}_g^n(t)} \quad (2.37)$$

With these definitions, the neutron precursor equation 1.3b, integrated over energy and space, can be written as

$$\frac{d}{dt} \hat{c}_{eff,iprec}(t) + \lambda_{iprec} \hat{c}_{eff,iprec}(t) = \frac{\hat{\beta}_{eff,iprec}(t)}{\hat{\Lambda}_{iprec}(t)} \hat{T}_{eff}(t) \quad (2.38)$$

This is known as the point-kinetics precursor equation. It is an inhomogeneous first order differential equation. To solve it, it is integrated from $t-\Delta t$ to t . The resulting convolution integral is integrated by parts and a Taylor series expansion is made of

$\hat{\beta}_{eff,iprec}(t) T_{eff}(t) / \hat{\Lambda}_{iprec}(t)$ about t or $t-\Delta t$. The resulting form is

$$\hat{c}_{eff,iprec}(t) = e^{-\lambda_{iprec}\Delta t} \hat{c}_{eff,iprec}(t - \Delta t) + \frac{1}{\lambda_{iprec}} \left[1 - e^{-\lambda_{iprec}\Delta t} \right] \frac{\hat{\beta}_{eff,iprec}(t)}{\hat{\Lambda}(t)} \hat{T}_{eff}(t) + O(\Delta t^2) \quad (2.39)$$

Assuming proper initial conditions, the right side of Eqn. 2.39 is known, and the effective neutron precursor densities are determined. They are then used in the point kinetics equation to determine reactivity [H1]. The equation for the amplitude function, also known as the point-kinetics amplitude equation, is derived by integrating 1.3a over energy and space. If we employ the definitions used in the point-kinetics precursor equation, we are left with an equation for reactivity

$$\hat{\rho}(t) = \hat{\beta}_{eff}(t) + \frac{\hat{\Lambda}(t)}{\hat{T}_{eff}(t)} \left[\frac{d}{dt} \hat{T}_{eff}(t) - \sum_{iprec=1}^{nprec} \lambda_{iprec} \hat{c}_{eff,iprec} - q_{eff}(t) \right] \quad (2.40)$$

where

$$\hat{\beta}_{eff}(t) = \sum_{iprec=1}^{nprec} \hat{\beta}_{eff,iprec}(t)$$

$$q_{eff}(t) \equiv \frac{1}{K_0} \sum_{g=1}^G \sum_{n=1}^N \Phi_{g,n}^* Q_g^n(t) V_n$$

The time derivative in Eqn. 2.29 is estimated from a backwards difference formula.

The inverse kinetics method is applied to the instrumented synthesis method by first calculating the flux at each step by the synthesis formula in Eqn. 2.18 Then

amplitude, delayed neutron fractions, and prompt neutron lifetime are calculated by Eqns. 2.23, 2.24, and 2.25 respectively. This leads to the determination of the effective neutron precursor concentrations by Eqn. 2.28, and finally the reactivity by Eqn. 2.29.

An examination of Eqns. 2.23 and 2.24 reveals that the delayed neutron fractions and the prompt neutron lifetime are defined as time-dependent quantities, dependent upon the changing fission cross sections. This appears to defeat the purpose of having a method that calculates flux without explicit knowledge of feedback effects. However, experience has shown that both of these quantities change very little over time [H1,J1], and that allowing them to remain constant is a small approximation.

2.7 CONCLUSIONS FROM THE NUMERICAL TESTS

As was mentioned in Chapter 1, the original theory of the instrumented synthesis method was laid out by Jacqmin in a 1991 Ph.D. thesis [J1]. As part of this work, numerical tests were performed in which several transients in a large PWR core were simulated using the QUANDRY code [S2]. The “detectors” used were simply thermal flux readings from a number of nodes over time. In other words, the “detector” responses were all given by

$$\Sigma^j = \delta_{g2} \delta_{nn'} \quad (2.41)$$

The n_j are the nodes containing the detectors and the fluxes are taken only from the thermal group (group two of a two-group model). The flux readings were taken directly from QUANDRY output.

The results were largely successful, but were made under somewhat idealized circumstances that we are unlikely to encounter in an experimental evaluation. These points are reviewed below.

Probably the most significant difference is the accuracy of the expansion functions. The QUANDRY model of the reactor was used to generate shape functions at several different points during the transients. In essence, the shape functions were the reactor. It is highly unlikely that the same accuracy can be achieved in analyzing the MITR core.

Another related difference is the lack of knowledge of the Σ^j . The synthesis method relies heavily upon Eqn. 2.6 being a valid description of the detector output as a function of flux. It is certainly valid in a theoretical sense. But the inference of flux through the instrumented synthesis method requires that Σ^j be known at all times for all conditions. Spectral or electronics changes in the flux may change the Σ^j . For a sophisticated control systems, an on-line calibration would be necessary to ensure complete knowledge of the detector responses. Such a system was not present for this experimental evaluation.

This knowledge is further complicated by the relationship between the actual flux and the theoretical prediction of the flux. In Eqn. 2.10, we have substituted the synthesis approximation for the flux in the expression for detector count rate. The

implicit assumption is that the detectors will reflect what the flux is *over an entire node*. If the shape functions are generated for large node sizes, there may well be a combination of them that accurately reflects the average flux over that same region in the actual core. But the flux at the detector locations may be much larger or smaller than that average flux. Thus even if the response of a detector to a particular flux is known through factory specifications, how the flux at the detector locations relates to the average flux in a node must still be determined. This is in stark contrast to the numerical evaluation. There, the detector responses were the fluxes themselves. There was no uncertainty in the measurements.

The method of determining the Σ^j is postponed until Chapter 6. But the reader should remain aware of this important difference between the numerical and experimental evaluations.

In developing the numerical evaluation of the instrumented synthesis method, Jacqmin correctly realized that detectors will have certain random variations, or *noise*, associated with the measurements. With artificial noise added to the simulated detector readings, the synthesis method actually generated negative fluxes for certain cases. Such problems were largely solved with the use of filters which may be required for the experimental evaluation.

There is also the issue of instrumentation. The experimental trials will rely on relatively few (nine) detectors, placed at the core periphery. The majority of the tests conducted by Jacqmin [J1] were with 80 simulated in-core detectors. This resulted in a highly overdetermined system of equations ($J \gg K$). In the tests conducted with

only four detectors, a good degree of accuracy was retained, although not the same as with more detectors. This accuracy was severely degraded in the presence of noise. Additionally, the four-detector trials took data from the center of the core, not at the edge. The unavoidable placement of the detectors at the edge of the MITR, and their small number, may combine to worsen the synthesis in the experimental case.

Finally, there should be some mention of the accuracy we can hope to achieve. For the numerical simulations, several transients were analyzed [J1]. These included operational transients, such as withdrawal of a bank of control rods, and startup transients, which included a simulation of feedback during a startup transient. For many of these transients, the relative residuals remained below 5%, indicating a good synthesis. Since a reference flux vector was available from QUANDRY, comparisons could be made the flux in each node, and were found to be generally with 1-5%. These results worsened with the addition of noise, leading to large errors in some cases.

Though absolute standards are difficult to apply, a residual of less than 5-8% and less than 2% error in power would be a very positive indication of a successful synthesis. Since there is no reference reactivity to which to compare, these are harder to quantify. One possibility is to compare the reactivity as determined by the synthesis method to the measured rod worths determined by the Reactor Operations Group.

2.8 FLOW OF THE EXPERIMENTAL EVALUATION

A flowchart is given in Figure 2 detailing how the experimental evaluation will proceed. The flowchart is divided into three areas. The largest section is the *theoretical prediction*, referring to the solution of equations 1.4. The data for these equations and how the solutions are determined are discussed in Chapters 3 and 5. Briefly, to solve the diffusion and precursor equations, data in the form of cross sections are needed. These data will be obtained from previously generated microscopic cross sections and newly generated number densities. These cross sections will be for a fine mesh model of the MIT Research Reactor. To reduce complexity for the synthesis, collapsing routines will be employed to create larger nodes. By using discontinuity factors to account for errors in homogenization, these large-node results should match the fine-mesh results. The coarse-mesh model will be used to generate static flux shapes, $\underline{\psi}^k$, for use in the synthesis. It can also be one method of predicting flux, power, and reactivity in various transients. As discussed before, however, such predictions will have no coupling to the physical system.

The *empirical measurements* are detailed in Chapter 4. These are the detector readings given by the $\underline{C}(t)$ vector. The detector responses, $\underline{\Sigma}^j(t)$, will be discussed in Chapter 6. By using these values, fluxes at the detector locations can be inferred. These fluxes can be compared to the synthesis value of the flux at that location, and an error in the synthesized flux is determined. Also, a ratio of current to power can be

determined for each detector. This allows a direct calculation of the power by in-core instrumentation, which can then be compared to the synthesis value.

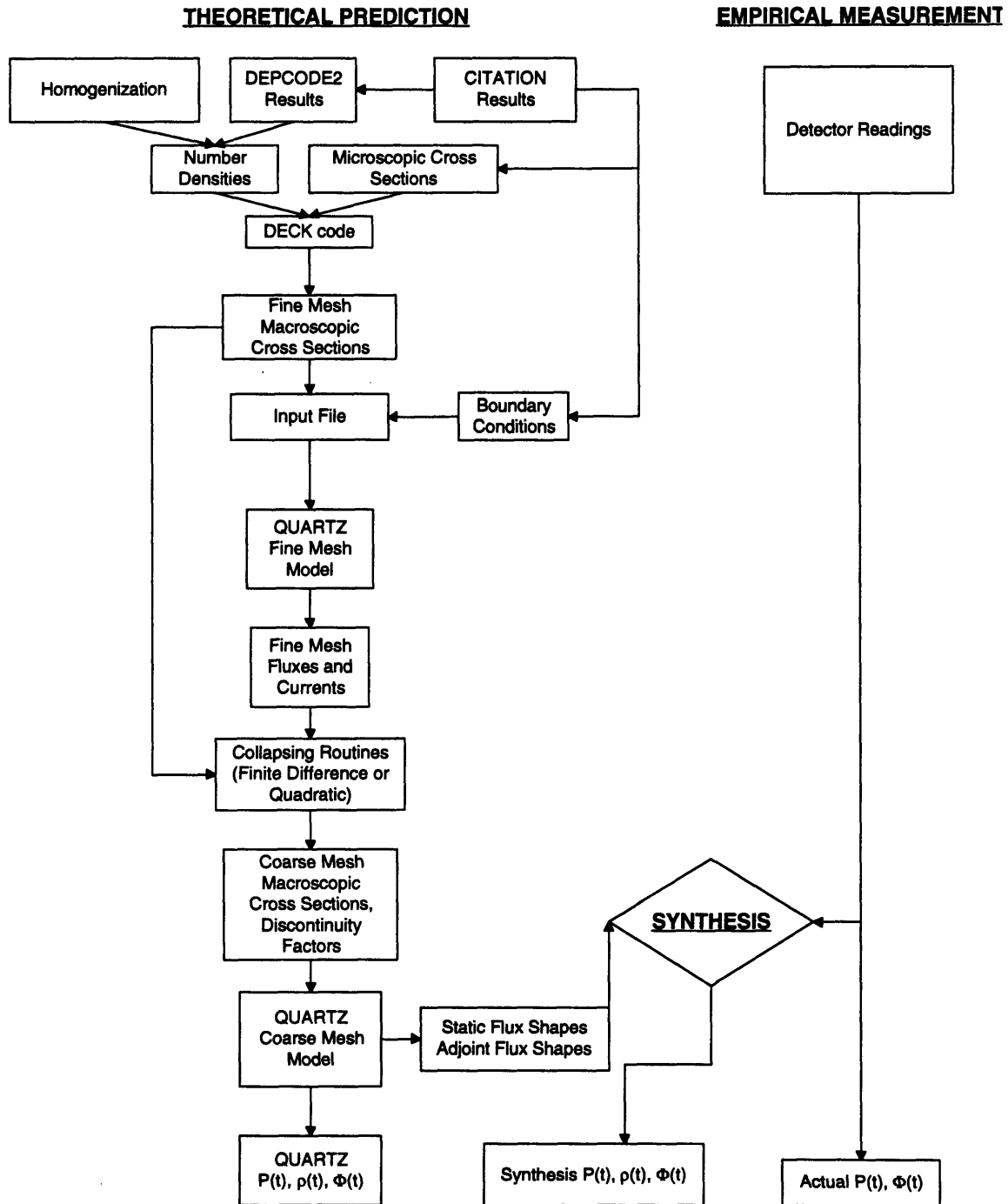


Figure 2.2. Flowchart of Experimental Evaluation

Finally, the static flux shapes from the theoretical prediction (Chapter 5) are combined with the count rates in the *synthesis* process. This process and the results are described in Chapter 6, and the conclusions presented in Chapter 7.

Chapter 3

The QUARTZ Code

3.1 THEORY

Recall from Chapter 1 the neutron and precursor equations:

$$\begin{aligned} \frac{d}{dt} \left[\frac{1}{v_g} \bar{\Phi}_g^n(t) \right] = & -\frac{1}{V_n} \sum_{p=1}^P A_p \bar{J}_g^n(p, t) \cdot n_p - \Sigma_g^n(t) \bar{\Phi}_g^n(t) + \sum_{\substack{g'=1 \\ g' \neq g}}^G \Sigma_{gg'}^n(t) \bar{\Phi}_{g'}^n(t) \\ & + \chi_{pg} (1 - \beta) \sum_{g'=1}^G v \Sigma_{fg'}^n(t) \bar{\Phi}_{g'}^n(t) + \sum_{iprec=1}^{nprec} \chi_{iprec, g} \lambda_{iprec} \bar{C}_{iprec}^n \end{aligned} \quad (1.2.4a)$$

and

$$\frac{d}{dt} \bar{C}_{iprec}^n(t) = \beta_{iprec} \sum_{g=1}^G v \Sigma_{f, g}^n \bar{\Phi}_g^n - \lambda_{iprec} \bar{C}_{iprec}^n \quad (1.2.4b)$$

Solving these equations is the basis of the theoretical determination of neutron flux. A large number of different codes have been developed to accomplish this task. The one employed for this work will be the QUARTZ code (*QUAdratic Reactor code in Triangle-Z geometry*). The code denoted Version 1.0 was developed by Thomas DeLorey in 1993 as part of a Ph.D. thesis [D1]. Versions 2.0 and 3.0 were developed as part of the present thesis. Version 3.0 is the final iterate and will be discussed here.

In addition to corrections to the original code, Version 3.0 includes a number of additions that will be presented in this chapter. Most of these additions have to do with supernodal analysis where fine mesh results are collapsed to a coarse mesh. This reduces the number of unknowns, decreasing the complexity of the flux shapes used in the instrumented flux synthesis project. It also allows transient analyses to be conducted in much shorter times. Supernodal transient analysis has been investigated for a number of applications. This work represents the initial application to the MIT Research Reactor, and to triangular geometry in particular.

3.2 EXPRESSIONS FOR CURRENT IN TRIANGULAR GEOMETRY

This section is a brief summary DeLorey's thesis [D1]. Interested readers are urged to consult his work, *A Transient, Quadratic Nodal Method for Triangular-Z Geometry*, as a more complete explanation of nodal methods applied to triangular geometries. The summary presented here is used to put forth equations used in the supernodal methods described in Section 3.3.

It was stated in Chapter 2 that an approximation to the current across the P surfaces of a node would have to be made to reduce the number of unknowns from $1+n_{prec}+P$ to $1+n_{prec}$. The $1+n_{prec}$ unknowns are the volume average flux $\bar{\Phi}_g^n$ and the precursor concentrations c_{iprec}^n . This approximation is known as Fick's Law, given in the continuous energy and space form in Eqn. 1.7. The approximation can also be made in the group and node form, and can be formulated in a variety of ways. The traditional approximation has been the finite difference approximation, but a higher-order quadratic approximation can also be made. Both possibilities are available in the QUARTZ code, and both are presented below.

Since the code is specific to triangular geometries, we shall make the discussion specific to them. Below is a schematic of two adjoining triangular nodes¹.

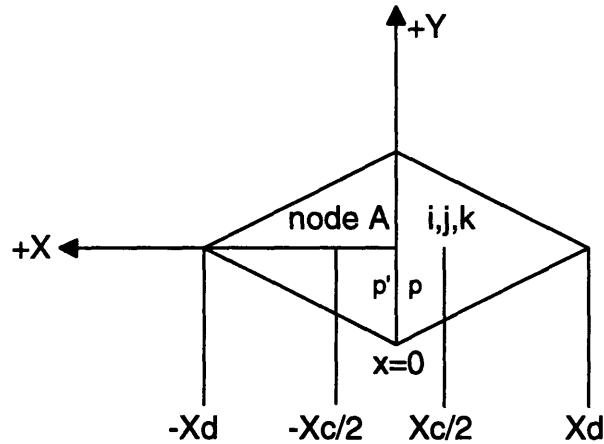


Figure 3.1. Planar Coupling of Node I,J,K Through the Finite Difference Current Formulation

¹ A similar diagram appears in DeLorey's thesis. There, however, the +X direction is directed into the node I,J,K, in contradiction to way the currents are calculated in QUARTZ. Although the definitions used in his work are consistent throughout, the positive X-direction is reversed here to preserve consistency with QUARTZ, i.e. the current is positive in the direction of the outward normal from node I,J,K.

Node A is the adjacent node. This notation is used to preserve generality in writing the following equations for currents across any of the five faces of a three-dimensional node.

The altitude of the triangle is given by

$$X_d = \frac{\sqrt{3}}{2} S \quad (3.1)$$

where S is the length of the side of the isosceles triangle. The center-to-center distance between nodes is

$$X_c = \frac{\sqrt{3}}{3} S \quad (3.2)$$

The component of the current crossing the common face of the nodes in the +X direction is

$$J_x(x, y, E) = -D(x, y, E) \frac{\partial}{\partial x} \Phi(x, y, E) \quad (3.3)$$

If this equation is integrated over the transverse direction, Y , and energy ΔE_g , and the following definitions are made

$$\bar{J}_{g,X}^{i,j,k}(p) \equiv \frac{\int_{\Delta E_g} dE \int_{-S/2}^{+S/2} dy J_x(x=0, y, E)}{\int_{-S/2}^{+S/2} dy} \quad (3.4a)$$

$$D_g^{i,j,k} \equiv \frac{\int_{\Delta E_g} dE \int_0^{X_d} dx \int_{-y(x)/2}^{+y(x)/2} dy D(x, y, E) \Phi(x, y, E)}{\int_{\Delta E_g} dE \int_0^{X_d} dx \int_{-y(x)/2}^{+y(x)/2} dy \Phi(x, y, E)} \quad (3.4b)$$

$$\frac{\partial}{\partial x} \bar{\Phi}_g^{i,j,k}(p) \equiv \frac{\int_{\Delta E_g} dE \int_{-S/2}^{S/2} dy \frac{\partial}{\partial x} \Phi(x=0, y, E)}{\int_{-S/2}^{S/2} dy} \quad (2.4c)$$

$$y(x) = S - \frac{2}{\sqrt{3}} x \quad (3.4d)$$

so that $D(x, y, E)$ is replaced by its flux weighted, energy-group value, we obtain the following form of Fick's Law

$$\bar{J}_{g,x}^{i,j,k}(p) \equiv -D_g^{i,j,k} \frac{\partial}{\partial x} \bar{\Phi}_g^{i,j}(p) \quad (3.5)$$

At this point we have related the current to the surface averaged flux $\bar{\Phi}_g^{i,j,k}(p)$. Some discrete differencing must be done to approximate the derivative in Eqn. 3.5. The QUARTZ code allows for two different formulations. For both formulations we may define a volume averaged flux

$$\bar{\bar{\Phi}}_g^{i,j,k} \equiv \frac{1}{V_{ijk}} \int_{\Delta E_g} dE \int_0^{x_j} dx \int_{-y(x)/2}^{+y(x)/2} dy \Phi(x, y, E) \quad (3.6)$$

and a transverse averaged flux

$$\bar{\Phi}_g^{i,j,k}(x) \equiv \frac{1}{y(x)} \int_{\Delta E_g} dE \int_{-y(x)/2}^{+y(x)/2} dy \Phi(x, y, E) \quad (3.7)$$

The Finite Difference Formulation. The finite difference approximation for the derivative makes use of the value of $\Phi(x, y, E)$ at $x = 0$. The transverse averaged flux becomes

$$\overline{\Phi}_g^{i,j,k}(x) \equiv \frac{1}{y(0)} \int_{\Delta E_g} dE \int_{-S/2}^{+S/2} dy \Phi(x=0, y, E) \quad (3.8)$$

where the limits of integration have been fixed to reflect integration over the surface at $x = 0$. By using Eqn. 3.6 and 3.8, the derivative is approximated by the change between the surface and volume averaged fluxes, yielding the finite difference expression for current across face p .

$$\overline{J}_{g,X}^{i,j,k}(p) \equiv -D_g^{i,j} \left[\frac{\overline{\Phi}_g^{i,j,k} - \overline{\Phi}_g^{i,j,k}(p)}{X_C/2} \right] \quad (3.9)$$

An expression analogous to Eqn. 3.9 can be written for *Node A*. By applying the conditions of continuity of current and continuity of flux at $x = 0$, the current at $x = 0$ can be expressed in terms of the volume averaged fluxes $\overline{\Phi}_g^{i,j,k}$ and $\overline{\Phi}_g^{NodeA}$.

It is possible to correct Eqn. 3.9 by introducing a *discontinuity factor*. The purpose of this quantity is to correct the finite difference formulation for not only the approximation of the derivative, but also for errors introduced by homogenization as well as for the use of Fick's Law itself. The resulting equation is

$$\bar{J}_{g,X}^{i,j,k}(p) = -D_g^{i,j,k} \left[\frac{\bar{\Phi}_g^{i,j,k}(p) - \bar{\Phi}_g^{i,j,k}}{f_{g,p}^{i,j,k}} \right] \frac{X_C/2}{X_C/2} \quad (3.10)$$

Similarly, for *NodeA* ,

$$\bar{J}_{g,X}^{NodeA}(p') = -D_g^{NodeA} \left[\frac{\bar{\Phi}_g^{NodeA} - \bar{\Phi}_g^{NodeA}(p')}{f_{g,p'}^{NodeA}} \right] \frac{X_C/2}{X_C/2} \quad (3.11)$$

After introducing the discontinuity factors, we continue to apply the continuity of flux to the uncorrected, physical fluxes $\bar{\Phi}_g^{i,j}(p) = \bar{\Phi}_g^{NodeA}(p')$. If the discontinuity factors on either side of the surface are not equal, the corrected fluxes will be unequal, or discontinuous.

By applying this condition, as well as the continuity of current, we can obtain a final expression for current.

$$\bar{J}_{g,X}^{i,j,k}(p) = -\bar{J}_{g,X}^{NodeA}(p') = \frac{2}{X_C} \left[\frac{1}{D_g^{i,j,k}} + \frac{1}{D_g^{NodeA}} \frac{f_{g,p'}^{NodeA}}{f_{g,p=1}^{i,j,k}} \right]^{-1} \left[\bar{\Phi}_g^{i,j} - \frac{f_{g,p'}^{NodeA}}{f_{g,p}^{i,j,k}} \bar{\Phi}_g^{NodeA} \right] \quad (3.12)$$

Note that the discontinuity factors appear in ratios, not as individual factors.

There is also an expression for the current at the boundary. The current may be expressed in terms of the surface averaged flux as specified by an albedo boundary condition, given in Eqn. 3.13.

$$\alpha_{g,p}^{i,j,k} \bar{J}_{g,X}^{i,j,k}(p) = \beta_{g,p}^{i,j,k} \bar{\Phi}_g^{i,j,k}(p) \quad (3.13)$$

Since the current at the surface can still be expressed in terms of the corrected surface flux, we may employ Eqn. 3.10 and substitute for the surface averaged flux in Eqn. 3.13.

This leaves, for the current at the surface of the reactor,

$$\bar{J}_{g,X}^{i,j,k}(p) = \frac{2}{X_c} \left[\frac{\beta_{g,p}^{i,j,k}}{D_g^{i,j,k}} + \frac{2}{X_c} \frac{\alpha_{g,p}^{i,j,k}}{f_{g,p}^{i,j,k}} \right]^{-1} \left[\beta_{g,p}^{i,j,k} \bar{\Phi}_g^{i,j,k} \right] \quad (3.14)$$

The expressions for current in the axial directions analogous to Eqns. 3.12 and 3.14 are identical to those equations excepting that X_c is replaced by Z_d , the center-to-center distance between axial nodes.

When these expressions for current are substituted into the static form of Eqn. 1.2.4a, we have

$$\begin{aligned}
& \frac{A_{p=1}}{V_{ijk}} \cdot \frac{2}{X_c} \left[\frac{1}{D_g^{ijk}} + \frac{1}{D_g^{i-1,j,k}} \frac{f_{g,p'=2}^{i-1,j,k}}{f_{g,p=1}^{ijk}} \right]^{-1} \left[\overline{\overline{\Phi}}_g^{ijk} - \frac{f_{g,p'=2}^{i-1,j,k}}{f_{g,p=1}^{ijk}} \overline{\overline{\Phi}}_g^{i-1,j,k} \right] \\
& + \frac{A_{p=2}}{V_{ijk}} \cdot \frac{2}{X_c} \left[\frac{1}{D_g^{ijk}} + \frac{1}{D_g^{i+1,j,k}} \frac{f_{g,p'=1}^{i+1,j,k}}{f_{g,p=2}^{ijk}} \right]^{-1} \left[\overline{\overline{\Phi}}_g^{ijk} - \frac{f_{g,p'=1}^{i+1,j,k}}{f_{g,p=2}^{ijk}} \overline{\overline{\Phi}}_g^{i+1,j,k} \right] \\
& + \frac{A_{p=3}}{V_{ijk}} \cdot \frac{2}{X_c} \left[\frac{1}{D_g^{ijk}} + \frac{1}{D_g^{i+1,j+1,k}} \frac{f_{g,p'=3}^{i+1,j+1,k}}{f_{g,p=3}^{ijk}} \right]^{-1} \left[\overline{\overline{\Phi}}_g^{ijk} - \frac{f_{g,p'=3}^{i+1,j+1,k}}{f_{g,p=3}^{ijk}} \overline{\overline{\Phi}}_g^{i+1,j+1,k} \right] \\
& + \frac{A_{p=4}}{V_{ijk}} \cdot \frac{2}{X_d} \left[\frac{1}{D_g^{ijk}} + \frac{1}{D_g^{i,j,k+1}} \frac{f_{g,p'=5}^{i,j,k+1}}{f_{g,p=4}^{ijk}} \right]^{-1} \left[\overline{\overline{\Phi}}_g^{ijk} - \frac{f_{g,p'=5}^{i,j,k+1}}{f_{g,p=4}^{ijk}} \overline{\overline{\Phi}}_g^{i,j,k+1} \right] \\
& + \frac{A_{p=5}}{V_{ijk}} \cdot \frac{2}{X_d} \left[\frac{1}{D_g^{ijk}} + \frac{1}{D_g^{i,j,k-1}} \frac{f_{g,p'=4}^{i,j,k-1}}{f_{g,p=5}^{ijk}} \right]^{-1} \left[\overline{\overline{\Phi}}_g^{ijk} - \frac{f_{g,p'=4}^{i,j,k-1}}{f_{g,p=5}^{ijk}} \overline{\overline{\Phi}}_g^{i,j,k-1} \right] \\
& + \sum_g^{ijk} \overline{\overline{\Phi}}_g^{ijk} = \sum_{g'=1}^G \sum_{gg'}^{ijk} \overline{\overline{\Phi}}_g^{ijk} + \frac{\chi_g}{\lambda} \sum_{g'=1}^G v \sum_{f,g'}^{ijk} \overline{\overline{\Phi}}_{g'}^{ijk}
\end{aligned} \tag{3.15}$$

For i even, $(i-1,j-1,k)$ replaces $(i+1,j+1,k)$ on the third line of equation 3.15. For faces $p=1,p=2$, or $p=3$ on a boundary, lines 1, 2, or 3 respectively are replaced with

$$\frac{A_p}{V_{ijk}} \frac{2}{X_c} \left[\frac{\beta_{g,p}^{ijk}}{D_g^{ijk}} + \frac{2}{X_c} \frac{\alpha_{g,p}^{ijk}}{f_{g,p}^{ijk}} \right]^{-1} \left[\beta_{g,p}^{ijk} \overline{\overline{\Phi}}_g^{ijk} \right] \tag{3.16}$$

If $p=4$ or $p=5$ lies on a boundary, lines 4 or 5 are replaced with Eqn. 3.16 with X_d used rather than X_c .

The Quadratic Formulation. There is another, more accurate way of approximating the current. Instead of approximating $\Phi(x, y, E)$ at $x = 0$ as in Eqn. 3.8, it is assumed to be a quadratic polynomial varying in the domain from $x \in [0, X_d]$ as defined in Figure 3.1.

Referring to this figure, the polynomial representation of $\Phi(x, y, E)$ is set to equal the

surfaced averaged flux $\bar{\Phi}_g^{i,j,k}(p)$ at $x = 0$, the point flux $\Phi_g^{i,j,k}(X_d, 0)$ when $x = X_d$, and the volume averaged flux when integrated over the node according to

$$\frac{1}{V^{ijk}} \int_0^{x_d} dx y(x) \bar{\Phi}_g^{i,j,k}(x) = \bar{\bar{\Phi}}_g^{i,j,k} \quad (3.17)$$

By enforcing these restrictions, we obtain an expression for $\bar{\Phi}_g^{i,j,k}(p)$ found in Eqn. 3.5.

The expression is quadratic in x , and its analytical derivative can be taken. By evaluating the derivative at each surface of the node, the current across each surface of every node can be determined.

Because the current is continuous across the node surfaces, expressions for current across a surface can be made for node IJK or adjoining nodes. The assumed quadratic form of $\Phi(x, y, E)$ results in a complicated coupling. In each node, each I-J surface (those of the triangle) couples the node to three additional nodes. This is in contrast to the single adjacent node coupled to node IJK by the finite difference formulation. The following figure demonstrates the coupling.

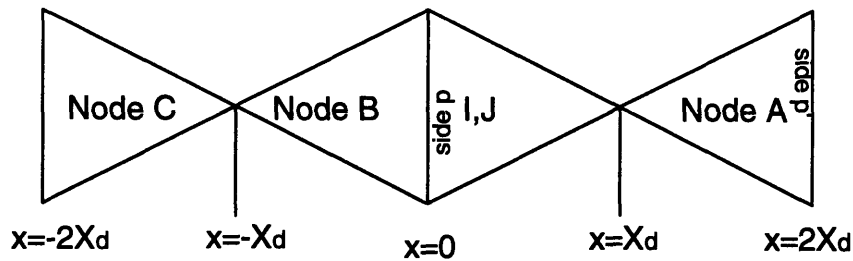


Figure 3.2. Planar Coupling of Node I,J,K Through the Quadratic Current Formulation, Ref. [D1]

Using this coupling, we can write the following general formula for the quadratic current across a surface in the I-J directions.

$$\bar{J}_g^{ijk}(p) = \left\{ \frac{X_d}{20} \cdot \frac{f_{g,p}^{ijk}}{D_g^{ijk}} \left[\frac{4D_g^{NodeA} + 5D_g^{ijk}}{D_g^{NodeA} + D_g^{ijk}} \right] \right\}^{-1} \times \left\{ \begin{array}{l} -\bar{\Phi}_g^{ijk}(p) - f_{g,p}^{ijk} \cdot \frac{X_d}{20} \cdot \frac{\bar{J}_g^{NodeA}(p')}{D_g^{NodeA} + D_g^{ijk}} \\ + f_{g,p}^{ijk} \cdot \frac{D_g^{ijk} + \frac{6}{5} D_g^{NodeA}}{D_g^{ijk} + D_g^{NodeA}} \cdot \bar{\Phi}_g^{ijk} \\ - f_{g,p}^{ijk} \cdot \frac{D_g^{NodeA}}{5[D_g^{NodeA} + D_g^{NodeA}]} \cdot \bar{\Phi}_g^{NodeA} \end{array} \right\} \quad (3.18)$$

A similar equation can be written for the current at $x = 0$ in terms of Node B and Node C. When these equations are combined and the surface flux at $x = 0$ eliminated, we are left with the following equation for current across a surface in the I-J directions ($p=1,2, \text{ or } 3$).

$$\bar{J}_g^{ijk}(p) = - \left\{ \frac{X_d}{20D_g^{NodeB}} \left[\frac{4D_g^{NodeC} + 5D_g^{NodeB}}{D_g^{NodeC} + D_g^{NodeB}} \right] + \frac{X_d}{20D_g^{ijk}} \frac{f_{g,p}^{ijk}}{f_{g,p'}^{NodeB}} \left[\frac{4D_g^{NodeA} + 5D_g^{ijk}}{D_g^{NodeA} + D_g^{ijk}} \right] \right\} \times \left\{ \begin{array}{l} \frac{D_g^{NodeC}}{5[D_g^{NodeC} + D_g^{NodeB}]} \bar{\Phi}_g^{NodeC} + \frac{D_g^{NodeB} + \frac{6}{5} D_g^{NodeC}}{D_g^{NodeB} + D_g^{NodeC}} \bar{\Phi}_g^{NodeB} \\ \frac{f_{g,p}^{ijk}}{f_{g,p'}^{NodeB}} \cdot \frac{D_g^{ijk} + \frac{6}{5} D_g^{NodeA}}{D_g^{ijk} + D_g^{NodeA}} \bar{\Phi}_g^{ijk} + \frac{f_{g,p}^{ijk}}{f_{g,p'}^{NodeB}} \cdot \frac{D_g^{NodeA}}{5[D_g^{ijk} + D_g^{NodeA}]} \bar{\Phi}_g^{NodeA} \\ \frac{X_d}{20} \cdot \frac{\bar{J}_g^{NodeC}(p)}{D_g^{NodeC} + D_g^{NodeB}} + \frac{f_{g,p}^{ijk}}{f_{g,p'}^{NodeB}} \cdot \frac{X_d}{20} \cdot \frac{\bar{J}_g^{NodeA}(p')}{D_g^{NodeA} + D_g^{ijk}} \end{array} \right\}^{-1} \quad (3.19)$$

For the axial direction ($p=4 \text{ or } 5$) we write

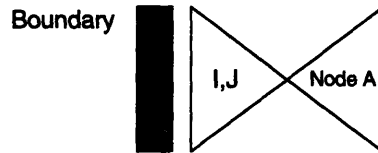
$$\bar{J}_g^{ijk}(p) = \left\{ \frac{Z_d f_{g,p}^{ijk}}{3D_g^{ijk}} \right\}^{-1} \times \left\{ -\bar{\Phi}_g^{ijk}(p) + f_{g,p}^{ijk} \bar{\Phi}_g^{ijk} + \frac{Z_d f_{g,p}^{ijk}}{6D_g^{ijk}} \bar{J}_g^{ijk}(p) \right\} \quad (3.20)$$

Here again, an analogous equation for current across the same surface may be written in terms of quantities from *Node A*. Combining the two equations and eliminating the surface flux term, we are left with an expression for the current in the axial direction.

$$\bar{J}_g^{ijk}(p) = \left\{ \frac{Z_d}{3D_g^{NodeA}} + \frac{f_{g,p}^{ijk}}{f_{g,p'}^{NodeA}} \cdot \frac{Z_d}{3D_g^{ijk}} \right\}^{-1} \left\{ \begin{array}{l} \frac{f_{g,p}^{ijk}}{f_{g,p'}^{NodeA}} \bar{\Phi}_g^{ijk} - \bar{\Phi}_g^{NodeA} + \frac{Z_d}{6D_g^{ijk}} \cdot \frac{f_{g,p}^{ijk}}{f_{g,p'}^{NodeA}} \bar{J}_g^{ijk}(p') \\ -\frac{Z_d}{6D_g^{NodeA}} \bar{J}_g^{NodeA}(p') \end{array} \right\} \quad (3.21)$$

At the boundaries, the current is still related to the flux through Eqn. 3.13. Because of the extended coupling, nodes adjoining the boundary are also affected by the boundary condition. This coupling is manifested in the I-J directions in five possible scenarios. The currents for these five cases are presented below. These formulas were derived for the Instrumented Flux Synthesis Project. If the change in sign convention is taken into account, they are identical to formulas derived for the original QUARTZ code [D1].

- Case 1: Nodes B and C External to Problem



$$\bar{J}_g^{ijk}(p) = -\frac{\beta_{g,p}^{ijk}}{\Gamma_1} \left\{ -\Gamma_2 \bar{\Phi}_g^{ijk} + \Gamma_3 \bar{\Phi}_g^{NodeA} + \Gamma_4 \bar{J}_g^{NodeA}(p') \right\} \quad (3.22)$$

where

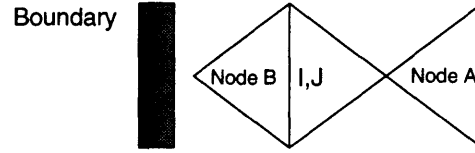
$$\Gamma_1 \equiv \frac{X_d}{20} \cdot \frac{f_{g,p}^{ijk}}{D_g^{ijk}} \beta_{g,p}^{ijk} \cdot \frac{5D_g^{ijk} + 4D_g^{NodeA}}{D_g^{ijk} + D_g^{NodeA}} + \alpha_{g,p}^{ijk}$$

$$\Gamma_2 \equiv f_{g,p}^{ijk} \cdot \frac{D_g^{ijk} + \frac{6}{5} D_g^{NodeA}}{D_g^{ijk} + D_g^{NodeA}}$$

$$\Gamma_3 \equiv f_{g,p}^{ijk} \cdot \frac{D_g^{NodeA}}{5(D_g^{ijk} + D_g^{NodeA})}$$

$$\Gamma_4 \equiv f_{g,p}^{ijk} \cdot \frac{X_d/20}{D_g^{ijk} + D_g^{NodeA}}$$

- Case 2: Node C External to Problem



$$\bar{J}_g^{ijk}(p) = \frac{-1}{\Gamma_1} \cdot \left\{ \Gamma_2 \bar{\Phi}_g^{NodeB} - \Gamma_3 \bar{\Phi}_g^{ijk} + \Gamma_4 \bar{\Phi}_g^{NodeA} + \bar{J}_g^{NodeA}(p') \right\} \quad (3.23)$$

where

$$\Gamma_1 \equiv \frac{X_d}{20} \cdot \frac{f_{g,p}^{ijk}}{f_{g,p'}^{NodeB}} \cdot \frac{5D_g^{ijk} + 4D_g^{NodeA}}{D_g^{ijk} + D_g^{NodeA}} + \frac{X_d}{D_g^{NodeB}} \cdot \frac{X_d \beta_{g,point}^{NodeB} + 3D_g^{NodeB} \alpha_{g,point}^{NodeB}}{5X_d \beta_{g,point}^{NodeB} + 12D_g^{NodeB} \alpha_{g,point}^{NodeB}}$$

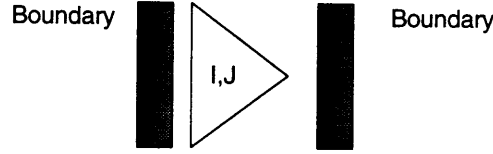
$$\Gamma_2 \equiv \frac{6X_d \beta_{g,point}^{NodeB} + 12D_g^{NodeB} \alpha_{g,point}^{NodeB}}{5X_d \beta_{g,point}^{NodeB} + 12D_g^{NodeB} \alpha_{g,point}^{NodeB}}$$

$$\Gamma_3 \equiv \frac{f_{g,p}^{ijk}}{f_{g,p'}^{NodeB}} \cdot \frac{D_g^{ijk} + \frac{6}{5} D_g^{NodeA}}{D_g^{ijk} + D_g^{NodeA}}$$

$$\Gamma_4 \equiv \frac{f_{g,p}^{ijk}}{f_{g,p'}^{NodeB}} \cdot \frac{D_g^{NodeA}}{5(D_g^{ijk} + D_g^{NodeA})}$$

$$\Gamma_5 \equiv \frac{f_{g,p}^{ijk}}{f_{g,p'}^{NodeB}} \cdot \frac{X_d/20}{D_g^{ijk} + D_g^{NodeA}}$$

- Case 3: Nodes A and B External to Problem



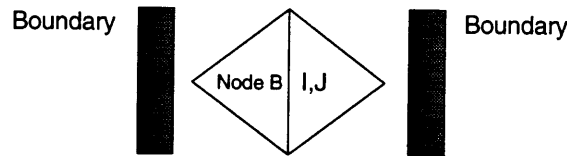
$$\bar{J}_g^{ijk}(p) = \frac{\beta_{g,p}^{ijk}}{\Gamma_1} \Gamma_2 \bar{\bar{\Phi}}_g^{ijk} \quad (3.24)$$

where

$$\Gamma_1 \equiv \frac{X_d}{D_g^{ijk}} f_{g,p}^{ijk} \beta_{g,p}^{ijk} \cdot \frac{X_d \beta_{g,point}^{ijk} + 3D_g^{ijk} \alpha_{g,point}^{ijk}}{5X_d \beta_{g,point}^{ijk} + 12D_g^{ijk} \alpha_{g,point}^{ijk}} + a_{g,point}^{ijk}$$

$$\Gamma_2 \equiv f_{g,p}^{ijk} \cdot \frac{6X_d \beta_{g,point}^{ijk} + 12D_g^{ijk} \alpha_{g,point}^{ijk}}{5X_d \beta_{g,point}^{ijk} + 12D_g^{ijk} \alpha_{g,point}^{ijk}}$$

- Case 4: Nodes A and C External to the Problem



$$J_g^{ijk}(p) = \frac{-1}{\Gamma_1} \cdot \left\{ -\Gamma_2 \bar{\bar{\Phi}}_g^{ijk} + \Gamma_3 \bar{\bar{\Phi}}_g^{NodeB} \right\} \quad (3.25)$$

where

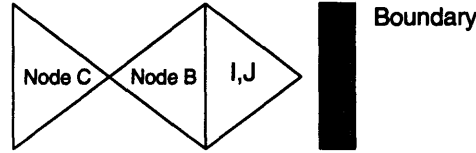
$$\Gamma_1 \equiv \frac{X_d}{D_g^{ijk}} \cdot \frac{f_{g,p}^{ijk}}{f_{g,p'}^{NodeB}} \cdot \frac{X_d \beta_{g,point}^{ijk} + 3D_g^{ijk} \alpha_{g,point}^{ijk}}{5X_d \beta_{g,point}^{ijk} + 12D_g^{ijk} \alpha_{g,point}^{ijk}}$$

$$+ \frac{X_d}{D_g^{NodeB}} \cdot \frac{X_d \beta_{g,point}^{NodeB} + 3D_g^{NodeB} \alpha_{g,point}^{NodeB}}{5X_d \beta_{g,point}^{NodeB} + 12D_g^{NodeB} \alpha_{g,point}^{NodeB}}$$

$$\Gamma_2 \equiv \frac{f_{g,p}^{ijk}}{f_{g,p'}^{NodeB}} \cdot \frac{6X_d \beta_{g,point}^{ijk} + 12D_g^{ijk} \alpha_{g,point}^{ijk}}{5X_d \beta_{g,point}^{ijk} + 12D_g^{ijk} \alpha_{g,point}^{ijk}}$$

$$\Gamma_3 \equiv \frac{6X_d \beta_{g,point}^{NodeB} + 12D_g^{NodeB} \alpha_{g,point}^{NodeB}}{5X_d \beta_{g,point}^{NodeB} + 12D_g^{NodeB} \alpha_{g,point}^{NodeB}}$$

- Case 5: Node A External to Problem



This case in node IJK is the same as Case 2 in node I-1,JK. In the QUARTZ code, the indices are switched to the latter node, and Case 2 is solved.

- Axial Boundary Condition:

$$\bar{J}_g^{ijk}(p) = \frac{\beta_{g,p}^{ijk}}{\alpha_{g,p}^{ijk} + f_{g,p}^{ijk} \beta_{g,p}^{ijk} \frac{Z_d}{3D_g^{ijk}}} \left\{ f_{g,p}^{ijk} + \frac{Z_d}{6D_g^{ijk}} f_{g,p}^{ijk} \bar{J}_g^{ijk}(p') \right\} \quad (3.26)$$

In both the interior nodes and the boundaries, the quadratic expressions for current are themselves dependent upon currents across other surfaces. Previous work [G2,B3] has shown that a simultaneous solution of the quadratic currents does not converge. What has been proposed instead is a non-linear iteration method [S3]. In this method, the finite difference equations are solved, and the finite difference currents are calculated from these

results. These currents are then used to calculate the quadratic currents. The solution process implemented in QUARTZ is illustrated in Figure 3.

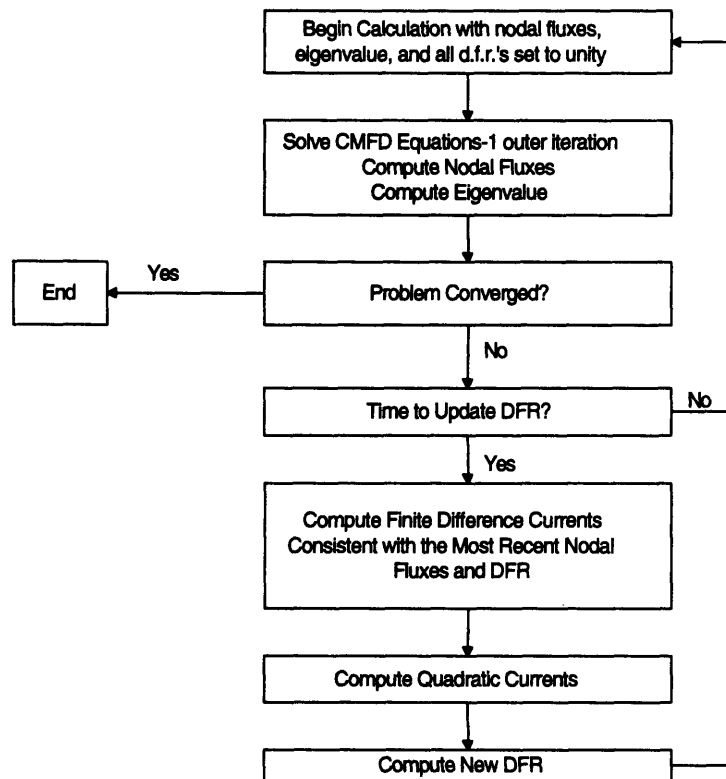


Figure 3.3. Non-linear Iteration Method in QUARTZ. Ref. [D1]

It is hoped that by using the finite difference equations, the well established stability characteristics of those equations can be employed in solving for the nodal fluxes. This is coupled with a higher order approximation of the current through the quadratic current calculations and discontinuity factor updates.

3.3 SUPERNODAL ANALYSIS IN TRIANGULAR GEOMETRY

In the previous section, we discussed how the nodal averaged fluxes were determined using the nodal diffusion equations with two different approximations for the current, the finite difference and quadratic formulations. These approximations are made to replicate reference results through the use of discontinuity factors.

Nothing has yet been said about how to obtain these reference results to calculate the discontinuity factors. If none are available, the discontinuity factors must be set to unity. In this case, the mesh must be fine enough to lessen the effect of homogenization errors, increasing the calculational time.

In using the QUARTZ code to generate flux shapes for use in the synthesis project, it is desirable to keep the number of nodes to a minimum, i.e. maximizing the mesh size. For this reason, an accurate reference case should be used to generate discontinuity factors for a coarse mesh model.

There is also a motivation to develop coarse mesh models for transient analysis of the MITR core. Such analyses can be performed using QUARTZ. While transient analyses could be performed with a fine mesh model, the computational times for accurate results may be prohibitively expensive. A coarse mesh model brings such times to a manageable level.

There are a number of options for the generation of reference results. Given the complexity of the MITR core, one could be naturally led to use Monte Carlo methods. Such methods are extremely useful in describing complex geometries and provide a great

deal of information, including surface averaged currents and volume averaged fluxes. A model of the MITR already exists [R1] and has been used extensively in support of other projects at the reactor. The code used to model the reactor is MCNP, version 4A [B2]

In fact, a previous attempt was already made at using this model to generate cross sections and flux shapes for the Instrumented Synthesis Project [K2]. However, because of edits not present in the present version of MCNP, the effort could not be brought to a successful conclusion. This does not, however, eliminate simply using MCNP to generate the flux shapes themselves. This possibility will be discussed more in Chapter 5.

In the absence of the Monte Carlo model, we are left with homogenizing a fine mesh model of the reactor. It seems reasonable to use the same code system to generate both the fine and coarse mesh results. The fine mesh results serve as the reference cases, from which discontinuity factors are derived for the large node cases.

The steps in generating coarse mesh results are as follows:

1. Perform a fine node calculation, using all discontinuity factors equal to 1.0.
2. Fluxes found in the fine mesh are used to determine flux-averaged cross sections for the coarse mesh as well as coarse mesh average fluxes.
3. Volume-averaged fluxes and surface-averaged currents for the large nodes are found from small node results.
4. Discontinuity factors for the large nodes are determined from these coarse mesh volume averaged fluxes and surface averaged currents.
5. QUARTZ is used to generate coarse mesh fluxes which are used as flux shapes for the instrumented synthesis of actual fluxes in the reactor.

Steps 2-4 were incorporated into the QUARTZ code, developed to support the instrumented synthesis project. The details of those steps are given below.

Step 2: Determination of flux-averaged cross sections

We wish to find cross sections for a large node, denoted n , made up of smaller nodes, denoted u . The fine mesh cross sections are multiplied by the corresponding flux, then divided by the summation of all the fluxes in node n . In this way, the total reaction rate of the interaction in question is preserved. For reaction α , the large node cross section is

$$\Sigma_{\alpha,g}^n = \frac{\sum_{u \in n} \Sigma_{\alpha,g}^u \bar{\Phi}_g^u V^u}{\sum_{u \in n} \bar{\Phi}_g^u V^u} \quad (3.27)$$

Step 3. Determination of volume-average fluxes and surface-averaged currents

The volume-averaged flux is found by summing the flux×volume products of the small nodes within each large node, then dividing by the large node volume. For small nodes u contained within large node n

$$\bar{\Phi}_g^n = \frac{\sum_{u \in n} \bar{\Phi}_g^u V^u}{\sum_{u \in n} V^u} \quad (3.28)$$

The surface averaged currents are defined analogously, but only for fine mesh surfaces lying on the large node surface.

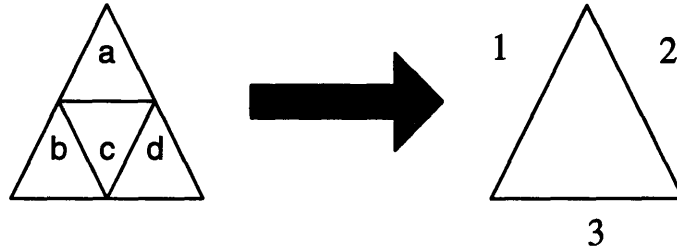


Figure 3.4. Fine Mesh Collapsing

In Figure 3.4, side 1 of small nodes a and b are used to find the current across side 1 of the large node. Similarly, side 2 of nodes a and d are used in determining the current across side 2 of the large node. Note that the currents across the boundaries of small node c are not used in determining the currents across any of the faces of the large node. For small node surfaces p lying on large node surface P ,

$$\bar{J}_g^n(P) = \frac{\sum_{u \in n} \sum_{p \in P} \bar{J}_g^u(p) A^u(p)}{\sum_{u \in n} \sum_{p \in P} A^u(p)} \quad (3.29)$$

Step 4: Determination of large node discontinuity factors.

The equations for the finite difference approximation for current are given in Eqns. 3.10 and 3.13 for faces in the interior and on the boundary of the reactor. Analogous

equations for the quadratic approximation are Eqns. 3.18, 3.20, and 3.22 through 3.26. In all of these cases, the approximations have been corrected through the use of discontinuity factors. If we wish to generate large node flux shapes from small node results, we must calculate these discontinuity factors. Each of the equations for current are solved for the discontinuity factor $f_{g,p}^{ijk}$. Once the average fluxes, currents, and cross sections have been determined from the fine mesh results, discontinuity factors are calculated according to those equations. They are given without derivation below.

Finite Difference

- All Nodes Internal

$$f_{g,p}^{ijk} = \frac{\bar{\Phi}_g^{ijk}(p)}{\bar{\Phi}_g^{ijk} - \frac{X_C}{2D_g^{ijk}} J_g^{ijk}(p)} \quad (3.30)$$

Note that in the expression for the internal discontinuity factors, the surface averaged flux across side p , $\bar{\Phi}_g^{ijk}(p)$, appears. However, the discontinuity factors in the internal nodes always appear in ratios. Since the surface averaged flux is the same at the interface of two nodes, it drops from the ratio. However, because QUARTZ reads in discontinuity factors and not their ratios from the input, some value for $\bar{\Phi}_g^{ijk}(p)$ must be used. That value is completely arbitrary. In the implementation of the collapsing subroutines in the QUARTZ code, it is assigned the fast flux in the first small node. Again, any value other than zero is acceptable.

- Node on a Boundary

Here, the surface flux is related to the current by the an albedo condition, given by

Eqn. 3.13

$$\frac{f_{g,p}^{ijk}}{\alpha_{g,p}^{ijk}} = \frac{1}{\frac{\beta_{g,p}^{ijk}}{J_g^{ijk}(p)} \left[\bar{\Phi}_g^{ijk} - \frac{X_c}{2D_g^{ijk}} J_g^{ijk}(p) \right]} \quad (3.31)$$

Quadratic

- All nodes internal, p=1,2,3

$$f_{g,p}^{ijk} = -\bar{\Phi}_p^{ijk} \times \left\{ \frac{X_d}{20D_g^{ijk}} \left[\frac{4D_g^{NodeA} + 5D_g^{ijk}}{D_g^{NodeA} + D_g^{ijk}} \right] J_g^{ijk}(p) + \frac{X_d}{20} \left[\frac{1}{D_g^{NodeA} + D_g^{ijk}} \right] J_g^{NodeA}(p') \right. \\ \left. - \frac{D_g^{ijk} + \frac{6}{5} D_g^{NodeA}}{D_g^{ijk} + D_g^{NodeA}} \bar{\Phi}_g^{ijk} + \frac{D_g^{NodeA}}{5[D_g^{NodeA} + D_g^{ijk}]} \bar{\Phi}_g^{NodeA} \right\}^{-1} \quad (3.32)$$

- All nodes internal, p=4,5

$$f_{g,p}^{ijk} = \bar{\Phi}_{g,p}^{ijk} \times \left\{ \bar{\Phi}_g^{ijk} - \frac{Z_d}{3D_g^{ijk}} J_g^{ijk}(p) + \frac{Z_d}{6D_g^{ijk}} J_g^{ijk}(p') \right\}^{-1} \quad (3.33)$$

Discontinuity factors for large nodes on the boundary are also calculated.

- Case 1: Node B External

$$\frac{f_{g,p}^{ijk}}{\alpha_{g,p}^{ijk}} = \frac{1}{\frac{\beta_{g,p}^{ijk}}{J_g^{ijk}(p)}} \times \left\{ \begin{aligned} & -\frac{X_d}{20D_g^{ijk}} \left[\frac{4D_g^{nodea} + 5D_g^{ijk}}{D_g^{nodea} + D_g^{ijk}} \right] J_g^{ijk}(p) - \frac{X_d}{20} \left[\frac{1}{D_g^{nodea} + D_g^{ijk}} \right] J_g^{nodea}(p') \\ & + \frac{D_g^{ijk} + \frac{6}{5}D_g^{nodea}}{D_g^{ijk} + D_g^{nodea}} \overline{\overline{\Phi}}_g^{ijk} + \frac{D_g^{nodea}}{5[D_g^{nodea} + D_g^{ijk}]} \overline{\overline{\Phi}}_g^{nodea} \end{aligned} \right\}^{-1} \quad (3.34)$$

- Case 2: Node C External

$$f_{g,p}^{ijk} = \overline{\overline{\Phi}}_p^{ijk} \times \left\{ \begin{aligned} & -\frac{X_d}{20D_g^{ijk}} \left[\frac{4D_g^{nodea} + 5D_g^{ijk}}{D_g^{nodea} + D_g^{ijk}} \right] J_g^{ijk}(p) - \frac{X_d}{20} \left[\frac{1}{D_g^{nodea} + D_g^{ijk}} \right] J_g^{nodea}(p') \\ & \frac{D_g^{ijk} + \frac{6}{5}D_g^{nodea}}{D_g^{ijk} + D_g^{nodea}} \overline{\overline{\Phi}}_g^{ijk} - \frac{D_g^{nodea}}{5[D_g^{nodea} + D_g^{ijk}]} \overline{\overline{\Phi}}_g^{nodea} \end{aligned} \right\}^{-1} \quad (3.35)$$

- Case 3: Nodes A and B External

$$\frac{f_{g,p}^{ijk}}{\alpha_{g,p}^{ijk}} = \frac{1}{\frac{\beta_{g,p}^{ijk}}{J_g^{ijk}(p)}} \times \left\{ \begin{aligned} & -\frac{X_d}{D_g^{ijk}} \left[\frac{X_d \beta_{g,point}^{ijk} + 3D_g^{ijk} \alpha_{g,point}^{ijk}}{5X_d \beta_{g,point}^{ijk} + 12D_g^{ijk} \alpha_{g,point}^{ijk}} \right] J_g^{ijk}(p) \\ & + \frac{6X_d \beta_{g,point}^{ijk} + 12D_g^{ijk} \alpha_{g,point}^{ijk}}{5X_d \beta_{g,point}^{ijk} + 12D_g^{ijk} \alpha_{g,point}^{ijk}} \overline{\overline{\Phi}}_g^{ijk} \end{aligned} \right\}^{-1} \quad (3.36)$$

- Case 4: Nodes A and C External

$$f_{g,p}^{ijk} = \bar{\Phi}_g^{ijk}(p) \times \left\{ \begin{aligned} & - \frac{X_d}{D_g^{ijk}} \left[\frac{X_d \beta_{g,point}^{ijk} + 3D_g^{ijk} \alpha_{g,point}^{ijk}}{5X_d \beta_{g,point}^{ijk} + 12D_g^{ijk} \alpha_{g,point}^{ijk}} \right] J_g^{ijk}(p) \\ & + \frac{6X_d \beta_{g,point}^{ijk} + 12D_g^{ijk} \alpha_{g,point}^{ijk}}{5X_d \beta_{g,point}^{ijk} + 12D_g^{ijk} \alpha_{g,point}^{ijk}} \bar{\bar{\Phi}}_g^{ijk} \end{aligned} \right\}^{-1} \quad (3.37)$$

- Case 5: Node A External

$$f_{g,p}^{ijk} = \bar{\Phi}_g^{ijk}(p) \times \left\{ \begin{aligned} & - \frac{X_d}{D_g^{ijk}} \left[\frac{X_d \beta_{g,point}^{ijk} + 3D_g^{ijk} \alpha_{g,point}^{ijk}}{5X_d \beta_{g,point}^{ijk} + 12D_g^{ijk} \alpha_{g,point}^{ijk}} \right] J_g^{ijk}(p) \\ & + \frac{6X_d \beta_{g,point}^{ijk} + 12D_g^{ijk} \alpha_{g,point}^{ijk}}{5X_d \beta_{g,point}^{ijk} + 12D_g^{ijk} \alpha_{g,point}^{ijk}} \bar{\bar{\Phi}}_g^{ijk} \end{aligned} \right\}^{-1} \quad (3.38)$$

- Axial Boundary Condition

$$\frac{f_{g,p}^{ijk}}{\alpha_{g,p}^{ijk}} = \frac{1}{\frac{\beta_{g,p}^{ijk}}{J_g^{ijk}(p)}} \times \left\{ - \frac{Z_d}{3D_g^{ijk}} J_g^{ijk}(p) + \bar{\bar{\Phi}}_g^{ijk} + \frac{Z_d}{6D_g^{ijk}} J_g^{ijk}(p') \right\}^{-1} \quad (3.39)$$

The implementation of the node-collapsing routines begins with reaching a converged solution for the eigenvalue and fluxes in the fine-mesh problem. Once the converged solution is attained, large node cross sections, fluxes, and currents are calculated. Those fluxes and currents are then used to calculate discontinuity factors

according to Eqns. 3.30 and 3.31 or 3.32 through 3.39. It is important to realize discontinuity factors for either finite difference or quadratic current approximations can be calculated regardless of the fine mesh solution method. In other words, a finite difference solution method may be used in the fine mesh, but discontinuity factors may be calculated such that the quadratic approximation may be used with the coarse mesh. The coarse mesh, quadratic result should still replicate the fine mesh, finite difference result.

The determination of discontinuity factors from a quadratic, fine mesh solution can be illustrated in Figure 3.5.

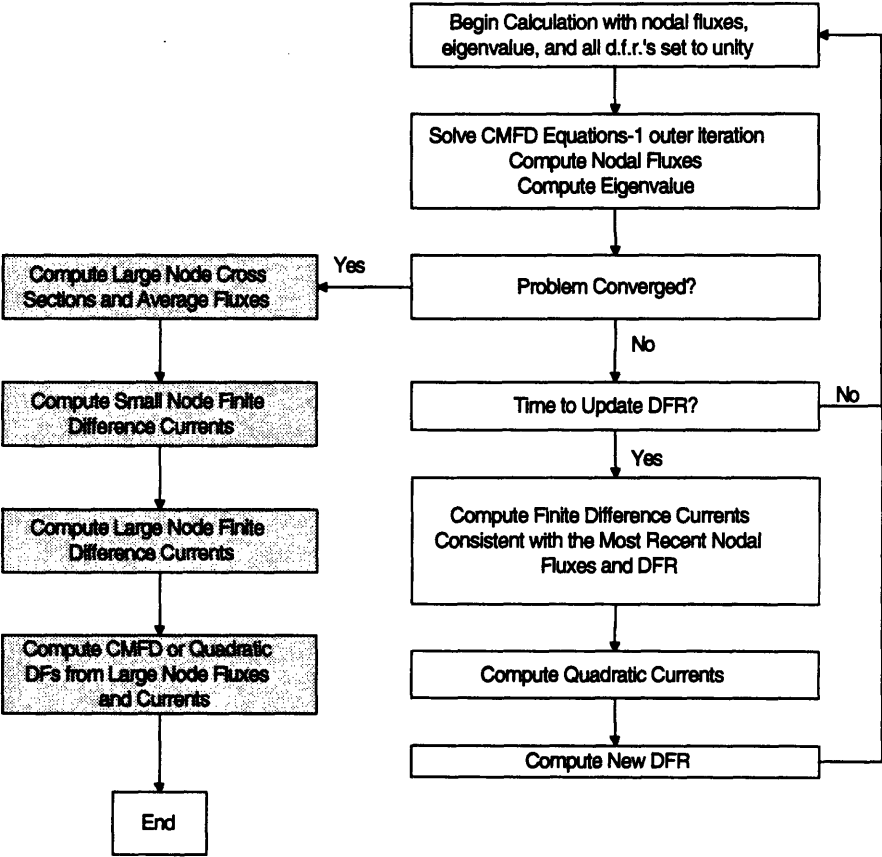


Figure 3.5. Generation of Discontinuity Factors from a Quadratic Fine Mesh Solution

This can be compared to Figure 3.3. The collapsing routines illustrated above are shaded in gray.

3.4 SUPERNODAL RESULTS

With the use of discontinuity factors, we expect the large node fluxes and eigenvalues to match closely those of the fine mesh problems. A number of results are presented in Chapter 5 as part of the MITR model. They show good agreement between the coarse mesh and fine mesh cases. In those cases, the MITR was modeled at a number of different power levels and control blade configurations using a fine mesh. The node structure was collapsed, and cross sections, fluxes, and currents were calculated for these larger nodes. Discontinuity factors were determined, and the large node cases were submitted for calculation again. Both the eigenvalue and the fluxes matched excellently with the fine mesh calculations.

Some smaller cases are listed here to illustrate the accuracy of the supernodal procedures. They are based on the problem used by DeLorey to test the quadratic method in Version 1.0 of QUARTZ. The problem consists of 24 nodes and one or two fissionable materials. The perimeter boundary conditions are given with each case. Detailed specifications are given in Appendix 1.

To generate reference results, each large node is subdivided into 256 smaller nodes for a total of 6144 nodes in the reference problem. The collapsing routines are then employed to reduce the number of nodes to the original 24 and to calculate discontinuity

factors on all faces for each of the 24 nodes. These discontinuity factors should allow the large node results to match the small node eigenvalue and fluxes.

Case I: Homogeneous, $\alpha = 2.0$ $\beta = 1.0$ [zero net returning current]

Fine Mesh k_{eff}	CMFD k_{eff} DFs $\neq 1$	Quadratic k_{eff} DFs $\neq 1$	CMFD avg/max error in thermal flux	Quadratic avg/max error in thermal flux
1.03880	1.03879	1.03879	0.0014%/0.0029%	0.0013%/0.0029%

For this particular albedo boundary condition, the CMFD and quadratic supernodal solutions perform equally well. It is presumed that the higher order quadratic solution demands less of its discontinuity factors. A fixed set of quadratic discontinuity factors could be used over a wide range of conditions with less error than a fixed set of finite difference factors used over the same range.

These results can be compared to large node results when the discontinuity factor ratios are set to unity:

Fine Mesh k_{eff}	CMFD k_{eff} DFs = 1	Quadratic k_{eff} DFs = 1	CMFD avg/max error in thermal flux	Quadratic avg/max error in thermal flux
1.03880	1.04314	1.01452	4.62%/6.84%	0.52%/0.83%

Obviously the use of discontinuity factors provides a vast improvement over traditional methods. It is interesting to note that, although the error in the quadratic estimate of the flux is better than the CMFD, the eigenvalue is much worse. DeLorey makes some explanations of this phenomena, attributing the problem to nodes at the boundary where the flux changes dramatically.

“A study performed by Gehin [G3] comparing quadratic, cubic, and quartic polynomial methods in Cartesian geometry has shown that the quadratic nodal method is capable of producing accurate node-averaged fluxes, but

can give poor estimates of the current at surfaces. This is because the quadratic method has few degrees of freedom.”
[D1]

In supernodal methods, the currents from the fine mesh solution are used to generate discontinuity factors for the coarse mesh. If the quadratic method is incapable of reproducing those currents at the boundaries, even with the benefit of discontinuity factors, the quadratic supernodal eigenvalues may be less accurate than the CMFD supernodal eigenvalues.

Case II: Homogeneous, $\alpha = 0.0$ $\beta = 1.0$ [zero flux]

Fine Mesh k_{eff}	CMFD k_{eff} DFs $\neq 1$	Quadratic k_{eff} DFs $\neq 1$	CMFD avg/max error in thermal flux	Quadratic avg/max error in thermal flux
1.02694	1.02694	1.02694	0.0016%/0.0030%	0.0055%/0.0107%

Again, the quadratic and CMFD supernodal solutions are extremely close to the fine mesh solutions. The CMFD supernodal solution appears to do better in reproducing the flux vector. These results compared to coarse mesh results with unity discontinuity factors yield

Fine Mesh k_{eff}	CMFD k_{eff} DFs = 1	Quadratic k_{eff} DFs = 1	CMFD avg/max error in thermal flux	Quadratic avg/max error in thermal flux
1.02694	1.03209	0.99525	5.62%/8.53%	0.41%/0.96%

The use of discontinuity factors is again a vast improvement.

Case III: Heterogeneous, $\alpha = 1.0$ $\beta = 0.0$ [zero current] CMFD fine mesh solution

Fine Mesh k_{eff}	CMFD k_{eff} DFs $\neq 1$	Quadratic k_{eff} DFs $\neq 1$	CMFD avg/max error in thermal flux	Quadratic avg/max error in thermal flux
1.23892	1.23891	1.23891	0.0111%/0.0194%	0.0557%/0.0903%

Comparison with unity discontinuity factors yields

Fine Mesh k_{eff}	CMFD k_{eff} DFs = 1	Quadratic k_{eff} DFs = 1	CMFD avg/max error in thermal flux	Quadratic avg/max error in thermal flux
1.23892	1.25122	1.23939	4.37%/11.27%	0.557%/1.21%

The use of discontinuity factors is especially evident in the CMFD case, where the maximum error in the flux is reduced by almost three orders of magnitude. Note that, although the supernodal scheme determines flux weighted cross sections from the fine node results, all the large nodes for Case III consisted entirely of either material #1 or material #2. The cross sections remain the same as in the fine mesh case.

The results also lend weight to the assertion that it is the current at the boundary that affects the accuracy of the quadratic solution. When a zero current boundary condition is used, as in Case III, the quadratic estimate of the eigenvalue is as accurate as the CMFD prediction when discontinuity factors are used. When the factors are set to unity, the quadratic prediction of both flux and eigenvalue is far more accurate than the CMFD prediction.

The final case demonstrates that discontinuity factors can be generated from a quadratic fine mesh solution.

Case IIIb: Heterogeneous, $\alpha = 1.0$ $\beta = 0.0$ [zero current] Quadratic fine mesh solution

Fine Mesh k_{eff}	CMFD k_{eff}	Quadratic k_{eff}	CMFD avg/max error in thermal flux	Quadratic avg/max error in thermal flux
1.23884	1.23884	1.23890	0.0135%/0.0227%	0.0586%/0.1420%

The above cases have illustrated that discontinuity factors for either a coarse mesh finite difference or quadratic solution can be generated from a fine mesh solution. The coarse mesh fluxes and eigenvalues match the fine mesh solutions very closely. Furthermore, the coarse mesh discontinuity factors can be generated independently of the fine mesh solution method.

From the above cases, it seems that the CMFD supernodal solutions do a better job of matching the fine mesh results. The problem of currents at the boundaries may prevent the quadratic supernodal method from matching the fine mesh currents at these locations. Although both supernodal methods appear to do an excellent job in matching fine mesh solutions, it would appear prudent to use the CMFD method with appropriate discontinuity factors for the large node problems.

A number of cases will be presented in Chapter 5 in which reference fine mesh models of the MITR are collapsed to large node problems with results in good agreement with the reference cases.

3.5 CONVERGENCE OF THE SOLUTION METHODS

The finite difference equations written in Eqn. 3.15 can be put into matrix form as

$$\underline{\underline{\mathbf{L}}}\Phi = \frac{1}{\lambda} \underline{\underline{\mathbf{M}}}\Phi \quad (3.40)$$

where

$$\underline{\underline{\mathbf{L}}} \equiv \text{the loss operator}$$

$\underline{\underline{\mathbf{M}}}$ \equiv the fission source operator

The flux vector can be determined through an iterative process called the power method

[N1]. Multiplying each side of Eqn. 3.40 by $\underline{\underline{\mathbf{L}}}^{-1}$ allows us to write

$$\underline{\underline{\Phi}} = \frac{1}{\lambda} \underline{\underline{\mathbf{R}}} \underline{\underline{\Phi}} \quad (3.41)$$

where

$$\underline{\underline{\mathbf{R}}} = \underline{\underline{\mathbf{L}}}^{-1} \underline{\underline{\mathbf{M}}}$$

In the power method, the value of the flux vector and eigenvalue at the $m+1$ iteration can be written in terms of quantities from iteration m .

$$\underline{\underline{\Phi}}^{(m+1)} = \frac{1}{\lambda^{(m)}} \underline{\underline{\mathbf{R}}} \underline{\underline{\Phi}}^{(m)} \quad (3.42)$$

$$\lambda^{(m+1)} = \lambda^{(m)} \frac{\langle \underline{\underline{\mathbf{w}}}, \underline{\underline{\Phi}}^{(m+1)} \rangle}{\langle \underline{\underline{\mathbf{w}}}, \underline{\underline{\Phi}}^{(m)} \rangle} \quad (3.43)$$

At each iteration, the $\underline{\underline{\mathbf{L}}}$ matrix must be inverted. For large matrices involving more than two energy groups, this is best accomplished by an iterative method. Thus we have a two-level iteration scheme. The iterations used to find the flux vector and eigenvalue are called *outer iterations*. The inversion of the $\underline{\underline{\mathbf{L}}}$ matrix is accomplished using *inner iterations*.

When applying an iterative method to inverting $\underline{\underline{\mathbf{L}}}$, the mathematical properties of the matrix become important in determining whether the method will converge to the correct solution. Specifically, properties of $\underline{\underline{\mathbf{L}}}$ will determine what properties the iteration matrix, formed as part of the iterative method, possesses. For example, if a Jacobi method is employed, its iteration matrix formed from $\underline{\underline{\mathbf{L}}}$ is

$$\underline{\underline{\mathbf{M}}}_J = \underline{\underline{\mathbf{D}}}^{-1}(\underline{\underline{\mathbf{B}}} + \underline{\underline{\mathbf{U}}}) \quad (3.44)$$

where

$\underline{\underline{\mathbf{D}}}$ \equiv the diagonal of $\underline{\underline{\mathbf{L}}}$

$\underline{\underline{\mathbf{B}}}$ \equiv the lower triangular matrix of $\underline{\underline{\mathbf{L}}}$

$\underline{\underline{\mathbf{U}}}$ \equiv the upper triangular matrix of $\underline{\underline{\mathbf{L}}}$

It can be proven that if largest eigenvalue of the iteration matrix, known as the spectral radius, is less than one, the iterative method will indeed converge to the exact solution [N1]. For large matrices, however, determining all the eigenvalues is a very difficult or even impossible task. We instead look to other properties of $\underline{\underline{\mathbf{L}}}$ that tell us whether the iterative method will converge.

The particular property we are interested is diagonal dominance. A matrix $\underline{\underline{\mathbf{L}}}$ is diagonally dominant by columns if

$$|l_{k,k}| \geq \sum_{l \neq k} |l_{k,l}| \quad (3.45)$$

and diagonally dominant by rows if

$$|l_{k,k}| \geq \sum_{l \neq k} |l_{l,k}| \quad (3.46)$$

In most cases the phrase “diagonal dominance” refers to diagonal dominance by columns.

A matrix is irreducibly diagonally dominant if it is diagonally dominant and

$$|l_{k,k}| > \sum_{l \neq k} |l_{k,l}| \quad (3.47)$$

for at least one value of k .

It is proven by both Varga [V1] and Gherchanoc [G3] that for $\underline{\underline{L}}$ diagonally dominant, the Jacobi iterative scheme will converge to the exact solution. Thus if there is a method to guarantee diagonal dominance of $\underline{\underline{L}}$, we can guarantee that $\underline{\underline{L}}$ can be properly inverted at each outer iteration.

To determine the properties of the CMFD system of equations, we refer to Eqn.

3.15 and make the following definitions.

$$\mathcal{D}_{u+}^l \equiv \frac{1}{h_u^l} \cdot \left[\frac{h_u^l}{2D_g^{lmn}} + \frac{f_{g,u+}^{l-1,m,n}}{f_{g,u-}^{lmn}} \cdot \frac{h_u^{l-1}}{2D_g^{l-1,m,n}} \right] \quad (3.48)$$

$$\mathcal{D}_{u-}^l \equiv \frac{1}{h_u^l} \cdot \left[\frac{h_u^l}{2D_g^{lmn}} \cdot \frac{f_{g,u-}^{lmn}}{f_{g,u+}^{l-1,m,n}} + \frac{h_u^{l-1}}{2D_g^{l-1,m,n}} \right] \quad (3.49)$$

Using these definitions in Eqn. 3.15, the CMFD equations can be cast for i odd as,

$$\begin{aligned} & \left[\begin{array}{cccc} \mathcal{D}_{x+}^i \overline{\overline{\Phi}}_g^{ijk} - \mathcal{D}_{x-}^i \overline{\overline{\Phi}}_g^{i-1,j,k} & + \mathcal{D}_{x-}^{i+1} \overline{\overline{\Phi}}_g^{ijk} - \mathcal{D}_{x+}^{i+1} \overline{\overline{\Phi}}_g^{i+1,j,k} & & \\ + 0 & - & 0 & + \mathcal{D}_{y-}^{i+1,j+1} \overline{\overline{\Phi}}_g^{ijk} - \mathcal{D}_{y+}^{i+1,j+1,k} \overline{\overline{\Phi}}_g^{i+1,j+1,k} \\ + \mathcal{D}_{z+}^k \overline{\overline{\Phi}}_g^{ijk} - \mathcal{D}_{z-}^k \overline{\overline{\Phi}}_g^{i,j,k-1} & + \mathcal{D}_{z-}^{k+1} \overline{\overline{\Phi}}_g^{ijk} - \mathcal{D}_{z+}^{k+1} \overline{\overline{\Phi}}_g^{i,j,k+1} & & \end{array} \right] + \sum_g^{ijk} \overline{\overline{\Phi}}_g^{ijk} \\ & = \frac{\chi_g}{\lambda} \sum_{g'=1}^G \nu \sum_{f,g'}^{ijk} \overline{\overline{\Phi}}_{g'}^{ijk} + \sum_{\substack{g'=1 \\ g' \neq g}}^G \sum_{gg'}^{ijk} \Phi_{g'}^{ijk} \end{aligned} \quad (3.50)$$

and for i even as

$$\begin{aligned} & \left[\begin{array}{cccc} \mathcal{D}_{x+}^i \overline{\overline{\Phi}}_g^{ijk} - \mathcal{D}_{x-}^i \overline{\overline{\Phi}}_g^{i-1,j,k} & + \mathcal{D}_{x-}^{i+1} \overline{\overline{\Phi}}_g^{ijk} - \mathcal{D}_{x+}^{i+1} \overline{\overline{\Phi}}_g^{i+1,j,k} & & \\ + \mathcal{D}_{y+}^j \overline{\overline{\Phi}}_g^{ijk} - \mathcal{D}_{y-}^j \overline{\overline{\Phi}}_g^{i-1,j-1,k} & + 0 & - & 0 \\ + \mathcal{D}_{z+}^k \overline{\overline{\Phi}}_g^{ijk} - \mathcal{D}_{z-}^k \overline{\overline{\Phi}}_g^{i,j,k-1} & + \mathcal{D}_{z-}^{k+1} \overline{\overline{\Phi}}_g^{ijk} - \mathcal{D}_{z+}^{k+1} \overline{\overline{\Phi}}_g^{i,j,k+1} & & \end{array} \right] + \sum_g^{ijk} \overline{\overline{\Phi}}_g^{ijk} \\ & = \frac{\chi_g}{\lambda} \sum_{g'=1}^G \nu \sum_{f,g'}^{ijk} \overline{\overline{\Phi}}_{g'}^{ijk} + \sum_{\substack{g'=1 \\ g' \neq g}}^G \sum_{gg'}^{ijk} \Phi_{g'}^{ijk} \end{aligned} \quad (3.51)$$

We have introduced the removal cross section, defined as

$$\sum_g^{ijk} \equiv \sum_{i,g}^{ijk} - \sum_{gg}^{ijk} \quad (3.52)$$

The zeroes have been added to highlight the differences between the *i even* and *i odd* cases. The loss matrix $\underline{\underline{L}}$ consists of the operations on the left sides of Eqns. 3.50 and 3.51. By examining these equations, we can write the diagonal and off diagonal elements of $\underline{\underline{L}}$. For *i odd*, the diagonal elements for node IJK are

$$\mathcal{D}_{x+}^i + \mathcal{D}_{x-}^{i+1} + \mathcal{D}_{y-}^{i+1,j+1} + \mathcal{D}_{z+}^k + \mathcal{D}_{z-}^{k+1} + \sum_g^{ijk}$$

and for *i even* they are

$$\mathcal{D}_{x+}^i + \mathcal{D}_{x-}^{i+1} + \mathcal{D}_{y+}^j + \mathcal{D}_{z+}^k + \mathcal{D}_{z-}^{k+1} + \sum_g^{ijk}$$

To write the off diagonal elements, note that in the CMFD equations *i odd* nodes are coupled only to *i even* nodes in the I-J directions, and *i even* nodes are coupled only to *i odd* nodes. Thus the rest of the elements in the column sum to

$$\mathcal{D}_{x+}^i + \mathcal{D}_{x-}^{i+1} + \mathcal{D}_{y-}^{i+1,j+1} + \mathcal{D}_{z+}^k + \mathcal{D}_{z-}^{k+1}$$

for *i odd* and

$$\mathcal{D}_{x+}^i + \mathcal{D}_{x-}^{i+1} + \mathcal{D}_{y+}^j + \mathcal{D}_{z+}^k + \mathcal{D}_{z-}^{k+1}$$

for *i even*. It would appear that the condition of column diagonal dominance is satisfied if the \mathcal{D}_μ^i are non-negative. An examination of Eqns. 3.48 and 3.49 show that this is true for non-negative discontinuity factor ratios.

The use of discontinuity factor ratios into the CMFD equations introduces an extra degree of freedom. So long as the discontinuity factor ratios are calculated consistently, the diffusion coefficients may be given arbitrary values. In an idea first put forth by Aragonés and Ahnert [A1], the diffusion coefficients may be changed to guarantee that all

discontinuity factor ratios are positive. If we re-arrange Eqn. 3.12, the discontinuity factor ratio for an interior face can be written as

$$\frac{f_{g,p'}^{NodeA}}{f_{g,p}^{ijk}} = \frac{\overline{\Phi}_g^{ijk} - \overline{J}_{g,X}^{ijk}(p) \frac{X_c}{2D_g^{ijk}}}{\overline{\Phi}_g^{iNodeA} + \overline{J}_{g,X}^{ijk}(p) \frac{X_c}{2D_g^{NodeA}}} \quad (3.50)$$

To maintain positive discontinuity factor ratios, the following conditions must be satisfied:

$$D_g^{ijk} > \frac{\overline{J}_{g,X}^{ijk}(p)}{\overline{\Phi}_g^{ijk}} \cdot \frac{X_c}{2} \quad \text{if } \overline{J}_{g,X}^{ijk}(p) > 0 \quad (3.51a)$$

or

$$D_g^{NodeA} > \frac{\overline{J}_{g,X}^{ijk}(p)}{\overline{\Phi}_g^{iNodeA}} \cdot \frac{X_c}{2} \quad \text{if } \overline{J}_{g,X}^{ijk}(p) < 0 \quad (3.51b)$$

The Aragonés and Ahnert scheme is implemented in QUARTZ only as a part of the quadratic solution scheme. At each discontinuity factor ratio update, the diffusion coefficients are checked such that

$$D_g^{ijk} = \max_p \left[D_g^{ijk}, \frac{\overline{J}_{g,X}^{ijk}(p)}{\overline{\Phi}_g^{ijk}} \cdot \frac{X_c}{2} \right] \quad \text{for all } \overline{J}_{g,X}^{ijk}(p) > 0 \quad (3.52)$$

If $\overline{J}_{g,X}^{ijk}(p) < 0$, $\overline{J}_{g,X}^{NodeA}(p') > 0$ and the condition stated in Eqn. 3.52 will be checked when the node sweep reaches *NodeA*.

After new diffusion coefficients have been determined, the discontinuity factor ratios can be updated, and the new loss matrix $\underline{\underline{L}}$ is constructed. After the implementation of Eqn. 3.52, this matrix is guaranteed to be diagonally dominant.

Gherchanoc [G3] has implemented a similar scheme in CONQUEST-SN, a supernodal diffusion theory code in Cartesian coordinates. In that particular implementation, diffusion coefficients may be different for each face of a node. This allows diffusion coefficients to be raised for faces adjoining internal nodes and lowered for faces at the boundary. Directionally dependent coefficients are not used in QUARTZ Version 3.0. Instead, the maximum diffusion coefficient over all sides of a node is used as the updated diffusion coefficient.

To test the diagonal dominance routines, a highly absorbing material ($\Sigma_2 = 0.7476 \text{ cm}^{-1}$) was placed near the center of the Case III problem presented in Section 3.4. Without changing diffusion coefficients, the code did not converge to a solution. With the implementation of the Aragonés and Ahnert algorithm, column diagonal dominance was retained and a solution was reached. This example is a particularly extreme one, since the calculated thermal flux at the center of the absorbing region is much lower than the surrounding nodes.

The motivation for developing the diagonal dominance routines came from the desire to model correctly the control blades in the MITR model. Such highly absorbing regions can lead to numerical instabilities in the quadratic solution method. As an initial trial, the diffusion coefficient enlargement scheme was applied to a quadratic solution of one plane taken from the MITR model. The problem assumed the control blades inserted. Boundary conditions around the perimeter were also taken from the MITR model with the exception of the thermal group. Zero current boundary conditions were used, rather than

the incoming thermal current actually present, to eliminate the possibility of negative entries from the boundary in the diagonal of $\underline{\underline{L}}$.

The code failed to converge to a solution whether the diffusion coefficients were enlarged or kept constant. Convergence to a solution is measured by the change in the eigenvalue and the relative change in the power in the fueled nodes from one iteration to the next. These are given in Eqns. 3.53 and 3.54.

$$|\lambda^{(m+1)} - \lambda^{(m)}| \tag{3.53}$$

$$\max_i \left| \frac{P_i^{(m+1)} - P_i^{(m)}}{P_i^{(m)}} \right| \tag{3.54}$$

The convergence of the power in the fueled nodes is illustrated for both methods in Figure 3.6 and Figure 3.7.

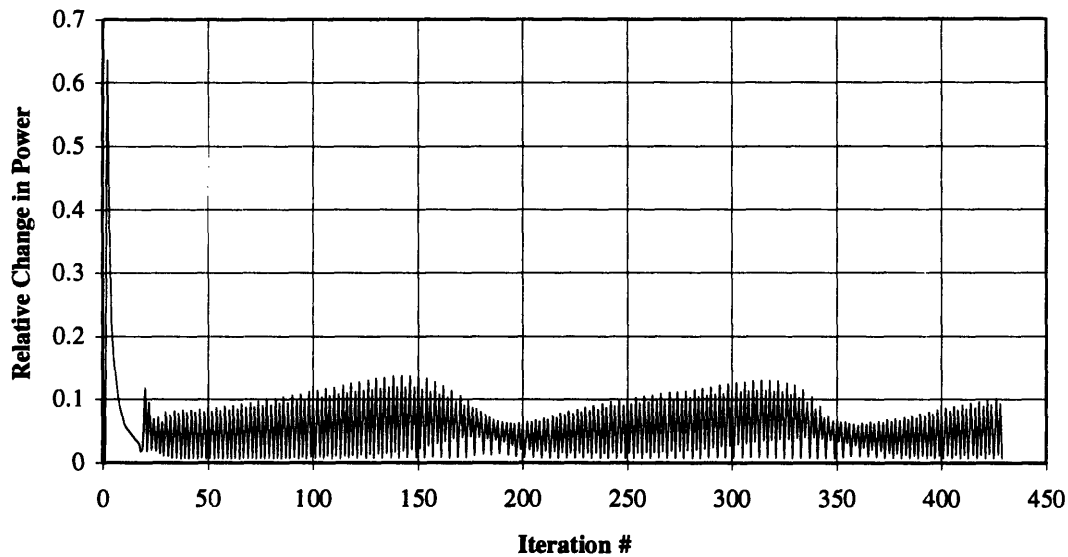


Figure 3.6. Power Convergence with No Change in Diffusion Coefficients

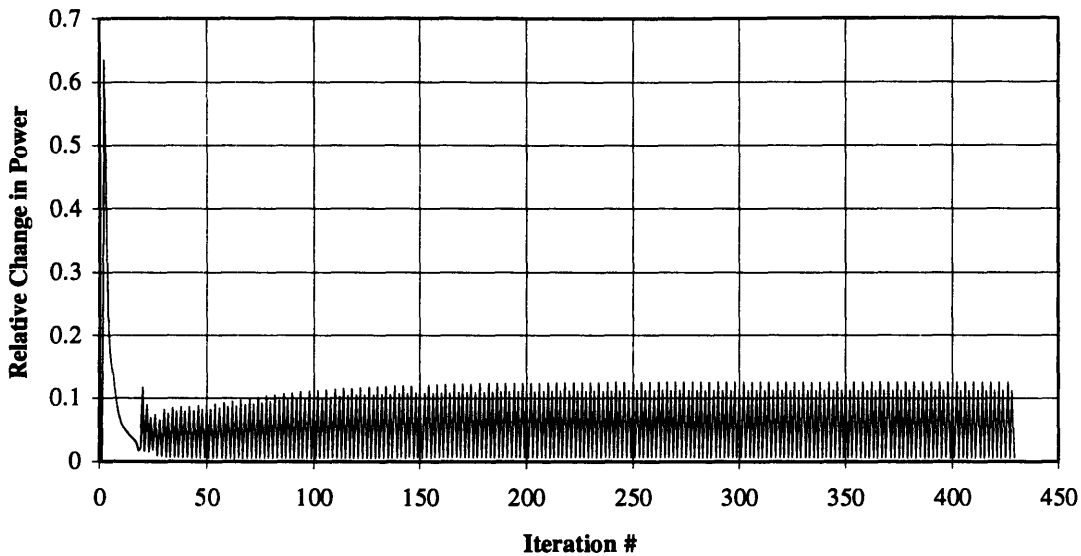


Figure 3.7. Power Convergence with Changing Diffusion Coefficients

A close investigation of the inner iterations for each method revealed that negative discontinuity factor ratios were indeed present if the diffusion coefficients were not changed. Diagonal dominance of the iteration matrix was lost at some points during the iterations. When the diffusion coefficients were increased such that Eqn. 3.52 was satisfied for all nodes, all discontinuity factor ratios were positive, and diagonal dominance was restored to within machine precision. As is evidenced by Figure 3.7, however, this does not guarantee convergence of the non-linear iteration method.

Guaranteeing diagonal dominance will only guarantee convergence when the quadratic method itself converges. Unfortunately, there is at present no mathematical condition that assures convergence of the quadratic method. The diagonal dominance routines remain a part of QUARTZ, and should allow the code to be used to solve most problems that could not be solved previously. However, as evidenced above,

guaranteeing diagonal dominance of the loss matrix does not guarantee convergence of the non-linear iteration method. The situation is worsened when the current at the boundary is directed *into* the model, as between the core tank and the reflector in the MITR. In such scenarios, positive discontinuity factor ratios at the boundary would be achieved by lowering the diffusion coefficients rather than raising them (see Eqn. 3.31). This, however, may cause discontinuity factor ratios for interior faces of the node to become negative. This difficulty is circumvented by using directionally dependent diffusion coefficients as in CONQUEST-SN [G3].

For the purpose of using QUARTZ to generate flux shapes, a finite difference scheme will be used for both the fine and coarse mesh flux shapes. This should be suitably accurate for proper syntheses.

3.6 CORRECTIONS TO THE QUARTZ CODE

In addition to the added capabilities described above, a number of corrections have been made to the QUARTZ code. They are not new additions to the code, but changes in the code that allow proper implementation of routines already present. The two most notable corrections are proper determination of the adjoint flux and reactivity.

In calculating the adjoint, a converged forward solution is first determined. The spatial and energy transpose of the leakage matrix is then taken, and the $v\Sigma_f$ and χ parameters are switched, then transposed in energy, as is the scattering matrix. The

Chebyshev Cyclic Semi Iterative method is used for the inner iterations, and the Wielandt method is used for the outer iterations.

In Version 1.0 of QUARTZ, the transpose of the leakage matrix was improperly determined. A proper adjoint could be calculated only if all discontinuity factors were equal to one. An incorrect calculation would result for CMFD solutions with non-unity discontinuity factors, or for *any* quadratic solution. The non-linear iteration method uses discontinuity factor updates that change the values of the discontinuity factors used in the leakage matrix. These problems have been corrected in Version 3.0 of the code, and the adjoint flux and eigenvalue are now correctly determined under all circumstances.

The determination of reactivity requires subtracting quantities that are normally very close together. Roundoff error in the computer becomes extremely important. In Version 3.0, a number of quantities related to calculating reactivity are changed from 4-byte to 8-byte precision. This greatly reduces the error in the reactivity determination, which amounted to as much as \$0.10 of reactivity when applied to the MITR model at steady state. Implementing the correction required some loss in the generality of the programming. Porting the code from one computer platform to another now requires the changing of some statements in several subroutines. These changes are outlined in the QUARTZ manual included with Version 3.0 of the code.

3.7 SUMMARY

A new version of the QUARTZ code has been written. In addition to corrections of the adjoint flux and reactivity determinations, several new capabilities have been added. These include the ability to perform supernodal analyses as well as ensure diagonal dominance of the leakage matrix for convergence of the inner iterations.

The supernodal analyses produce results that agree very closely with reference, fine mesh results. This provides us with a tool to generate flux shapes for use in the instrumented synthesis work as applied to the MITR.

Chapter 4

Description of the Experiment

4.1 INTRODUCTION

In Chapter 3, the QUARTZ code was described. This neutronics code was modified to allow supernodal analysis to be performed, generating coarse mesh results from fine mesh, reference calculations. The purpose of these modifications was to create a tool by which flux shapes, denoted $\underline{\psi}^k$ in Chapter 2, could be generated. Recall from Chapter 2 that these flux shapes are combined using detector measurements, denoted $\underline{C}(t)$, from an operating reactor. Thus the flux shapes should closely model the reactor under various conditions such that combinations of them can model the reactor under *any* condition likely to be encountered during the experiment. Before we discuss the model of the

reactor used to generate these flux shapes, it is instructive to discuss first the physical system it will be simulating. That is the subject of this chapter.

4.2 PREVIOUS WORK

It was mentioned in Chapter 3 that a previous attempt by Kuo was made to generate shape functions for use in the Instrumented Synthesis Project [K2]. There was also earlier work on collecting the detector measurements for the project. Work by Selby [S4] was the initial attempt to collect detector counts rates in the MITR-II. The experimental evaluation of both that work and the present evaluation involved digital recording of the detector count rates using a computer-based data acquisition system. The system could never be made to function correctly for Selby's work. As a consequence, only static data that could be read from ammeters were recorded. No transient experiments were performed.

Some of the experimental apparatus has changed in going from Selby's thesis to the present evaluations. But a considerable amount of ground work, including much of the experimental procedure laid out in Appendix 5, came from this initial attempt. Readers should consult his thesis as a complement to the present evaluation.

4.3 DESCRIPTION OF THE MITR-II

Much mention has been made of the physical system in which the detector measurements were made. This section provides a more detailed description of the Massachusetts Institute of Technology Reactor, dubbed MITR-II.

In Figure 4.1, the MCNP model of the core is shown. It consists of 27 fuel elements containing fuel highly enriched (>93%) in U^{235} . Usually, either three or five element positions are occupied by dummy elements made entirely of aluminum.

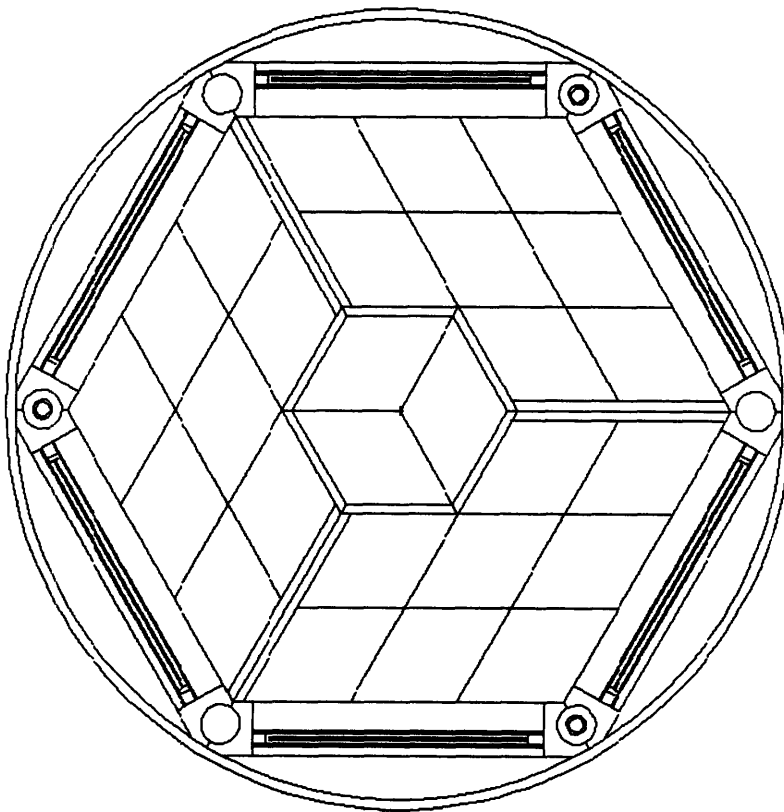


Figure 4.1. MCNP Model of the MITR-II Core [Ref. R1]

At the periphery of the reactor are six shim blades and six corresponding vent holes. The shim blades are made of borated stainless steel. The boron serves as a neutron poison, providing reactivity control in the reactor. As the blades are inserted, they displace water which is sent out the water vent holes. The core is contained in an aluminum core tank which is surrounded by a D₂O reflector. At the top of the core is a flow shroud, a hexagonal piece of aluminum used to guide coolant exiting the core further into the water above the core, promoting better coolant mixing. The vent holes extend into this shroud.

The fuel elements are drawn in Figure 4.2. They consist of 15 plates, grooved for improved heat transfer. The fresh fuel contains approximately 510 g of U²³⁵ in a UAl_x composite. The fuel “meat” is clad in aluminum, and H₂O serves as the coolant and moderator. The fuel elements in the core are grouped into three rings. The innermost ring, consisting of three elements, is denoted the A-ring. The second ring, or B-ring, contains nine elements. The outermost C-ring contains 15 elements.

The shim blades, or control blades, normally move as a unit or “bank.” The positions of the control blades are recorded in inches above the bottom of the blade guide, a slot in which the blades move up or down along the core periphery. The bottom of the guide is one inch above the bottom of the active fuel. A recorded shim bank height of 0805 means the blades are 8.05” above the bottom of the guide, or 9.05” above the bottom of the active fuel.

In the interior of the core is a hexagonal absorber region. It is visible in Figure 4.1 between the A- and B-rings. The lower half of the absorber is solid aluminum, while the upper half contains stainless steel inserts. The inserts are doped with boron depleted in B^{10} , the isotope of boron responsible for its high thermal neutron capture cross section. These inserts, in addition to the shim bank, shift the thermal neutron flux peak to the bottom half of the core. The inserts can be removed from the absorber, leaving only water in the gap.

The presence of the D_2O reflector causes a number of fast neutrons that leak out of the reactor to be returned as thermal neutrons. The current of thermal neutrons at the core tank will be directed *into* the core. This makes the reflector an important part of maintaining criticality.

The core sits at the bottom of a large tank below many feet of water. This is illustrated in Figure 4.3.

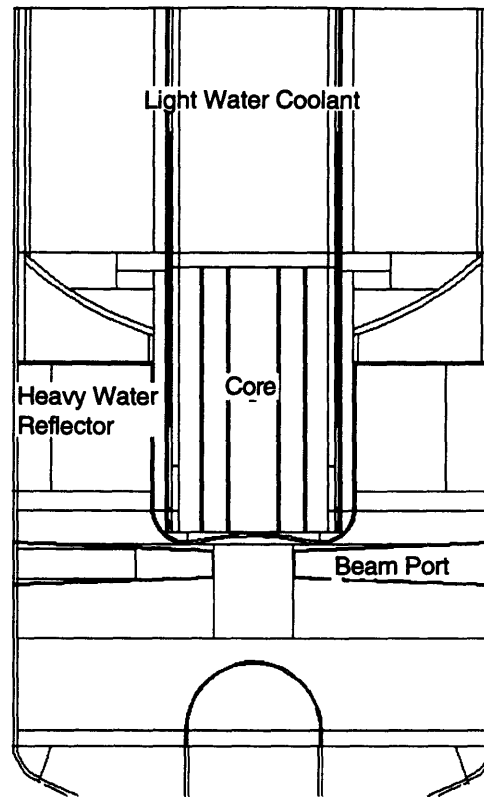


Figure 4.3. MCNP Cross Section of MITR Core Tank [Ref. R1]

A lid covers the core tank during normal operation. It can be removed for refueling, maintenance, or installation of experiments in the core.

A regulating rod constructed of aluminum and cadmium is used for fine reactivity control of the reactor. Even at “steady state” conditions, the regulating rod is likely to continue moving to counteract small changes in reactivity.

The MITR-II core is a highly neutronically coupled core. Changes in the flux in one region of the core are reflected throughout the core. As such, it is a relatively poor system to test the instrumented synthesis method. Large power reactors that are more loosely coupled would provide much better conditions for evaluation of the method.

Obviously, restrictions make such reactors unavailable for tests such as these. Research reactors such as the MITR-II provide an alternative.

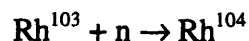
4.4 DESCRIPTION OF THE DATA ACQUISITION

The object of the experimental part of the instrumented synthesis evaluation is to collect detector measurements from the MITR-II under a number of conditions, both static and transient. These measurements will be combined with flux shapes at a later time.

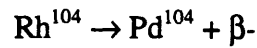
The first task is to select measurement devices. There are several constraints on these devices to make them effective.

- a) They must be proportional to neutron flux. This is a rather obvious requirement, and eliminates detectors designed to detect other types of radiation such as gamma rays.
- b) They must be fast-acting. One of the proposed advantages of the instrumented synthesis method is its ability to combine detector measurements with flux shapes and accurately synthesize a flux *in real time*. If the detector takes several minutes, or even seconds, to reach an equilibrium count rate, this advantage is destroyed.

One example is the rhodium detector. It detects neutrons by first absorbing them in the following reaction



The resulting isotope Rh^{104} is unstable, and decays by beta emission



The beta particle is charged. This charge is collected on a central anode, and a measurable current, proportional to the number of decays, is recorded. Unfortunately, the decay occurs with a half-life of 42.3 seconds. This means that minutes will pass before the absorption and decay rates come to equilibrium after a change in power. This would not be a suitable detector for use as a controller, where changes in power need to be recognized instantly.

- c) The response to a given neutron flux must be consistent, or at least predictable. If a particular detector's response to a neutron flux changes, and that change is not taken into account in the synthesis, inaccurate predictions of the flux level at that detector location will result. These predictions will adversely affect the synthesis method's ability to reconstruct the flux.

Requirements (a) and (b) are satisfied by *fission chamber detectors*. These detectors are lined with U^{235} . When thermal neutrons strike the detector, there is a chance that the neutrons will be absorbed by the U^{235} , which in turn will undergo fission with a certain probability. If a U^{235} nucleus does fission, charged fission products are created. They are

collected on a metal lead in the center of the detector, and a current is created. This current is proportional to the number of fissions, therefore the number of thermal neutrons impinging on the detector. A very simplified schematic is presented in Figure 4.4.

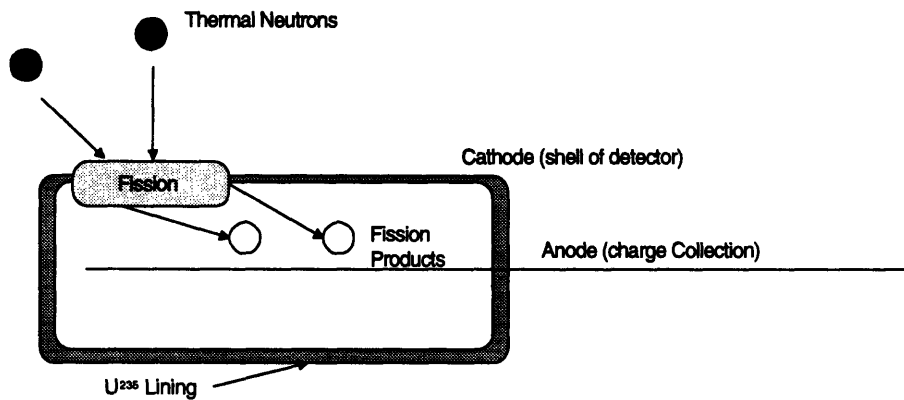


Figure 4.4. Schematic of Fission Chamber Operation

Fission chambers produced by Imaging and Sensing Technology were selected for use in the instrumented synthesis evaluation. Two models of detectors, NY10336 and WL23798, were used.

There are several things to keep in mind relating to the third requirement, consistency of the detector's response. First, the fission cross section of U^{235} changes with the energy of the incoming neutron. If the spectrum, or energy distribution, of the flux at the detector location changes, the response of the detector will change. Second, a U^{235} nucleus is destroyed each time a fission takes place. Less U^{235} means a lower current for the same thermal neutron flux, also changing the response of the detector. Finally, the efficiency of the charge collection will change with the voltage difference from anode to cathode. If the battery's potential used to provide this voltage is slowly consumed, the

voltage difference will decrease. All of these situations affect how the detector will respond to a given neutron flux. The last two, U^{235} depletion and changing voltage, are not expected to affect the experimental evaluations. The experiment is on a time scale of hours while voltage changes and U^{235} depletion take place over weeks or months of continuous usage. Spectral changes, however, could be seen over the course of the experiments. One way to take this into account is to relate the measured current versus predicted flux at several points during the experiment when spectral changes are expected to be significant.

In an effort to determine the relative response of the detectors, a normalization test was conducted using one of the beam ports beneath the reactor core. At constant reactor power, each of the detectors was inserted individually into the beam port, and their currents recorded. Although the magnitude of the flux at the tip of the beam port was not known, each of the detectors was presumably subjected to the same flux. A relative, if not absolute, response of each of the detectors could be determined. In addition to these relative responses, the manufacturers of the fission chambers also included absolute responses as a part of the technical specifications of each detector. These absolute responses, given in $\text{amperes}/\frac{\text{neutrons}}{\text{cm}^2\text{-s}}$, can be compared to the experimentally determined relative responses.

Detector #	Normalized Experimental Response	Normalized Factor Specified Response
1	0.868	0.612
1b	0.891	0.823
1c	0.859	0.681
2	0.745	0.747
2b	1.000	1.000
2c	0.718	0.750
3	0.963	1.030
3b	1.081	1.116
3c	0.945	0.884

Table 4.1. Normalized Detector Responses

There is an obvious discrepancy between the experimental responses and the factory-specified responses. It is difficult to determine what types of electronics were used to obtain the factory specifications or what other variable conditions existed. As discussed in Chapter 6, there will also be some uncertainty about the placement of the detectors within the vent holes that could affect the relative responses. In the end, the detector responses were related to the theoretical prediction of the flux at each detector location. This provides a suitable means of evaluating the success of the synthesis method, but would probably be too simplistic for applying the method to an automated control system. It is extremely important that a robust and accurate calibration scheme, one that accounts for spectral changes in the reactor as well as longer term changes in the core and detectors, be developed if the synthesis method is to be applied for reactor control.

With the measurement devices selected, placing them becomes a concern. A total of nine fission chambers were available for use in the project. A system designed by Selby to accommodate three fission chambers was adapted for the present evaluation with nine

such detectors. Three aluminum guide tubes, each approximately fifteen feet in length, were used to house the fission chambers. The guide tubes have an outer diameter of 1/2", making them small enough to fit inside the water vent holes in the flow shroud and core housing. They are also wide enough to contain the fission chambers inside them. The guide tubes were employed for two purposes. First, leaving the fission chambers exposed to radioactive coolant would contaminate them, making them difficult to handle after the experiment was concluded. Second, coolant flow past the chambers would cause them to vibrate. This could introduce additional noise, or uncertainty, into the measurements.

The fission chambers are inserted into the tubes, three per tube. The placement of the fission chambers in the tube is illustrated in Figure 4.5.

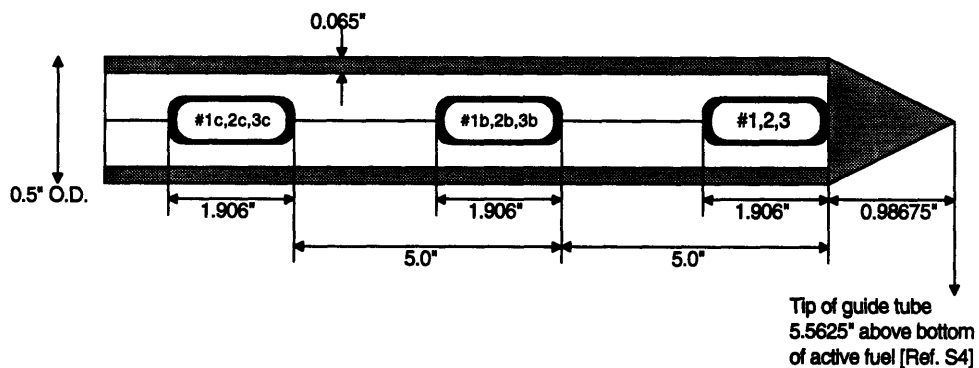


Figure 4.5. Schematic of Fission Chamber Placement in Guide Tube

The ten inch axial difference between the first and third fission chambers allows the axial change of the flux to be recorded. The detectors at the bottom of each string of fission chambers are numbers 1, 2, and 3. Numbers 1b, 2b, and 3b are the middle detectors, and numbers 1c, 2c, and 3c are at the top of the strings.

Once the fission chambers have been inserted into the aluminum guide tubes, they are placed into three of the water vent holes. They are denoted in the figure below along with the shim blade designations.

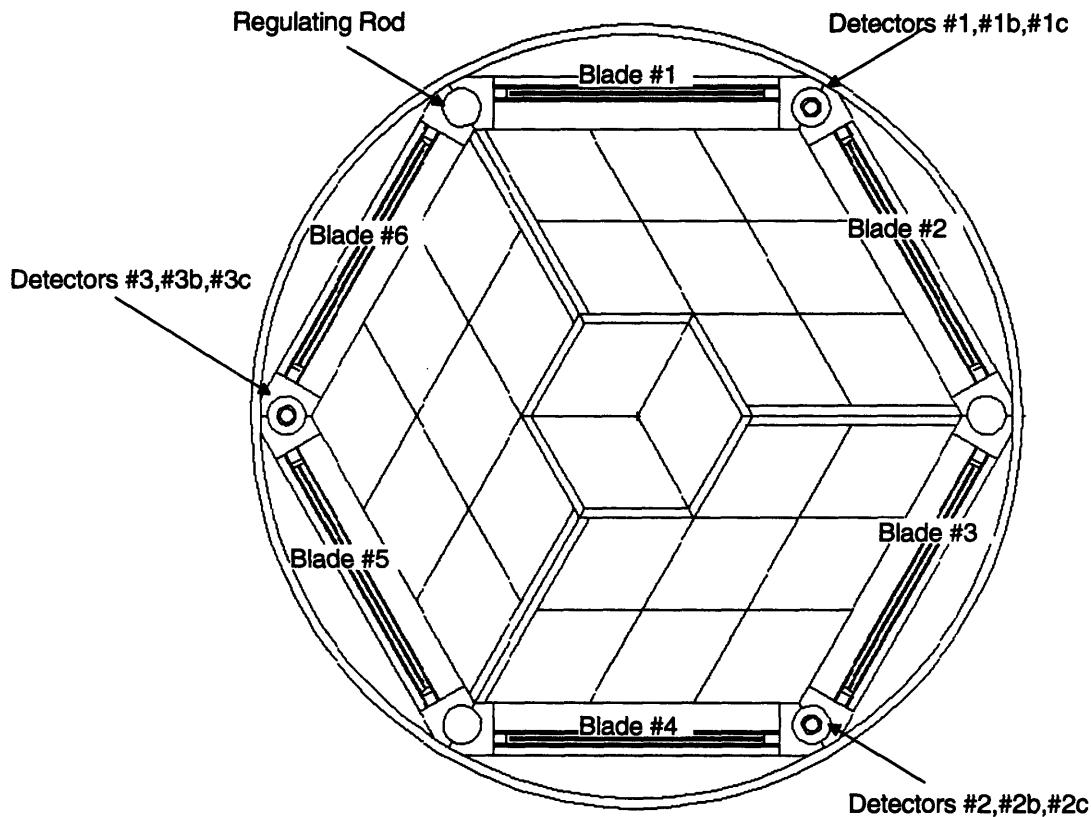


Figure 4.6. Placement of Fission Chambers in the Core

Because the vent holes do not extend all the way to the bottom of the active fuel region, the chambers at the bottom of the guide tubes (#1, #2, or #3) sit just below the midplane of the reactor, approximately 5-1/2 inches above the bottom of the active fuel region.

It would be preferable to have some instrumentation inside the core, rather than only on its periphery. However, because of the vent holes' proximity to the control

blades, placement in these locations does offer the potential to record flux peaks and depressions as the blades move. But the most compelling reason to use the vent holes is that they offer the most convenient way to make measurements. For an automated control system, a more robust placement strategy that includes instrumentation in the core would be desirable.

The reactor lid was removed to insert the tubes into the water vent holes. The lid remained off to allow the tubes to protrude out of the core tank. Because the lid was off during the experiment, certain restrictions applied to the operation of the reactor. One regulatory restriction was the power of the reactor was to be kept below 100 kW. Another concern was the high radiation levels over the core tank. When operating at 50 kW with the lid off, these levels can approach 500 mrem/hour. The use of nine fission chambers rather than three allowed the detectors to remain in fixed positions throughout the experiment. This was in contrast to earlier work when the fission chambers were moved up and down the guide tubes to provide axial measurements. Such movements required a second individual, besides the experimenter, to stand over the core tank and perform the adjustments. When no movement of the chambers is required, only the experimenter is needed at the reactor top, and he may be located below the top of the core tank, greatly reducing his exposure.

Battery packs consisting of two 67.5 volt batteries connected in series were used to provide the voltage used for charge collection in the fission chambers. Ammeters were also used to measure the current coming from the fission chambers. The connections were

made to the fission chambers through an isolation box, also sold by Imaging and Sensing Technology. The connections were made according to Figure 4.7.

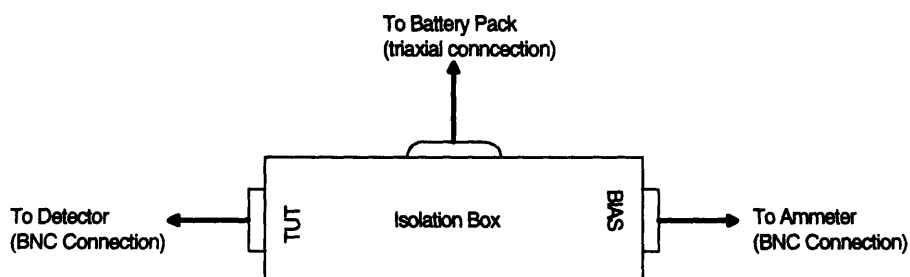


Figure 4.7. Connections to Fission Chamber and Ammeter

It is likely that the connections were made incorrectly in Selby's work, causing the high voltage from the battery pack to be directed to the ammeters rather than the fission chamber detectors. *Readers interested in repeating the synthesis experiments should ensure that the connections are made according to Figure 4.7. Failure to do so will ruin the ammeters.*

The ammeters used as part of the instrumented synthesis project were Keithley Model 480 Autoranging Picoammeters. The currents coming from the fission chambers typically ranged from 0.01 to 10 microamperes (10^{-6} amperes, μA). The ammeters used could detect currents as low as picoamps (10^{-12} amperes, pA).

At steady state, currents can be read directly from the display on the ammeters. For transient measurements, however, some type of automated recording procedure was necessary. For this purpose, each of the ammeters has what is called an *analog output*, generated by the ammeter to allow recording of the measured currents by another device.

The analog output works in the following manner: each ammeter has measurement ranges beginning with 0-2 pA and increasing by one decade to 0-2 mA. Within each of the ranges, an analog signal between zero and two volts is created proportional to the measured current. For example, a 1 μ A current measured on a 0-2 μ A range would generate an analog signal of 1 volt. The same 1 μ A current measured on a 0-200 μ A scale would generate a 0.01 volt signal. As the measured current changes, so does the voltage of the output signal.

The recording of these analog signals was accomplished in a two step process. The analog signals were sent first to an analog-to-digital converter. This converter, sold by Data Translations of Marlboro, MA, was installed in a 386-based personal computer. A “screw terminal board” was used to receive the analog signals from the ammeter which are directed to the A/D converter¹. Once the signals have been digitized, they may be recorded and analyzed. The signals were recorded using the Global Lab software, also sold by Data Translations. The recorded data can be analyzed using the Global Lab software or any number of other programs that manipulate data.

Three ammeters were used to record currents from nine detectors. A simple switchbox was constructed to allow the signal measured by the ammeter to be taken from one of three detectors. The final layout of the data acquisition systems is shown in Figure 4.8.

¹ The signals are most accurately recorded if the “differential” mode is used on the screw terminal board. When this mode is used, a maximum of seven signals can be received at the board.

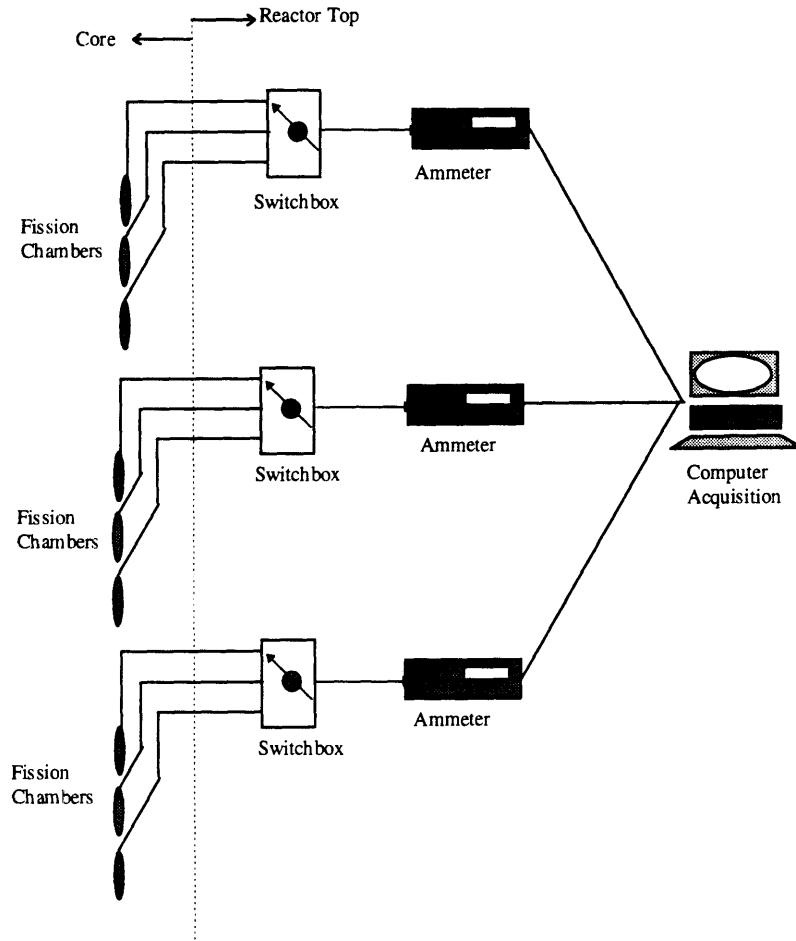


Figure 4.8. Schematic of Data Acquisition

4.5 DESCRIPTION AND RESULTS OF THE EXPERIMENT

4.5.1 DESCRIPTION OF EXPERIMENT

Data were taken in four separate experiments. The first two experiments, performed on December 6 and December 12, 1993, were halted before completion. The third and fourth experiments, conducted on April 24, 1994, and March 23, 1995, were run to completion.

The fuel loadings were denoted cores #106 and #110 respectively. The results from these experiments are the measurements used in the experimental evaluation. In each experiment, both static and transient measurements were taken. The process for each measurement is outlined below.

Static Measurements: The reactor was brought to a particular shim blade configuration. Criticality was maintained using the regulating rod. Data were taken from one group of fission chambers for thirty seconds. After thirty seconds, the signals to the ammeter were switched at the switchbox, and data from the next group of fission chambers were taken. In this way, data from all nine fission chambers were collected using only three ammeters.

Transient Measurements: A particular transient was initiated and carried to completion while data were taken from one group of fission chambers. At the completion of the transient, the reactor was returned to the condition at the initiation of the transient. The signals to the ammeters were then switched to the next group of ammeters. The transient was repeated two more times, so that measurements were taken for each of the three groups of fission chambers (#1-2-3, #1b-2b-3b, and #1c-2c-3c). Recording data in this way assumed that the transients could be replicated each of the three times they were performed. A more accurate method would be to use additional ammeters such that the signal from each fission chamber is measured at the same time. The cost of the ammeters made this an unattractive option.

The exception to the transient procedure listed above is the dropping of shim blade #1. Regulations prohibit the withdrawal of a shim blade once the blade has been dropped

(as distinguished from a controlled insertion). This transient was left until the last part of the experiment, and was followed by the scram of the reactor. It also means that readings from only three fission chambers could be taken. There was no opportunity to repeat the experiment.

The static and transient experiments conducted are listed below:

Static Measurements (at 1, 10, and 50 kW)
Flat Shim Bank Height
Tilted Configuration #1
Tilted Configuration #2

Transient Measurements
Insertion of Shim Blade #3
Insertion of Shim Blade #6
Withdrawal of Shim Blade #6
Shim Blade #1 Dropped
Reactor Scram

Table 4.2. Measurements for Evaluation of the Instrumented Flux Synthesis Method

The tilted configurations are detailed in Figure 4.9 and Figure 4.10. The control blade numbers are given below the blades. Above the blades are the inches above the shim bank height that the blade is placed. By depressing the flux on one side of the reactor and raising it on the other, the flux is shifted from one side to the other. The blackened circles represent the approximate locations of the detectors.

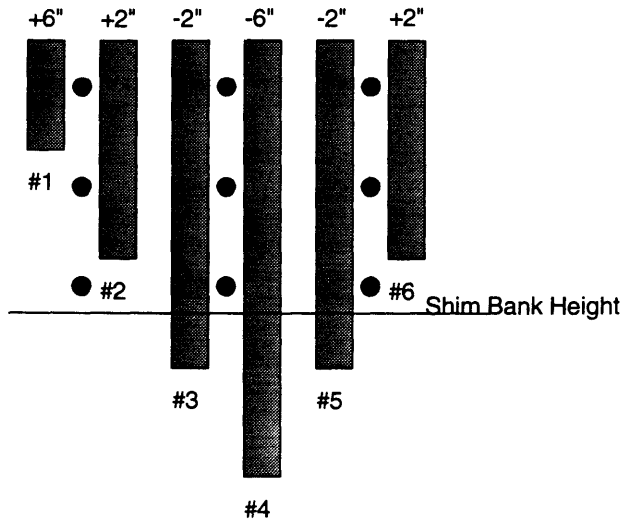


Figure 4.9. Tilt Configuration #1

The flux is shifted to the other side of the reactor by adjusting the control blades.

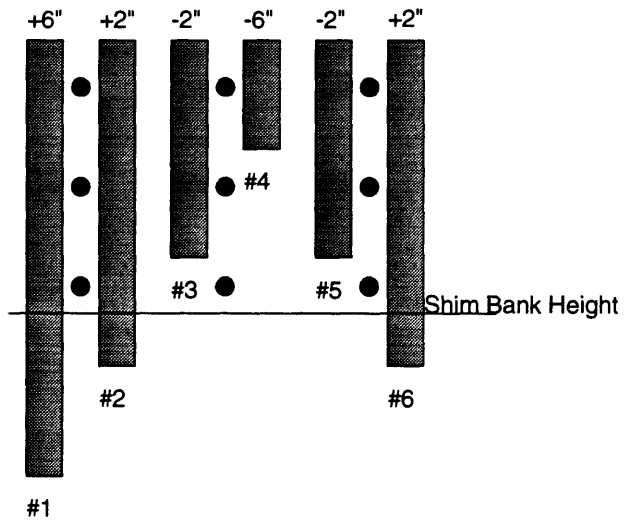


Figure 4.10. Tilt Configuration #2

In actually performing the experiment, the blades were not always able to be placed according to the specifications above. Some adjustments were made at the time of the experiments to allow criticality to be maintained. The complete procedures for each of the experiments as well as the recorded shim blade positions are given in Appendix 5.

4.5.2 RESULTS OF EXPERIMENT

The data taken from some of the experiments listed in Table 4.2 will be presented here. These are the raw data only, not the final synthesized fluxes. It is, however, instructive to review the data for consistency as well as interesting to note the behavior of the reactor under various conditions.

As an example of data taken from static measurements, measurements taken from the 50 kW, flat shim bank configuration are presented. Data are shown for both cores #106 and #110.

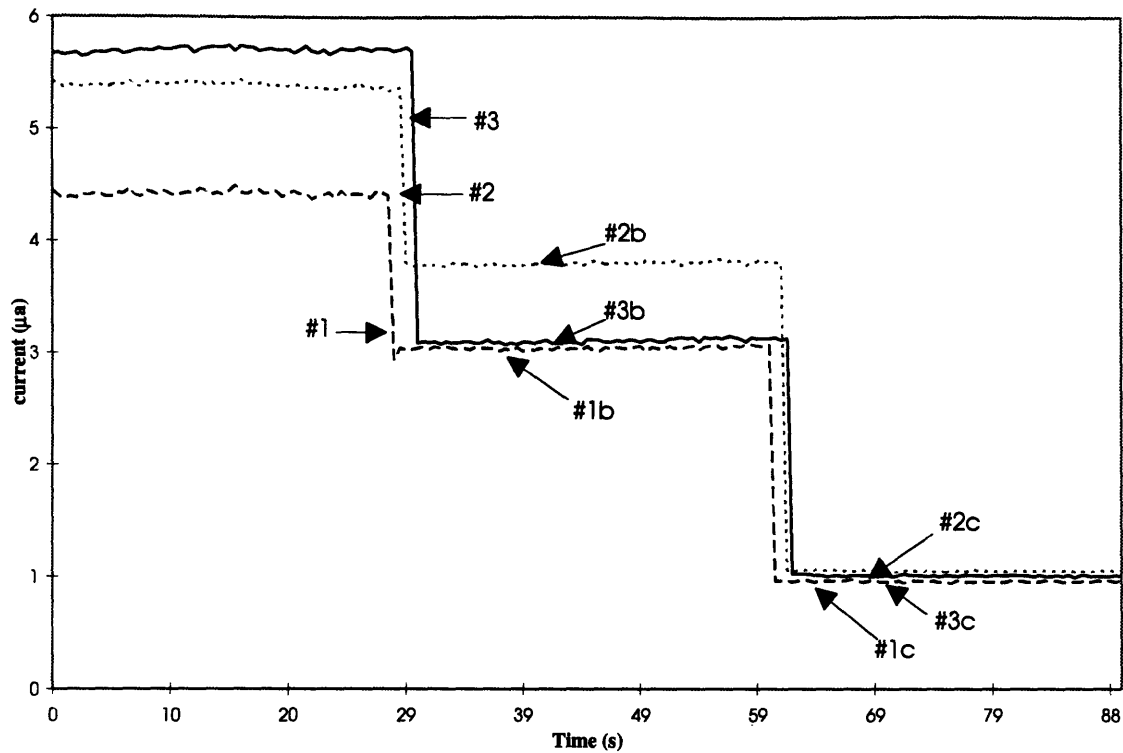


Figure 4.11. Static Measurements at 50 kW, Core #106

The points at which the signals to the ammeters were switched are clearly visible. In performing the synthesis analysis, the data will be assumed to occur all at the same time, over a 25-30 second period. The signals are fairly constant over the measurement period, with some random variation, or noise, in the signal.

The experiment was repeated in core #110. Figure 4.12 is the plot of the results. It should be noted that only eight detectors were used in core #110. At the time the experiment was installed, one battery pack had lost most of its potential and one isolation box was missing. Detector #2c was not used for this second experiment.

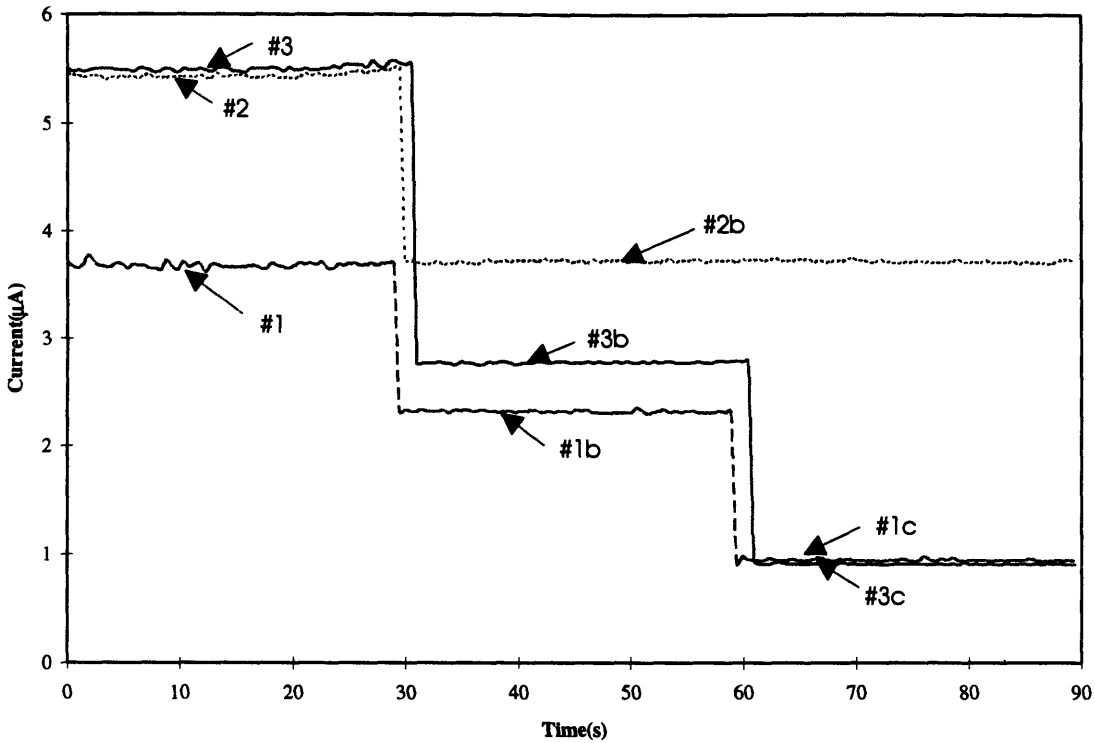


Figure 4.12. Static Measurements at 50 kW, Core #110

Notice that most of the detector responses have changed in going from core #106 to core #110. The most dramatic change was in detector #2. The reason for this change was probably the change of battery packs used to power this particular detector. There are less drastic changes in the responses of the other detectors as well, especially those further down into the core. There are several possible reasons. The recorded shim bank height at the beginning of the transient in core #106 was 7.95". In core #110, the bank height was 9.00". This undoubtedly led to different levels of flux at each detector location. Finally, the batteries used to power the other detectors had lost some of their potential in the intervening year between the experiments, though not nearly to the degree as the

discharged unit. The lesson to be taken from these differences is that for significant changes in the core composition or configuration, the response of the detectors should be checked. For an automated control system, an on-line calibration system should be used.

One of the transients analyzed in both core #106 and core #110 was the insertion of shim blade #3. Signals from the three most deeply inserted fission chambers are plotted in Figure 4.13. The transient is initiated after 10-15 seconds by driving in shim blade #3 for ten seconds, then holding the blade in that position for 50 seconds. The reactor is then returned to its original condition.

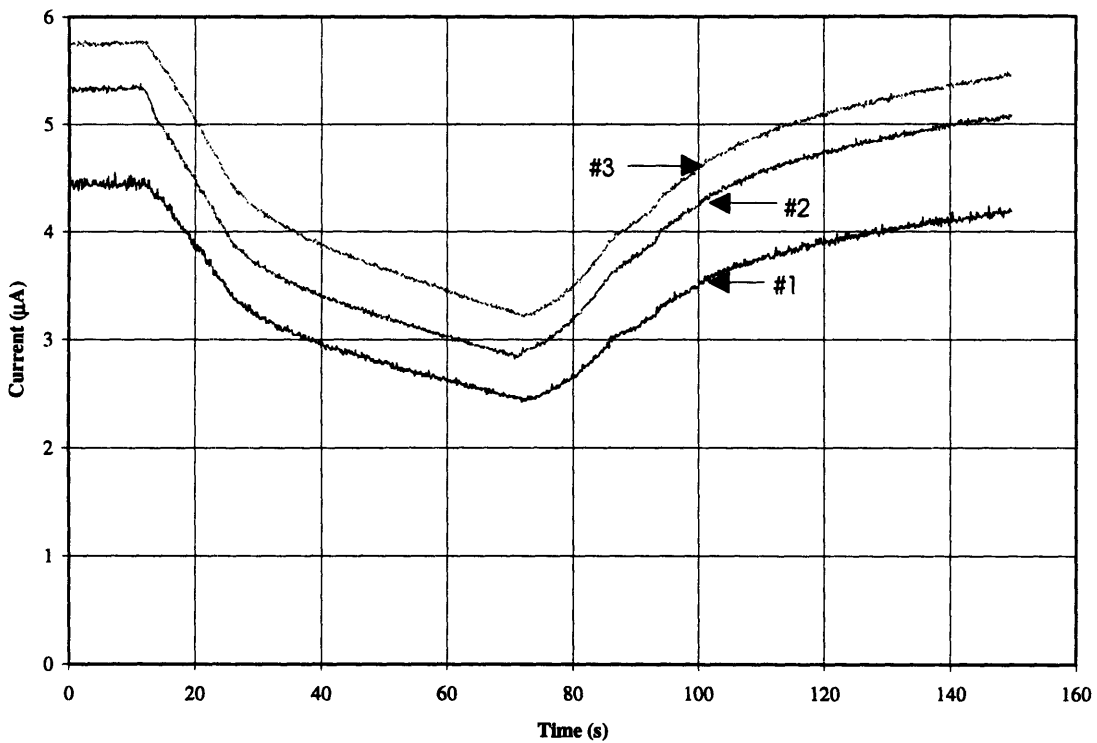


Figure 4.13. Flux Measurements, Shim Blade #3 Insertion, Core #106

There are several noteworthy features in Figure 4.13. A close examination of the currents shows a steeper drop at the initiation of the blade insertion followed by a less steep

decline. The initial drop in flux takes place while the blade is inserted. When the insertion stops and the blade is held in place, the power continues to decrease, but at a slower rate. The steeper drop is, of course, the change in the prompt neutron population, while the decline slows as delayed neutrons come into equilibrium.

The reactor remains subcritical as long as the blade is inserted below the critical shim bank height. After the blade is held in position for 50 seconds, the reactor is restored to its initial condition. This is evidenced by the increase in neutron flux over the last 70 seconds of the recorded transient.

The insertion of shim blade #3 was repeated in the experiments held in core #110. A look at Figure 4.14 shows many of the same features as Figure 4.13. There are some noteworthy differences, however. As in the case of the static measurements at 50 kW, detectors #2 and #3 give the same response at the start of the transient. The decrease in current from detector #2, however, is greater than #3. Detector #2 is next to the shim blade being inserted (#3). One would expect the greatest changes in both flux *amplitude* and *spectrum* to be seen at detector #2. We can confirm at least that the amplitude changes are strongest at the detector #2 location. Spectral effects are much more difficult to detect.

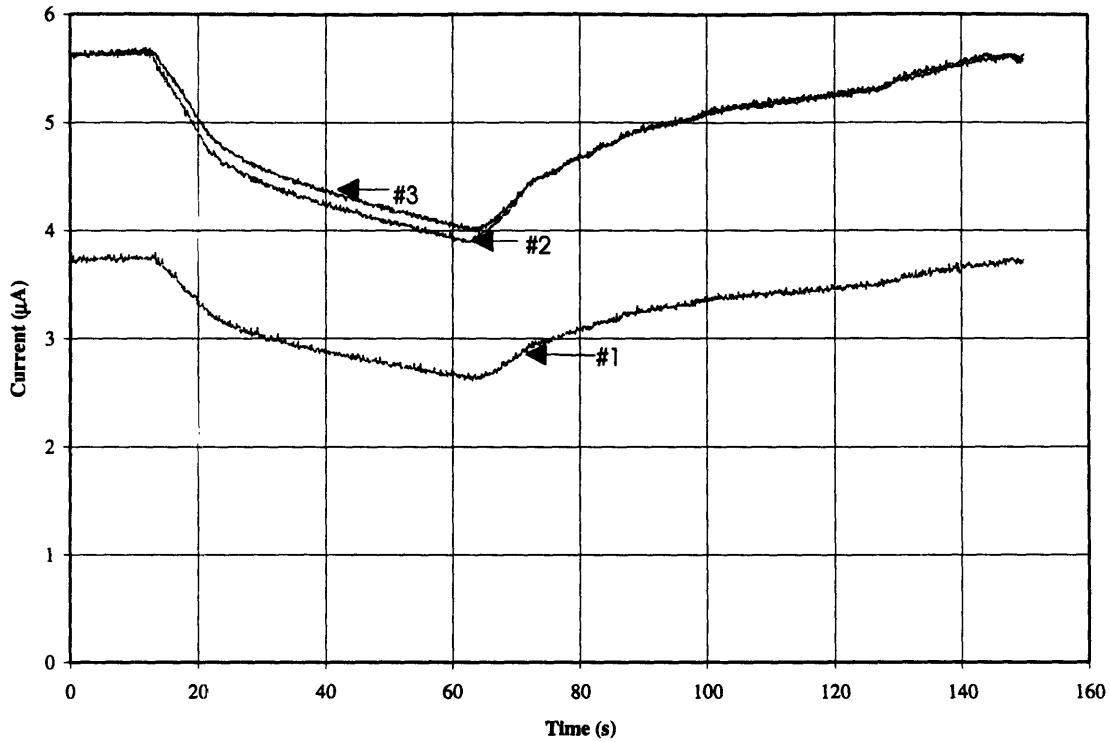


Figure 4.14. Flux Measurements, Shim Blade #3 Insertion, Core #110

The withdrawal of shim blade #6 was also performed for both sets of experiments. The reactor begins at 5 kW. The reactor is put on a 30 second period until power reaches 50 kW. The reactor is brought to steady state at 60 kW, then returned to its initial state for repetition of the experiment. We look first at core #106.

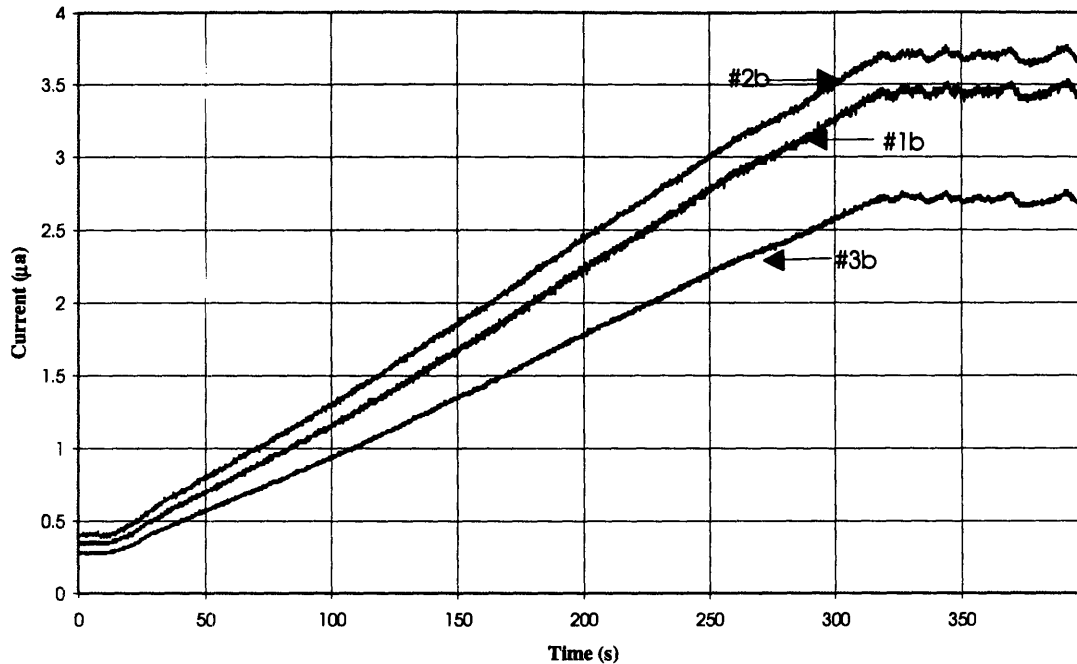


Figure 4.15. Flux Measurements, Shim Blade #6 Withdrawal, Core #106

The power was a smooth increase over the duration of the measurements. Notice the lack of overshoot at the end of the power increase. The MITR staff have been involved in a number of projects dealing with digital control and application of the dynamic period equation [B5]. Some of these concepts have been successfully applied to operation of the MITR. Proper implementation of the dynamic period equation allows a predictive response to changes in reactivity. One of the results of this work is the smooth leveling of power at the desired level, without surpassing the end power and then returning to it. The instrumented flux synthesis method fits into these schemes by providing a more accurate way of determining reactivity, one that does not depend upon assumptions made in the point-kinetics determination.

Unfortunately, the data from detectors at the bottom of the strings, #1, #2, and #3, were incorrectly recorded. In the synthesis evaluation, only six detectors will be used.

The blade withdrawal was repeated in core #110.

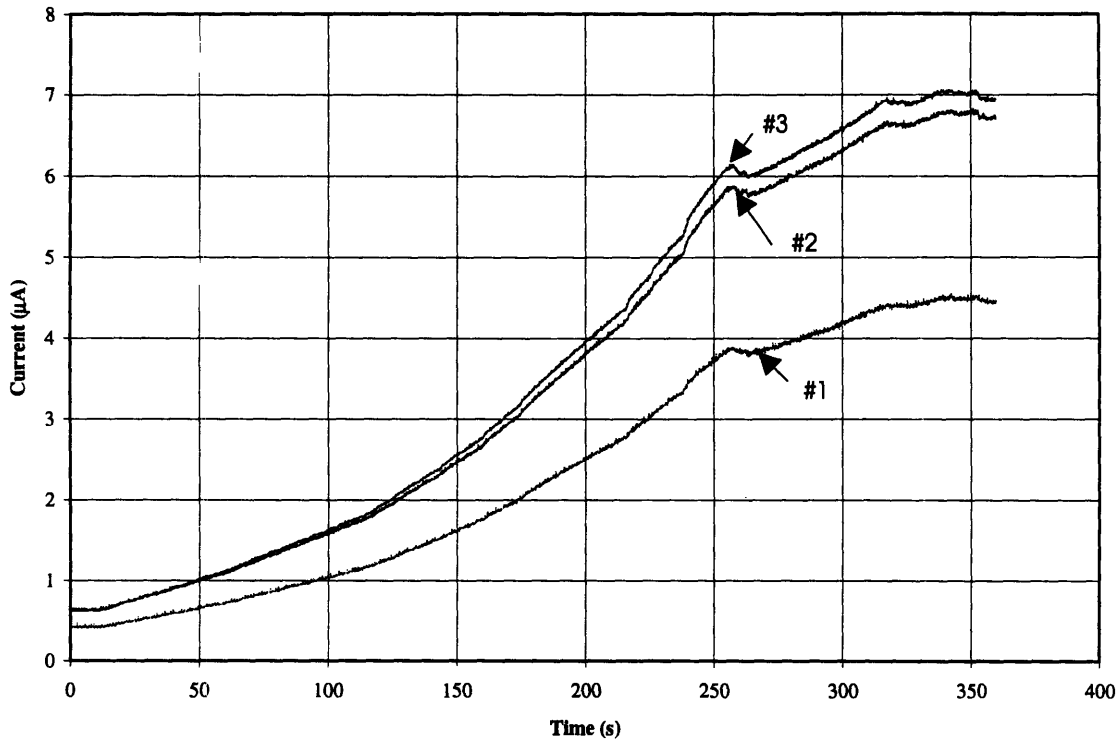


Figure 4.16. Flux Measurements, Shim Blade #6 Withdrawal, Core #110

Here, the ascension is not as smooth. Data were properly recorded for all nine detectors in core #110. The difference in accuracy of the synthesis method between cores #110 and #106 should provide some insight into the number and placement of detectors required for a good synthesis.

At the end of each experiment, shim blade #1 was dropped, making a large, rapid insertion of negative reactivity. In core #110, the blade dropped triggered a reactor

scram. But in core #106, the remaining blades were held at the shim bank height until a manual scram signal was sent. The signals from core #106 are recorded below.

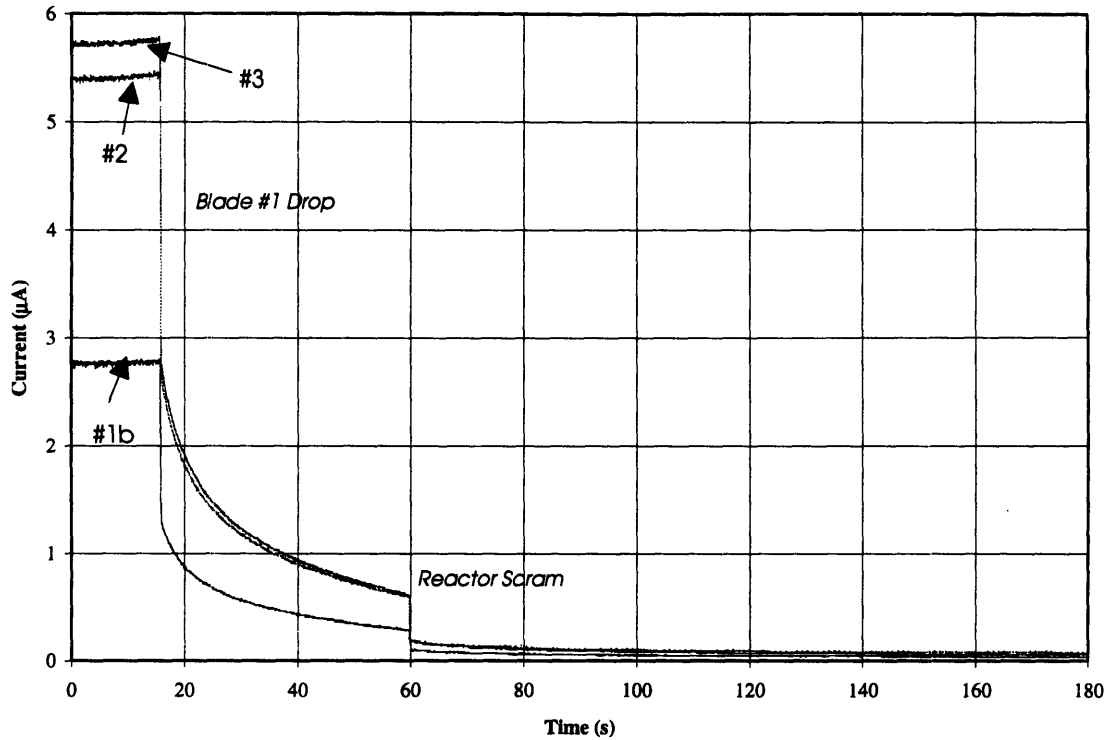


Figure 4.17. Shim Blade #1 Dropped, Followed by Reactor Scram, Core #106

Here we see in dramatic fashion the effect of delayed neutrons on the decrease in power. The precipitous decrease in power after the insertion of blade #1 is followed by a much slower decline as the delayed neutron precursors decay. A careful examination of the signals shows the same behavior after the scram.

4.6 SUMMARY

The focus of this chapter was to outline the experimental setup used to collect data for the evaluation of the instrumented synthesis method. The types of measurements were also outlined, and the raw data from those experiments presented. With the detector measurements taken, shapes functions can now be generated. That is the topic of the next chapter.

Chapter 5

MITR Model

5.1 INTRODUCTION

In Chapter 2, the idea behind the instrumented flux synthesis method was presented. For an experimental evaluation of that method, two crucial ingredients are required. The first is recording the detector measurements, denoted $\underline{C}(t)$, which are taken from an operating nuclear reactor. The second is selecting the expansion functions, denoted $\underline{\psi}^k$, which should represent the flux in the reactor at the time the measurements were taken.

Collecting the detector measurements was the subject of Chapter 4. Generating the flux shapes will be the topic of this chapter.

The generation of appropriate flux shapes is one of the most important differences between the numerical evaluation performed by Jacqmin [J1] and the experimental evaluation performed here. In the numerical evaluation, the “reactor” was a QUANDRY simulation of a large PWR. Flux shapes to be used in the synthesis were generated from this same simulation, the static calculations being made at various times during a particular transient. By virtue of this method, the flux shapes modeled the reactor *exactly* at various conditions. Even if the “reactor” were in a condition not modeled by any of the flux shapes, flux shapes near that condition could be combined to replicate it very precisely. There is no such guarantee when modeling a physical system. Although the flux shapes need not exactly replicate the physical system, they must be accurate enough to allow some combination to closely represent the reactor. An extreme example would be to model the MITR with cadmium elements at the center of the core rather than aluminum dummy elements. It is unlikely that any combination of flux shapes with that characteristic could reproduce operating conditions of the MITR.

This chapter is devoted to the model of the MITR developed as a part of the experimental evaluation of the instrumented synthesis method. The goal was to create a model of the reactor that was sufficiently accurate to allow combinations its flux shapes to closely match the flux shape in the reactor under static and transient conditions.

5.2 MOTIVATION FOR A NEW MODEL

The flux shapes, represented by the $G \times N$ column vectors $\underline{\psi}^k$, come from models used to approximate the flux distribution within a reactor. In this case, the reactor is the MITR.

There are two other models currently being employed to predict flux distribution and criticality in the MITR. The first is a finite difference diffusion theory model using the CITATION code package. This model has been used successfully by the MIT Reactor Operations Group for many years, and has been adapted to include depletion of the fuel. This model is best described by Bernard [B4]. The second model employs MCNP4A, a Monte Carlo code capable of accurately describing the complex structures in the MITR core. This model was also developed at MIT, by Redmond [R1], and has been shown to be quite accurate.

Recall from Chapter 3 that, although the MCNP model of the reactor is not suitable to provide a reference calculation from which discontinuity factors could be derived, it is still possible to use the flux shapes generated by the model as the expansion functions in the instrumented synthesis.

Despite the availability of two other MITR models, the model used in evaluating the instrumented flux synthesis method was developed using the QUARTZ code. The modifications to the code for the Instrumented Flux Synthesis Project were detailed in the Chapter 3.

It is certainly reasonable to wonder why a new model should be developed when two existing models, whose accuracy is well established, already exist. There are several reasons:

- a) The ease with which data could be manipulated using QUARTZ was much greater. Subroutines for the collapsing of spatial nodes and calculation of discontinuity factors could be easily incorporated into the body of the code. This decreased the amount of postprocessing necessary in going from small node to large node cases. Neither previous model offered this flexibility.
- b) The nature of a nodal code makes accurate, fast-running calculations with large node sizes possible. This also reduces the size of $\underline{\Psi}$ in the synthesis.
- c) QUARTZ can run time-dependent calculations, allowing the transients initiated as part of the synthesis experiment to be reproduced with a neutronics code. Neither CITATION nor MCNP possesses these capabilities.
- d) The triangular-Z geometry in QUARTZ better describes the geometry of the MITR core than the R- Θ -Z geometry used in CITATION. Both, however, pale in comparison to the geometric complexities represented in the MCNP model.

None of these points is enough to dismiss the previous models out of hand. Had effort been placed into making the MCNP or CITATION models work rather than development of a new model, either would probably have sufficed. However, through developing a new model the capability of the QUARTZ code was greatly enhanced and a more flexible and capable description of the MITR has been formed.

The process of generating the new model is first to create a fine mesh, three dimensional model that accounts for as many of the heterogeneities as is possible. This fine mesh model accounts for depletion effects and varying control blade positions. Once the fluxes and eigenvalue are found for a fine mesh model, the supernodal collapsing routines are employed, and a coarse mesh simulation is created. This coarse mesh model is then used to generate flux shapes for the instrumented synthesis as well as perform transient analyses of the experiments undertaken as a part of the instrumented synthesis project.

Although the already existing models were not used to generate flux shapes for the instrumented synthesis project, some attributes of both models were incorporated into the final QUARTZ model of the reactor. For this reason, it is instructive to review some of the important features of each model, especially as they are applied to the QUARTZ model.

5.3 THE CITATION MODEL

The CITATION [F1] model has been used since the 1970's to perform criticality calculations in the MITR-II. It consists of 23 planes, 19 radial divisions, and 30 azimuthal divisions for a total of 13,110 nodes, about half that of the QUARTZ model. The CITATION code runs on an IBM mainframe computer.

Because of the R- Θ -Z geometry used in the CITATION model, the geometry of the fuel elements as modeled by CITATION does not match the actual geometry. Also,

the CITATION model uses an active fuel length of 24". This is different than the actual active fuel length of 22.375". For these reasons, the macroscopic cross sections available from CITATION were not used directly in the QUARTZ model. The model did, however, provide three important pieces of information incorporated into the QUARTZ model: microscopic cross sections, U²³⁵ concentrations in depleted elements, and boundary conditions. These are discussed below.

5.3.1 MICROSCOPIC CROSS SECTIONS

QUARTZ uses macroscopic cross sections in any number of user specified groups. The definition of a macroscopic cross section involved two quantities: microscopic cross sections and number densities. For material J consisting of isotopes $j \in J$,

$$\Sigma_{g,\alpha}^J \equiv \sum_{j \in J} n^j \sigma_{\alpha,g}^j \quad (5.1)$$

With the exception of U²³⁵ and the lumped fission product, all number densities are calculated specifically for the QUARTZ model. But there needs to be a library of microscopic cross sections available for macroscopic cross section determination. The CITATION model provides this library. Listed in Table 5.1 are the materials available in the CITATION library, entitled MITXSC.

Material #	Material	Material #	Material	Material #	Material
1	U ²³⁵ C-ring 0-2"	21	D ₂ O	41	Graphite Reflector
2	U ²³⁸ C-ring 0-2"	22	Al reflector tank	42	D ₂ O
3	H ₂ O C-ring 0-2"	23	H ₂ O below core	43	Al
4	Al C-ring 0-2"	24	U ²³⁵ A-ring 12-24"	44	H ₂ O above core
5	U ²³⁵ A-ring 0-2"	25	U ²³⁸ A-ring 12-24"	45	Cd reg rod
6	U ²³⁸ A-ring 0-2"	26	Al A-ring 12-24"	46	FP asymptotic
7	H ₂ O A-ring 0-2"	27	H ₂ O A-ring 12-24"	47	H ₂ O
8	Al A-ring 0-2"	28	U ²³⁵ B-ring 12-24"	48	H ₂ O over core tank
9	U ²³⁵ A-ring 2-12"	29	U ²³⁸ B-ring 12-24"	49	Xenon-lower core
10	U ²³⁸ A-ring 2-12"	30	Al B-ring 12-24"	50	Xenon-upper core
11	Al A-ring 2-12"	31	H ₂ O B-ring 12-24"	51	FP 3000 hours
12	H ₂ O A-ring 2-12"	32	H ₂ O grid	52	Steel
13	Al B-ring 0-12"	33	Al grid	53	Hf spider (hex)
14	H ₂ O B-ring 0-12"	34	Al below core	54	Hf spider (arms)
15	U ²³⁵ B-ring 0-12"	35	Al w/ absorbers	55	H ₂ O reflector tank
16	U ²³⁸ B-ring 0-12"	36	Al upper structure	56	Al reflector tank
17	U ²³⁵ C-ring 2-12"	37	Void-beam port	57	Cd spider (hex)
18	U ²³⁸ C-ring 2-12"	38	Al lower structure	58	Cd spider (arms)
19	H ₂ O C-ring 2-12"	39	Mo ⁹⁹	59	H ₂ O edge of grid
20	Al C-ring 2-12"	40	Boron Stainless	60	Al edge of grid

Table 5.1. Microscopic Cross Sections Available from CITATION

The library has manually copied and saved to floppy disk for use with this project.

For materials in the fuel elements, the measurements are given as inches from the top of the fuel. Notice that different cross sections are available for elements in each of the rings as well as at different elevations.

The cross sections are in three groups, whose energy structure is given below.

Group #	Maximum Energy (eV)	Average Energy (eV)
1	1.0×10^7	5.4772×10^4
2	1.0×10^4	34.64
3	0.4	0.01

Table 5.2. CITATION Energy Group Structure

The delayed neutron fractions and precursor decay constants which will be used in the transient analyses are given in Table 5.3. CITATION also gives values for these constants, but those were discarded in favor of the values below.

Delayed Neutron Precursor Group	Decay Constants (s ⁻¹)	Fraction
1	0.0127	0.000247
2	0.0317	0.0013845
3	0.1150	0.001222
4	0.311	0.0026455
5	1.40	0.000832
6	3.87	0.000169

Table 5.3. Delayed Neutron Data

By summing the individual delayed neutron fractions, a total delayed neutron fraction of $\beta=0.0065$ is calculated.

5.3.2 U²³⁵ AND FISSION PRODUCT NUMBER DENSITIES

With the exception of U²³⁵, fission products, and B¹⁰, all number densities are determined through a triangular homogenization process discussed in Section 5.4. U²³⁵ and fission products are taken from the CITATION model of the MITR-II based upon burnup of each element.

Although the CITATION code does not itself perform depletion analyses, post-processing codes entitled DEPCOD and DEPCOD2 have been written by Bernard [B4] and are used to calculate the depletion of U²³⁵ in fuel elements from cycle to cycle. DEPCOD2 will determine U²³⁵ concentrations in all of the fuel elements based upon

exposure in the MITR core. The fission products are modeled in DEPCOD2 as a single, lumped fission product. The concentration of the fission products is based upon the depletion of U^{235} .

The results of the DEPCOD2 calculations have also been used in the MCNP model of the MITR. In a code called DEplete [R2], the U^{235} number densities are read from DEPCOD2 output, corrected for differences in volumes between the CITATION and MCNP models of the fuel elements, and used in the MCNP model. A flowchart of the DEplete code is shown in Figure 5.1

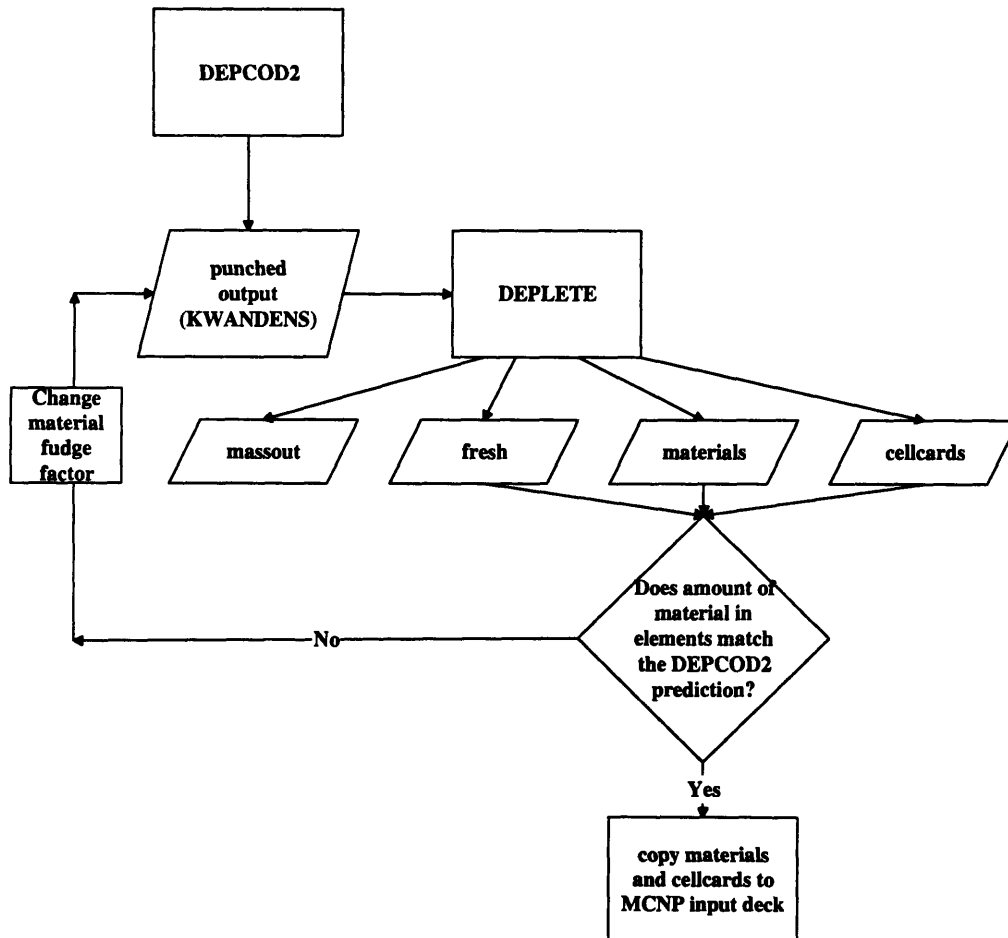


Figure 5.1. DEPELTE Code [Ref. R2] Flowchart

Portions of the DEplete code have been used to develop U^{235} and fission product number densities for the QUARTZ model. These adapted routines have been put into a program called DECK. The routines account for differences in the volumes of the actual elements versus the QUARTZ model. More detail about the code is in Appendix 4. It is sufficient to state at this time that, in addition determining U^{235} and fission product number densities, material compositions can be laid out with some automation and the position of the control blades can be easily altered, requiring only minor changes to the DECK input.

5.3.3 BOUNDARY CONDITIONS

Recall that the current at the surface of the reactor can be related to the flux by

$$\alpha_{g,p}^{i,j,k} \bar{J}_{g,X}^{i,j,k}(p) = \beta_{g,p}^{i,j,k} \bar{\Phi}_g^{i,j,k}(p) \quad (3.13)$$

Either previous MITR model can be used to determine the boundary conditions for the QUARTZ model. Both options were explored. Because of the difficulty in finding a suitable surface across which to tally the current in the MCNP model, it was discarded in favor of using the CITATION model.

The CITATION model extends deep into the heavy water reflector that surrounds the core tank. It would have been preferable to extend the QUARTZ model of the reactor this far as well. Unlike the CITATION model, however, all the nodes in the QUARTZ

model are restricted to the same size. This is not a programming limitation, but lies in the nature of the triangular geometry. Two smaller nodes, each generally with different currents across their surfaces, cannot abut a large node with a single current across its surface. This prevents the QUARTZ model from switching to large nodes in homogeneous regions like the reflector. Such a change would reduce the computational effort. To keep the fine-mesh QUARTZ model to a manageable number of nodes, it was extended only two inches into the reflector. Unfortunately, this means the model is tightly coupled to the boundaries. While the results for the static cases will be shown to be quite satisfactory, this may present a problem for transient measurements since changes in the physical system as the transient progresses are not reflected in the boundary conditions, which remain static.

Because surface averaged quantities are not directly calculated in CITATION, the current was estimated with a finite difference approximation using volume averaged fluxes. A schematic of an azimuthal slice from the CITATION model is illustrated in Figure 5.2.

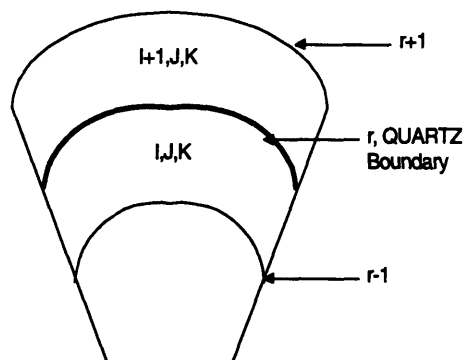


Figure 5.2. Schematic of CITATION Nodes Near the QUARTZ Boundary

The approximation for the current across the surface at r is

$$\bar{J}_{g,X}^{ijk}(p) \cong -D_g^{ijk} \frac{\bar{\Phi}_g^{i+1,j,k} - \bar{\Phi}_g^{ijk}}{X_c} \quad (5.2)$$

The albedo boundary condition is then estimated as

$$\frac{\beta_{g,p}^{ijk}}{\alpha_{g,p}^{ijk}} = \frac{\bar{J}_{g,X}^{ijk}}{\bar{\Phi}_g^{ijk}(p)} \cong \frac{-D_g^{ijk} [\bar{\Phi}_g^{i+1,j,k} - \bar{\Phi}_g^{ijk}] / X_c}{\bar{\Phi}_g^{ijk}} \quad (5.3)$$

where the quantities on the right side of Eqn. 5.3 are taken from CITATION at the approximate location of the QUARTZ boundary. This time, X_c is the center to center distance of two radial nodes.

There are a number of approximations made in using these boundary conditions. First, the CITATION surface used to estimate the boundary condition for QUARTZ is a cylinder. The QUARTZ boundary is a hexagon, meaning different points on the surface lie at different distances from the center of the model. Second, the QUARTZ boundary conditions cannot vary azimuthally. For a level positioning of the control blades, this restriction is a very minor one. But for tilted shim blade configurations, as were used in instrumented flux synthesis experiments, there was considerable variation in the current and flux at the boundary in the azimuthal direction.

For all cases, $\alpha_{g,p}^{ijk}$ was set to 1.0, and $\beta_{g,p}^{ijk}$ was solved according to Eqn. 5.3. The fluxes and diffusion coefficients were taken from the CITATION analysis of core #106. This was the core used for the first experiment. The same set of boundary conditions were used for core #110, the core for the second experiment. The detailed boundary conditions are given in the inputs decks, but approximate values are given below. The subscripts denote the group numbers.

Condition	β_1	β_2	β_3
Blades In	0.095	0.033	-0.045
Blades Out	0.095	0.033	-0.012

Table 5.4. QUARTZ Boundary Conditions Taken from CITATION ($\alpha_g = 1.0$)

The boundary conditions were allowed to vary axially. For planes in which the shim bank was partially inserted, the “Blades In” and “Blades Out” conditions were averaged together. Note that, in the thermal group, neutrons are *returning* across the boundary.

5.4 MCNP MODEL

The MCNP model of the MITR has been developed primarily by Redmond [R1]. It takes into account much of the geometrical complexity of the MITR with great precision. For this reason, it was used as an aide in homogenizing the MITR for triangular geometry. The process of homogenization is described below.

Triangular geometry was selected for analysis of the MITR because the fuel elements can be modeled well by triangles. A look at the cross section of the fuel element,

shown in Figure 4.2 should provide some insight into why the triangular geometry is well suited to modeling the fuel. The large rhombus in Figure 5.3 represents a fuel element.

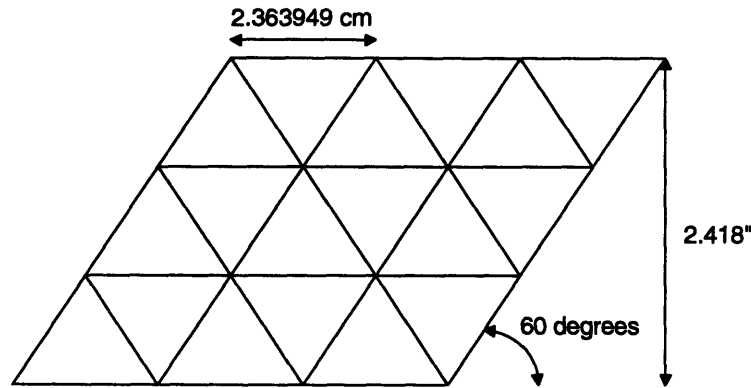


Figure 5.3. Fine Mesh Model of an MITR-II Fuel Element

Each element can be represented by a discrete number of nodes without homogenizing fuel material with surrounding structural material.

A word should be said about consistency of the specifications of the fuel elements in the QUARTZ and MCNP models of the reactor. The 2.418" measurement in Figure 5.3 is taken from MITR Design Drawing R3G-1. According to that measurement, the fuel elements are 7.092 cm on each side. Redmond, however, models the fuel elements as 6.9921 cm on each side in his MCNP calculations. The difference is that the intervening space between the two measurements is taken up by water in the MCNP model. This correctly models the physical system. In the QUARTZ model, the fuel number densities are smeared over the entire 7.092 cm distance. The coolant number density taken from the MCNP model is smeared over the entire 7.092 cm distance, then increased by a factor X ,

$$X \equiv \frac{2 \times \left[\frac{1}{2} \cdot 7.092 \text{cm} \cdot (\sin 60^\circ \cdot 7.092 \text{cm}) \right]}{2 \times \left[\frac{1}{2} \cdot 6.9921 \text{cm} \cdot (\sin 60^\circ \cdot 6.9921 \text{cm}) \right]} = 1.03$$

X is the ratio of the area of the two fuel element models. In this way, coolant within the fuel element as well as in the gap between fuel elements is included in the QUARTZ model.

Unfortunately, most of the surrounding structure cannot be modeled as well by triangles. For example, triangular nodes cannot be made to fit the cylindrical core tank exactly. For regions like these, we are left with two choices: (1) maintain the actual geometric description and homogenize each node dependent upon the amount of each material in the node, or (2) change the geometry to allow nodes to contain only one material.

An example of each homogenization scheme is given in the following figures. A triangular mesh is desired to model a region of core tank (in white) and surrounding moderator (in gray). Figure 5.4 is a demonstration of the first homogenization method.

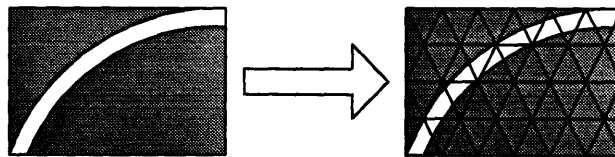


Figure 5.4. Homogenization Scheme #1 - Maintain Actual Geometry

The triangular mesh is laid over the unchanged geometry. Each triangular node must contain a homogeneous material. In a node containing both moderator and core tank, the homogeneous material consists of fractions of each material in accordance with the

amount of area occupied by that material. If 65% of the node is filled with moderator and 35% with core tank, the homogenous material in that node will consist of moderator at 65% of its nominal number density and core tank at 35% of its nominal number density. The resulting macroscopic cross section will be $\Sigma^{node} = 0.65\Sigma^{mod} + 0.35\Sigma^{tank}$.

The problem with such homogenization schemes is that, in general, each node will have a different fraction of materials occupying it. A quick glance at Figure 5.4 shows some nodes almost completely occupied by the core tank, while some have very little core tank material. Different compositions would have to be defined for each of them, increasing the complexity of the problem.

An alternative to this scheme is illustrated in Figure 5.5. Here, only two materials are defined: the core tank and the moderator.

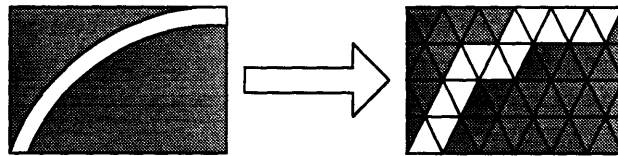


Figure 5.5. Homogenization Scheme #2 - Change Geometry to Define Fewer Materials

Without placing too much emphasis on the scale of the figures, it is reasonable to state that the materials in the triangular model do not occupy the same area as in the actual geometry. To preserve the total amount of material from the actual reactor, the number densities in the triangular model are changed to reflect the change in area. By preserving the total amount of material, the total reaction rate is also preserved.

As an example, consider the core tank in the MCNP and QUARTZ models. The inner radius of the core tank is 25.4 cm², and the outer radius is 26.053 cm². The cross sectional area is $\pi \times (26.035 \text{ cm}^2 - 25.4 \text{ cm}^2) = 102.65 \text{ cm}^2$. These are the same specifications used in the MCNP model. When the core tank is modeled in QUARTZ according to the second scheme (Figure 5.5), its cross sectional area is 392.00 cm². To preserve the total amount of material, the number density used in QUARTZ must be $102.65 \text{ cm}^2 / 392.00 \text{ cm}^2 = 26.19\%$ that of the MCNP model. The MCNP number densities of some of the more common materials in the MITR model are given in Table 5.5.

Material	Number Density (#/barn-cm)
Light Water (H2O) at 40 °C (0.9968 g/cc)	0.033337
Heavy Water (D2O) at 21 °C (1.10445 g/cc)	0.033324
Aluminum	0.060034

Table 5.5. Nominal Number Densities of Some MITR Materials

Using this method of homogenization greatly reduces the number of compositions that must be calculated. It also makes explicit modeling of the fuel elements possible. The hexagonal absorber that stands between the inner A-ring of fuel and the outer B- and C-rings is 0.5969 cm wide, smaller than the width of a triangular node. If the first homogenization method were used, fuel material from the B-ring would be homogenized with the hexagonal absorber. Also, fuel material from the C-ring would be homogenized with fuel material from the B-ring. Because the U²³⁵ number density is different in each fuel element, this such homogenizations would make assigning number densities more

difficult. By allowing the hexagonal absorber to take on the width of a full node, and reducing its number density concurrently, the fuel elements remain distinct from the absorber. Because the number density of the absorber material is reduced in the QUARTZ model, the transmission of neutrons through the material should be the same as the MCNP model.

Because the MCNP model already possesses detailed measurements and number densities, it is the most convenient way to determine number densities for the QUARTZ model. This is the most useful aspect of the MCNP model. All the number densities with the exception of U^{235} , fission products, and B^{10} in the control blades were determined in the above manner. Unlike the U^{235} data from the CITATION model, the number densities for structural material were the same for each fuel loading of the reactor.

5.5 CONTROL BLADES AND DETECTOR POSITIONS

The control blades are fabricated from stainless steel doped with natural boron. The natural boron consists of approximately 80% B^{11} and 20% B^{10} . B^{10} is a “1/v absorber,” meaning its neutron capture cross section increases as the energy, or velocity, of the neutron decreases. As such, the blades are very strong absorbers of thermal neutrons. They are used to provide reactivity control in the reactor.

Modeling the control blades is an especially challenging portion of the QUARTZ simulation. In the QUARTZ model, the control blades lie very close to the boundary of the system, where the reflector creates a large returning current of thermal neutrons.

These characteristics create two problems for the model. First, the combination of thermal flux suppression by the blades and a large returning thermal neutron current at the boundary creates very steep flux gradients near the edge of the model. These gradients present difficulties to the numerical schemes used to solve finite difference equations, especially when the non-linear iteration method is applied to allow a quadratic current approximation. Second, the proximity of the blades to the boundary makes the boundary conditions very tightly coupled to the control blade positions. An examination of Table 5.4 above reveals the dramatic change in the values of β in the albedo boundary condition when the control blades are inserted.

With these difficulties in mind, the model of the control blades was developed. The first problem was how to position the blades axially in the model. As stated in Chapter 4, the blades move up and down along the core periphery in slots in the core housing. The bottom of the slots are one inch above the bottom of the active fuel. Positions of the control blades are recorded in inches above the bottom of these slots. The difficulty in using these measurements directly is that the physical active fuel length (22.375") is different from the QUARTZ model (24"). A schematic of the problem is given below.

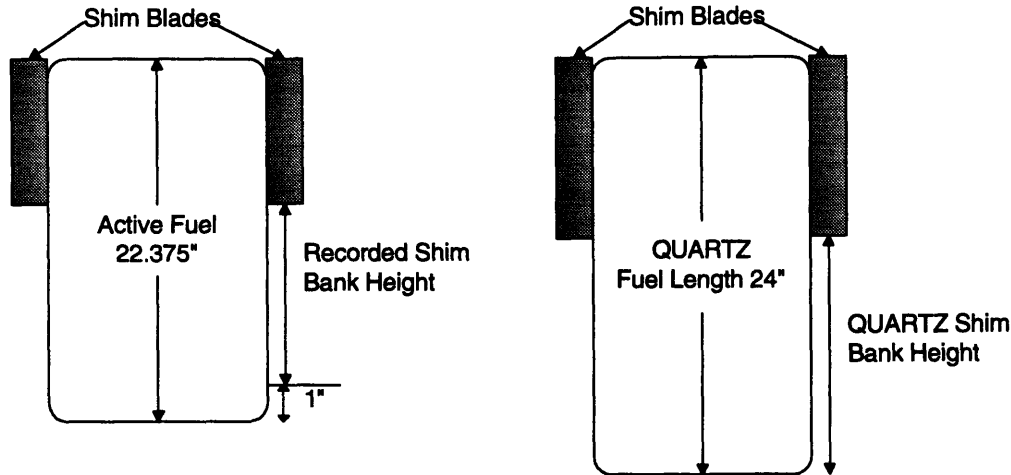


Figure 5.6. Actual vs. QUARTZ Shim Blade Positions

To define a shim bank height in the QUARTZ model, the fraction of the active fuel length below the shim blades in the physical system was determined. This same fraction was used in the QUARTZ model. For example, if the recorded shim bank height was 7.95", 8.95" or 40% of the active fuel is below the shim blades. If 40% of the active fuel is below the shim blades in the QUARTZ model, the blades should be placed 9.60" above the bottom of the active fuel.

In the evaluation of the instrumented synthesis method, different static and transient conditions were created by movement of the control blades. Neutron fluxes were measured by fission chambers located in water vent holes near the control blades. Since the movement of the blades affects the flux at the detector locations, the detectors' locations in the QUARTZ model should be consistent with the control blades' positions. The bottom of the lowest detectors rests 6.55" above the bottom of the active fuel region. In the QUARTZ model, this translates into $(24/22.375) \times 6.55 = 7.02$ " above the bottom of

the fuel. The detectors, each 1.906" long, do not fit wholly into each axial plane in the QUARTZ model. For example, the bottom detectors extend from halfway into plane #5 to halfway into plane #6. When comparing flux measurements at the detector locations to predicted values, there will be some error. For purposes of the evaluation, the detectors were assumed to be in planes #6 (bottom), #8 (middle) and #10 (top).

With the positioning of the control blades established, the number densities to be used must be determined. In the CITATION model, the only material used in the definition of the control blades is "borated stainless steel." It is unclear whether the microscopic cross section is that of boron or some mixture of boron and steel. To be sure, the B¹⁰ absorption cross section will dominate the reactions taking place at thermal energies, even if steel were included in the control blade definition. This single material will also be the only material in the QUARTZ model of the control blades. The remaining issue is the number density to be employed in QUARTZ. There are several options.

- a) *Use the MCNP value of B¹⁰ concentration, corrected for differences in volume between the models.* The B¹⁰ content in the control blades is given in MCNP as 0.1954% by weight of the control blade material. The density of the control blades are listed as 8.0271729 g/cm³. Using these facts yields a number density of B¹⁰ in the MCNP model of

$$0.001954 \times 8.0271729 \frac{\text{g}}{\text{cm}^3} \times \frac{1 \text{ gram} - \text{mol}}{10.012937\text{g}} \times \frac{6.024 \times 10^{23} \text{ nuclei}}{\text{gram} - \text{mol}} \times \frac{\text{cm}^2}{10^{24} \text{ barn}}$$

$$= 9.436 \times 10^{-4} \frac{\text{nuclei}}{\text{barn} - \text{cm}}$$

The control blades are actually two sheets of steel separated by small metal studs. A cross section of the area is shown in Figure 5.7.

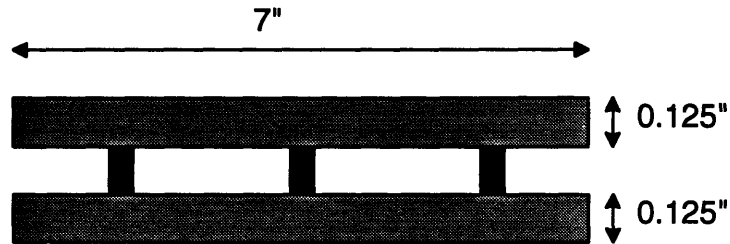


Figure 5.7. Control Blade Geometry

The total area of the borated steel plates is 1.75 in^2 , or 11.29 cm^2 . The control blades as modeled in QUARTZ have a cross sectional area of 36.30 cm^2 .

Additionally, to maintain consistency with the control blade positioning scheme discussed above, the number density should be reduced by a factor of $22.375/24$. Assuming the “Borated Stainless Steel” microscopic cross section in CITATION is that of B^{10} alone, the final number density of “Borated Stainless Steel” is

$$\begin{aligned} \text{QUARTZ \# density} &= 9.436 \times 10^{-4} \frac{\#}{\text{barn} - \text{cm}} \times \frac{11.29 \text{ cm}^2}{36.30 \text{ cm}^2} \times \frac{22.375 \text{ cm}}{24 \text{ cm}} \\ &= 2.374 \times 10^{-4} \frac{\#}{\text{barn} - \text{cm}} \end{aligned}$$

- b) Use the CITATION “Borated Stainless Steel” concentration, corrected for differences in volume between the models. The lengths of the cores in

CITATION and QUARTZ are the same. Only differences in the cross sectional area need to be treated. The cross sectional area of the control blades in CITATION is 13.05 cm^2 with a boron concentration of $9.02580 \times 10^{-4} \text{ #/barn-cm}$. The value in QUARTZ would be

$$\text{QUARTZ \# density} = 9.02580 \times 10^{-4} \frac{\#}{\text{barn - cm}} \times \frac{13.05 \text{cm}^2}{36.30 \text{cm}^2} = 3.245 \times 10^{-4} \text{ cm}^2$$

- c) *Replicate the transmission of thermal neutrons through the CITATION model of the control blades.* The control blades may be reasonably approximated as purely absorbing materials for neutrons at thermal energies. If we approximate the blades as slabs, the transmission of thermal neutrons through them is given by $\exp(-\Delta \times N \times \sigma_3)$. Δ is the thickness of the slab, N is the number density of the absorber, and σ_3 is the thermal removal cross section. If the transmission of thermal neutrons is to be matched in both cases, $\Delta \times N \times \sigma_3$ must be equal. The same microscopic cross section is used in both cases. If we take the width of the slab in the QUARTZ case to be the altitude of the triangular node, we obtain

$$\begin{aligned} \text{QUARTZ \# density} &= 9.02580 \times 10^{-4} \frac{\#}{\text{barn - cm}} \times \frac{0.635 \text{cm}}{2.363949 \text{cm} \times \sin 60^\circ} \\ &= 2.7995 \times 10^{-4} \frac{\#}{\text{barn - cm}} \end{aligned}$$

The final estimate, used to replicate thermal neutron transmission through the blades, was the one used in the QUARTZ model. First, since “Borated Stainless Steel” is never clearly defined, using it as the cross section for B^{10} alone may be incorrect. Second, by replicating the transmission through the blades, we account in some measure for the changes in self shielding in going from a blade 0.635 cm thick to one 2.047 cm thick. It is also hoped that the flux on the side of the control blades away from the core is better represented when the transmission is correct.

5.6 QUARTZ MODEL

Sections 5.3, 5.4, and 5.5 detailed how microscopic cross sections and number densities were determined for use in the QUARTZ model. These quantities were used as input data for a fine-mesh QUARTZ model of the MITR-II core. Additional details of the model, along with results, are presented in this section.

5.6.1 STEPS IN QUARTZ ANALYSIS

The QUARTZ model is a three-dimensional simulation of the MITR-II core. It consists of 16 planes extending from the midplane of the beam ports to the coolant above the core tank. The planes are two inches in height. The fuel elements are assumed to be 24 inches in length. Each plane consists of 1536 nodes for a total of 24,576 nodes in the three-

dimensional model. A finite difference solution method is used in the fine mesh.

Schematics of all 16 planes are presented in Appendix 3.

As much detail as was practical was incorporated into the model. The shim blades were modeled explicitly. The hexagonal absorber model also includes the steel inserts in the top half of the core. The aluminum tubes that house the fission chambers were also modeled. Those vent holes that did not contain aluminum tubes were modeled as containing only water. The dummy elements were also used.

To generate expansion functions for the instrumented synthesis process, flux shapes representative of the actual flux in the reactor must be created. The QUARTZ model of the MITR is employed for this purpose. Number densities for structural material are derived from the triangular homogenization process. The U^{235} loading of each fuel element, which changes for each new core, is taken from the CITATION data. With these data, the core in which experimental data were taken can be analyzed. Once the fine mesh cases have been analyzed, the nodes are collapsed to a coarse mesh. Discontinuity factors were determined in accordance with procedures outlined in Section 3.3. For the MITR-II case, the coarse mesh was also analyzed with a finite difference solution scheme. The flux shapes generated by these coarse mesh analyses are the expansion functions used in the instrumented synthesis, and are specific to the core in which the experiments took place. If the collapsing is done correctly, the coarse mesh eigenvalues and fluxes should closely match those of the fine mesh problems. The adjoint flux shapes, used as weighting functions in determining kinetics parameters, were also calculated using the large mesh models.

Each large node is the size of 16 smaller nodes.

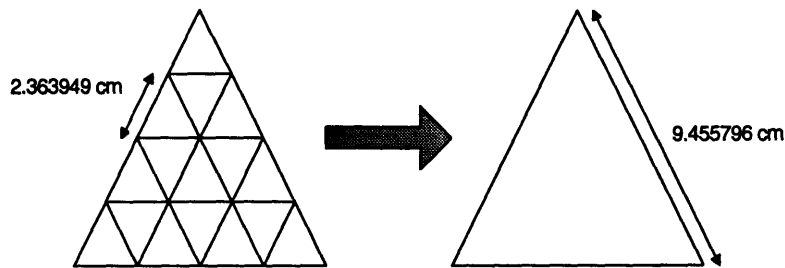


Figure 5.8. Large Node Size in the MITR-II Model

Although the number of nodes is decreased by a factor of 16, the reduction in computational time for the large mesh problems is much greater, decreasing from 1200 - 1600 CPU seconds to 25 CPU seconds, a factor of 50 to 60.

Once the static flux shapes are determined, the coarse mesh model can be used to analyze the transient experiments in the instrumented synthesis project. A blade insertion can be modeled as a change in cross section in the nodes occupied by a control blade. The transient analyses from the QUARTZ model can be compared to actual data as well as the synthesis approximation of the transient conditions.

It may be instructive here to look back at the thesis flowchart at the end of Chapter 2 for a more concise description.

In the next sections, results of the static calculations for two different fuel loadings of the MITR will be presented. Both the fine mesh and the coarse mesh results are given, although only the coarse mesh flux shapes will be used in the synthesis process. The transient results will be presented along with the synthesis results in Chapter 6.

5.6.2 STATIC RESULTS - CORE 106

The description of the experimental procedures in Chapter 4 outlines static and transient measurements made in the MITR core. Flux shapes were generated for each static condition. Flux shapes for the transients included the initial condition (usually one of the static conditions), the final condition, and one intermediate state.

Shim blade positions were taken from recorded measurements. The blades were positioned in the QUARTZ model according to procedures outlined in Section 5.5, and the appropriate power level was used. Table 5.6 summarizes the fine and coarse mesh models of the static conditions from the core #106 experiment. The recorded critical shim bank heights were 7.80" at 10 kW and 7.95" at 50 kW. There are several important results given in Table 5.6. First, the QUARTZ code is performing the supernodal analysis properly. Both the eigenvalue and fluxes are very close to the fine mesh reference results. Second, the eigenvalues are close to unity. Since all of the configurations in Table 5.6 were static measurements, the value of k_{eff} should be one. All of the k_{eff} values in Table 5.6 are close to this experimental value.

However, it should be noted that the eigenvalues for the tilted cases differ from those of the flat cases. This can be attributed to changes in the physical system at the boundary that are not reflected in changes in the boundary condition. Although QUARTZ can have different boundary conditions in the axial direction, the boundary conditions cannot change azimuthally. DeLorey makes reference to this limitation [D1], stating it is not a restriction of the geometry, only of the programming and results from a desire to

maintain the generality of the code. With the shim blades positioned so as to tilt the flux, conditions at the boundary will obviously change. This change was confirmed by simulating the flat and tilted blade configurations with the MCNP model of the reactor. As the configuration of the shim bank is changed, so is the current at the boundary. Because the boundary conditions remain constant, however, inaccurate predictions of the current returning across the boundary may result.

Power Level	Shim Blade Configuration	Fine Mesh k_{eff}	Coarse Mesh k_{eff}	Max Error in $\Phi_1/\Phi_2/\Phi_3$	Avg Error in $\Phi_1/\Phi_2/\Phi_3$
10 kW	Flat	0.992578	0.992588 (+0.001%)	0.0057% 0.0064% 0.0057%	0.0022% 0.0023% 0.0026%
10 kW	Tilt #1	0.994510	0.994522 (+0.001%)	0.0148% 0.0178% 0.0148%	0.0055% 0.0062% 0.0061%
10 kW	Tilt #2	0.994933	0.994946 (+0.001%)	0.0165% 0.0203% 0.0162%	0.0060% 0.0065% 0.0060%
50 kW	Flat	0.994753	0.994768 (+0.002%)	0.0079% 0.0096% 0.0078%	0.0031% 0.0033% 0.0033%
50 kW	Tilt #1	0.997191	0.997205 (+0.001%)	0.0190% 0.0228% 0.0188%	0.0072% 0.0079% 0.0077%
50 kW	Tilt #2	0.998964	0.998976 (+0.001%)	0.0112% 0.0132% 0.0109%	0.0041% 0.0044% 0.0043%

Table 5.6. QUARTZ Model of Core #106 Static Conditions

A simple example of the problem is presented in Figure 5.9. The source of thermal neutrons returning across the boundary is composed of fast neutrons that have leaked from the system and are reflected back by the heavy water at thermal energies. This is

represented by the boundary conditions. Where the blades are inserted, the thermal flux is depressed. Therefore β is made more negative to simulate the proper amount of returning thermal neutrons. Where the blades are absent, replaced by water, the flux is high. β is less negative here. Problems arise, however, when the blade positions vary azimuthally around the reactor.

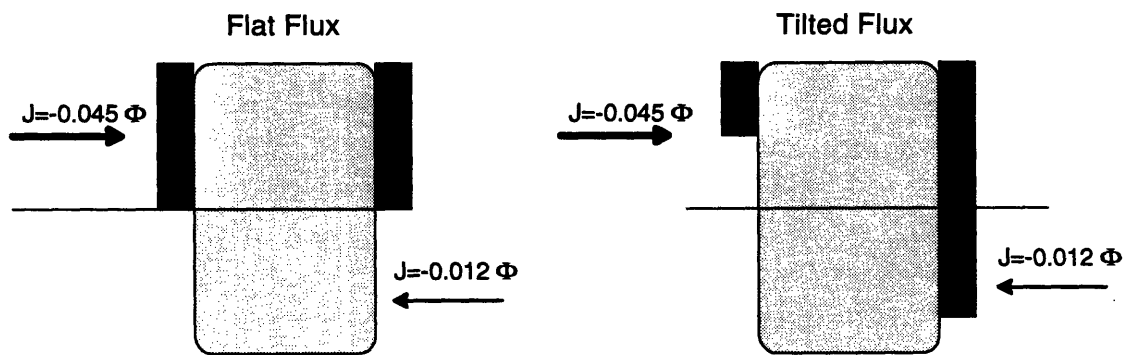


Figure 5.9. Flux Tilts Using Flat Boundary Conditions

Now there are regions where the blades have been removed, increasing the flux near the boundary, but with no corresponding reduction of β to account for the higher flux. Very large currents are simulated at the boundary, increasing the thermal neutron population dramatically. This is, of course, offset by the insertion of other control blades. At these locations, the blades depress the thermal flux. At the same time, the current at the boundary cannot be increased to simulate the actual condition of still large thermal currents returning to the reactor. Though these are competing effects, the above scenario tends to increase the thermal neutron population, raising k_{eff} . An alternative is presented in Figure 5.10.

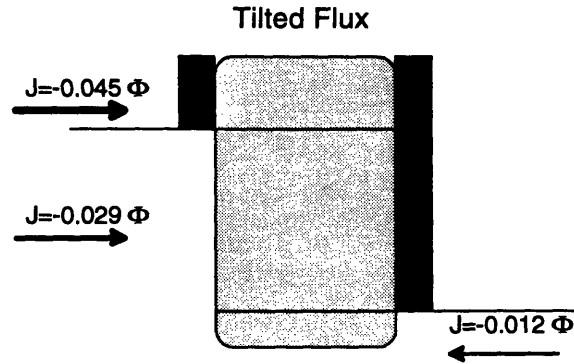


Figure 5.10. Flux Tilts Using Average Boundary Conditions

Here, the boundary conditions for the planes partially occupied by control blades are averaged. Both schemes, with and without averaging, were attempted. The results for core #106 are presented below.

Power	Condition	Δk^* , no averaging	Δk^* , averaging
10 kW	Tilt #1	0.0107	0.0019
10 kW	Tilt #2	0.0111	0.0024
50 kW	Tilt #1	0.0101	0.0026
50 kW	Tilt #2	0.0119	0.0042

Table 5.7. Effects of Averaging Boundary Conditions on Tilted Eigenvalues
 (* Δk =difference from flat eigenvalue)

The results are much better when boundary conditions for partially filled planes are averaged. As will be shown below, the flux measurements are also much closer to experimental results when the boundary conditions are averaged.

Finally, it is important to realize that the QUARTZ model of the reactor does not account for thermal-hydraulic feedback. The differences in the eigenvalues between the 10 kW and 50 kW cases result from different shim bank heights, as recorded during the experiment. The 50 kW measurements were made near the end of the experiment. By

this time, thermal feedback in the fuel and moderator had become apparent, and some fission products had begun to accumulate. The critical shim bank height for the 50 kW measurements was slightly higher than for the 10 kW measurements because of these effects. Since the QUARTZ model does not account for feedback, the eigenvalue increases as the shim bank is raised.

Flux shapes were generated for the transient measurements as well. The eigenvalues of those models are listed below, although the comparison to the fine mesh fluxes has been omitted.

Power Level	Shim Blade Configuration	Fine Mesh k_{eff}	Coarse Mesh k_{eff}
10 kW	#1 Dropped	0.970557	0.970567
25 kW	#6 at 8.52"	0.997866	0.997879
25 kW	#6 at 9.08"	0.999104	0.999119
50 kW	#3 at 7.42"	0.993298	0.993310
50 kW	#3 at 6.89"	0.992210	0.992227
50 kW	#6 at 7.60"	0.993662	0.993671
50 kW	#6 at 7.24"	0.992868	0.992883

Table 5.8. Flux Shapes Generated for the Transient Measurements in Core #106

The initial shim bank height for the drop of blade #1 was 7.95". For the insertion of blade #3, the bank was also initially at 7.95", as it was before the insertion and withdrawal of blade #6. Notice that the eigenvalues for the transient flux shapes are consistent with the static cases. For example, the eigenvalue when blade #6 is raised to 8.52" is higher than the flat shim bank case at 50 kW. When the blade is raised to 9.08", the eigenvalue is higher still. Lowering blade #3 causes the eigenvalue to decrease.

Finally, the blades were withdrawn to plane #15 and completely inserted through plane #3. These flux shapes complete the library of expansion functions for core #106.

Power Level	Shim Blade Configuration	Fine Mesh k_{eff}	Coarse Mesh k_{eff}
10 kW	All Rods In	0.932200	0.932218
10 kW	All Rods Out	1.04647	1.04651

Table 5.9. Other Flux Shapes Generated for Core #106

To this point, only the eigenvalues have been compared to experimental values. Although this is an important indicator of the accuracy of the model, it is not the only one available. We can further determine the efficacy of the model by looking at the flux shapes as predicted by the QUARTZ model. Detailed on the following pages are planar plots of the thermal flux at selected elevations in core #106. Note that the plots are not to scale and appear compressed in the vertical direction. The program used to plot the flux data does not account for node size, only the values of flux at a given X-Y-Z location.

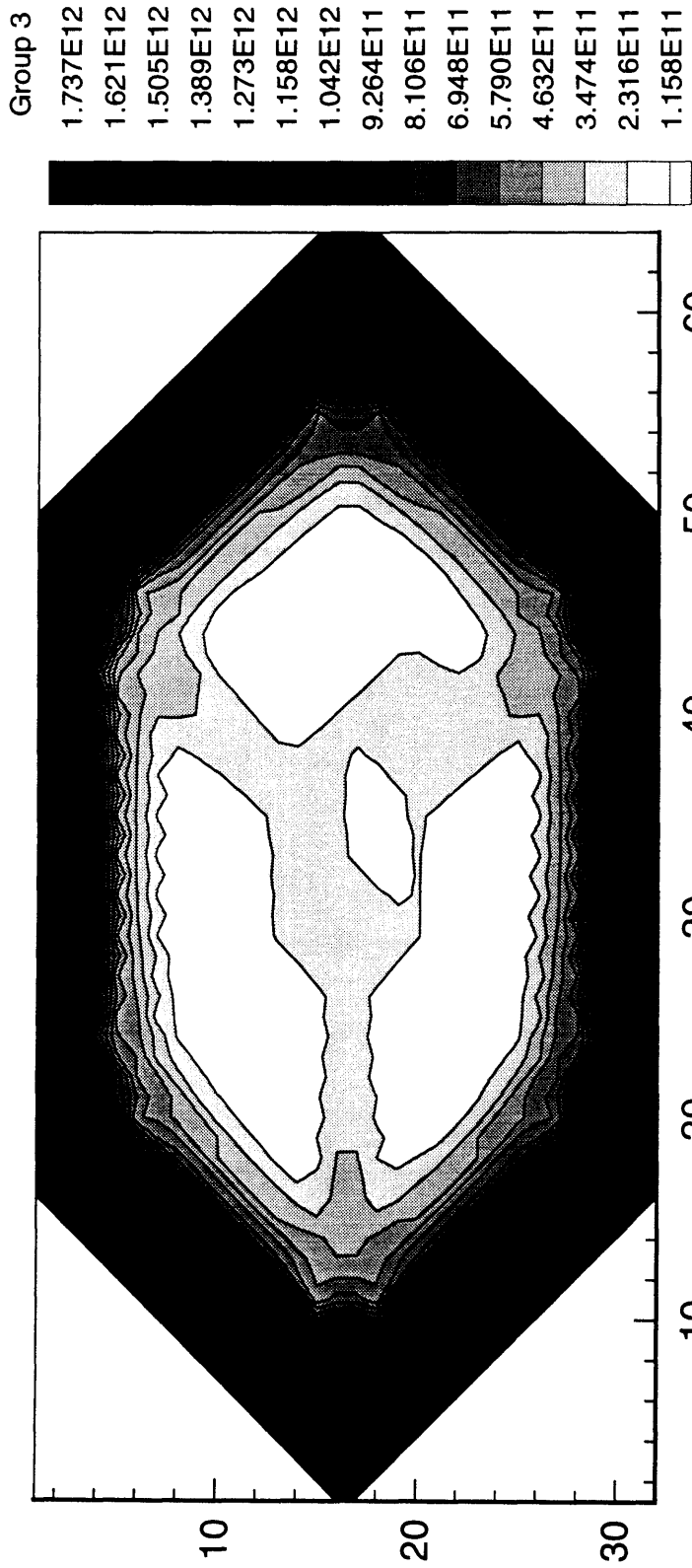


Figure 5.11. Core #106 Plane #6 Flat Shim Bank - 50 kW - Thermal Flux

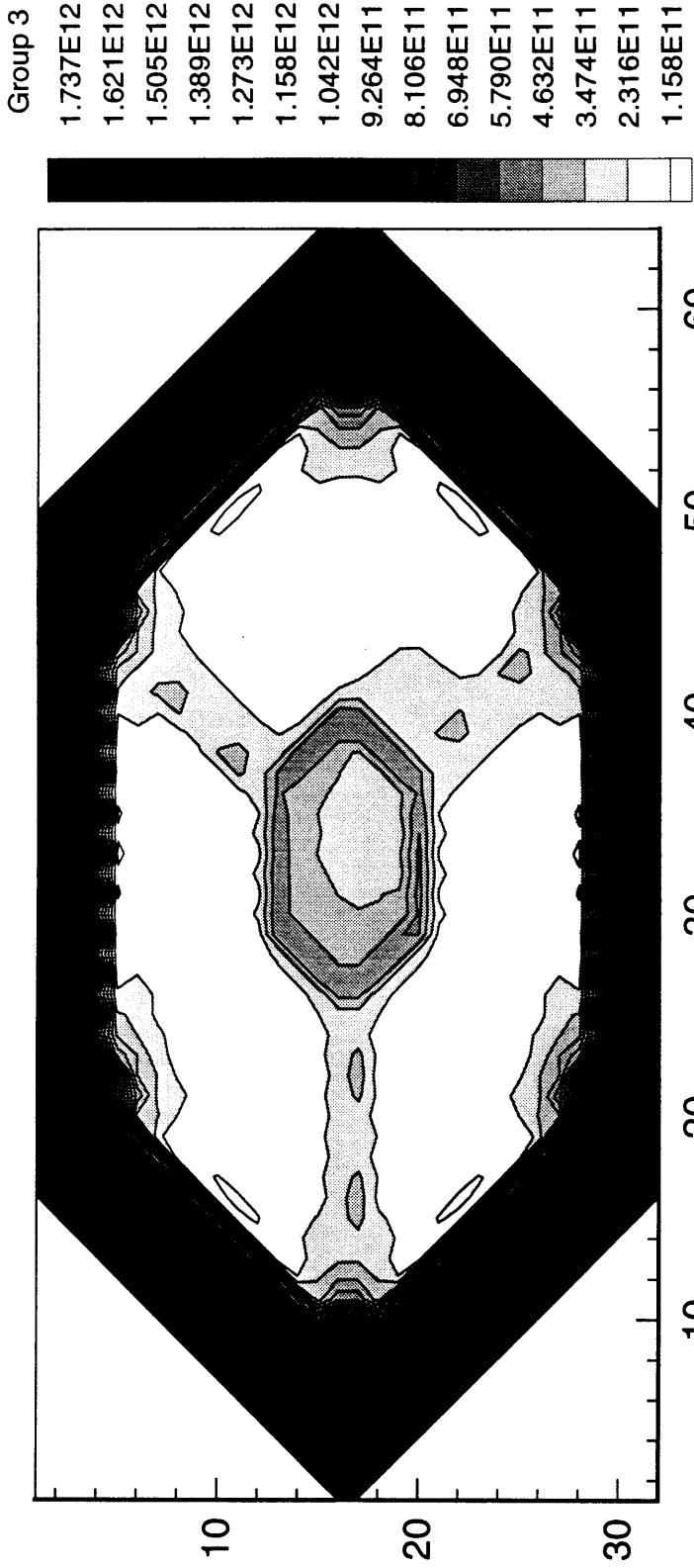


Figure 5.12. Core #106 Plane #8 Flat Shim Bank - 50 kW - Thermal Flux

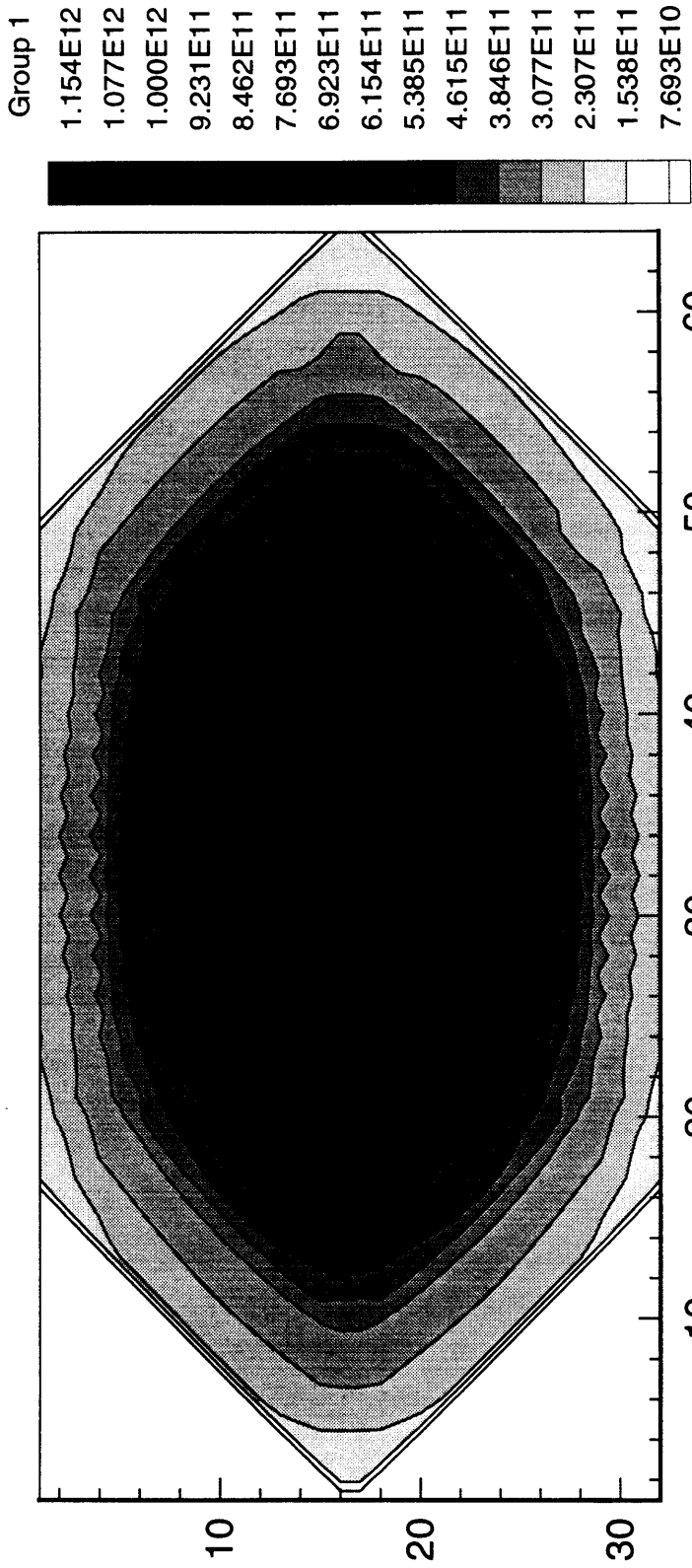


Figure 5.13. Core #106 Plane #8 Flat Shim Bank - 50 kW - Fast Flux

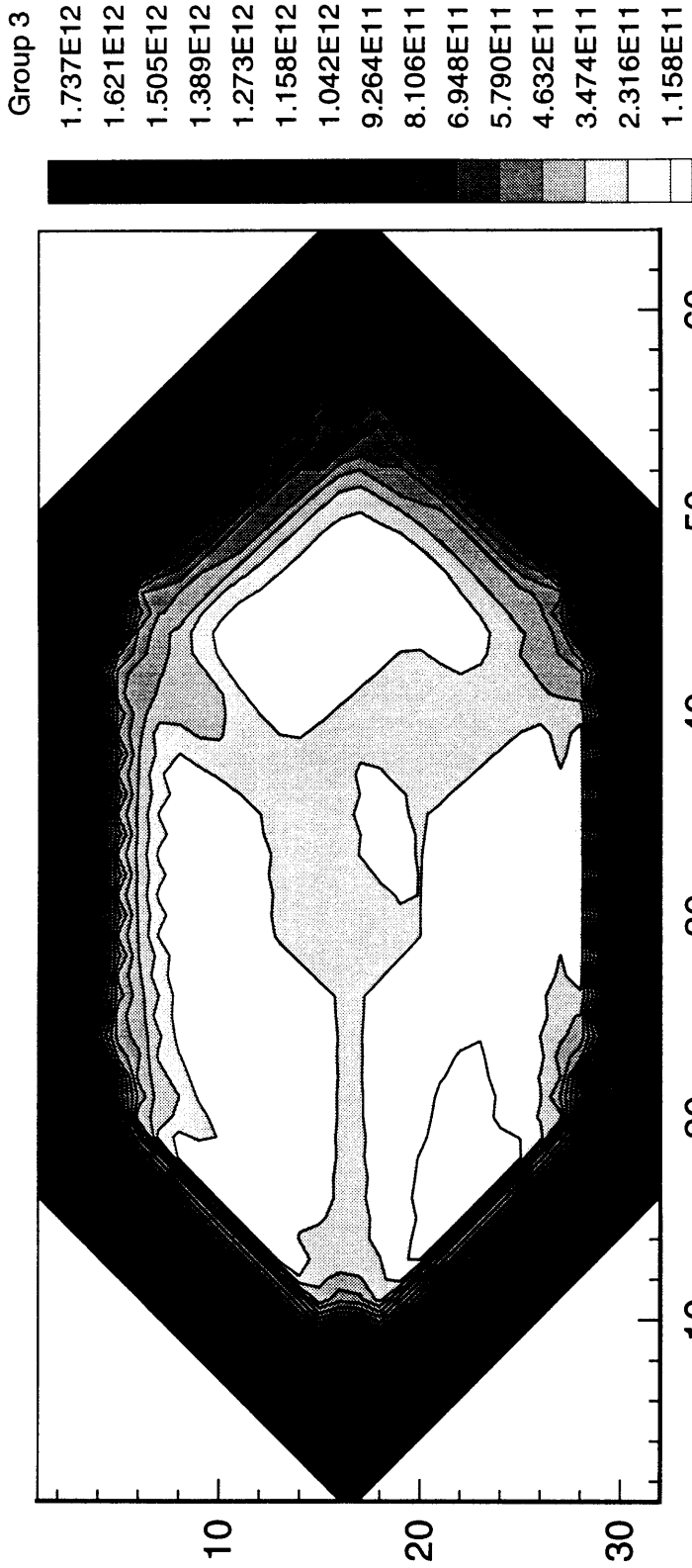


Figure 5.14. Core #106 Plane #7 Tilt #1 - 50 kW - Thermal Flux

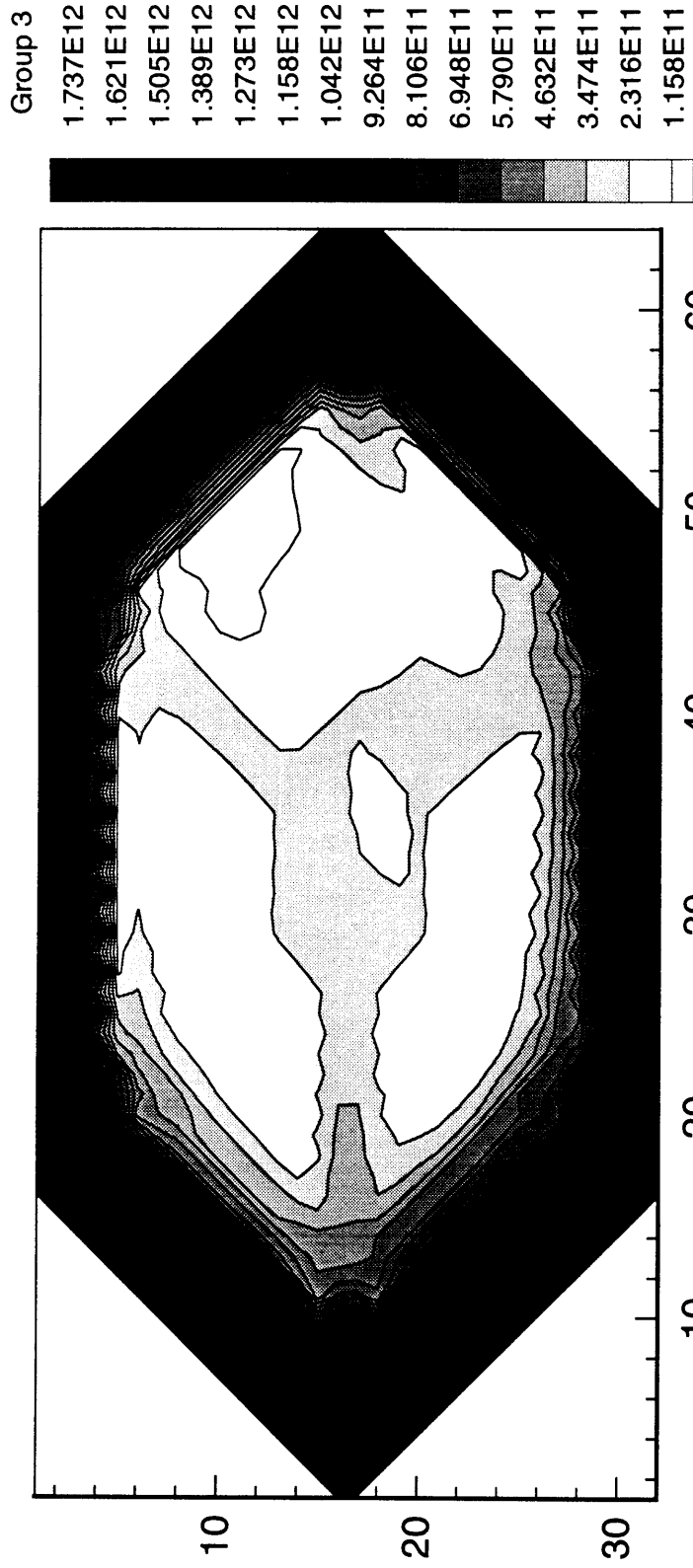


Figure 5.15. Core #106 Plane #7 Tilt #2 - 50 kW - Thermal Flux

There are several characteristics of the core that can be evidenced in the model [Figure 5.11]. First, portions of the arms of the hexagonal absorber are evident, extending out from the A-ring to the core housing. Along these arms and in the center of the reactor are small regions where the thermal flux increases. These are the aluminum dummy elements. The dummy elements are placed in positions according to the core loading pattern, which may change from core to core.

Where the active fuel elements are placed, the thermal flux is depressed, correctly showing the strong absorption of thermal neutrons in the fuel. An example of this is in the center of the core, where a flux depression indicates an active fuel element among two aluminum dummy elements. Away from the center of the core, past the core tank, the thermal flux increases sharply. This increase reflects the presence of D_2O in the model of the reflector, as well as the large returning currents at the boundary of the system.

The control blades are not evidenced in Figure 5.11. Plane #6 of core #106 lies below the shim bank height. The guide slots into which the blades are inserted are instead filled with water at this elevation. If we move to a plane above the shim bank height [Figure 5.12], the control blades become evident. Where increasing thermal flux was evident inside the core tank in Figure 5.11, Figure 5.12 shows severe flux depressions. A look at the fast flux shows it to be undisturbed by the control blades [Figure 5.13]. All of these characteristics match, at least qualitatively, those in the physical system.

In addition to the flat shim blade configurations, flux tilts in the reactor core were initiated by putting the control blades in asymmetric positions. These tilts were replicated in the QUARTZ model by using the procedure outline in Section 5.5. Plots of the tilted

flux configurations are given in Figure 5.14 and Figure 5.15. In Figure 5.14, the effects of control blades #3, #4, and #5 are visible. The steepest depression is caused by blade #4, which is completely inserted through plane #7. Blades #3 and #5 are partially inserted. The flux tilt is shifted to the other side of the core by withdrawing blades #3, #4, and #5 and inserting #6, #1, and #2 [Figure 5.15].

The two existing models of the MITR can also be used to quantify the accuracy of the QUARTZ model. A CITATION calculation was made for Core #106 with the shim blades pulled to a shim bank height of 16.00". The calculation was repeated in QUARTZ and MCNP and the fluxes in three fuel elements were compared. Plots of the thermal fluxes are given in the following figures. In each case, the fluxes edited from MCNP are given error bars representing one standard deviation, and the location of the MCNP fluxes are adjusted to apply to a 24" core. In this way, measurements from all three models are consistent.

In the first figure, the flux in element A2 from all three models versus axial distance from the bottom of the fuel is plotted.

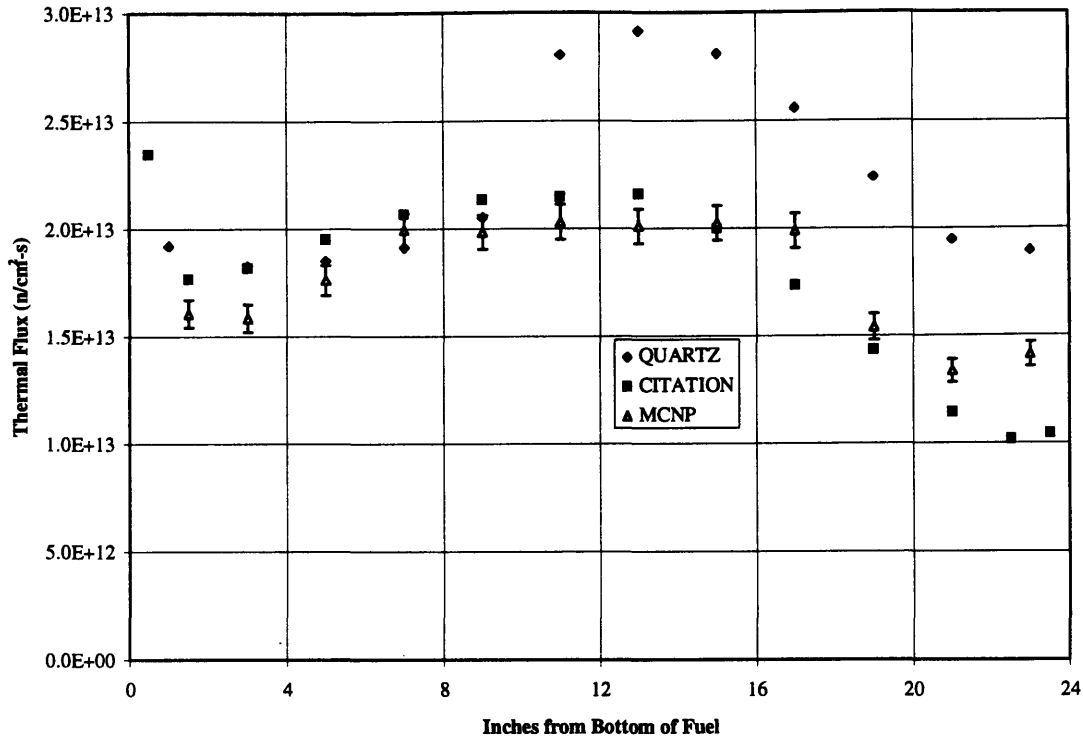


Figure 5.16. Thermal Flux in Element A2 vs. Axial Position

Near the bottom of the fuel, the fluxes from all three models are closely matched. As we approach the top of the core, the discrepancies widen. In all three models, the stainless steel inserts used in the hexagonal absorber to suppress flux have been removed, replaced with water. This water will serve to increase the thermal flux. The most dramatic effect is seen in the QUARTZ model, suggesting that some part of the model is incorrectly exaggerating the flux peak. Conversely, the CITATION model does not exhibit as much of a peak. The qualitative behavior of all three models remains quite similar, however.

In element B4, the agreement between all three models is quite good. In this case, the QUARTZ model more closely matches the MCNP data, considered to be the most accurate model.

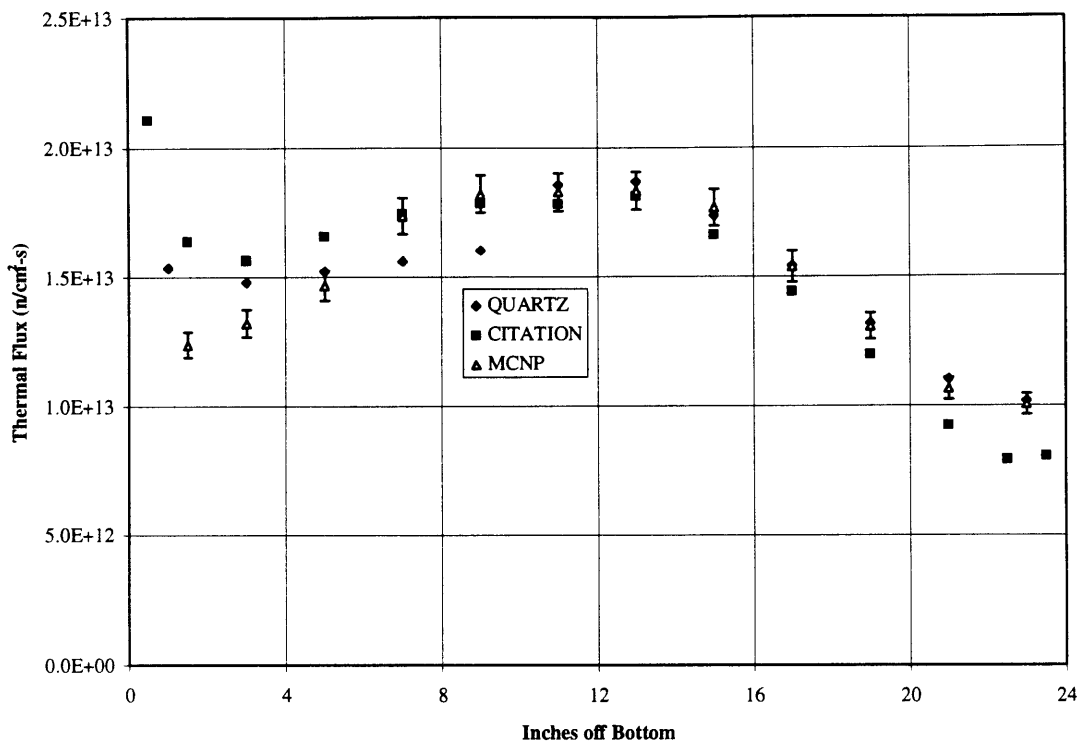


Figure 5.17. Thermal Flux in Element B4 vs. Axial Position

Note that the flux is lower in this element than in A2. Finally, we compare the fluxes in element C10 [Figure 5.18]. Agreement is, again, quite good between the QUARTZ and MCNP models. A detailed examination of the remaining fuel elements shows that, in elements in the C-ring at the corners of the reactor, the flux is generally overestimated. It is likely that material definitions in this region may be incorrectly defined. It should also be noted that, in the MCNP and CITATION models of the fuel, the U^{235} concentration is radially dependent within each element. This dependence is averaged out in the QUARTZ model. This averaging may be more damaging in the C-ring elements, which are generally at higher burnups than interior elements.

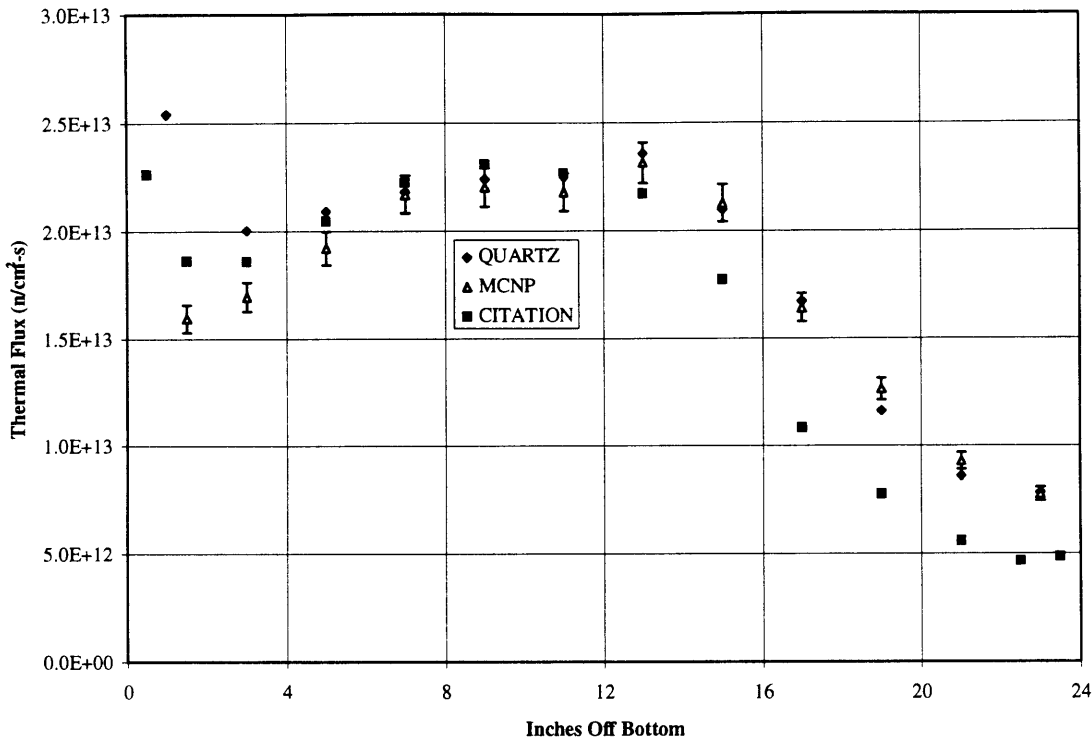


Figure 5.18. Thermal Flux in Element C10 vs. Axial Position

The final assessment of the QUARTZ model, when compared to the CITATION and MCNP models, is that the QUARTZ model generally does a good job in matching fluxes in most fuel elements, but certainly there are improvements that can be made.

Finally, a comparison can be made to the flux measurements in the reactor core made as a part of the instrumented synthesis experiments. The complication with this comparison is the uncertainty of the detector response. This uncertainty was alluded to in Chapter 4. Because the absolute detector responses are not known, one possibility is to calculate the ratio of the detector currents for the shim blade configurations corresponding to flat and tilted flux shapes. These ratios can be compared to the ratio of the fluxes at the detector locations in the QUARTZ model. This method presumes the detector response,

though unknown, remains unchanged in the flat and tilted configurations. This is one of the drawbacks of the comparison. Any changes in spectrum at the detectors in the physical system are not reflected in the model. Nevertheless, it is one of the few available experimental measurements providing validation and does offer some insight into the accuracy of the model.

In the QUARTZ model, the water vent holes in which the detectors are placed are modeled by six nodes for each vent hole per plane. The tilted-to-flat flux ratio for each of these nodes for each shim blade configuration is compared to the tilted-to-flat detector currents in the physical system.

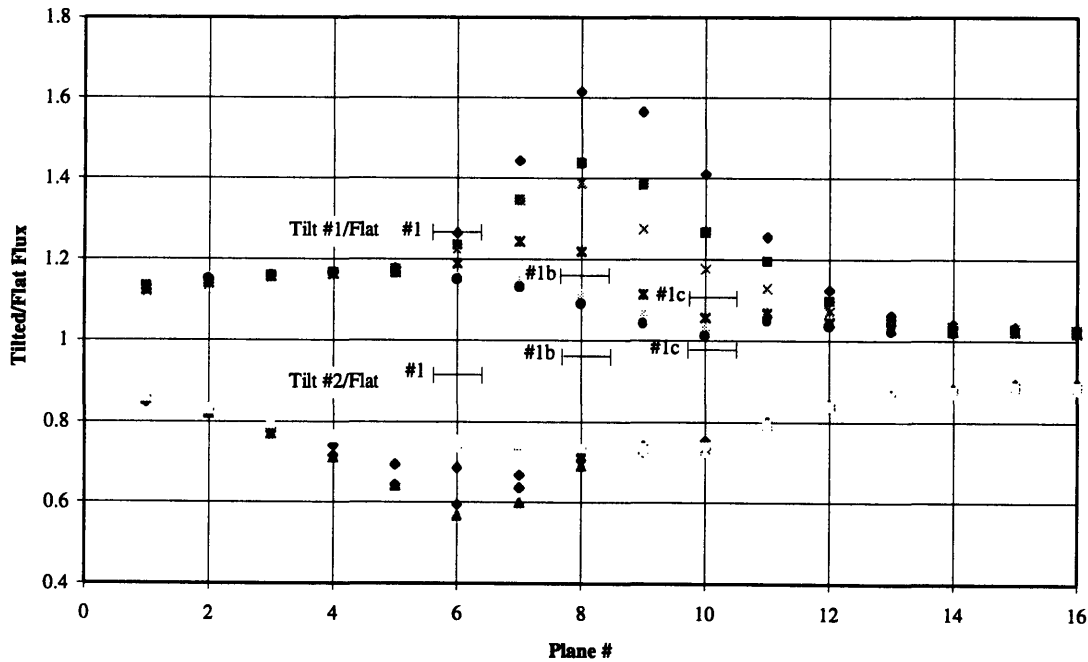


Figure 5.19. Comparison of Tilted-to-Flat Measurements (bars) to QUARTZ Predictions (dots), Core #106 at 10 kW, Vent Hole #1

Recall that the detector positions in the physical system roughly correspond to plane #6 in the QUARTZ model for detectors #1, #2, and #3. Detectors #1b, #2b, and #3b are in plane #8, and detectors #1c, #2c, and #3c are in plane #10. The upper bars in Figure 5.19 are the ratio of the currents of the first flux tilt measurements to the flat flux measurements taken from detectors #1, #1b, and #1c. The lower bars are the ratio of the currents of the second flux tilt measurements to the flat flux measurements for the same detectors. Bars are used to denote the fact that the detector positions correspond only approximately to planes in the QUARTZ model. The upper dots are the ratios of the QUARTZ fluxes from the first flux tilt and the flat flux in each of the six nodes per plane representing the water vent hole #1. The lower dots are the QUARTZ flux ratios of the second flux tilt and the flat flux in the same nodes. The ratios are plotted axially along the water vent hole. In planes #6, #8, and #10, the dots representing the QUARTZ model should match the bars showing the actual measurements.

As evidenced in Figure 5.19, the agreement is much better between measurement and prediction when the flux is raised at a detector location through flux tilting. In this case, the measurements are within the spread of the predicted data in the six nodes representing the water vent hole. For detectors #1, #1b, and #1c in water vent hole #1, the flux is higher in the first tilt configuration. When the flux is lowered in tilt #2, the agreement worsens. This trend is consistent at water vent hole #3, where detectors #2, #2b, and #2c are housed.

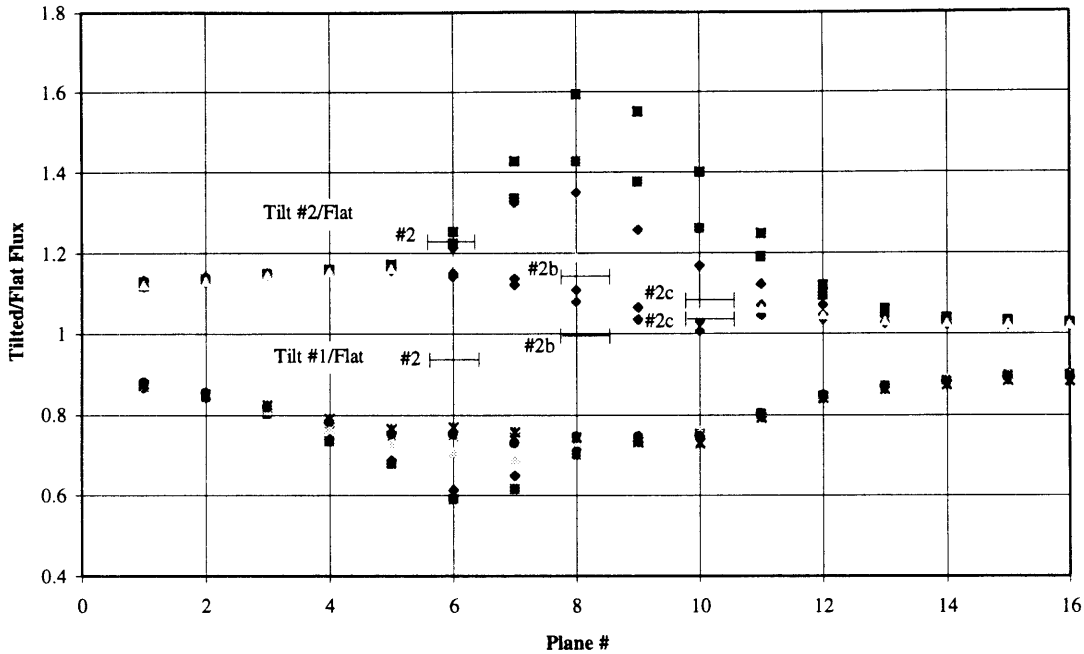


Figure 5.20. Comparison of Tilted-to-Flat Measurements (bars) to QUARTZ Predictions (dots), Core #106 at 10 kW, Vent Hole #3

At this location, the flux is lowered in the first tilt and raised in the second. But the agreement continues to remain better when the flux is raised than when lowered.

There are three likely explanations. First, there is the possibility of change in response in the detectors as the flux is lowered. A noticeable change in detector response takes place when the power is changed from 10 to 50 kW. Second, the difference in height between the two models has been discussed. It is possible that the assumed location of the blades and detectors in the QUARTZ model is inaccurate. But the most likely reason lies in the azimuthally constant boundary conditions. The detector locations are near the boundary of the QUARTZ model, between the control blades. In these

locations, they are affected by the conditions at the boundary. If the control blades are tilted but the conditions at the boundary of the model are not, the flux at the detector locations may be incorrectly predicted.

It was mentioned earlier in this section that the effect of averaging the rods-in and rods-out boundary conditions for tilted flux shapes decreased the difference between the flat flux and tilted flux eigenvalues. This also improves the agreement between the measured and predicted detector response. The above QUARTZ analyses were performed with averaged boundary conditions. If the same, unaveraged boundary conditions were used in the tilted cases as in the flat case, the following results are obtained.

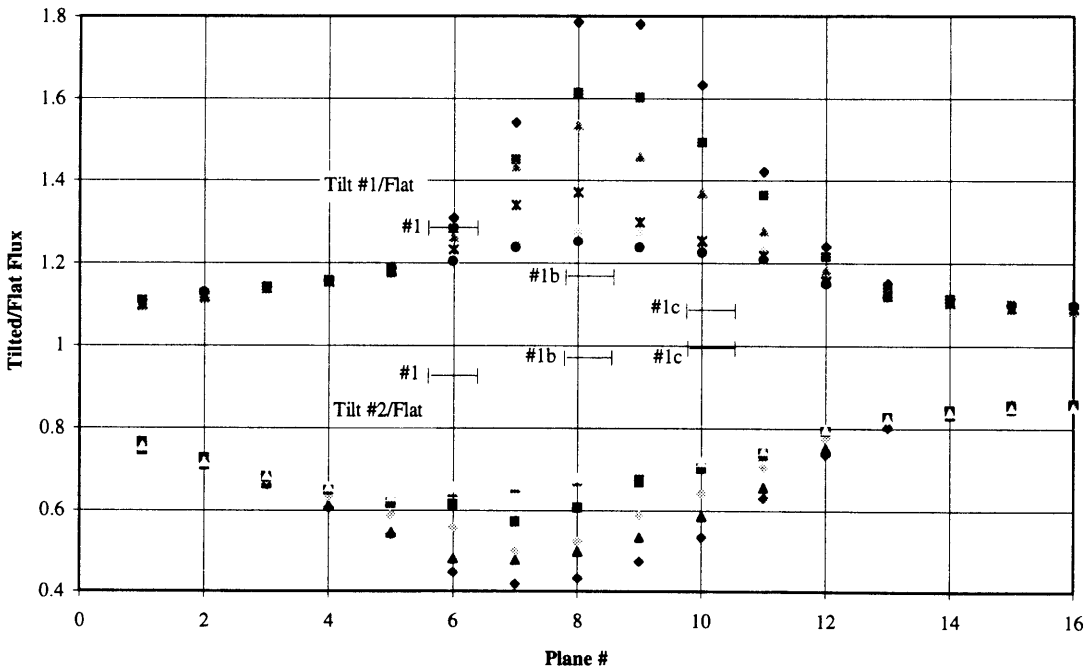


Figure 5.21. Comparison of Tilted-to-Flat Measurements (bars) to QUARTZ Predictions (dots) with Unaveraged Boundary Conditions, Core #106 at 10 kW, Vent Hole #1

The agreement is worse for both tilted configurations. A much more dramatic change in flux is predicted in QUARTZ at the detector locations than is actually measured. Using the averaged boundary conditions [Figure 5.19] improves the agreement between prediction and physical system.

Flux shapes for several conditions in the synthesis experiments in Core #106 have been generated. Comparisons of the eigenvalues and the fluxes have been made to both experimental data as well as data from previous models. The following conclusions can be drawn from these comparisons:

- The fluxes generated by the QUARTZ model generally show good agreement with the previous MITR models, the accuracy of which has been well established. Further refinement for positions near the corners of the reactor is desirable.
- The characteristics of the QUARTZ model qualitatively reflect those of the physical system.
- The prediction of criticality in the flat shim blade configurations is close to that of the physical system. Eigenvalues are close to unity for all the static conditions modeled.
- The comparisons to the experimental data were generally good. Discrepancies are attributed to azimuthally constant boundary conditions which do not reflect the physical situation in the core.

With these points in mind, it appears probable that the QUARTZ model will be sufficiently accurate for use in the instrumented synthesis method. It is important to remember, however, that individual flux shapes need not precisely replicate the conditions of the reactor at any given time. The synthesis method works by forming *combinations* of flux shapes. It would be highly unlikely that the flux could be accurately reconstructed from wildly inaccurate shape functions. However if the shape functions closely represent the flux in the core, an accurate synthesis can be achieved.

5.6.3 STATIC RESULTS - CORE #110

For Core #110, only the eigenvalue results will be presented. The character of the flux shapes remains substantially unchanged from Core #106.

The critical shim bank height for Core #110 at 10 kW was 8.90", and 9.00" at 50 kW. The fine and coarse mesh results for the static flux shapes are given in Table 5.10. Again, there is excellent agreement between the coarse and fine mesh models of the reactor.

Power Level	Shim Blade Configuration	Fine Mesh k_{eff}	Coarse Mesh k_{eff}	Max Error in $\Phi_1/\Phi_2/\Phi_3$	Avg Error in $\Phi_1/\Phi_2/\Phi_3$
10 kW	Flat	1.00415	1.00415 (+0.000%)	0.0092%	0.0035%
				0.0109%	0.0038%
				0.0091%	0.0035%
10 kW	Tilt #1	0.989186	0.989194 (+0.001%)	0.0160%	0.0059%
				0.0194%	0.0066%
				0.0163%	0.0063%
10 kW	Tilt #2	0.987891	0.987900 (+0.001%)	0.0177%	0.0065%
				0.0221%	0.0072%
				0.0173%	0.0065%
50 kW	Flat	1.00537	1.00537 (+0.000%)	0.0048%	0.0018%
				0.0058%	0.0020%
				0.0049%	0.0020%
50 kW	Tilt #1	0.990837	0.990844 (+0.001%)	0.0196%	0.0073%
				0.0238%	0.0082%
				0.0196%	0.0076%
50 kW	Tilt #2	0.995147	0.995158 (+0.001%)	0.0146%	0.0054%
				0.0184%	0.0061%
				0.0149%	0.0056%

Table 5.10. QUARTZ Model of Core #110 Static Conditions

Additional flux shapes were generated to analyze the transients as well as all-rods-in and all-rods-out conditions. The shim blade positions are recorded positions, which are adjusted for the QUARTZ model.

Power Level	Shim Blade Configuration	Fine Mesh k_{eff}	Coarse Mesh k_{eff}
10 kW	#1 Dropped	0.975603	0.975611
25 kW	#6 at 9.77"	1.00621	1.00622
25 kW	#6 at 10.64"	1.00996	1.00998
50 kW	#3 at 8.67"	1.00307	1.00308
50 kW	#3 at 8.33"	1.00200	1.00201
50 kW	#6 at 8.64"	1.00304	1.00306
50 kW	#6 at 8.29"	1.00187	1.00188

Table 5.11. Flux Shapes Generated for the Transient Measurements in Core #110

A comparison of the eigenvalues in Table 5.11 with that of the flat shim blade configurations in Table 5.10 shows them to be consistent: insertion of blades lowers the eigenvalue, withdrawal of blades raises the eigenvalue.

5.7 APPLICATION TO THE MITR FUEL MANAGEMENT PROGRAM

The QUARTZ model was developed, in part, because of its ability to model triangular geometries. Since the fuel elements in the MITR core are rhomboid shaped, this geometry is particularly suited for application to the MITR.

In the previous section, comparison was made among the QUARTZ model, the MCNP model, and the CITATION model of the MITR. Although the QUARTZ model did not match the results of these models at all locations, further refinement of material definitions could certainly improve the accuracy of the QUARTZ model. With this improvement in accuracy would come the potential for the QUARTZ model to replace the CITATION model as the neutronics code used in the MITR fuel management program.

As it stands the current fuel management program consists of a neutronic analysis performed using CITATION. The model has been used successfully for a number of years, and codes have been written that compute depletion based upon this model. The fuel management program employed by the MITR is illustrated in Figure 5.22.

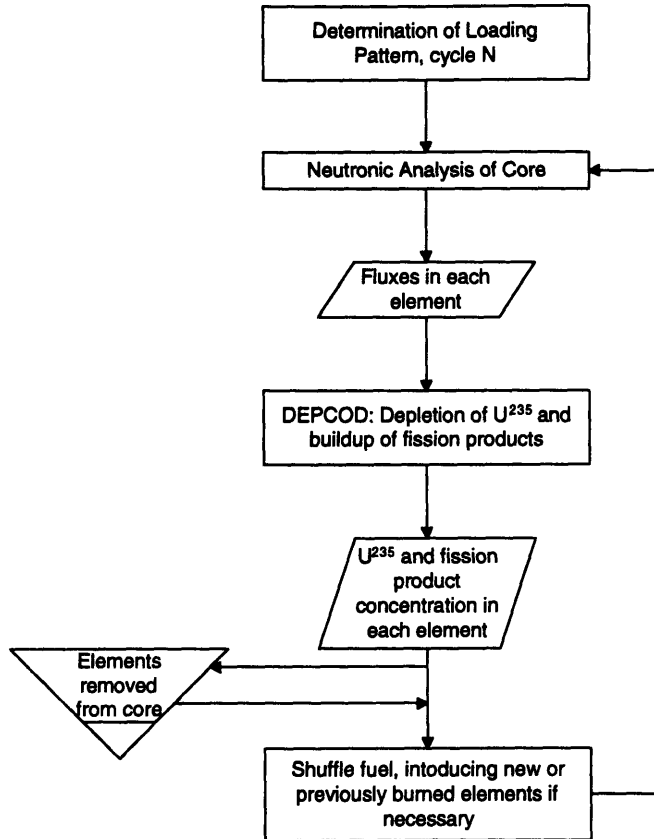


Figure 5.22. Current MITR Fuel Management Program

Currently, the “Neutronic Analysis of Core” is performed using CITATION. However, the QUARTZ model could easily be inserted in place of the CITATION analysis. The DECK code already uses output directly from DEPCOD to generate an input deck for QUARTZ. The only additional interface code required would be one to put the fluxes generated by QUARTZ into a format suitable for DEPCOD. The DEPCOD program would also have to be adjusted for triangular geometry.

The use of QUARTZ would have several advantages. First, it can be used easily on either a PC or workstation, as opposed to the large mainframe computer required by CITATION. This greatly increases both the speed of computations and the convenience

of data handling. Second, with the incorporation of the supernodal routines, the fine mesh model could be used to calculate detailed depletion in each fuel element. The elements would be represented explicitly, rather than by varying element volumes as is currently done for the CITATION model. The fine mesh results could be collapsed to a coarse mesh, and transient studies could be performed¹. A thermal-hydraulic model of the MITR has already been developed by McGuire [M1] and could be incorporated into the QUARTZ code rather easily.

There is another option that could be included in a newly designed fuel management program. The ORIGEN code, developed at Oak Ridge National Laboratory, is a point depletion code that has been used with increasing frequency throughout the nuclear industry. While the incorporation of ORIGEN into the fuel management scheme, used to replace DEPCOD, would be more complicated, it would track the buildup of individual fission products, rather than the “lumped fission product” currently used in DEPCOD.

A final redesigned fuel management scheme might look like this.

¹ Although collapsing of the nodes would not be necessary to perform transient analyses, it would dramatically decrease the computational effort required.

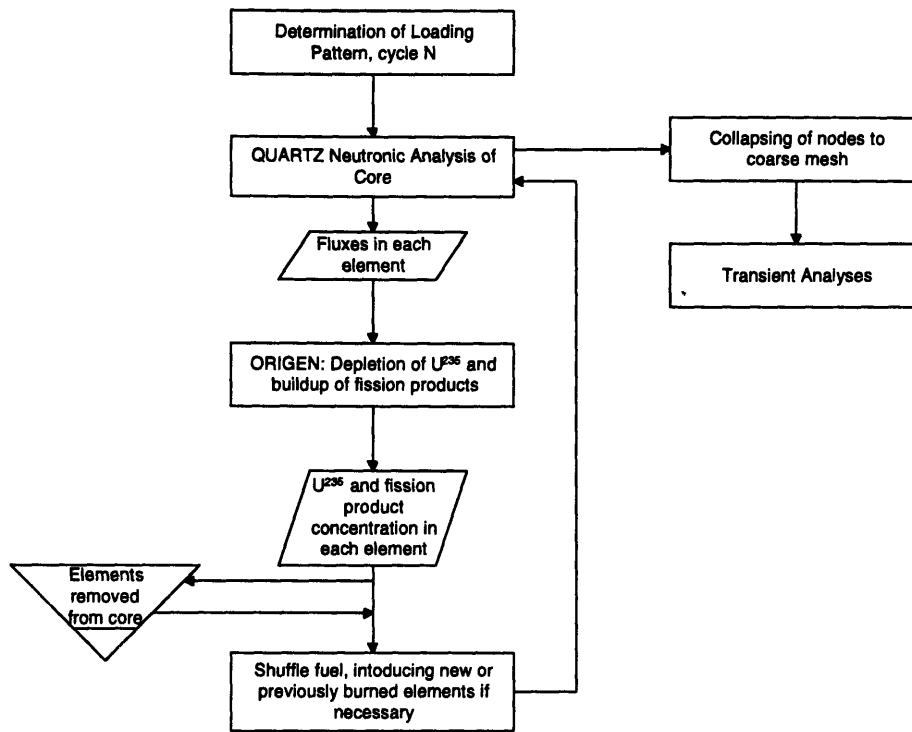


Figure 6.23. Possible Redesigned MITR Fuel Management Program

The scheme has much the same character as the present scheme. However, it can be implemented on a desktop computer, has the potential for significantly more accurate depletion, and offers the possibility of analyzing transients heretofore not performed for the MITR core.

5.8 SUMMARY

A model of the MITR has been developed using the QUARTZ code. Fluxes and eigenvalues from the fine mesh model have been compared to previous models as well as experimental data and shown to be in generally good agreement with both. The

supernodal procedures developed in Chapter 3 have been applied to the model and shown to work effectively. These large-node flux shapes will be combined with the detector measurements described in Chapter 4 to synthesize fluxes for the MITR in various conditions. Though the model will be used in this thesis specifically for evaluating the instrumented synthesis method, the possible application to the MITR fuel management program was discussed. The results of the synthesis evaluations are given in the next chapter.

Chapter 6

Evaluation of the Experiments

6.1 INTRODUCTION

In the previous chapters, the basis of the instrumented synthesis project was outlined. In Chapter 2, the method was explained. It was shown how precomputed flux shapes, or expansion functions, could be combined with measurements from an operating reactor to synthesize the detailed flux shape in the reactor. The residual between the actual and the reconstructed count rates was put forth as one measure of the success of the synthesis. The QUARTZ code was modified to allow flux shapes to be created for the synthesis. These modifications were detailed in Chapter 3. In Chapter 4, the method for collecting

the detector measurements was outlined, along with the physical system the flux shapes would be modeling. The actual model was presented in Chapter 5 and was shown to be generally in good agreement with previous work as well as experimental measurements, although further refinement is necessary before incorporation into the MITR fuel management program.

This chapter will detail the final step in the process, the actual application of the synthesis method to the experiments. The goal of the project was to show whether the synthesis method could successfully be applied to an operating reactor. It will be shown in this chapter that the synthesis method can accurately reflect changes in reactor conditions. Further, its performance is superior to methods based upon a single, unchanging flux shape. Such methods are the current basis for reactivity meters.

6.2 DETERMINATION OF DETECTOR RESPONSE AND EVALUATION OF THE INSTRUMENTED SYNTHESIS

In Chapter 2, two important differences were noted between the experimental and numerical evaluation of the instrumented synthesis method. The first was the absence of a reference flux vector, the second was the response of the fission chamber detectors. The way these issues are addressed in the experimental evaluation affects the way the synthesis can be analyzed. Each issue is discussed below.

6.2.1 DETERMINATION OF DETECTOR RESPONSE

Recall the expression for count rate (or current) for detector j from Chapter 2.

$$C^j(t) = \underline{\Sigma}^{(j)T} \underline{\Phi}(t) \quad (2.8)$$

This states that for a given physical flux in the reactor, $\underline{\Phi}(t)$, the transpose of the response of detector j , $\underline{\Sigma}^{(j)T}(t)$, will produce a current $C^j(t)$. There needs to be some way of determining what that response will be. For the instrumented synthesis method, the response is determined by taking an average measurement at some static condition and dividing by the QUARTZ prediction of the thermal flux in the large node containing the detector.

$$\Sigma_{syn}^j \equiv \frac{C_{ave}^j}{\Phi_3} \quad (6.1)$$

Given the uncertainties in the detector response discussed in Chapter 4, this seemed to be the most reasonable approach to determining detector response.

The constant C_{ave}^j would be difficult to determine theoretically. It accounts for several physical effects. First of all, the large node flux used in Eqn. 6.1 will differ from the flux in each of the small nodes contained in it. Since the detectors reside in water vent holes near at the edge of the core, the flux in the fine mesh nodes representing the vent

holes will generally be higher than the coarse node flux. Figure 6.1 can be used for illustration. When the coarse mesh nodes are used to determine the detector response, it must be remembered that the physical flux at the detector location will be different from the large node flux.

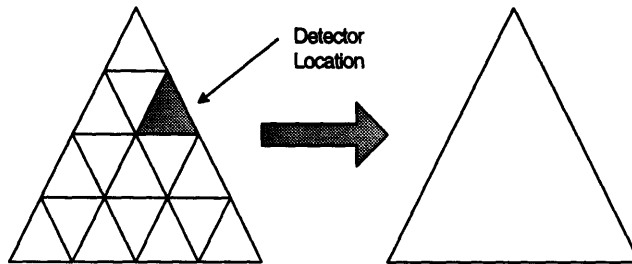


Figure 6.1. Node Collapsing at Detector Location

This difference between flux at the detector and flux over the entire node is also a function of control blade motion. Since the detectors sit closely to the control blades, some blade material is averaged into the large nodes in the QUARTZ model containing the detectors. As the positions of these blades change, the ratio of the flux at the detector to the large node flux may change.

It also must be recognized that the QUARTZ model used to determine the response of the detector cannot be guaranteed to be correct at the detector locations. This means that the flux predicted by the detector using the response in Eqn. 6.1 may be different than the physical flux at that location. The effect of Eqn. 6.1 on the synthesis evaluation is given in Section 6.2.2.

6.2.2 EVALUATION OF THE INSTRUMENTED SYNTHESIS

6.2.2.1 The Residual

The manner in which the detector responses were determined, as outlined in Section 6.2.1, affects the evaluation of the synthesis method. What will be shown in the following section is that the present evaluation determines the effectiveness of the synthesis method as a dynamic tool, one that properly reflects changes in the core from an initial condition. This is in contrast to accurately predicting the absolute flux level within the core. This does not appear to significantly compromise the evaluation, but should be kept in mind as the results are reviewed.

As stated in Chapter 2 and at the beginning of Section 6.1, the absence of a reference flux vector complicates the evaluation of the synthesis method. The presence of a reference flux in the numerical evaluation allowed the reconstructed flux to be compared to the “correct answer.” Errors could be easily quantified. Since such a reference does not exist in the experimental evaluation, another method must be used to evaluate the success of the synthesis under experimental conditions.

One such method is the residual, defined in Chapter 2 as the difference between the measured detector count rates and the reconstructed count rates. In matrix form, it is represented as a 2-norm, $\|\underline{C}(t) - \underline{AT}_{LS}(t)\| / \|\underline{C}(t)\|$, where the relative residual has been expressed as the ratio of the residual to the measured count rates. Because the count rates are available in real time, this quantity provides a useful way of assessing the accuracy of

the synthesis on-line. It also does not rely on a theoretical prediction of the flux to provide a reference.

There is an implicit assumption, however, in using this quantity as an estimate of the success of the synthesis in reproducing the flux in the reactor. The residual, in its most general definition, is simply the difference between the reconstructed count rate vector and the measured count rate vector. To use this quantity as a measure of the error in the flux implies that the detector response functions, $\Sigma^j(t)$, are accurately known. In other words, knowledge of the count rate of the detectors is the same as knowledge of the flux at the detector location.

In Section 6.2.1, the determination of the detector responses was discussed. The final determination, Eqn. 6.1, uses an average of the ratio $C^j(t)/\overline{\Phi}_3^j$ under several static conditions to determine the detector response. This response, denoted Σ_{syn}^j , has the effect of forcing the count rates, when converted to flux level, to match some average QUARTZ prediction. If the initial condition of an experiment is close to this average condition, and the shape functions used to determine that average condition are included in the synthesis, one would expect a very low residual for this initial condition. The reconstructed count rates are close to the actual count rates because, in some sense, they are guaranteed to be. A non-zero residual for this case would indicate that (1) the noise in the detector current brings the $C^j(t)$ away from the C_{ave}^j used to determine the detector response, (2) the flux shape responsible for the detector reading is not included in the space of functions used for the synthesis, or (3) the condition of the reactor is not near the

average condition used for the response calibration. Certainly a combination of these three factors is possible.

At first glance, using the residual may appear to be a completely circular evaluation of the synthesis. However, it should be remembered that the detector responses were determined for some average condition. As transients are initiated and the flux shape in the reactor changes, the core is no longer in that average condition. If the system is sufficiently well instrumented, a small residual in a transient case would indicate that the synthesis method is correctly reflecting changes from the initial state of the core by using a proper mixture of predetermined shape functions.

This method is not as satisfying as accurately predicting the absolute flux levels in the core. For such an evaluation, the physical response of the detector to a given flux must be accurately known, as well as the differences between flux at the detector location and the prediction of flux in the large node containing the detector.

In summary, a low residual in the following transient analyses would indicate that the shape functions can be combined using detector readings to accurately reflect changes in flux shape and amplitude from some average initial condition. To take the next step and state that the fluxes obtained by this process are the fluxes in the physical reactor would require that detailed knowledge of the detector responses be obtained. Though this was not obtained for the current evaluation, this knowledge would almost certainly be available for large power reactors.

The residual is the quantity most directly related to quantifying how well the synthesis method is combining shape functions to synthesize a flux. We would, however,

like to make use of any other quantities available to enhance the evaluation. Normalized detector readings and reactivity offer two possibilities.

6.2.2.2 Normalized Detector Readings

The synthesis method will produce a flux for each node in the reactor. For those nodes occupied by fuel, a value for the power in that node can be calculated using theoretically determined fission cross sections. The power from all the nodes in the reactor can be summed, and a total reactor power can be calculated. This power, derived from the synthesized flux, can be compared to the detector measurements taken from the reactor at the time of the experiment.

It is important to realize that the detector measurements are not directly proportional to reactor power. For example, the transients analyzed were initiated by insertion or withdrawal of a single shim blade. The flux will increase at different rates at different points throughout the reactor. The power, as determined by the synthesis method, is a global quantity. The detector readings measure flux only at particular locations.

The comparison is further complicated by the way in which the experimental evaluation was conducted. Each of the transients, with the exception of the blade-drop transient, were repeated three times. A review of Chapter 4 illustrates that measurements from nine detectors needed to be recorded using only three ammeters¹. As a result, the

¹ As mentioned in Chapter 4, the cost of additional ammeters to provide real time measurements from all nine fission chambers proved prohibitively expensive. For a control system, simultaneous readings from all instruments would be needed.

experiments were repeated three times to allow three groups of measurements. Although the transients were closely replicated in most cases, there will be slight differences between the transients in each case. As a result, the power produced by the synthesis code will differ from each group of detector readings by differing amounts.

6.2.2.3 Reactivity

In addition to power, the flux shape produced by the synthesis method can also be used to calculate reactivity. There are two possible ways to determine reactivity using this flux shape. This first would be to employ the flux shape in the definition of reactivity, given in Chapter 2 as

$$\rho(t) \equiv \frac{\langle W(\underline{r}, E) | M(t) - L(t) | S(\underline{r}, E, t) \rangle}{\langle W(\underline{r}, E) | M(t) | S(\underline{r}, E, t) \rangle} \quad (2.31)$$

where the flux can be written in terms of the shape function $S(\underline{r}, E, t)$ and the amplitude function $T(t)$ as

$$\Phi(\underline{r}, E, t) = S(\underline{r}, E, t)T(t) \quad (6.2)$$

Determination of the reactivity in this fashion would require detailed knowledge of the fission operator $M(t)$ and the loss operator $L(t)$. These quantities may not be available during fast-acting or complicated transients.

Another method was also discussed in Chapter 2. It is the use of the inverse kinetics equations, repeated here for convenience.

$$\hat{c}_{eff,iprec}(t) = e^{-\lambda_{iprec}\Delta t} \hat{c}_{eff,iprec}(t - \Delta t) + \frac{1}{\lambda_{iprec}} \left[1 - e^{-\lambda_{iprec}\Delta t} \right] \frac{\hat{\beta}_{eff,iprec}(t)}{\hat{\Lambda}(t)} \hat{T}_{eff}(t) + O(\Delta t^2) \quad (2.39)$$

$$\hat{\rho}(t) = \hat{\beta}_{eff}(t) + \frac{\hat{\Lambda}(t)}{\hat{T}_{eff}(t)} \left[\frac{d}{dt} \hat{T}_{eff}(t) - \sum_{iprec=1}^{nprec} \lambda_{iprec} \hat{c}_{eff,iprec} - q_{eff}(t) \right] \quad (2.40)$$

The amplitude function, delayed neutron fraction, and prompt neutron lifetime given in Eqns. 2.39 and 2.40 are determined using the synthesized flux. The reactivity is then calculated based upon these quantities. If the parameters in the reactor were precisely known, the reactivity determined by these two methods should agree.

The reactivity calculated for the experimental evaluation employs inverse kinetics. This eliminates the need for detailed knowledge of the reactor conditions during complicated transients. From time to time throughout this chapter, the phrase “synthesis reactivity” will be used to refer to the reactivity as determined by the inverse kinetics equations using the synthesized flux. Strictly speaking, the instrumented synthesis only produces a flux shape. The determination of reactivity from that flux shape is external to the synthesis method.

6.3 THE SYNTHESIS CODE

To perform the syntheses for the instrumented flux synthesis project, the TROLS (TRiangular On-Line Synthesis) code is used. Much of the code has been adapted from

the NPS code used in Jacqmin's thesis. But there are some important changes. The code has been changed to accommodate triangular geometry and to be linked more closely to the QUARTZ code. The fission cross sections and production cross sections ($\nu\Sigma_f$) are entered through different files, allowing varying values for ν . The code has also been altered to allow it to read detector measurements as fluxes from QUARTZ or as data directly from the Global Lab data acquisition software. The former option allows the user to perform numerical experiments like those in Jacqmin's work. These experiments were performed as an early stage of this work to ensure changes made in writing TROLS were correct. The latter option is employed for the experimental evaluation. There are other additional input requirements detailed in the input guide kept with the TROLS code.

6.4 STATIC RESULTS

As discussed in the previous section, the detectors are normalized to an average condition as predicted by QUARTZ. At a static reactor condition, therefore, it is expected that the residual error should be quite low. However, it is still instructive to look at the static results for several reasons. First, although the reactor is placed in a static condition, it may not be the same condition used to normalize the detectors. The synthesis method must then combine various flux shapes to reproduce the condition at hand. Second, there will be measurement noise associated with detector readings. As Jacqmin [J1] pointed out, this noise can seriously degrade the results. It is useful to quantify the noise at a static condition before moving to transient results.

The static results presented are taken from the flat shim blade configuration at 50 kW in core #106. For the instrumented synthesis of the flux, two shape functions were used. The first approximated the flat shim blade configuration at 10 kW, using a recorded shim bank height of 7.80". The second approximated the flat shim blade configuration at 50 kW. The shim blades had been raised to a recorded height of 7.95" by this time. The two shape functions are combined to synthesize the flux in the reactor.

Although the results are intended to be static results, noise and small changes in the reactor condition will affect the measurements over time. The figures given below are plotted against time to gain some idea of the effects of noise on the synthesis.

It was mentioned in Chapter 2 that, by orthogonalizing the shape functions, spurious modes could be eliminated from the synthesis by zeroing the associated singular values. The value for the zeroing criterion must be large enough to eliminate spurious modes that contribute to the synthesis. Such modes will degrade the accuracy of the synthesized flux. However, if the criterion is too large, it will eliminate useful data from the synthesis, leading to large systematic errors. The effect of this zeroing criterion will be shown below.

The first results are values of the relative residual over time. For this case, the zeroing criterion is changed to ensure that both orthogonal modes are retained in the synthesis in one case, and the only one of the two is retained in the second case. The residual remains largely unchanged between the two.

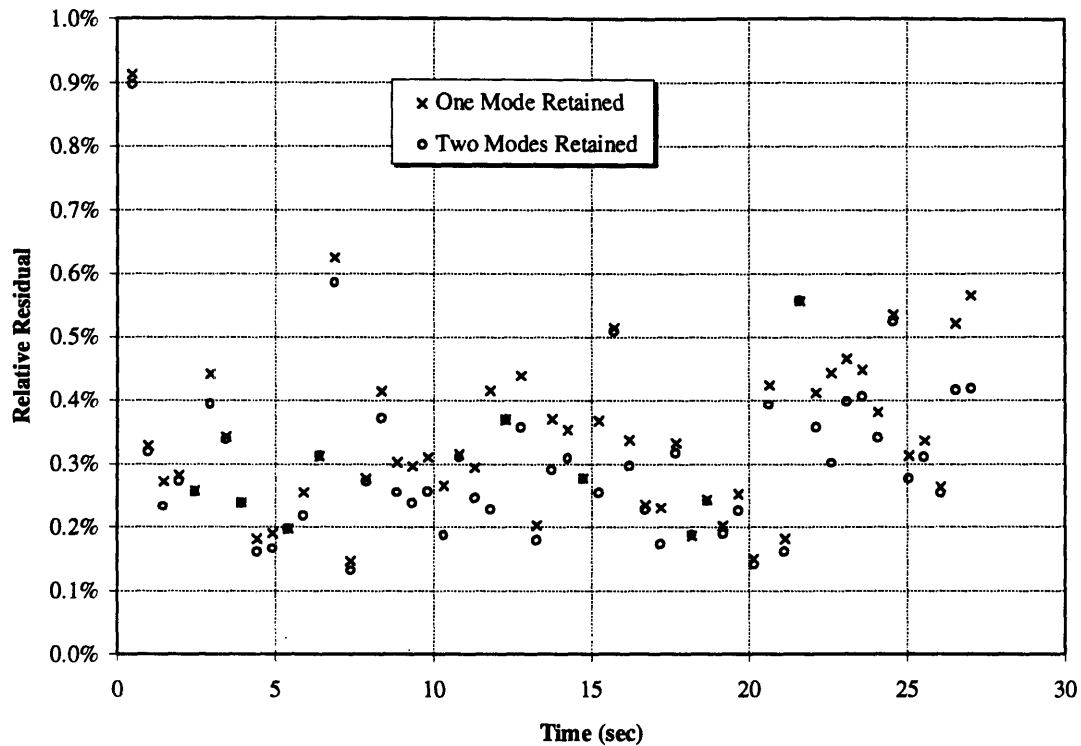


Figure 6.2. Relative Residual, Core #106 @ 50 kW
Flat Shim Bank, One and Two Orthogonal Modes Retained.

The residual remains very low, which is not surprising. The condition of the reactor does not vary considerably from the average condition for which the detectors were normalized. But Figure 6.2 does indicate that, even under “static” conditions, measurement noise can degrade the results, generating a residual approaching 0.5-1.0%.

The values of the mixing coefficients for the shape functions are plotted next. In Figure 6.3, one of the orthogonal modes is removed from the synthesis.

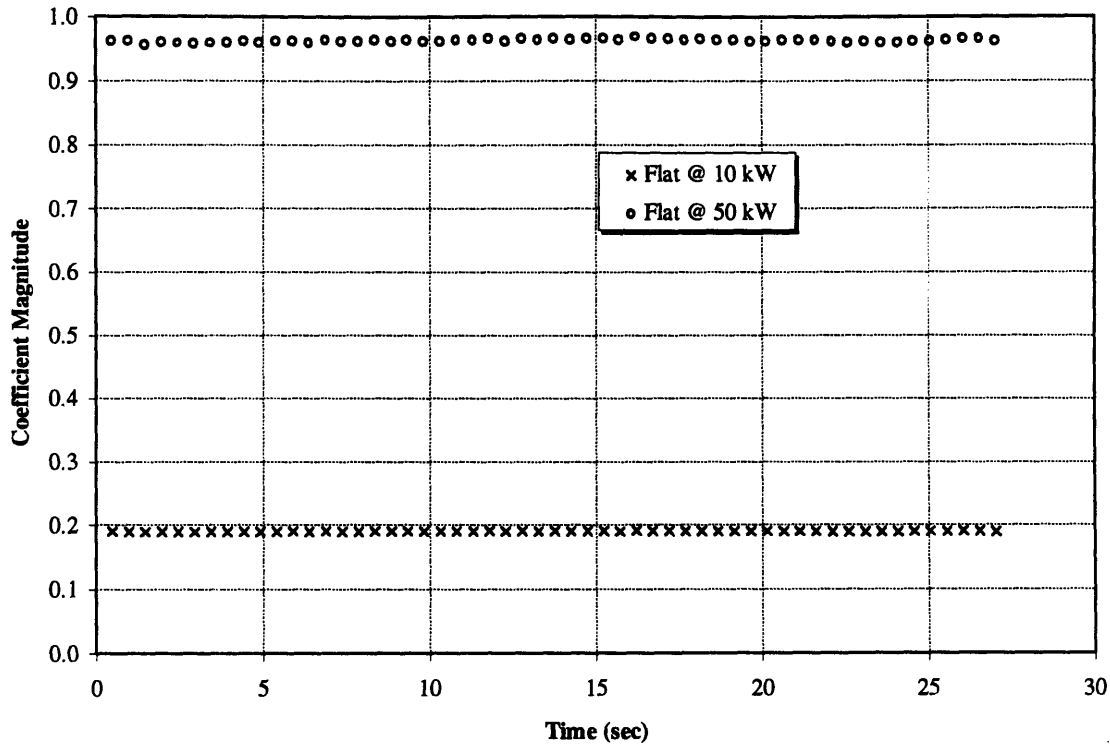


Figure 6.3. Mixing Coefficients, Core #106 @ 50 kW
Flat Shim Bank, One Mode Retained

The first piece of information to take away from Figure 6.3 is that although only one orthogonal mode is retained, both shape functions have a non-zero magnitude. On first glance, one might expect one of the shape functions to have been eliminated from the synthesis, leaving only remaining shape function. But what is eliminated from the synthesis are not the shape functions themselves, given by $\underline{\psi}^{(k)}$, but a linear combination of the shape functions, given by

$$\underline{\psi}'^{(i)} = \sum_{k=1}^K \underline{\psi}^{(k)} v_i^{(k)}, \quad i = 1, 2, \dots, K \quad (2.24)$$

In the same way, what is retained is a linear combination of shape functions as well. These smoothly varying coefficients combine to form the fundamental mode, least squares solution.

In Figure 6.4, both orthogonal modes are retained. Here, the mixing coefficients vary more erratically, suggesting a more spurious behavior.

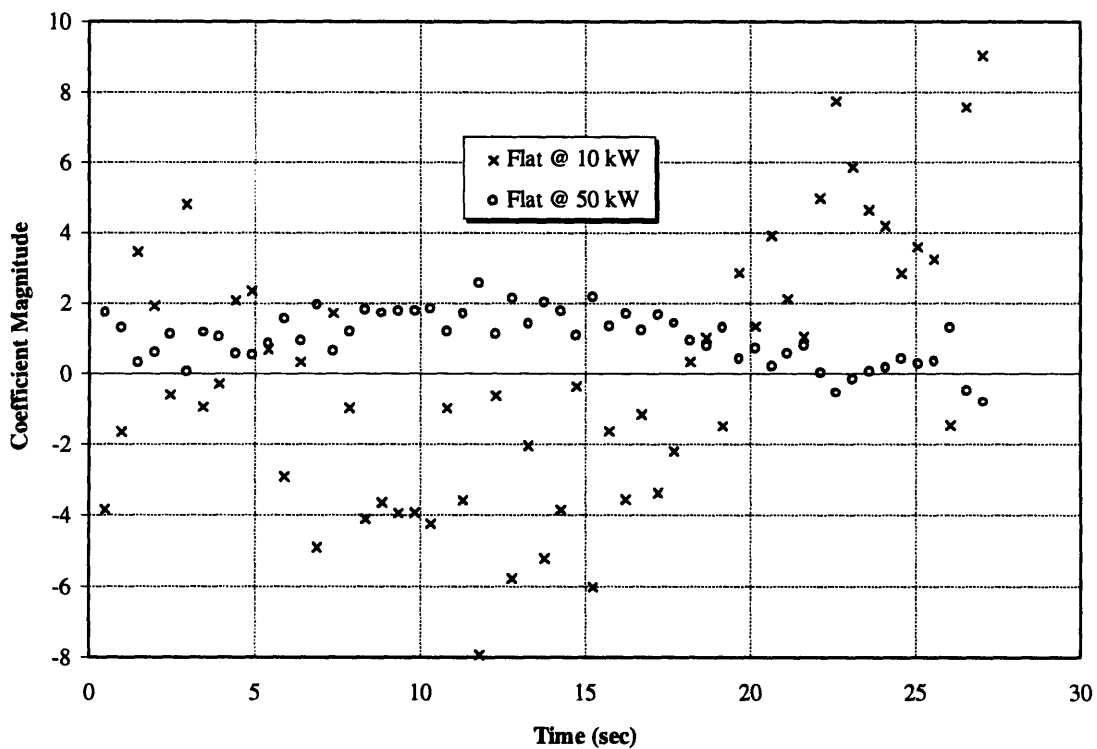


Figure 6.4. Mixing Coefficients, Core #106 @ 50 kW
Flat Shim Bank, Two Modes Retained

The results of the power and reactivity determinations from each of these cases are presented in the following figures.

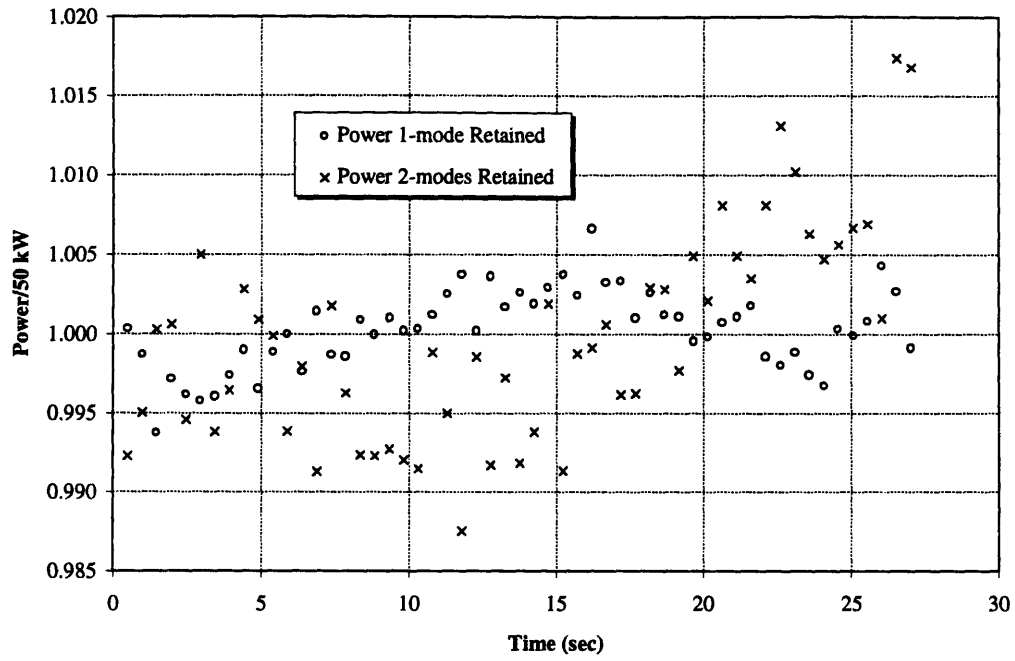


Figure 6.5. Comparison of Power in Core #106 @ 50 kW, One and Two Mode Synthesis

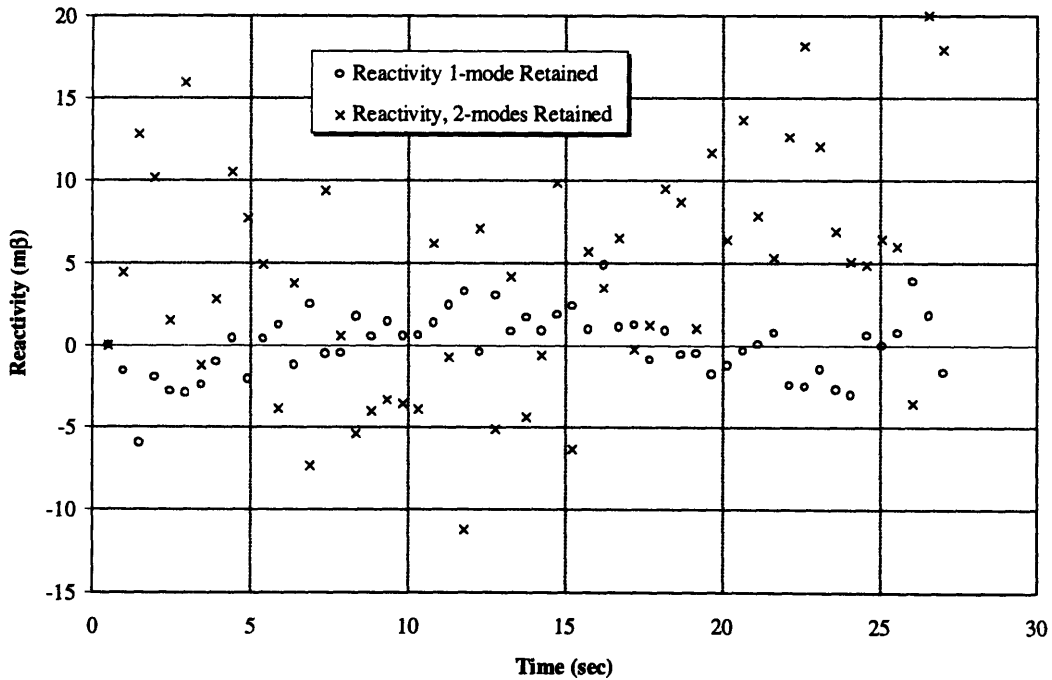


Figure 6.6. Comparison of Reactivity in Core #106 @ 50 kW One and Two Mode Synthesis

Figure 6.5 and Figure 6.6 are more helpful in determining the appropriate cutoff for the singular values. In the power comparison, the error in the one-mode synthesis is restricted to $\pm 0.5\%$. While the two-mode synthesis still maintains a low error, they are larger and more randomly dispersed than the one-mode results. The same is true in reactivity, where errors are limited to ± 5 millibeta when one mode is retained. From these results it was surmised that retaining both modes increased the sensitivity of the synthesis to spurious modes.

For these comparisons, the assumption has been made that the power in the reactor is held precisely at 50 kW with zero reactivity. However, regulating rod movement during each of the steady state measurements indicated that this was not precisely true. The reactivity worth of the regulating rod is small, however, and variations in its position during static measurements can be lumped with other sources of reactor noise. The conclusion to be drawn is that, for this evaluation, noise either in the instrumentation or in the reactor itself introduces a minimum error of 0.5% in the power and 5 millibeta in the reactivity.

The sensitivity of the instrumented synthesis method to noise can be illustrated by returning to Chapter 2. The higher order modes of the synthesis are characterized by smaller singular values. The modes, upon determining the pseudo-inverse matrix \underline{A}^* , are multiplied by the inverse of the singular value. This is a large number if the singular value is small. Noise in the detectors will contribute to these spurious modes. Increasing the singular value zeroing criterion will reduce the sensitivity of the method to noise, but may

do so at the expense of eliminating important information. Another alternative is to filter the detector measurements, an option that will be explored later in this chapter.

Having examined this case and others, the zeroing criterion was set to 5.0×10^{-4} . This appears to represent a good mixture of eliminating spurious modes while retaining important information.

The tilted cases retain the same character as the flat cases. The amount of noise is largely unchanged, and the zeroing criterion used above also appears to work well. One additional calculation that can be performed is the comparison of power tilting in the reactor as determined by the synthesis method to that determined by an MCNP calculation. Since the nodes in the synthesized flux do not correspond exactly to specific fuel elements, the comparison is somewhat difficult to make. The nodes come closest to occupying entire elements for five positions in the B-ring. A ratio of tilted power to flat power in these elements, as determined by the MCNP model, is compared to the tilted-to-flat power ratio as determined by the synthesis along several vertical sections. These sections roughly correspond to the fuel elements. The uncertainty in the MCNP values originate from the statistical nature of the code. The uncertainty in the synthesis values come from the fact that averages of the power over time from the “static” measurements were used. The tilt referred to is tilt #1 at 50 kW in core #106.

Element	MCNP Tilted-to-Flat Power Ratio	Synthesis Tilted-to-Flat Power Ratio
B1	1.014 ± 0.016	1.061 ± 0.010
B4	0.992 ± 0.016	0.974 ± 0.008
B6	1.010 ± 0.016	1.070 ± 0.010
B7	0.991 ± 0.015	0.963 ± 0.008
B9	1.041 ± 0.016	1.040 ± 0.016

Table 6.1. Tilted-to-Flat Power Ratio Comparisons

The peaking predicted by the synthesis method is more severe than the MCNP predictions. The differences could originate from several factors. The reactor at the time of the experiment may not have been in the same condition as modeled by MCNP. Also, the power as calculated by the synthesis method uses theoretical fission cross sections that may not precisely match the MCNP values. Finally, the improving the accuracy of the shape functions in the synthesis may bring the ratios closer to the MCNP prediction if the MCNP prediction is indeed the correct one.

6.5 TRANSIENT RESULTS

6.5.1 DISCONTINUOUS SYNTHESIS

As was discussed by Jacqmin [J1], the instrumented synthesis method can be improved by defining time domains in which certain shape functions are used. As the conditions of the reactor change, the type and/or number of shape functions can be altered to better synthesize the flux shape at that time.

As part of a control system, the selection of the shape functions could be automated. The selection of the functions would be most dependent upon the power level and position of the control rods. For the experimental evaluation, the shim blade positions will be the defining parameter. As the positions of the blades are altered, different shape functions are selected. For the flat shim blade configurations at the start of the transients,

two representative shape functions will generally be sufficient. For periods when the shape is changing, more functions may be included in the synthesis.

6.5.2 INSERTION OF SHIM BLADE #3 - CORES #106 AND #110

The first transient analyzed will be the insertion of shim blade #3. As described in Appendix 5, the blade is driven into the core for fifteen seconds in core #106 and ten seconds in core #110 at a speed of 4.25"/minute. After being held in this position in for 50 seconds, the blade is withdrawn and the reactor is returned to its original condition for repetition of the experiment.

The shape functions used in the synthesis are given below. Recorded shim blade positions are given.

Shape Function Number	Description
1	Shim Blades at 7.80", 10 kW
2	Shim Blades at 7.95", 50 kW
3	Shim Blades at 7.95", 50 kW Blade #3 at 7.42"
4	Shim Blades at 7.95", 50 kW Blade #3 at 6.89"

Table 6.2. Shape Functions Shim Blade #3 Insertion - Core #106

Shape Function Number	Description
1	Shim Blades at 8.90", 10 kW
2	Shim Blades at 9.00", 50 kW
3	Shim Blades at 9.00", 50 kW Blade #3 at 8.66"
4	Shim Blades at 9.00", 50 kW Blade #3 at 8.33"

Table 6.3. Shape Functions Shim Blade #3 Insertion - Core #110

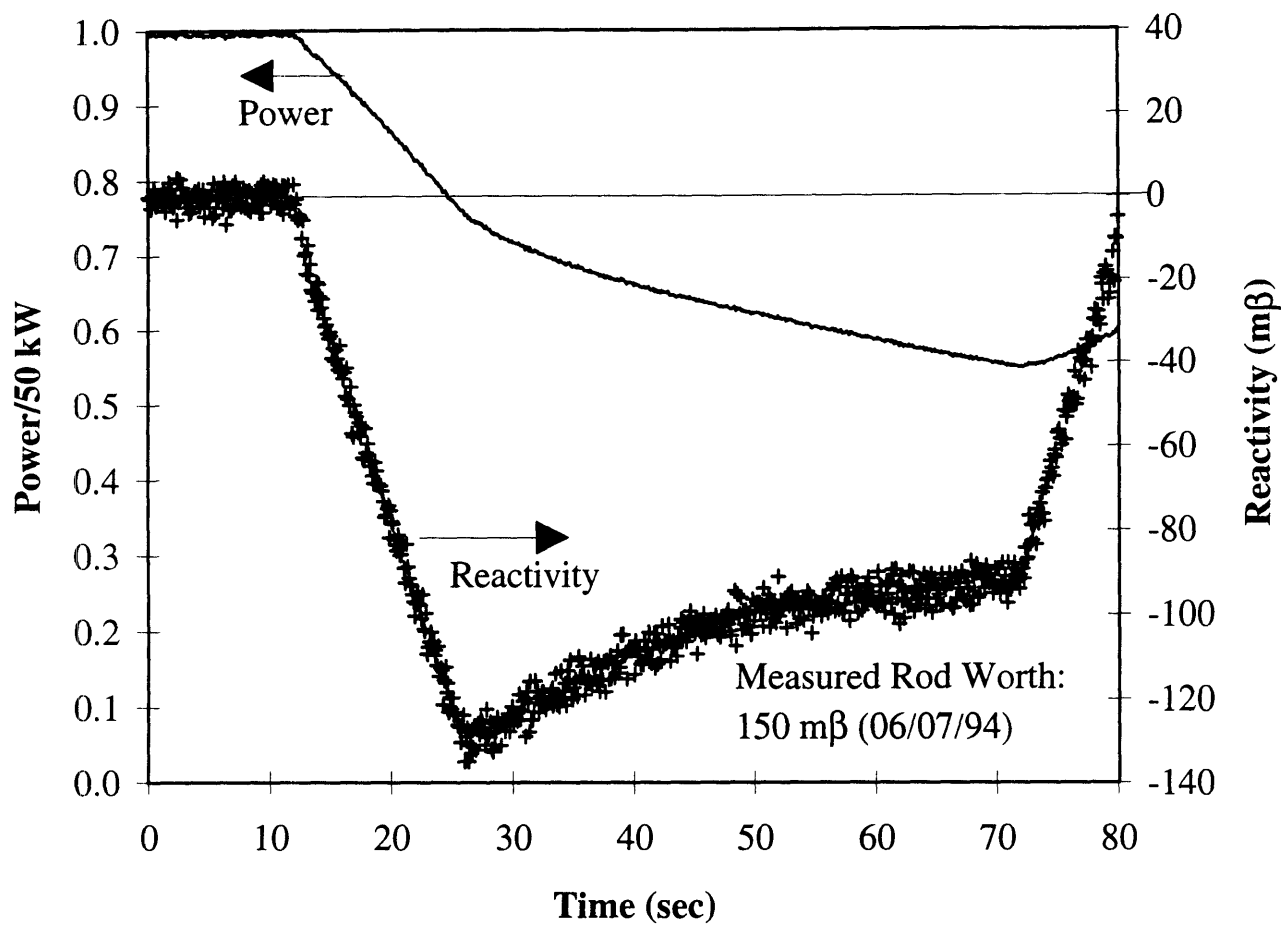


Figure 6.7 Power and Reactivity as Determined By Synthesis
Shim Blade #3 Insertion - Core #106

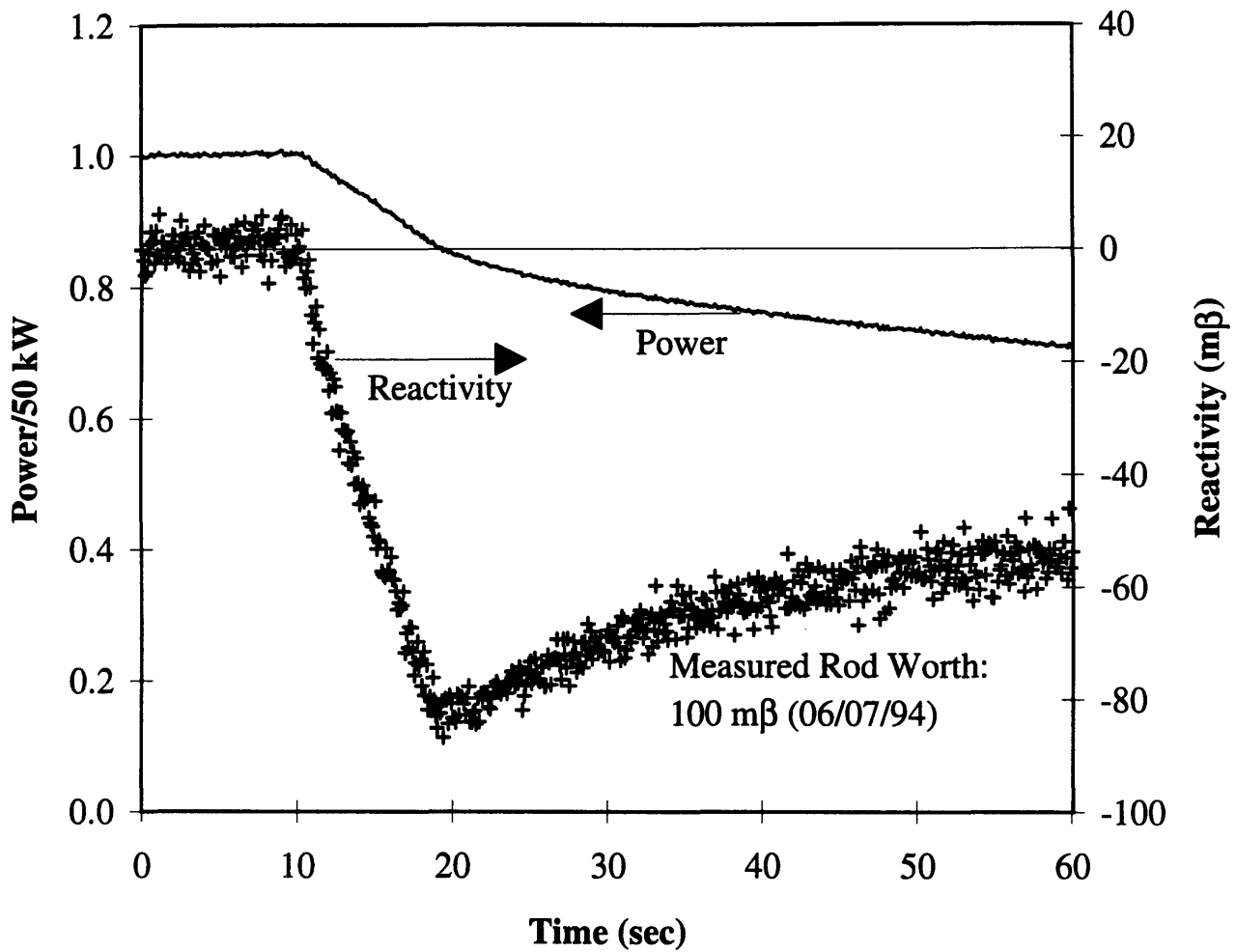


Figure 6.8 Power and Reactivity as Determined by Synthesis
 Shim Blade #3 Insertion - Core #110

The reactivity and power, as determined by the synthesis method, are given for each core in Figure 6.7 and Figure 6.8. (Recall that the power as determined by the synthesis is the synthesized flux multiplied by the fission cross sections in each node multiplied by an energy conversion factor.) In both cases, the reactivity as predicted by the synthesis is compared to the “Measured Rod Worth” as determined by the reactor operations group through rod drop measurements². It is important to realize that one would not expect the two values to match. The reactivity, as computed by inverse kinetics using the synthesized flux, is *not* the same definition of reactivity used by the Reactor Operations Group to assign reactivity worths to the shim blades. Although one might expect the values to be reasonably close, they should not be equal. There is no reference value to be compared to the reactivity as determined by the inverse kinetics equations employing the synthesized flux.

An examination of the synthesis reactivity shows what appears to be an anomaly between the time the blade is inserted and when it is withdrawn. To explain and correct it, Eqn. 2.40 is rearranged into the following form.

$$\hat{\rho}(t) = \hat{\beta}_{eff}(t) + \hat{\Lambda}(t) \left[\frac{d\hat{T}_{eff}(t)/dt}{\hat{T}_{eff}(t)} - \frac{\sum_{iprec=1}^{nprec} \lambda_{iprec} \hat{C}_{eff,iprec}}{\hat{T}_{eff}(t)} - \frac{q_{eff}(t)}{\hat{T}_{eff}(t)} \right] \quad (6.3)$$

² The worth of a control rod can be determined using “rod drop” measurements. Assume the reactor is operating at some initial power P_0 when a rod is dropped into the core, inserting $-d\rho$ reactivity into the core. The reactor power will come to some steady lower power level P_1 after a few prompt neutron lifetimes. The amount of reactivity inserted, in terms of the effective delayed neutron fraction β is given

$$\text{approximately as } \frac{\delta\rho}{\beta} = \frac{P_0}{P_1} - 1. \quad [D2]$$

For the evaluations plotted in Figure 6.7 and Figure 6.8, no source has been defined.

Therefore, $q_{eff}(t)$ is zero. At steady state, the $\frac{d}{dt}\hat{T}_{eff}(t)$ term is zero in the absence of noise. The decay of precursors as a fraction of total neutron population, given by the

$\frac{\hat{\Lambda}(t)}{\hat{T}_{eff}(t)} \sum_{iprec=1}^{nprec} \lambda_{iprec} \hat{c}_{eff,iprec}$ term, is matched by their production, $\hat{\beta}_{eff}(t)$. As blades are

inserted into or withdrawn from the MITR, the $\frac{d\hat{T}_{eff}(t)/dt}{\hat{T}_{eff}(t)}$ and $\frac{\sum_{iprec=1}^{nprec} \lambda_{iprec} \hat{c}_{eff,iprec}}{\hat{T}_{eff}(t)}$ terms

change, although the precursor term is usually much larger than the $\frac{d}{dt}\hat{T}_{eff}(t)$ term. As

the blade is moving, the prompt neutron population will change rapidly. For this particular transient, the population drops. The longer lived precursors, however, remain near their

initial population. This causes the $\frac{\sum_{iprec=1}^{nprec} \lambda_{iprec} \hat{c}_{eff,iprec}}{\hat{T}_{eff}(t)}$ term to grow, reflecting the rapid

decline in reactivity illustrated near the beginning of the transients in Figure 6.7 and Figure

6.8. After movement of the blade is stopped, the MITR is left in a subcritical condition,

but the rate of change of power slows as the delayed neutron precursors decay. For the

low power and natural circulation conditions for the synthesis experiments, little feedback

is expected, certainly none that would lower the temperature of the coolant. It would be

expected, then, that the reactivity would remain relatively flat after the blade is inserted.

For this to occur, the neutron population given by $\hat{T}_{eff}(t)$ would have to decrease at the

same rate as the decay of the precursors, given by $\sum_{iprec=1}^{nprec} \lambda_{iprec} \hat{C}_{eff,iprec}$. This keeps the ratio

$\frac{\sum_{iprec=1}^{nprec} \lambda_{iprec} \hat{C}_{eff,iprec}}{\hat{T}_{eff}(t)}$ equal to one, and the reactivity is unchanged. For a source free reactor,

this is precisely the case. What is seen in the above figures, however, is an increase in

reactivity. The numerator, $\sum_{iprec=1}^{nprec} \lambda_{iprec} \hat{C}_{eff,iprec}$, is decreasing more quickly than the

denominator, $\hat{T}_{eff}(t)$, leading to less negative reactivity as the precursors decay.

Physically, this points to another source of neutrons. Mathematically, the $q_{eff}(t)$ term must

be non-zero to provide a balancing term to $\sum_{iprec=1}^{nprec} \lambda_{iprec} \hat{C}_{eff,iprec}$. A small source term must be

included in the synthesis to obtain a more realistic determination of reactivity in non-

critical periods when the change in neutron population is dominated by the decay of

precursors. For the remaining calculations, a source term is included in the calculation.

For the #3 shim blade insertions, the power and reactivity are recalculated in Figure 6.9

and Figure 6.10.

The source term is most likely due to photoneutrons produced in the heavy water tank. Gamma rays produced in the reactor core will cause (γ, n) reactions in the heavy water. These neutrons may return to the core, providing a source of neutrons.

The gamma rays originate from two sources: the fission event and decay of fission products. The former gamma rays are created at the time of the fission and quickly reach the heavy water tank, producing neutrons. The photoneutrons produced by these gamma

rays are closely related in time to the power of the reactor. In fact, they could be considered part of the prompt neutron population. The photoneutrons resulting from gamma decay of fission products, however, appear long after the fission event. These photoneutrons are often counted among the traditional delayed neutron groups because of their character.

Only the more delayed photoneutrons will significantly affect the determination of reactivity. Rather than estimating a time constant for these delayed photoneutrons, an approximate constant source was employed. For the synthesis evaluation, its value was determined empirically. At 50 kW, $q_{eff}(t) = 5.0 \times 10^6$ neutrons/s produced the proper change in reactivity after a control blade insertion. This was used throughout the evaluation of core #106 for experiments at 50 kW. A slightly higher value, 7.0×10^6 neutrons/s, was used for core #110. Values approximately $1/10^{\text{th}}$ these amounts were used for transients beginning at 5 kW.

The source term seen in the MITR results from photoneutron production in heavy water. In commercial light water reactors, this source term will almost certainly be negligible. However, at startup, discrete neutron sources used in commercial reactors may affect the reactivity determination.

As illustrated in Figure 6.9 and Figure 6.10, the increase in reactivity seen previously is eliminated.

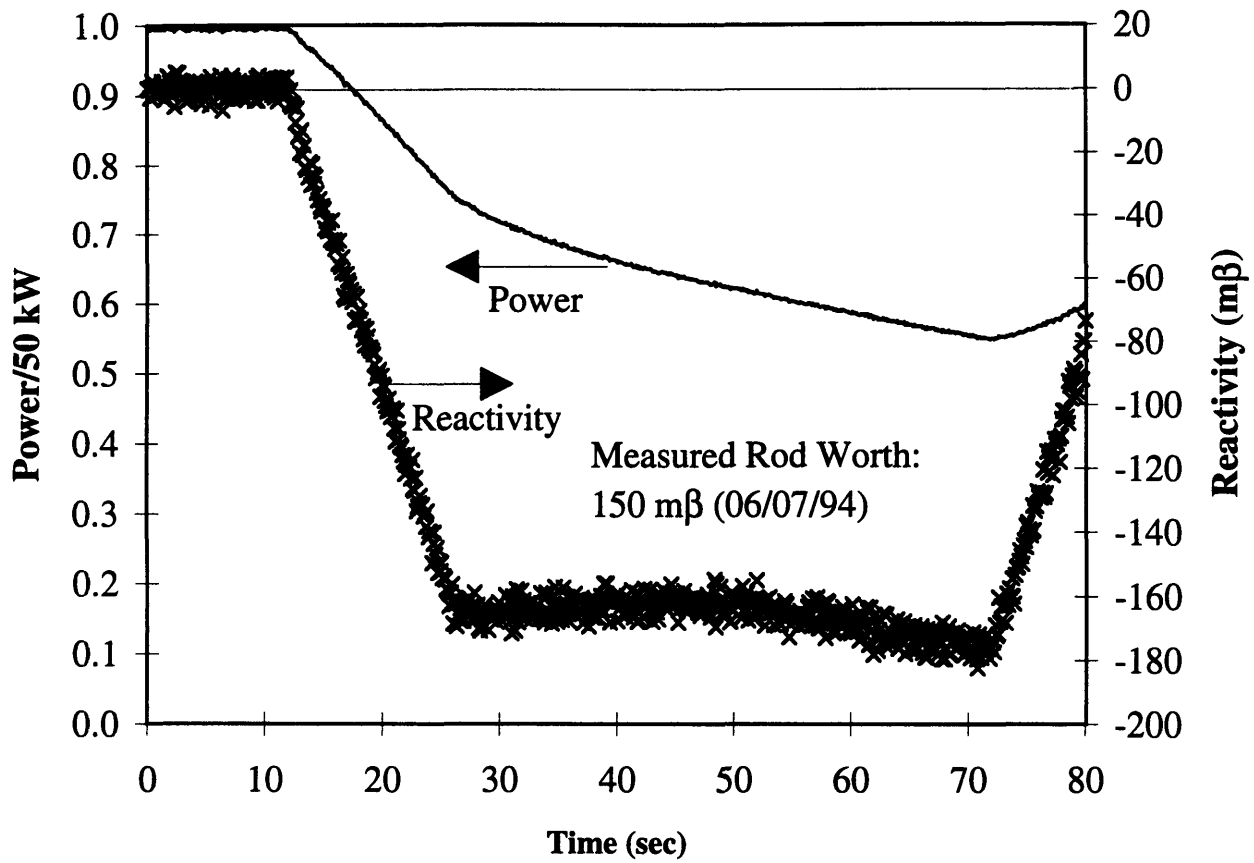


Figure 6.9 Power and Reactivity as Determined by Synthesis with Source Shim Blade #3 Insertion - Core #106

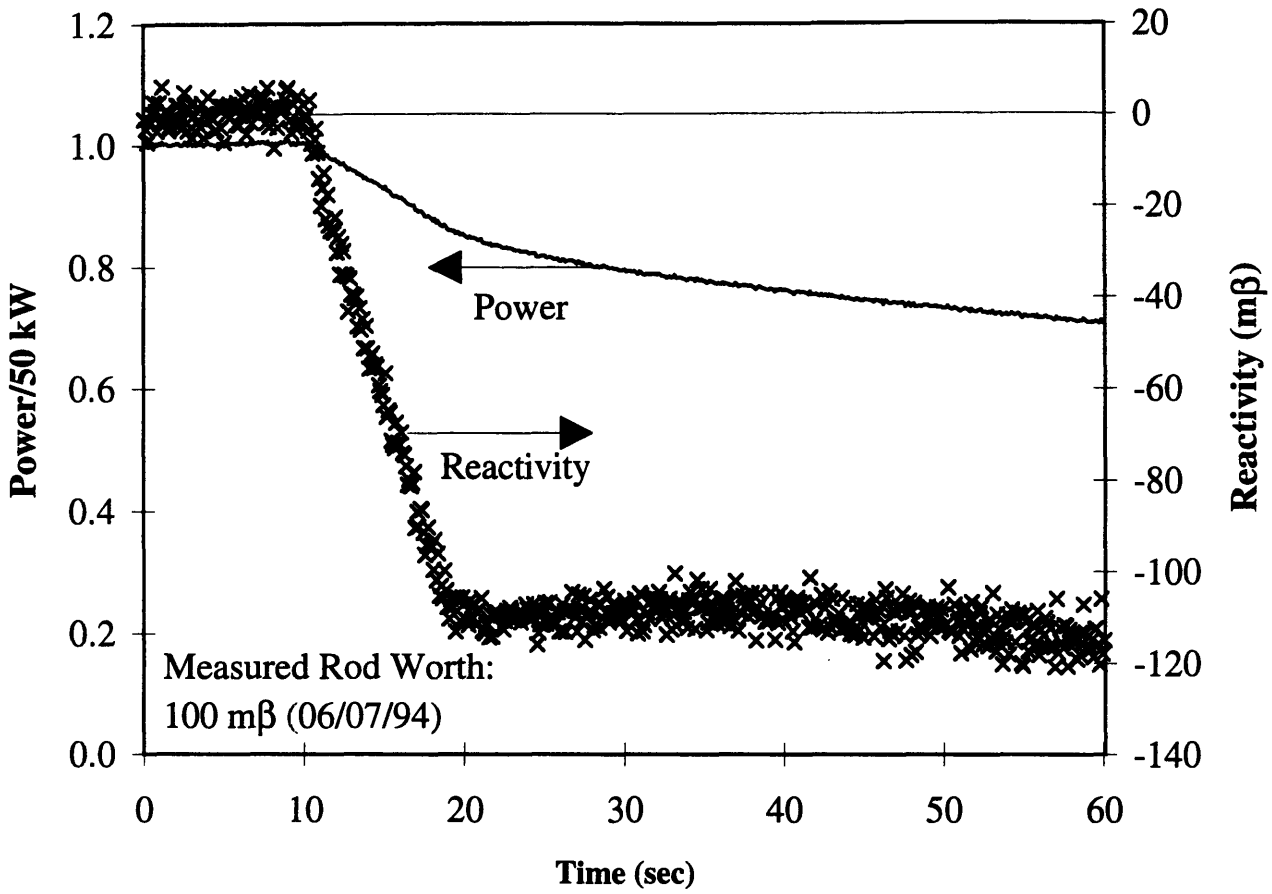


Figure 6.10 Power and Reactivity as Determined by Synthesis with Source Shim Blade #3 Insertion - Core #110

The power as determined by the synthesis method can be compared to the normalized detector readings. Each detector's readings are normalized to its average over the first ten seconds of the transient. The normalized values from all nine detectors are then averaged together. This is compared to the normalized power as determined by the synthesis method. As discussed earlier, the two are not exactly the same if the flux shape changes. The plots of the difference between the synthesis power and the detector measurements, along with the residual, are in Figure 6.11 and Figure 6.12.

We first examine Figure 6.11. The residual remains quite low throughout the transient. In fact, the change in residual from the beginning of the transient to the end remains under 2%. This equals or betters the accuracy attained by Jacqmin for his numerical evaluation of synthesis method [J1]. The transients evaluated there, however, tended to be more severe.

Note also that the residual does not begin at (or near) zero. If the detector responses had been normalized to the flux at the beginning of the transient, the residual would have begun at zero. The detectors were, instead, normalized to the static measurements made at a different point during the experiment. For evaluating the success of the synthesis, the change in residual over the course of the transient will be the important quantity.

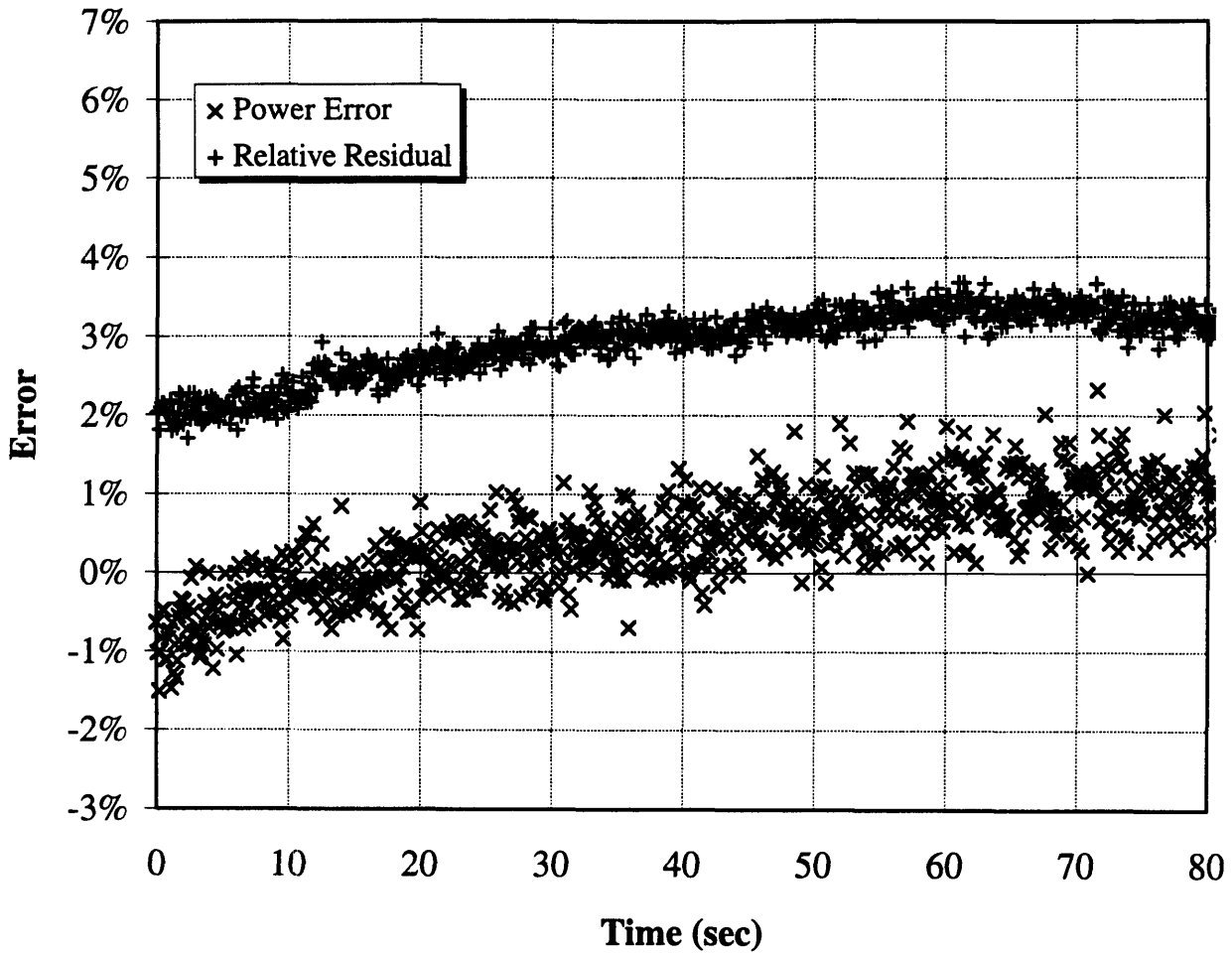


Figure 6.11 Relative Residual and Average Difference Between Synthesis Power and Normalized Detector Readings Shim Blade #3 Insertion - Core #106

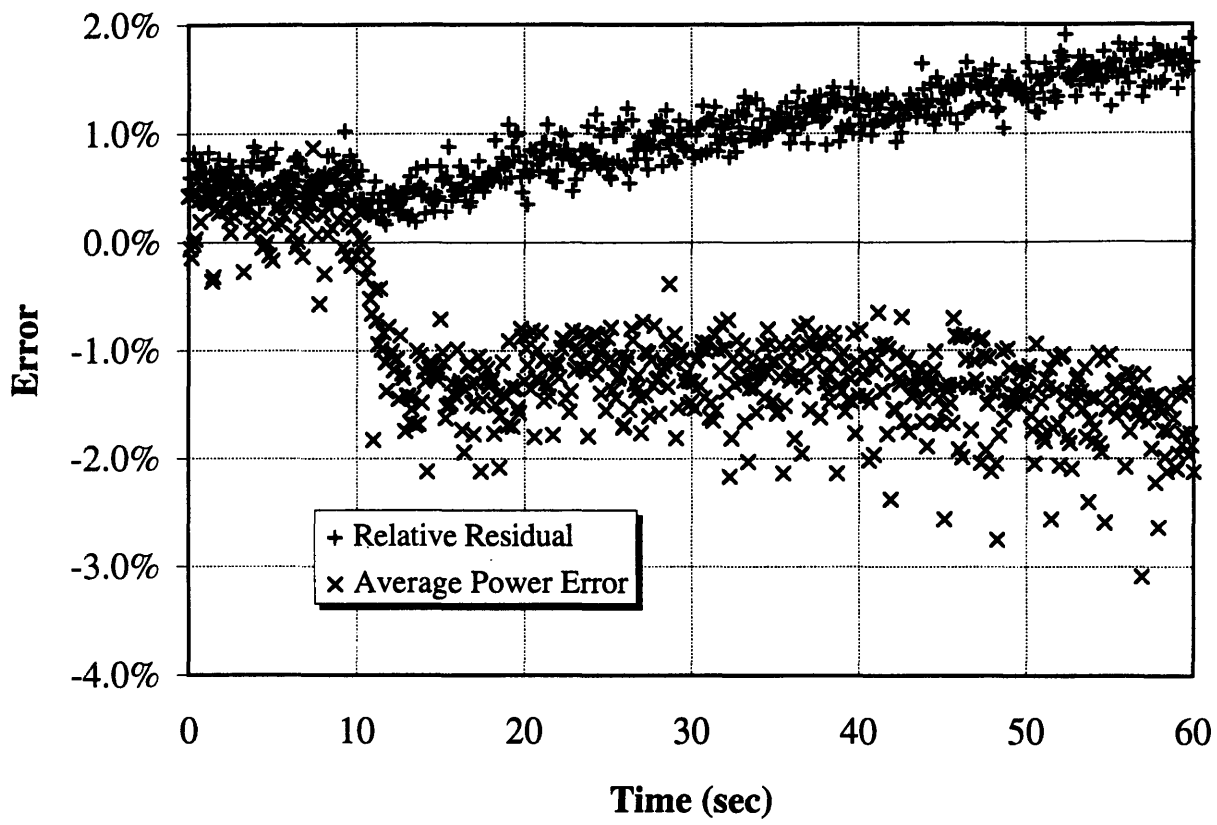


Figure 6.12 Relative Residual and Average Difference Between Synthesis Power and Normalized Detector Readings Shim Blade #3 Insertion - Core #110

As has been discussed, the measurements taken from the three groups of detectors may not reflect precisely the same transient. The measurements from all nine detectors were put into the synthesis code as though they were taken from the same time period. If the rod were moved slightly earlier in one group of measurements than another, this is taken to be a change in flux shape and will be treated as such when determining mixing coefficients. The power calculated from this synthesized flux, however, will differ from each group of detector readings to the degree that the “replication” of the transient differed. To illustrate, rather than comparing the power as predicted by the synthesis method to the average of all nine detector measurements, the power can be compared individually to each of the three groups of detectors. This comparison for core #106 is given in Figure 6.13. When compared to detectors #1,#2, and #3, the error remains steady and small, below 1% over the entire transient. But when averaged with the other detector readings which were taken from the second and third experimental trials, the effect is to change the error. In other words, the second and third trials are not exact replications of the first. The same type of behavior is seen in core #110 (Figure 6.14). The average of all nine detectors is used for the “reference” because it is consistent with the definition of the residual, which accounts for differences in the actual and reconstructed count rates at all nine detector locations.

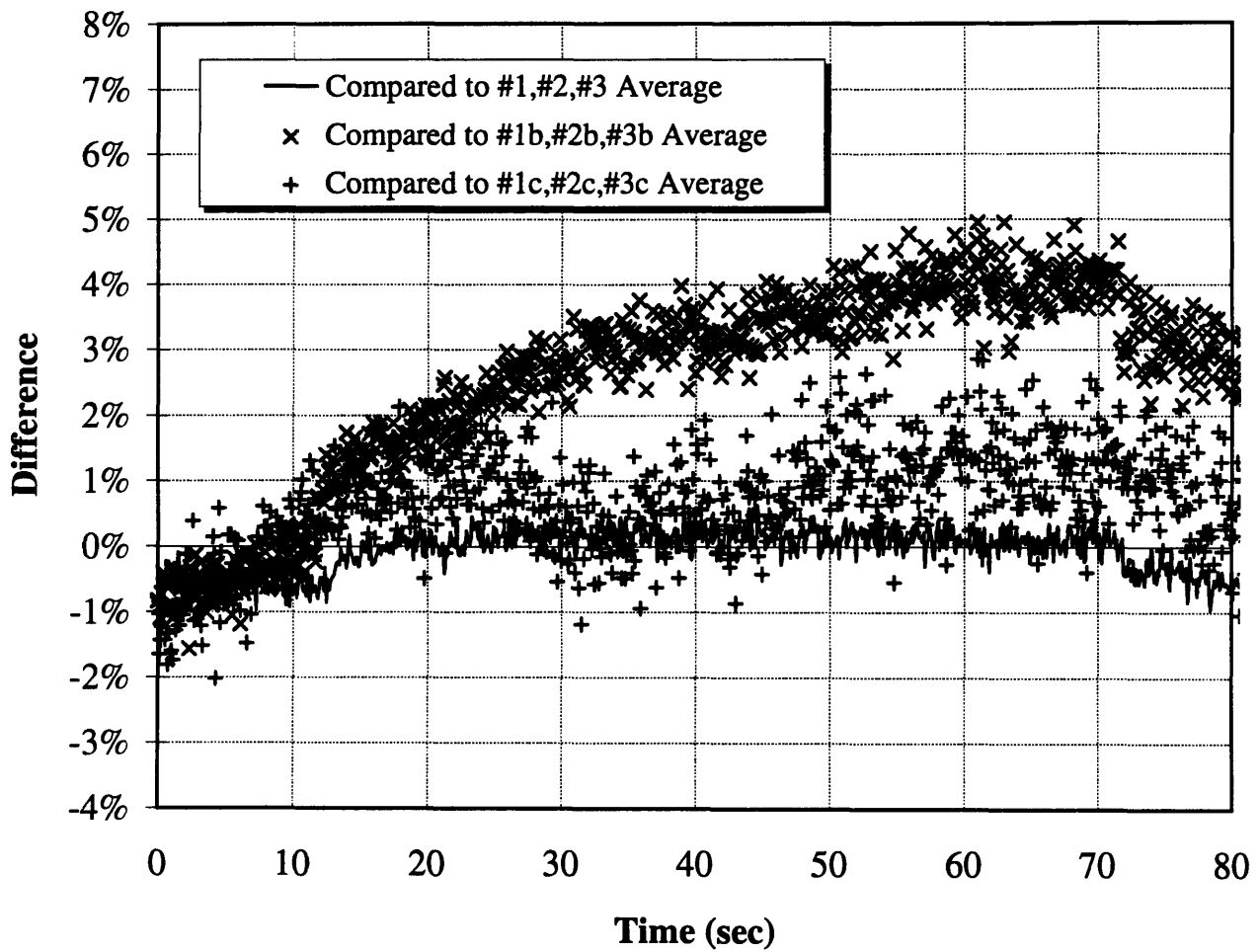


Figure 6.13. Differences Between Synthesis Power and Normalized Detector Readings Shim Blade #3 Insertion - Core #106

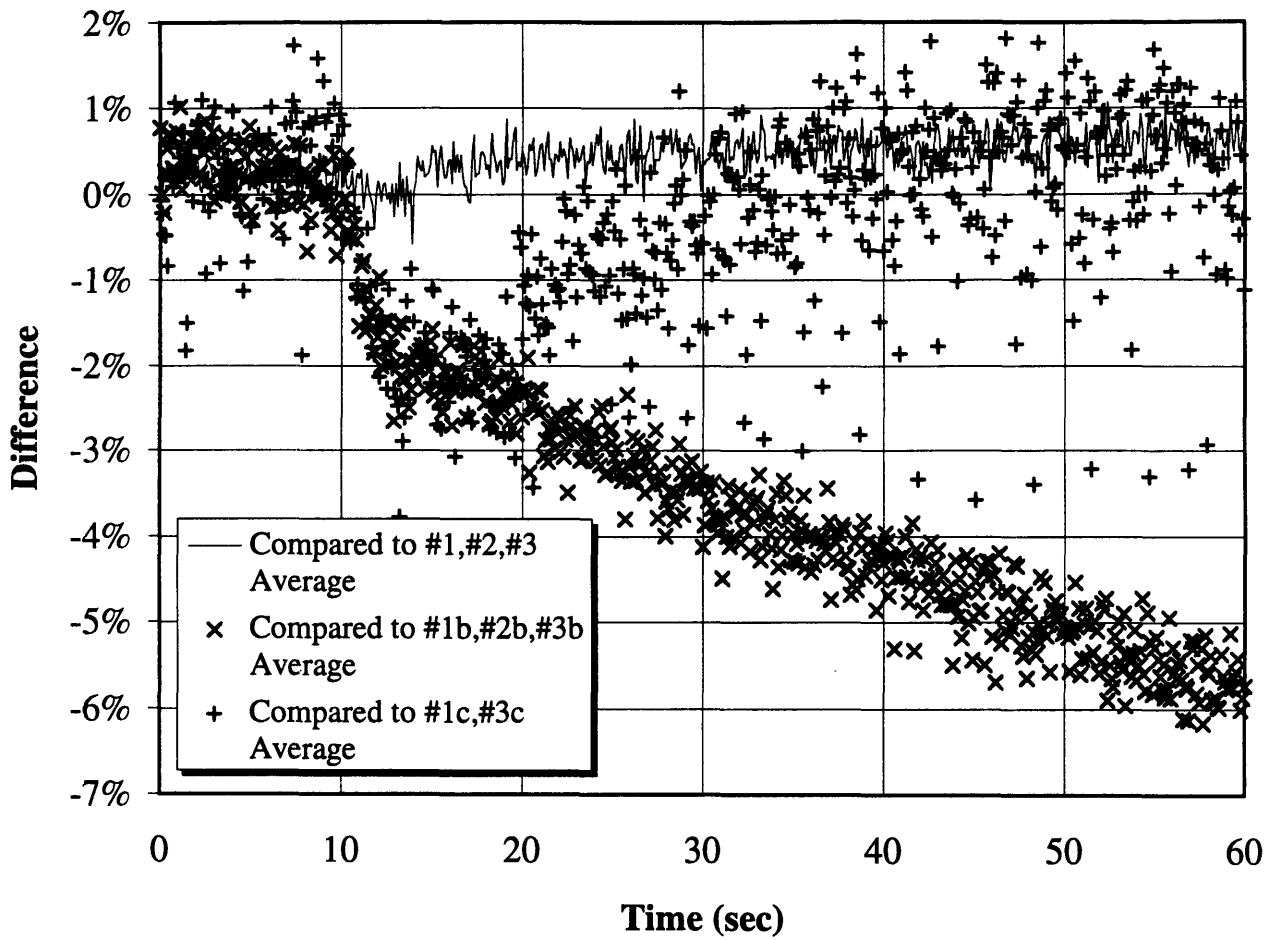


Figure 6.14. Differences Between Synthesis Power and Normalized Detector Readings
 Shim Blade #3 Insertion - Core #110

This effect is small in most all the transients, but does introduce a source of error into the evaluation. The residual and power errors given in the previous and following figures should then be viewed as an upper bound, not an average. The logic behind this statement stems from the fact that the synthesis method is attempting to fit shape functions to slightly different conditions assumed to take place at the same time. If measurements were made under exactly the same conditions, the results could only improve. In that sense, the results above give very positive indications of the synthesis method's ability to reflect changes in the core. For purposes of evaluating the synthesis, the residual remains the better tool in this case. A low residual indicates the synthesis is accounting for changes in flux shape. This is true even if the changes are non-physical, the results of inconsistent replication of the transient.

It has been purported that the instrumented synthesis method is superior to point kinetics methods because of its ability to account for changes in the flux shapes. One measure of this is to compare the residual of a synthesis calculation, using several flux shapes, to a point kinetics calculation. That comparison is made for core #106 below. For the point kinetics calculation, the flux shape for the recorded shim bank height of 7.95" at 50 kW was used.

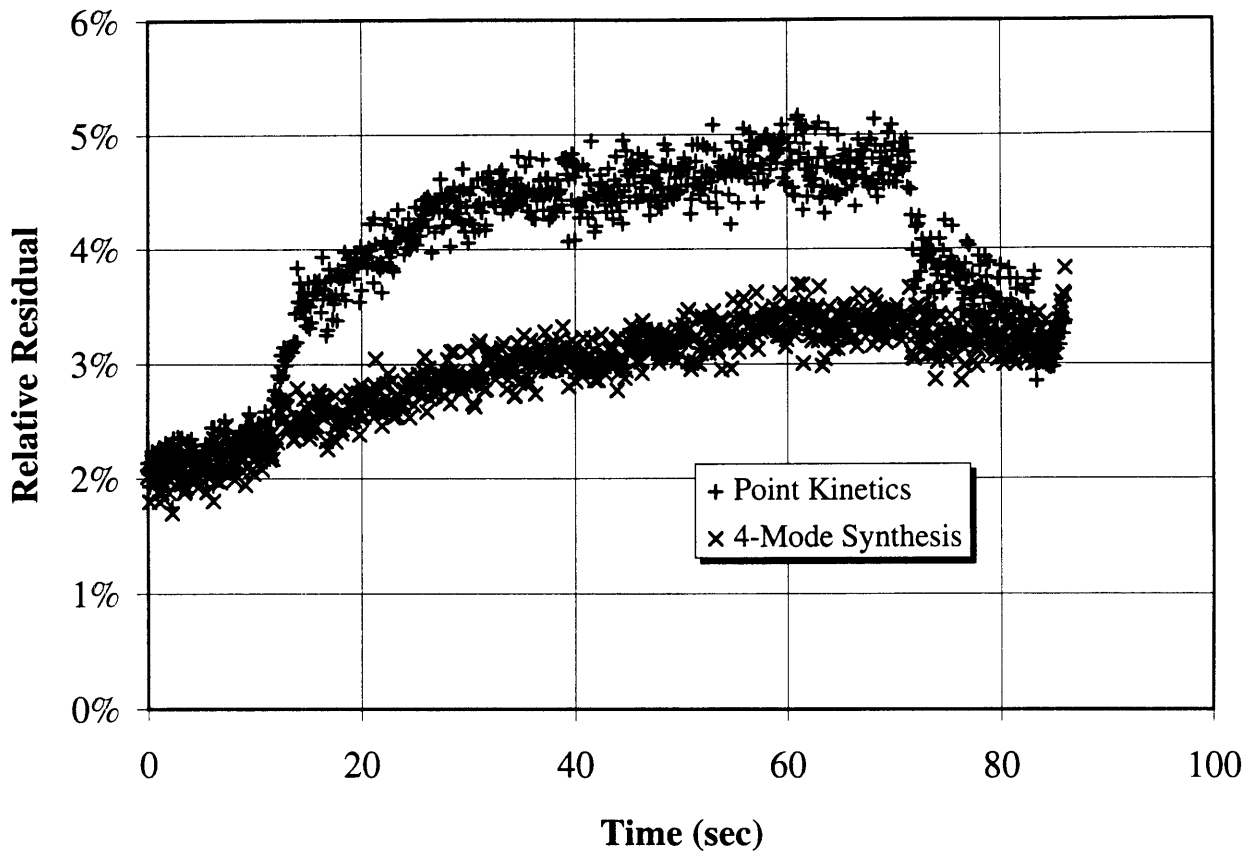


Figure 6.15 Comparison of Relative Residuals for Point Kinetics and Four-Mode Synthesis
Shim Blade #3 Insertion - Core #106

Over the first period, when the condition of the core remains essentially unchanged from its flat shim bank configuration, the difference between the two is almost negligible. But once the shim blade has begun to move, the differences are readily apparent. It is especially encouraging to see such differences given the small, tightly coupled nature of the core. As the blade is returned to its initial position, the point kinetics approximation improves.

There are two important conclusions that can be drawn from Figure 6.15. The first is that the synthesis method can indeed account for changes in the flux shape. Given that the residual is non-zero even for the synthesis method, it is of course impossible to state that all changes are perfectly accounted for. However, it does appear to keep errors acceptably low, and lower than point kinetics. The second conclusion concerns the evaluation method itself. The fact that changes in the flux shape are being reflected in the synthesized flux gives weight to the current interpretation of the residual. That is, a low residual in a sufficiently overdetermined system during the course of the transient is a good indication that the method is properly reflecting changes from some average initial condition.

Finally, a comparison can be made to the transient calculation using the QUARTZ code. The power and reactivity as determined by the synthesis method is compared to the QUARTZ results.

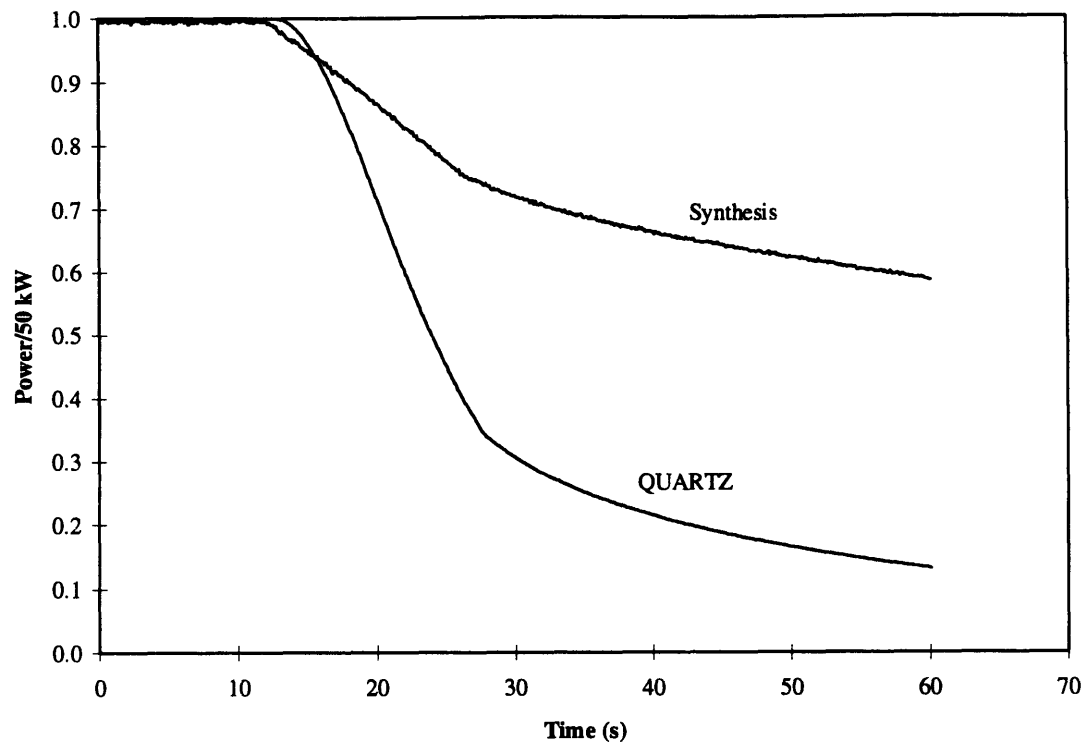


Figure 6.16. Comparison of Synthesis Power to QUARTZ Power
Shim Blade #3 Insertion - Core #106

There is an obvious discrepancy between the synthesis prediction of power and the QUARTZ prediction. The explanation is plainly seen in Figure 6.17. The amount of negative reactivity inserted by the control blade is much larger in the QUARTZ model than in the synthesis. Although this is a strike against the QUARTZ model of the reactor, it demonstrates the ability of the synthesis method to construct the flux from theoretical predictions that, themselves, do not match the physical condition when applied to a transient. A more accurate synthesis would be possible if more accurate shape functions were developed. But even with the present QUARTZ model, the synthesis process is still

able to accurately reflect the changes in core conditions through combinations of various shapes.

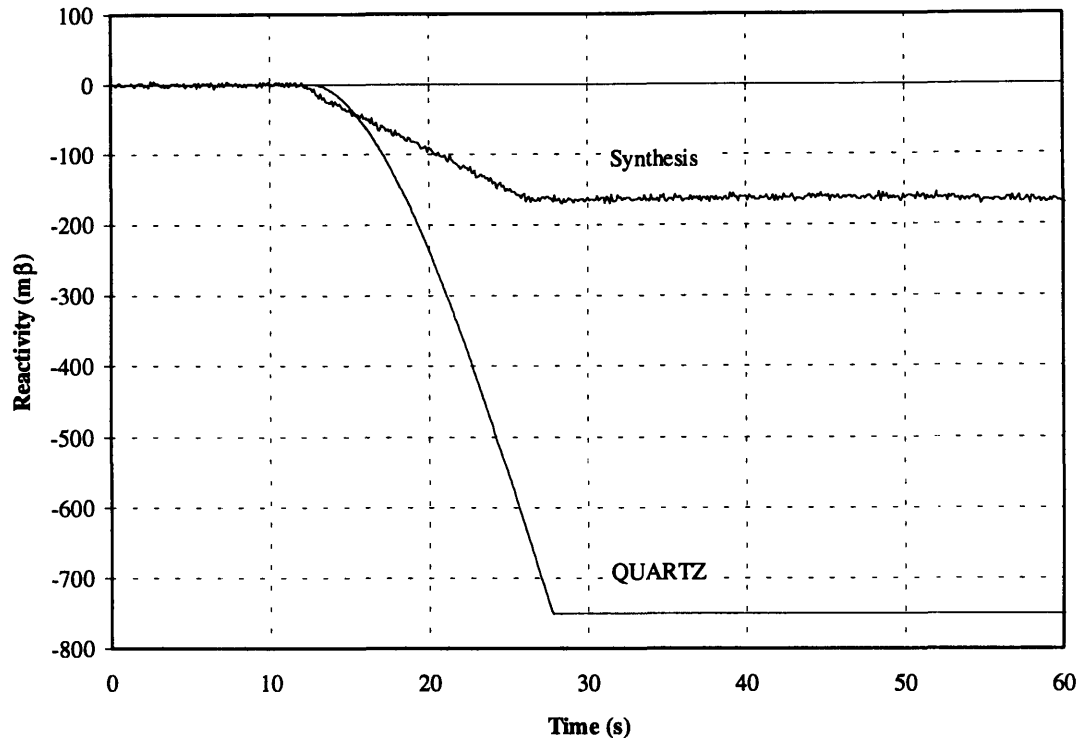


Figure 6.17. Comparison of Synthesis Reactivity to QUARTZ Reactivity Shim Blade #3 Insertion - Core #106

The inaccuracy of the QUARTZ model may derive from several sources, but probably most significant are the boundary conditions and the control blade model. The issue of static boundary conditions was mentioned in Chapter 5. As the control blades move, the physical conditions at the boundary will change. The boundary conditions in QUARTZ remain static, however. This effect is amplified because of the proximity of the control blades to the boundary. Altering the code to allow for changing boundary

conditions would unnecessarily complicate the transient solution. The better approach would be to enlarge the model, reducing the dependence upon the boundary conditions.

The modeling of the control blades may also be inaccurate. The worth of the blades appears to be much stronger in the transient QUARTZ model than predicted by the synthesis method. This would lead to the more severe power and reactivity changes seen in Figure 6.16 and Figure 6.17. This may be due to an incorrect fine mesh model of the blades. The three possible blade models in Chapter 5 leave some room for debate about the correct control blade specifications. Also, in collapsing the structure to the coarse mesh model, the homogenization of the control blade material with other surrounding may have increased the worth of the blades.

There is also the issue of feedback. The experiments were conducted at low power after a prolonged shutdown. Feedback is not expected to play a significant role during the experiment. However, any feedback that does arise is not reflected in the QUARTZ model.

6.5.3 INSERTION OF SHIM BLADE #6 - CORE #110

For the shim blade #6 blade insertion, only the data taken from core #110 are analyzed. The inconsistencies between the three trials in core #106 are too great to be considered to have been from one time period.

The shapes functions employed in the process are listed in Table 6.4.

Shape Function Number	Description
1	Shim Blades at 8.90", 10 kW
2	Shim Blades at 9.00", 50 kW
3	Shim Blades at 9.00", 50 kW Blade #6 at 8.65"
4	Shim Blades at 9.00", 50 kW Blade #6 at 8.29"

Table 6.4. Shape Functions Shim Blade #6 Insertion - Core #110

The first figure is of power and reactivity over time. The behavior is quite similar to that of shim blade #3 insertion. The agreement between reactivity as determined by the Reactor Operations Group and the instrumented synthesis process is again quite close. The plots of the residual and error in power show them to again be quite low (Figure 6.19). The anomalous changes in residual and power appear again as the result of imperfect replication of the experiment during the course of the three groups of measurements.

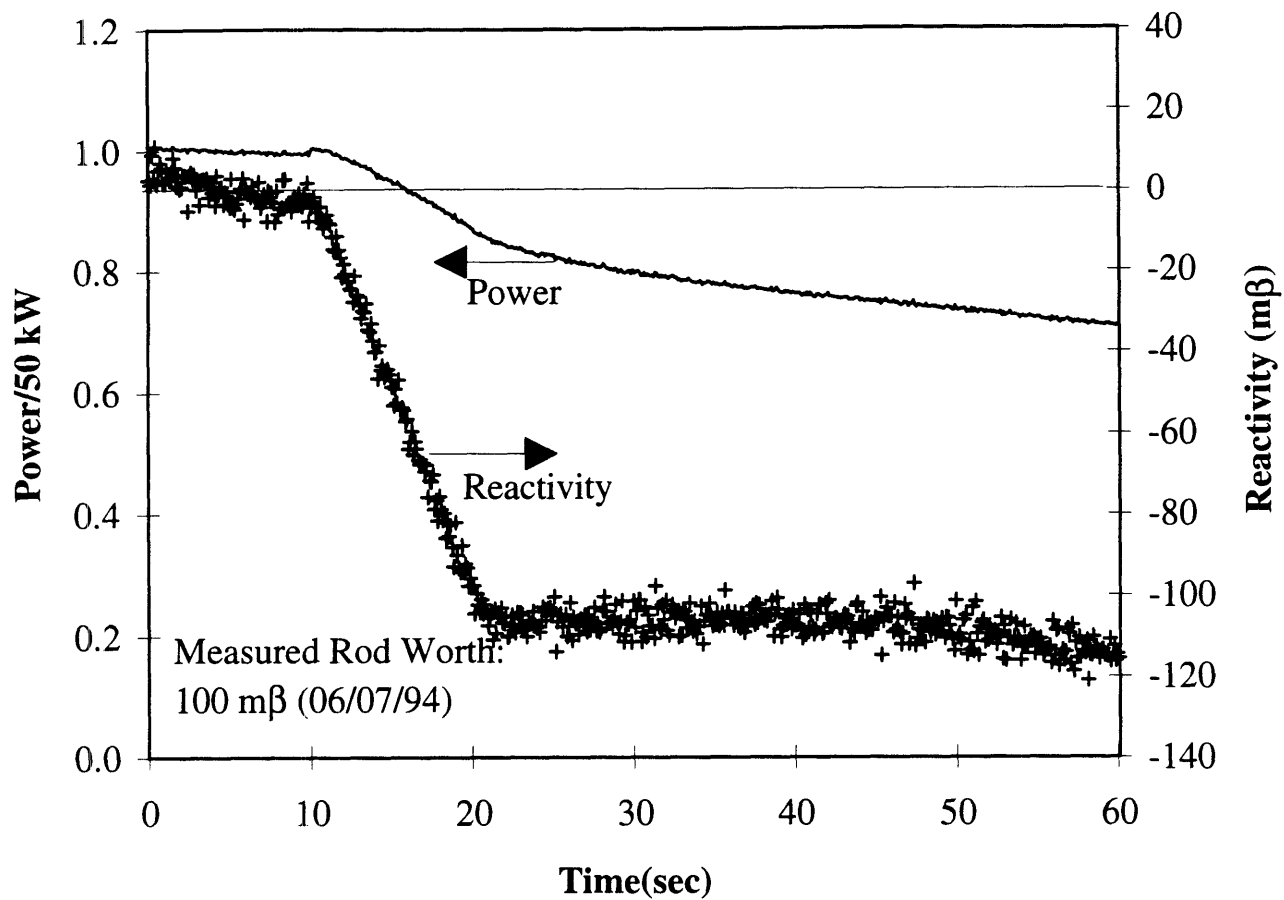


Figure 6.18 Power and Reactivity as Determined by Synthesis
Shim Blade #6 Insertion - Core #110

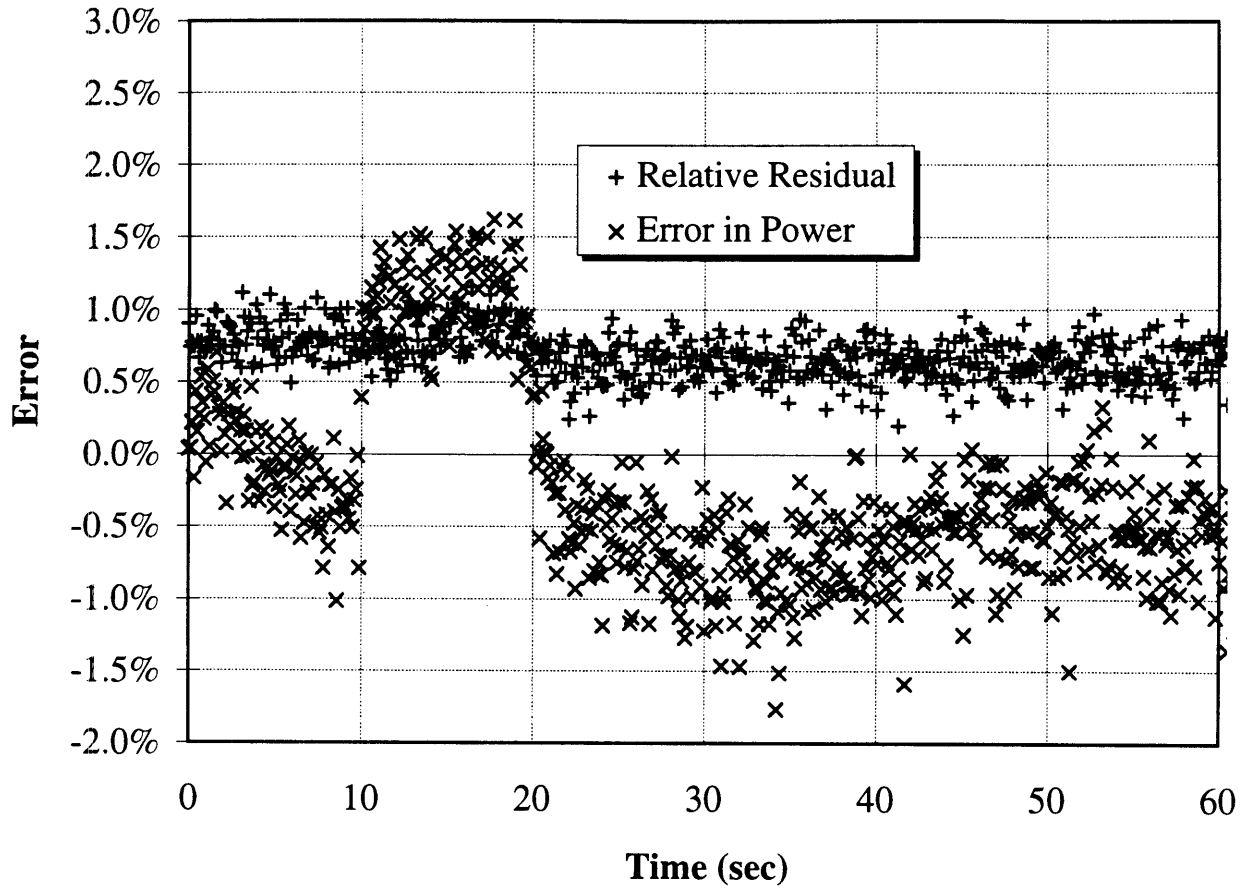


Figure 6.19 Relative Residual and Average Difference Between
 Synthesis Power and Normalized Detector Readings
 Shim Blade #6 Insertion - Core #110

The synthesis was accomplished for this transient using shape functions #1 and #2 in Table 6.4 for the first 10 seconds of the transient. At this point, movement of the blade was initiated and all four shape functions were employed. The mixing coefficients over time are plotted in Figure 6.20. The variation of the mixing coefficients in the first ten seconds suggests that the solution may be incorporating some spurious mode into the synthesis. Enlarging the zeroing criterion would eliminate this mode. However, since the results appear to be good, and for consistency with the other evaluations, the criterion is kept the same. For an automated control system, it would be prudent to maintain a constant zeroing criterion of the singular values.

The comparison of the synthesis residual to the point kinetics residual is presented in Figure 6.21. The residual for the synthesis calculation is smaller than the point kinetics determination, although even the point kinetics determination has a low residual and the difference between the two is small. For transients that do not initiate much of a change in the flux shape, point kinetics may be an appropriate approximation. This is especially true for tightly coupled cores like the MITR.

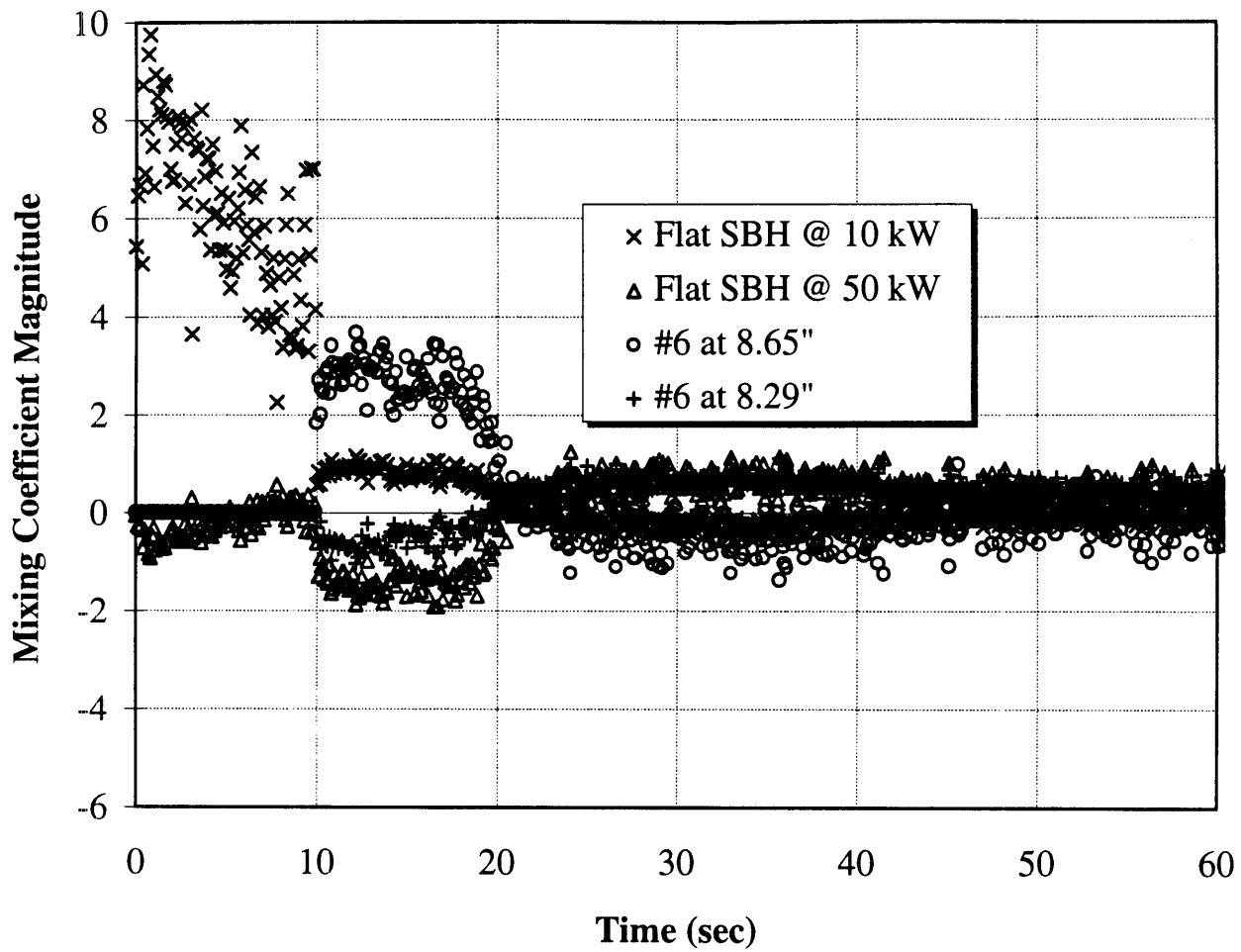


Figure 6.20 Mixing Coefficients over Time
Shim Blade #6 Insertion - Core #110

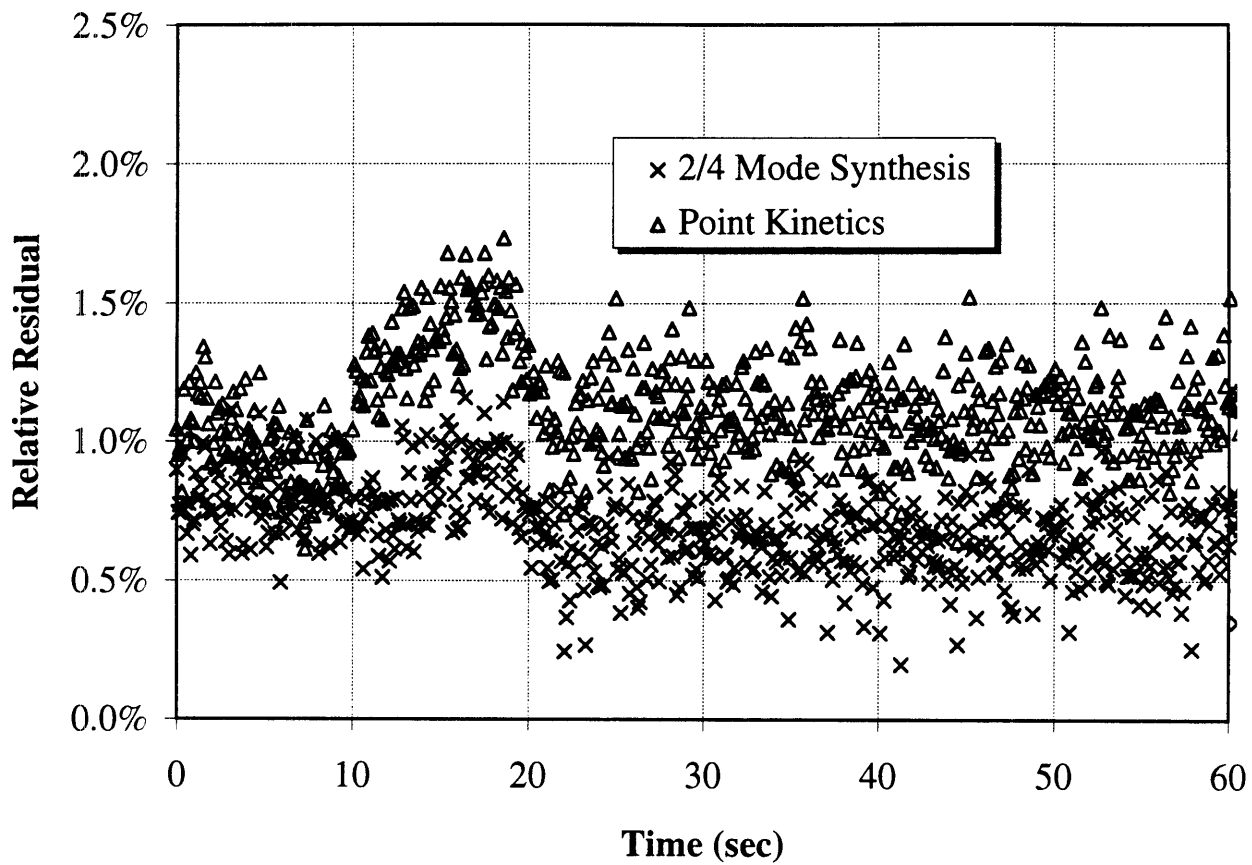


Figure 6.21 Comparison Relative Residuals for Point Kinetics and Four Mode Synthesis Shim Blade #6 Insertion - Core #110

6.5.4 WITHDRAWAL OF SHIM BLADE #6 - CORES #106 AND #110

The next experiments analyzed are increases in power by withdrawing shim blade #6. The experimental procedures call for withdrawal of the blade until a 30 second period is established. The power is allowed to increase from 5 kW to 50 kW. The blade is then to be reinserted, and power is leveled at 60 kW. The reactor is then returned to its initial condition and the experiment is repeated.

The shape functions used for the analysis of the withdrawal of shim blade #6 are as follows.

Shape Function Number	Description
1	Shim Blades at 7.80", 10 kW
2	Shim Blades at 7.95", 50 kW
3	Shim Blades at 7.95", 50 kW Blade #6 at 8.52"
4	Shim Blades at 7.95", 50 kW Blade #6 at 9.08"

Table 6.5. Shape Functions Blade #6 Withdrawal - Core #106

Shape Function Number	Description
1	Shim Blades at 8.90", 10 kW
2	Shim Blades at 9.00", 50 kW
3	Shim Blades at 9.00", 50 kW Blade #6 at 9.77"
4	Shim Blades at 9.00", 50 kW Blade #6 at 10.64"

Table 6.6. Shape Functions Blade #6 Withdrawal - Core #110

There was a problem recording data in core #106. As a result, measurements from only six of the nine detectors was recorded. The six detectors were those located at in the middle and top of the string of detectors, those most susceptible to noise. The results generally appear to be still good.

In core #106, the power and reactivity are seen to vary quite smoothly once the rod withdrawal begins. At the beginning of the transient, however, the effect of noise is seen. In the flat measurements illustrated in Figure 6.2 through Figure 6.6, the error in the reactivity at a static condition is approximately ± 5 millibeta. This error is increased at the initial power (5 kW) to more than ± 30 millibeta. At 5 kW, the signal to noise ratio is much lower than at 50 kW. At this power level, in fact, the response of the detectors may be somewhat suspect. Larger errors are also seen in the residual and power at the beginning of the transient (Figure 6.23). These errors decrease as the power increases.

This appears to be only a problem at very low power levels. However, it should be kept in mind in application to an automated control system. If the system is to be applied to the startup of a reactor, instrumentation should be ensured that it is accurate at “source range” or very low power levels.

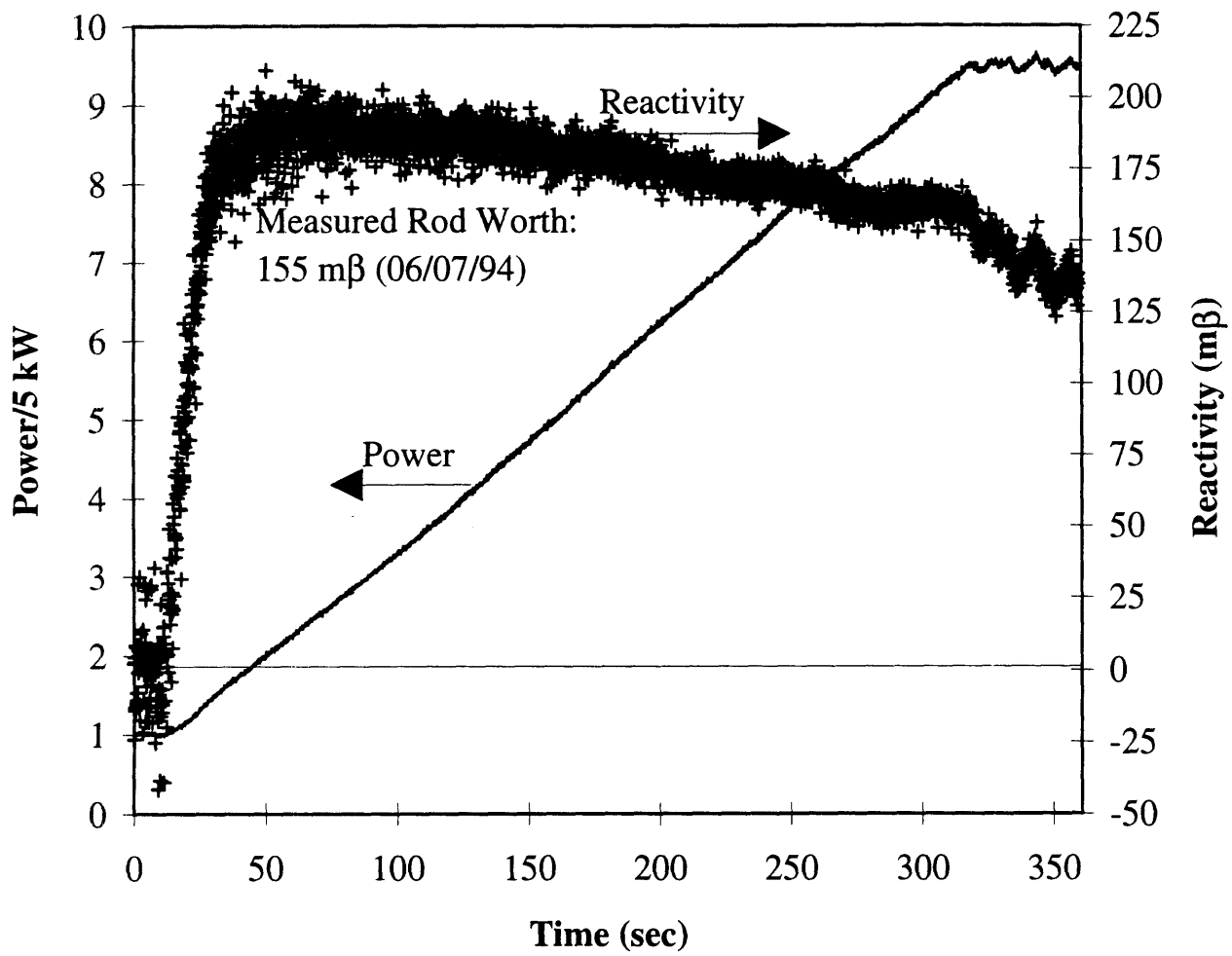


Figure 6.22 Power and Reactivity as Determined by Synthesis
Shim Blade #6 Withdrawal - Core #106

As the transient progresses, the reactivity is seen to decrease. It is possible that the moderator temperature could have increased over the period of the transient sufficiently to reduce reactivity. In this case, the decrease is a physical one. Another explanation is that the source, specified as a constant in the transient, is actually an exponentially changing source resulting from radioactive decay. Given the behavior seen in previous transients, the time constant for the source may be large. For shorter transients, then, a constant source will suffice. However, as the length of a transient increases, the time-dependent behavior will need to be known.

The erratic behavior in the error in the power again appears to be due to inconsistent replication of the experiment between the second and third trials. A comparison of the power as determined by the synthesis to the normalized detector readings of the second and third trials, given in Figure 6.24, shows the error to match very closely that of the second trial, but vary inconsistently from the third trial. The smooth residual would seem to indicate that the synthesis is matching what is seen as variations in the flux shape at a given time. These variations are, of course, the inconsistent replication of the transient between two different trials. Nonetheless, the synthesis method sees them as movement of a blade or some other erratic change in flux shape. The method accounts for those changes in shape, leading to a steadily decreasing residual error.

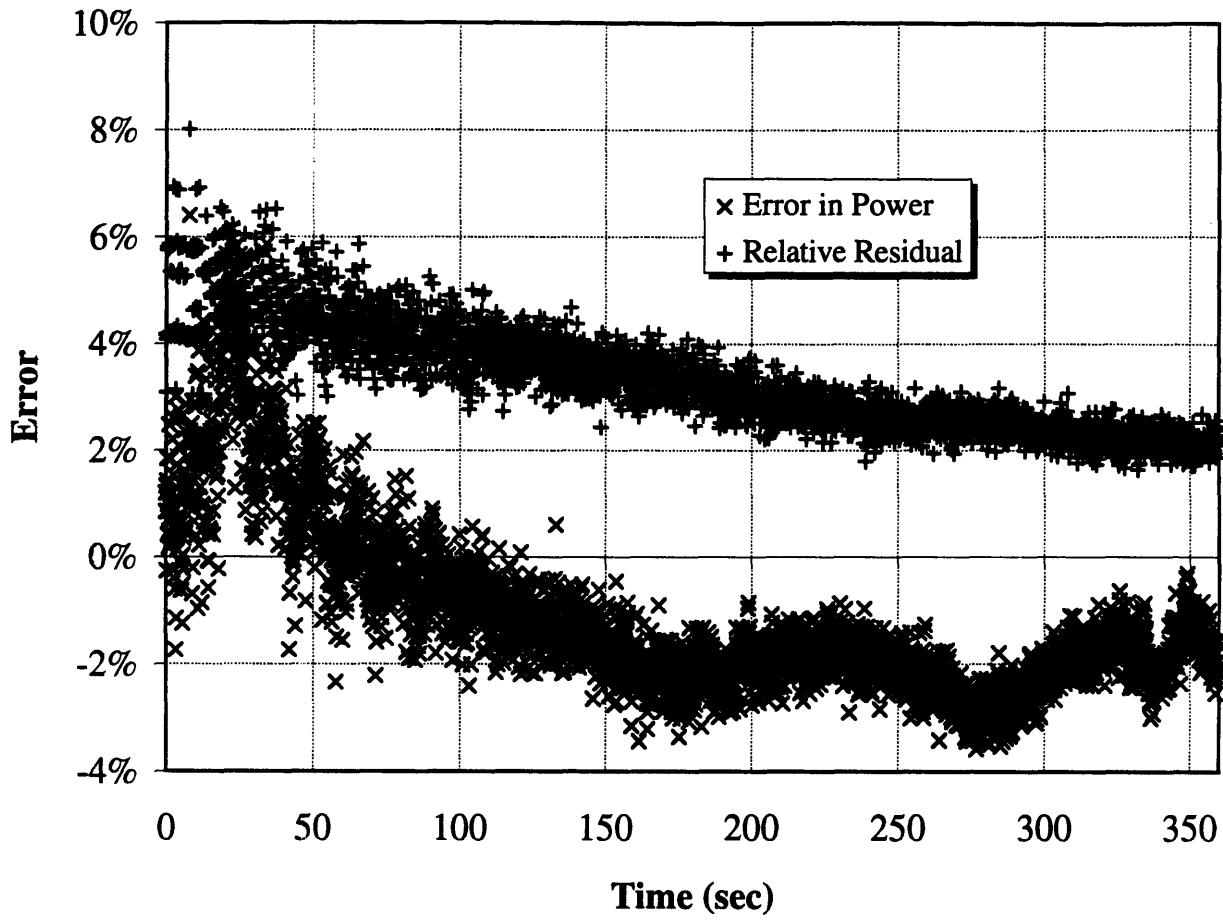


Figure 6.23 Relative Residual and Average Difference Between
 Synthesis Power and Normalized Detector Readings
 Shim Blade #6 Withdrawal - Core #106

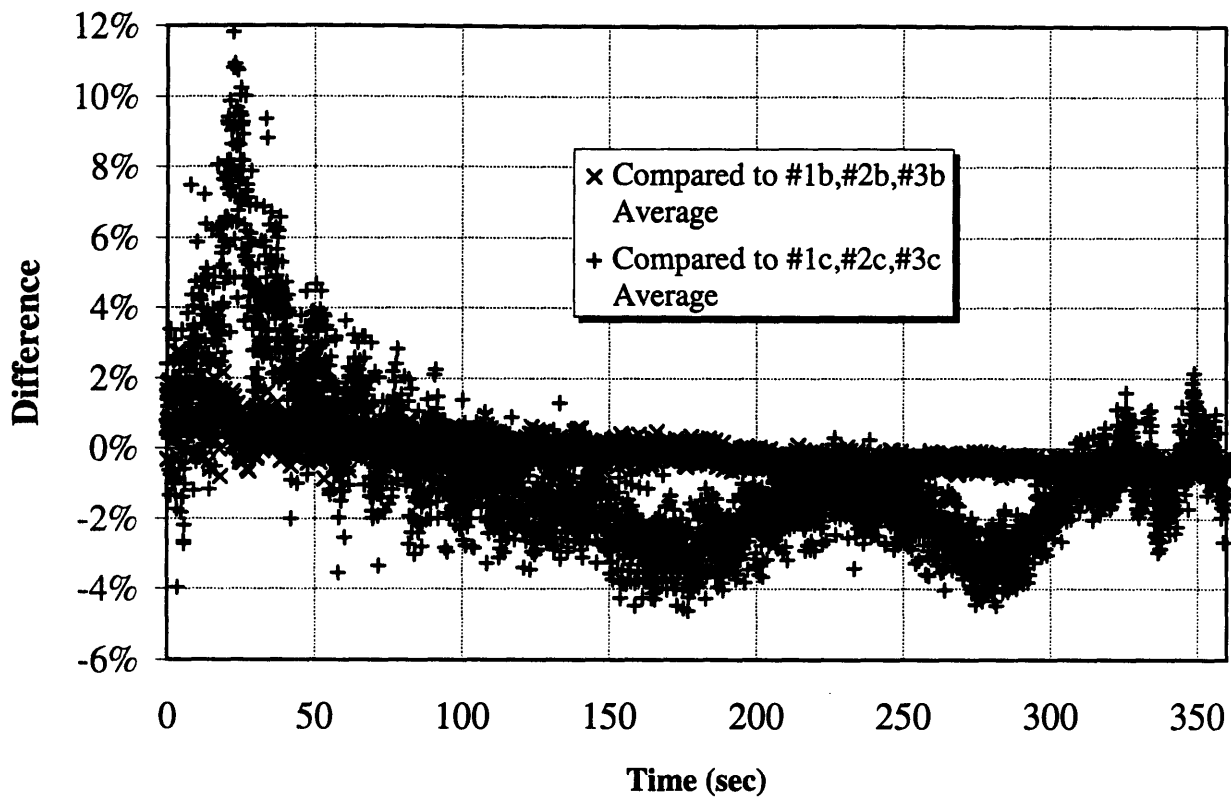


Figure 6.24 Difference Between Synthesis Power
and Normalized Detector Readings
Shim Blade #6 Withdrawal - Core #106

Eight detector measurements were recorded for the same transient in core #110. A less smooth increase in power and reactivity is seen. Here, the period appears to be maintained by the motion of either the regulating rod or the blade itself. Jumps in reactivity correspond to increases in the rate of power ascension.

The error in power and the relative residual are plotted in Figure 6.26. Once again, the error in power varies erratically while the residual remains smooth and small. A comparison to each of the groups of normalized detector readings (Figure 6.27) shows a smooth and small variation from the first group and erratic variations from the second and third. This appears to indicate the first trial of the experiment was marked by movement of either the control blade or the regulating rod, while the power ascension in the second and third trials are more smooth. This is confirmed by a careful examination of the detector readings, taken from each of the three trials, illustrated in Figure 6.28.

The residual of the four mode synthesis is compared to a point kinetics determination in Figure 6.29. This is the most dramatic evidence thus far that the synthesis method can properly account for changes in the flux shape.

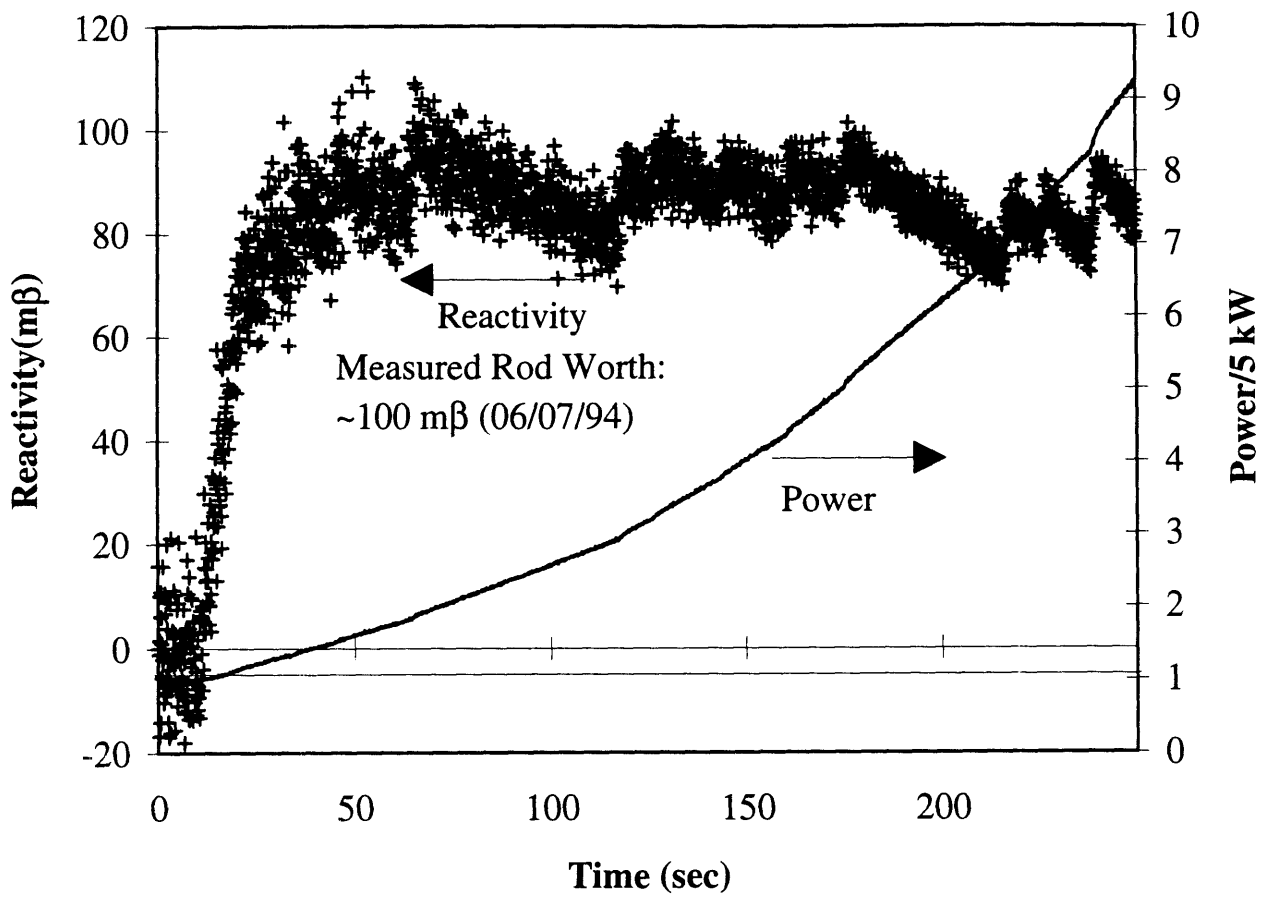


Figure 6.25 Power and Reactivity as Determined by Synthesis
Shim Blade #6 Withdrawal - Core #110

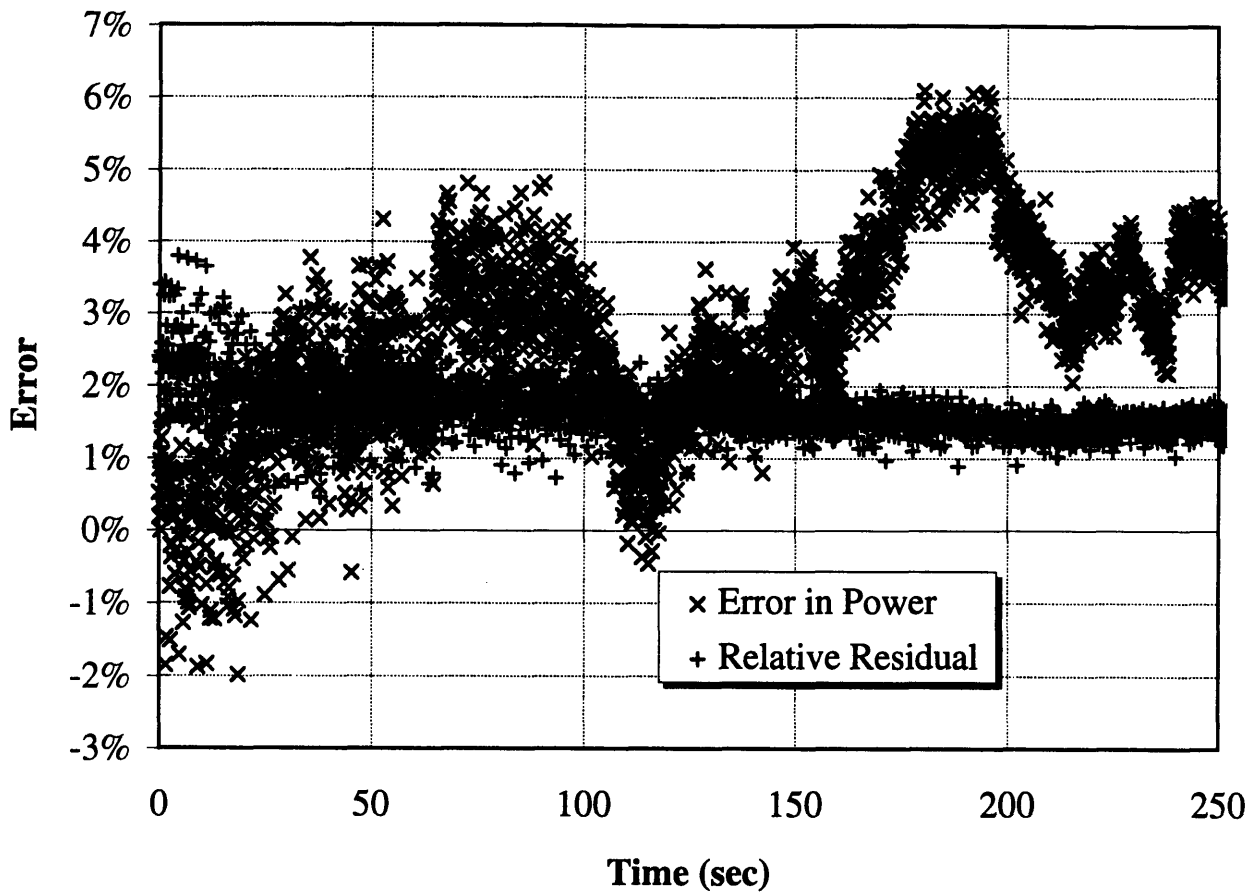


Figure 6.26 Relative Residual and Average Difference Between
 Synthesis Power and Normalized Detector Readings
 Shim Blade #6 Withdrawal - Core #110

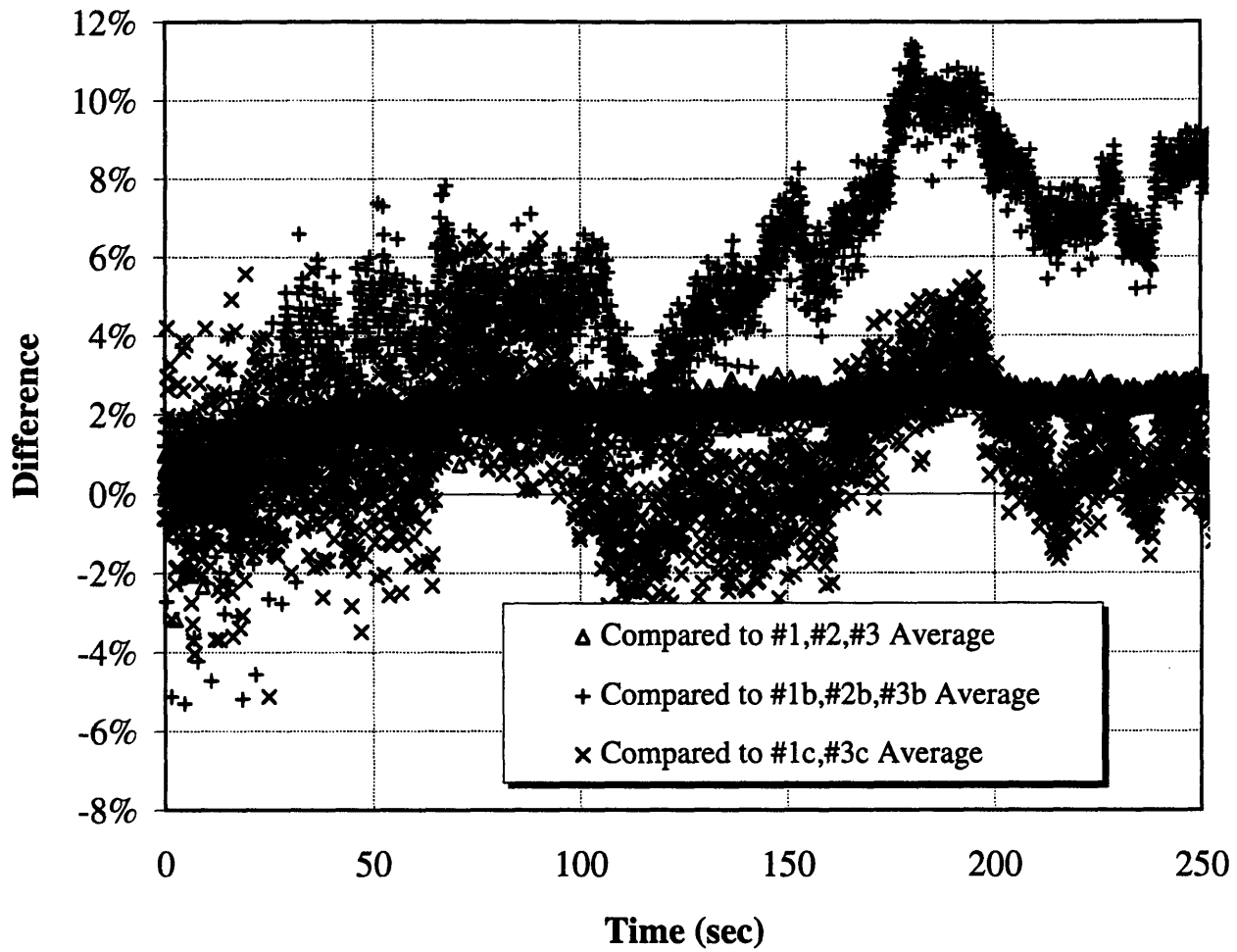


Figure 6.27 Difference Between Synthesis Power
and Normalized Detector Readings
Shim Blade #6 Insertion - Core #110

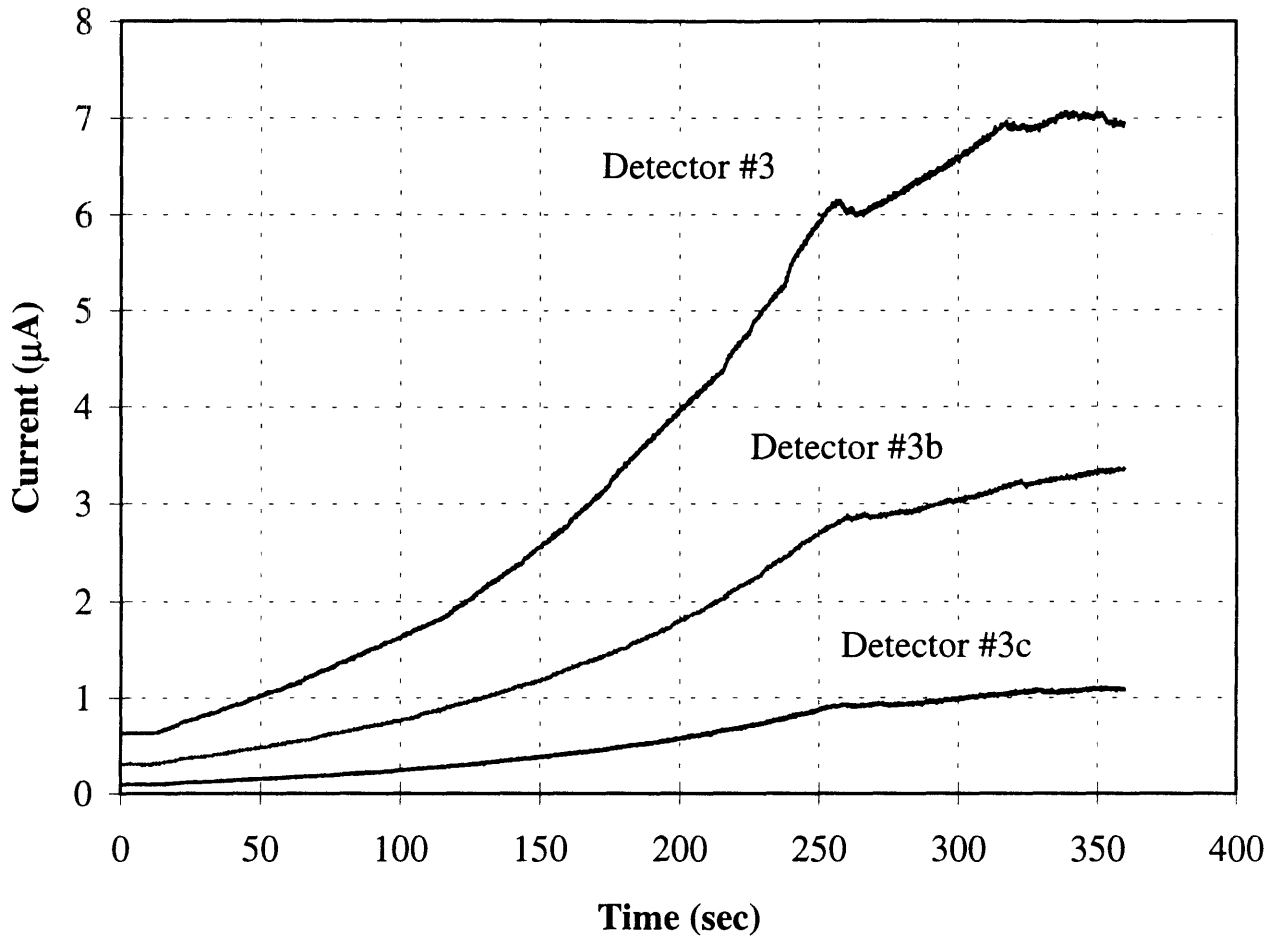


Figure 6.28 Detector Readings from Each of Three Trials
Shim Blade #6 Withdrawal - Core #110

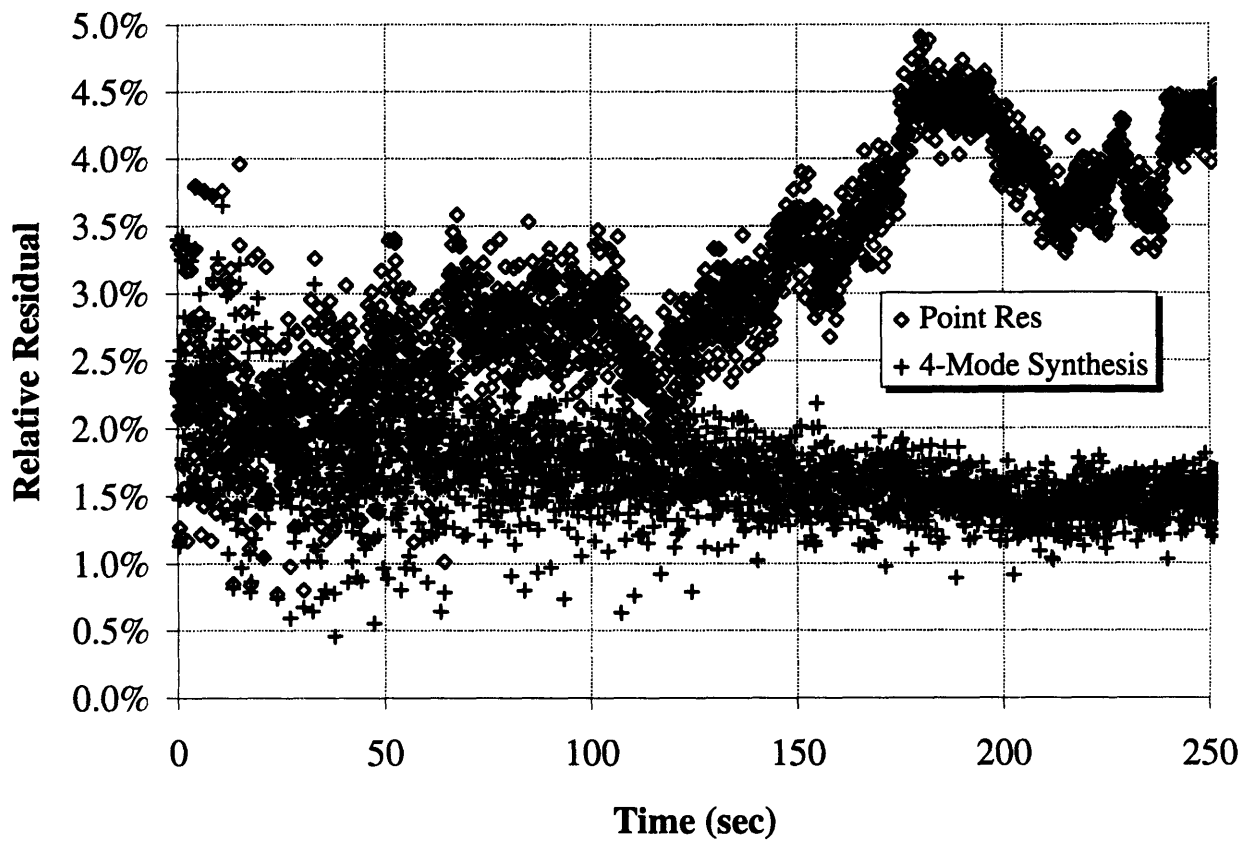


Figure 6.29 Comparison of Relative Residuals for Point Kinetics and Four Mode Synthesis
Shim Blade #6 Withdrawal - Core #110

Having reviewed this and the other transients, it is possible to revisit conclusions concerning the errors in the synthesis method. The synthesis method attempts to combine various shape functions to fit the count rates of a specified number of detectors. For the experimental evaluation, the transients were repeated three times such that measurements could be taken from each group of detectors. Each set of measurements are then assumed to have taken place during the same transient. Any inconsistencies between the transients are viewed by the method as changes in the flux shape. A low residual indicates that those changes are taken into account. The power that results from the synthesis, however, will also reflect those changes. This means that the power changes produced in one trial of the transient may not precisely match the power in another trial. The important issue, for purposes of evaluating the effectiveness of the method, is that the changes in shape are reflected. Were data to be taken simultaneously, the power would certainly match the conditions of the reactor. This has been seen in figures above in which the power determined by the synthesis closely matches power produced by at least one trial of a particular transient. It will also be seen in the last evaluation in Section 6.4.5.

As in the case for the blade insertion, we can also compare the blade withdrawal results to the QUARTZ prediction. The huge difference in power is due to the large overprediction of reactivity. This effect is exponential over time. But Figure 6.30 and Figure 6.31 again provide evidence that the synthesis method is able to effectively combine shape functions from theoretical predictions into a flux that properly reflects the changes in the physical system, even when the theoretical predictions themselves do not.

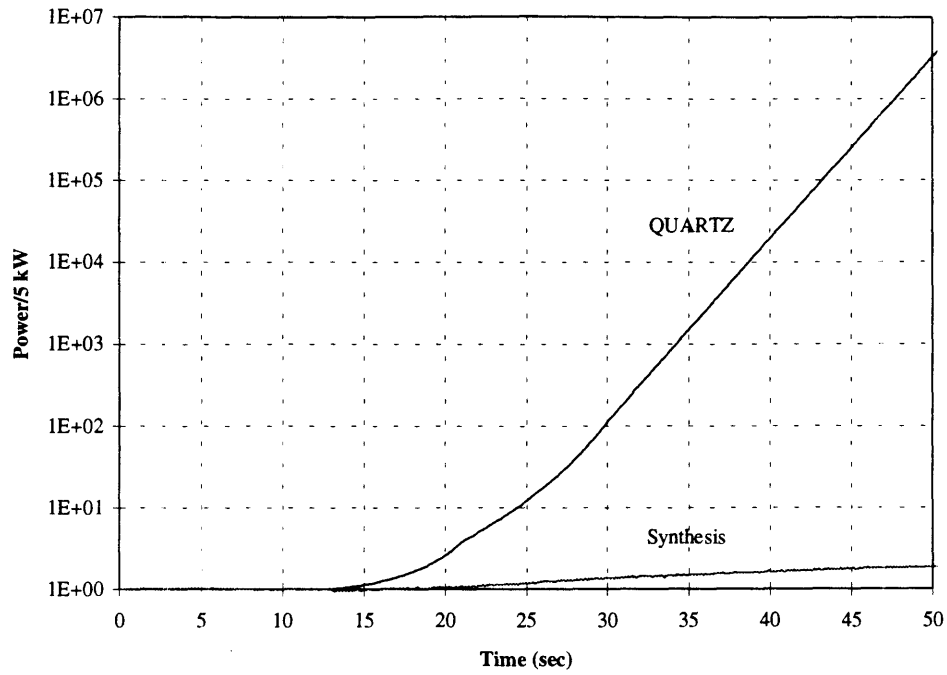


Figure 6.30. Synthesis Power Compared to QUARTZ Prediction
Shim Blade #6 Withdrawal - Core #106

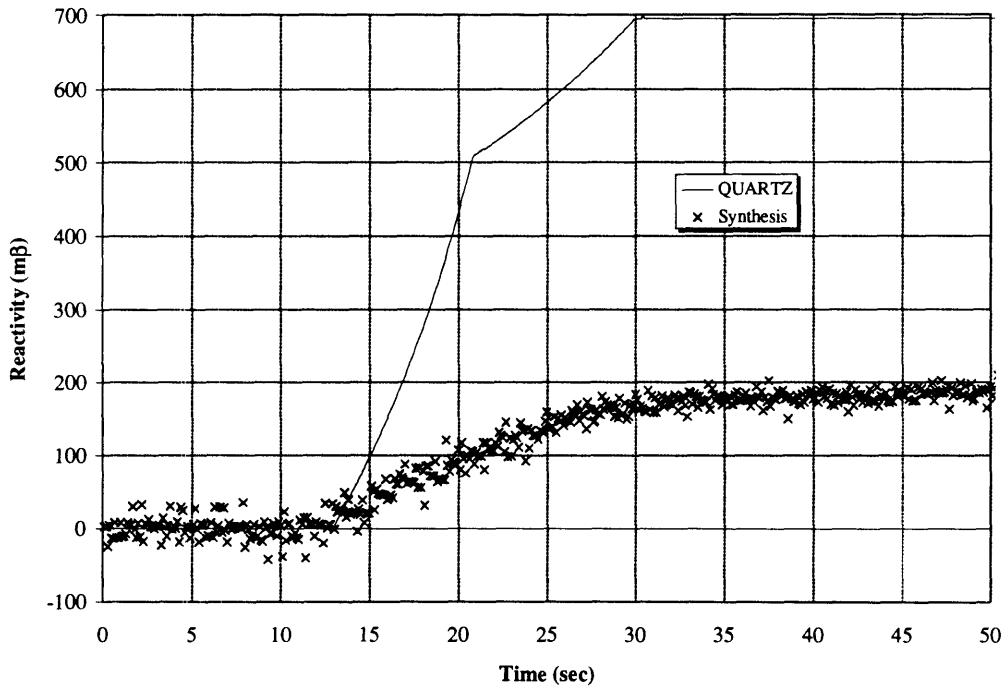


Figure 6.31. Synthesis Reactivity Compared to QUARTZ Prediction
Shim Blade #6 Withdrawal - Core #106

It has been explained in Chapter 2 and earlier in this chapter how the sensitivity of the synthesis method to noise is increased by the retention of more modes in the synthesized flux. By eliminating modes, this sensitivity is reduced. However, this may come at the expense of removing important information from the synthesis. Another option is to filter the detector readings themselves³. This option was attempted for the withdrawal of the shim blade #6, where a fading memory filter was used to smooth the detector measurements. The relative residual for the filtered counts is plotted in Figure 6.32. This can be compared to the residual given in Figure 6.23. As illustrated, the residual becomes smoother, but on average does not decrease. Similar results were obtained when the filter was used with other transients. This is in contrast to the results obtained by Jacqmin [J1]. There, the residual decreased significantly when the measurements were filtered. This may have to do with the nature of the analysis used. In the numerical evaluation, the correct flux was determined using QUANDRY and artificial noise added to this flux vector. In the experimental evaluation, the noise is intrinsically part of the measurement vector.

³ Filters for the instrumented synthesis method are explained in detail in Jacqmin's thesis [J1]

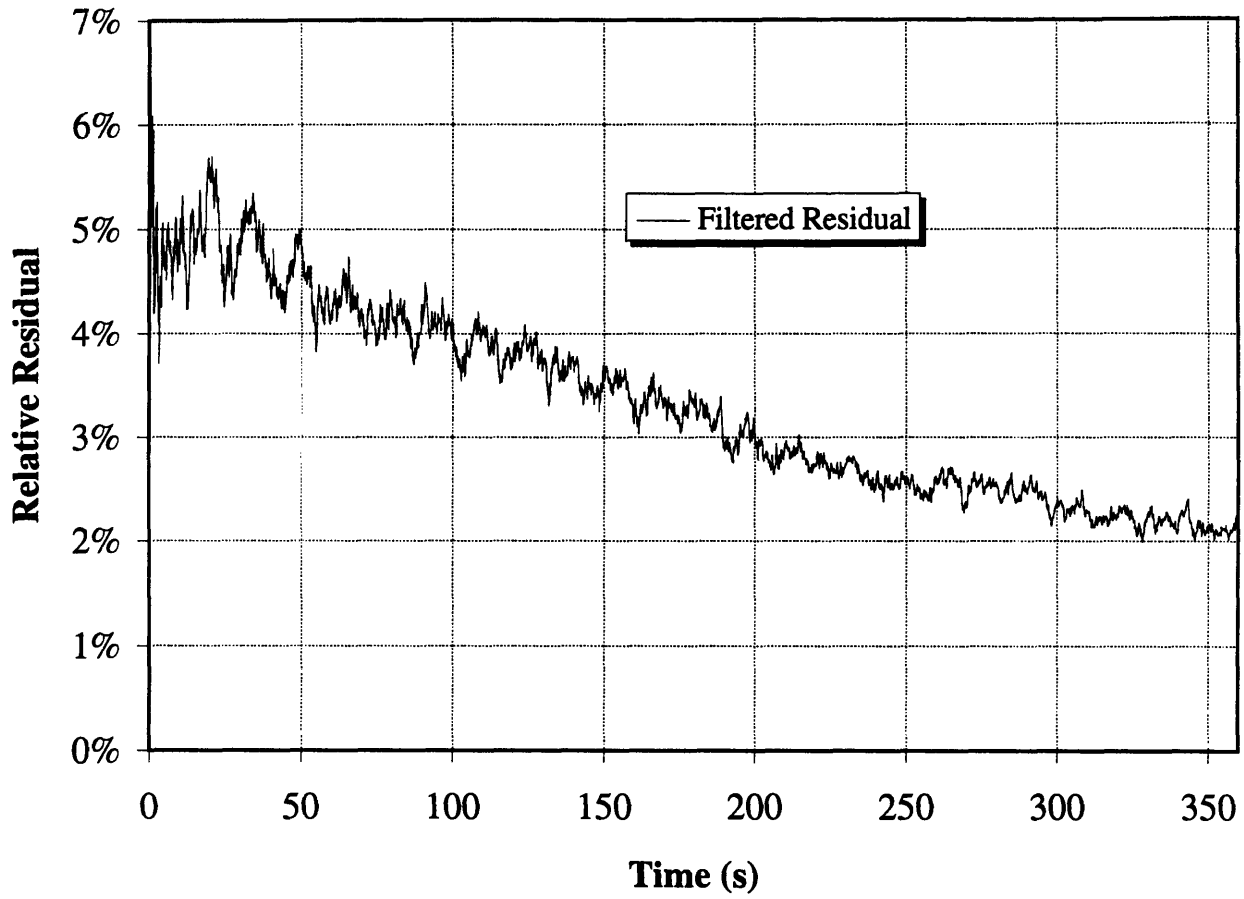


Figure 6.32 Residual for Filtered Detector Measurements
Shim Blade #6 Withdrawal - Core #106

6.5.5 SHIM BLADE #1 DROP - CORE #106

The final transient analyzed is the dropping of shim blade #1 into the core. In core #110, this immediately triggered a reactor scram. In core #106, the remaining blades remained at the critical shim bank height. It is this transient that will be analyzed.

Shape Function Number	Description
1	Shim Blades at 7.80", 10 kW
2	Shim Blades at 7.95", 50 kW
3	Shim Blades at 7.95", 10 kW Blade #1 dropped

Table 6.7. Shape Functions Shim Blade #1 Dropped - Core #106

This transient differs from the others in that the experiment was not repeated. Regulatory constraints prohibit the removal of the shim blade without a shutdown once it has been dropped into the reactor. For this reason, measurements from only three detectors, #2, #3, and #1b, are used. In order to maintain an overdetermined system, a maximum of two shape functions were used in the synthesis

By examining the relative residual in Figure 6.34, we see that it is low when two orthogonal modes are retained. The residual after the blade is dropped takes on a somewhat regular variation. Though the residual oscillates, it appears to do so between distinct values. This behavior may be explained by examining five seconds of the transient in detail. In Figure 6.35, the detector measurements are given between 30 and 35 seconds. What is seen are plateaus in the detector measurements followed by transitions

to the next discrete level. This behavior is the result of digital acquisition of the measurements at low power. The digital acquisition system will convert the current measurements into discrete numerical values. At low power, the change between these values is slow and distinct, resulting in plateaus between easily distinguishable transitions. When the values for the current change, the synthesis method will change the mixing coefficient magnitudes accordingly. At higher power levels, the digital signals appear much more continuous. At low power, however, the changes are between readily distinguishable discrete values. The resulting residual will, then, also change between discrete values, as evidenced in Figure 6.36. This regular behavior is lessened or eliminated when only one orthogonal mode is retained. In this case, the synthesis is attempting to reconstruct the flux in a least squares manner using only one mode. It cannot account as well for the changes in flux shape represented by the changing detector counts.

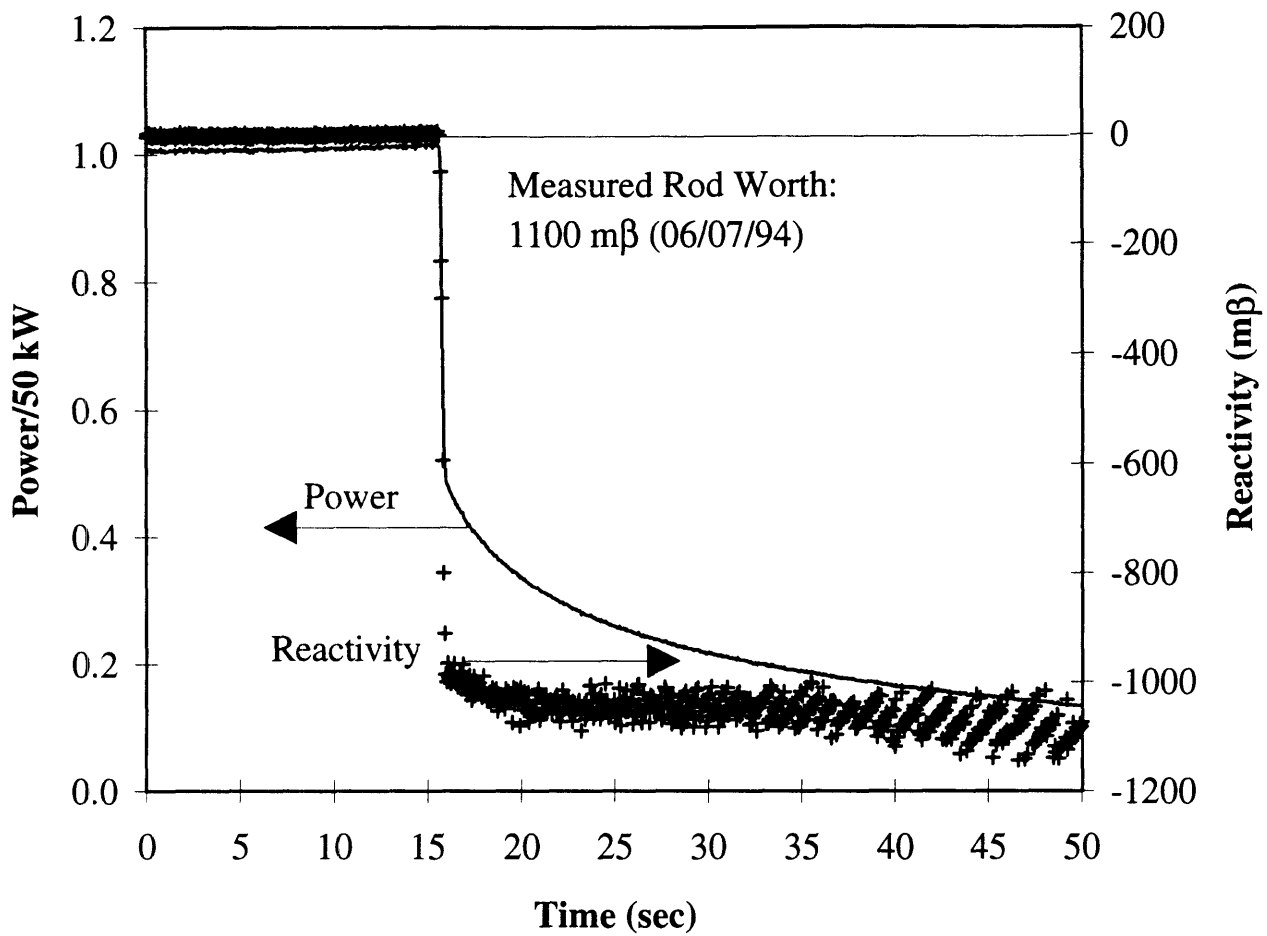


Figure 6.33 Power and Reactivity as Determined by Synthesis
Shim Blade #1 Drop - Core #106

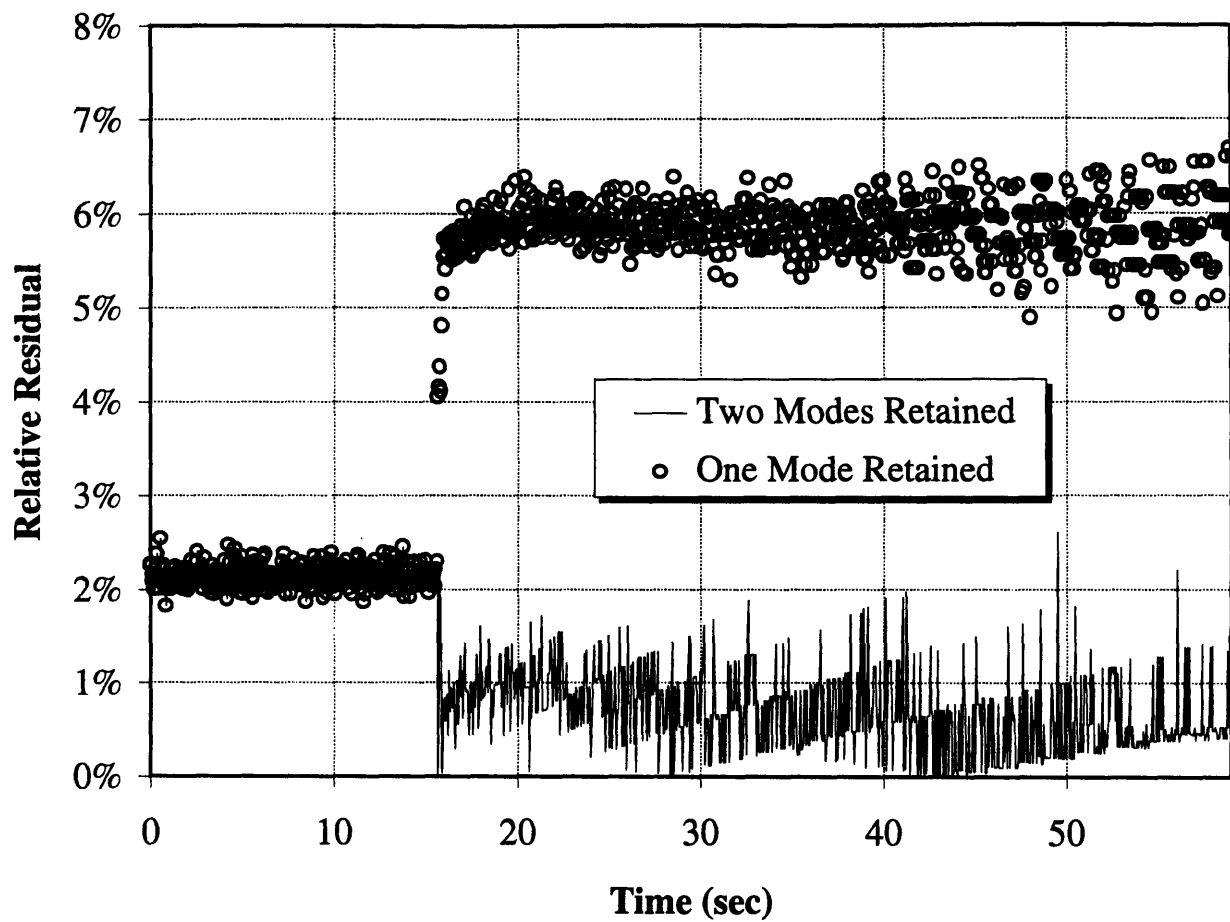


Figure 6.34 Relative Residual Retaining One and Two Modes
Shim Blade #1 Drop - Core #106

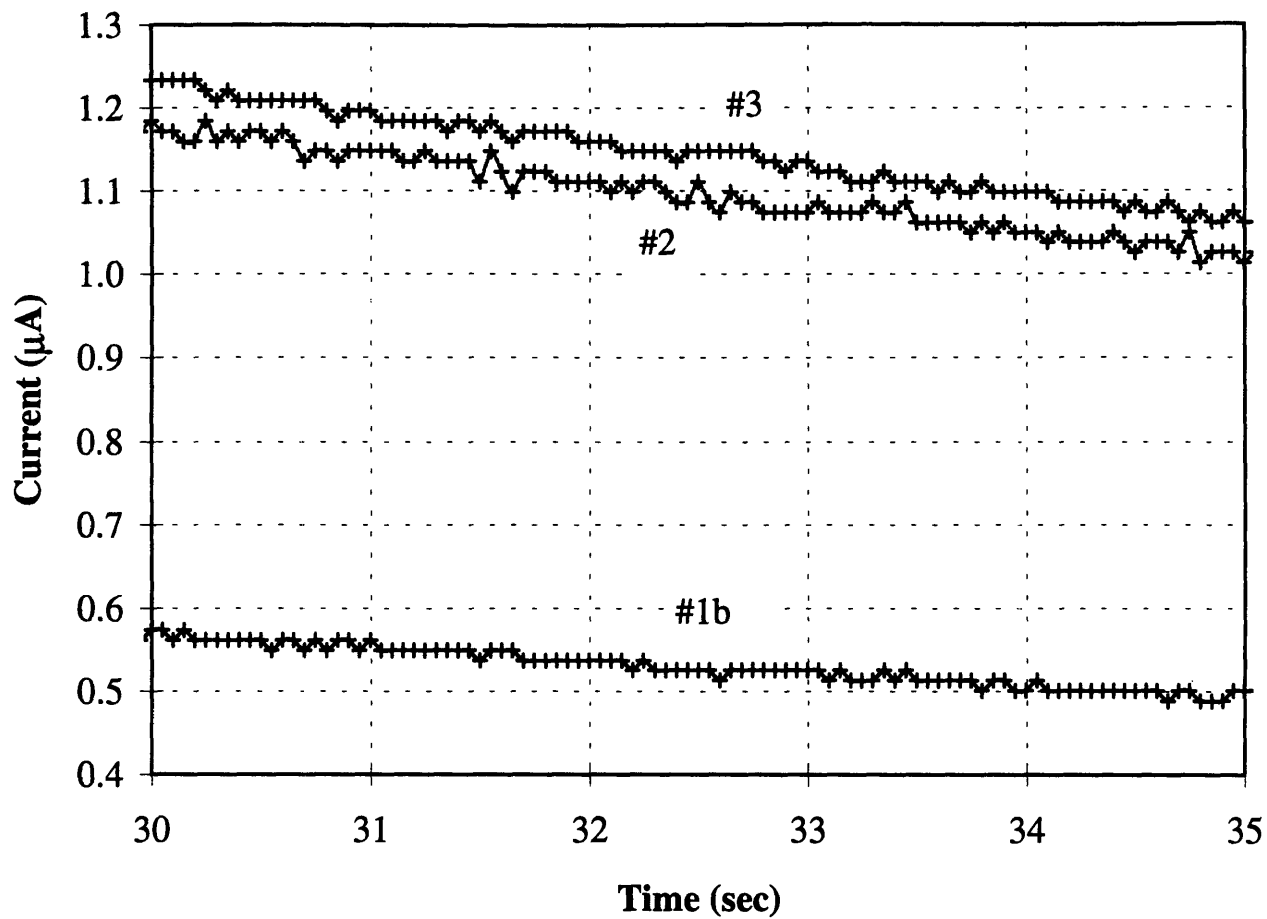


Figure 6.35 Detector Measurements After Blade Drop
Shim Blade #1 Drop - Core #106

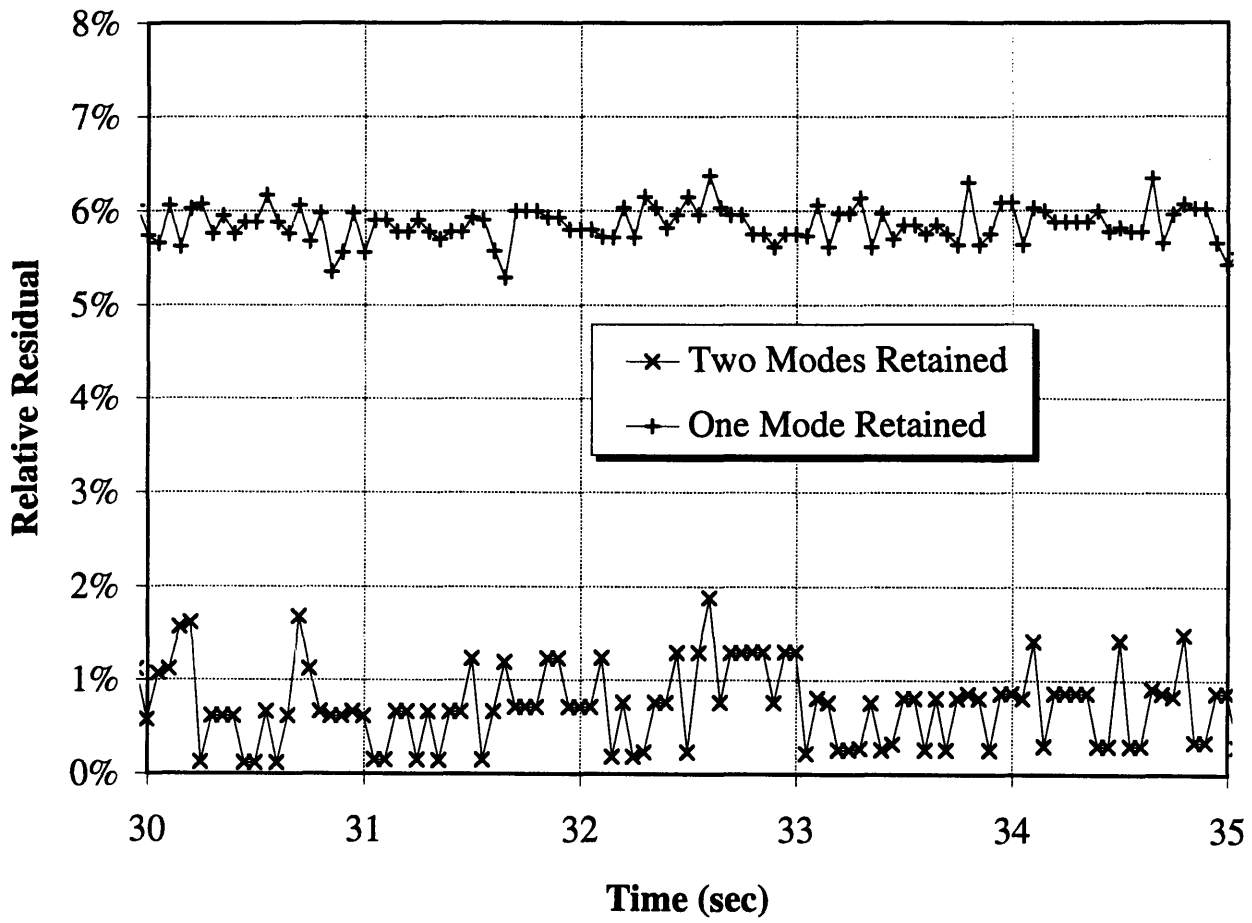


Figure 6.36 Relative Residual After Blade Drop
Shim Blade #1 Drop - Core #106

Although the residual for this analysis is quite low, it should be regarded with some caution. The residual is a valid assessment of the success of the synthesis only if the system is sufficiently overdetermined. For example, if three shape functions were to be used with the three detectors, the residual would be zero throughout the entire transient. However, the reconstructed flux may match the physical flux only at the detector locations. Only in a sufficiently overdetermined system does the residual serve as a good estimate of error. It is questionable whether three detectors and two shape functions qualifies as “overdetermined”.

What gives added confidence to the results are the low differences between normalized power and the normalized detector readings (Figure 6.37). For retaining two modes, the error in power remains low. This is especially encouraging considering that only three detectors were used. It is also important to note that the erratic changes in the power error found in evaluations where the experiment was repeated are not visible here.

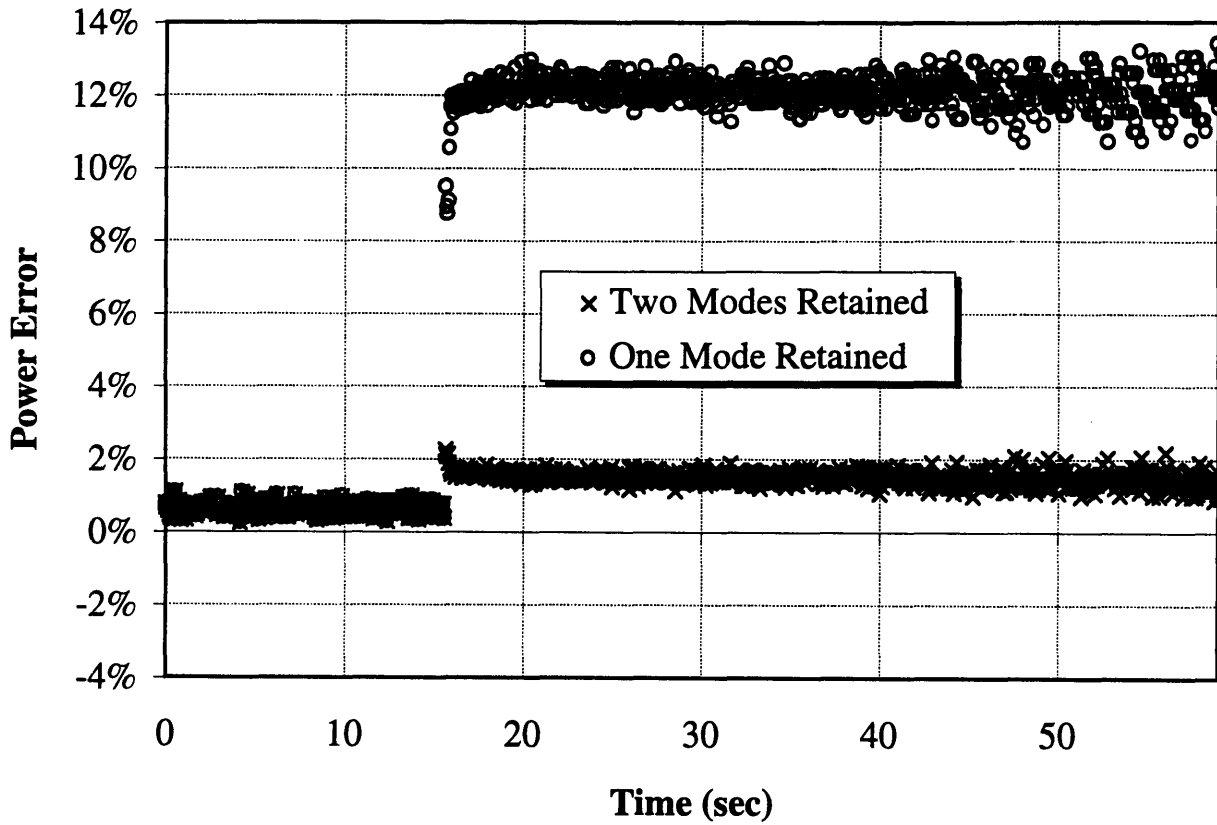


Figure 6.37 Difference Between Synthesis Power and Normalized Detector Readings, One and Two Modes Retained Shim Blade #1 Drop - Core #106

6.6 SUMMARY

The experimental evaluation of the synthesis method for several transient measurements has been presented in this chapter. Because of the way the detector responses are determined, the evaluation serves to show only whether the method is able to properly reflect changes in the reactor from some initial average condition. While this is not as satisfying as a prediction of the actual flux level, the essential feature of the method is validated through this method.

In the transients analyzed, the residual error was seen to be low. The erratic variations in power were seen to be caused by imperfect replication of the transients for different groups of detector measurements. The steady and low residuals show that these variations, seen by changes in flux shape by the synthesis method, are properly taken into account, giving a positive indication that the method can include such variations in its synthesized flux. The inclusion of a source term, unlikely to affect operation at higher powers in commercial plants, eliminated the unphysical increase in reactivity seen after blade insertions. The method was also seen to have lower residual errors than point kinetics evaluations.

The low errors bring with them the possibility of a more sophisticated reactivity meter. Even with flux shapes that individually did not replicate the flux shape in the core at all points, the synthesis method provided a way of determining reactivity that is superior to the point kinetics method. The meter could be used in the control room by an operator to accurately assess the reactivity in the core in real time.

There are, of course, shortcomings in the evaluation, having mainly to do with the detector response and flux shape issue. Were the detector responses to be known absolutely, or the flux shapes known to be sufficiently accurate throughout the core, the evaluation could be expanded to include correct predictions of the actual flux level throughout the core. The small number and placement of the detectors also places some restriction upon the robustness of the evaluation. However, the main expectations for the method, the ability to properly account for changes in reactor condition and compute power and reactivity based upon these changes, seem to have been realized. The results should be combined with Jacqmin's numerical evaluation for a more complete picture of the method.

Finally, it should be noted that all the synthesis calculations were determined faster than real time. The computations were made under somewhat idealized circumstances. Few detectors and shape functions resulted in small matrices for use in the singular value decomposition method. There were also few discontinuities when the shape functions were altered. However, the calculations were performed on a personal computer with no multi-tasking capability. A sufficiently optimized code used on a dedicated workstation should easily be able to maintain real time speed.

Chapter 7

Conclusion

7.1 SUMMARY OF RESULTS

In the previous chapters, the results of several topics associated with the experimental evaluation of the Instrumented Flux Synthesis Method have been presented. They are summarized here, along with conclusions and recommendations for future research

- The QUARTZ code was modified to allow fine-mesh results to be collapsed to a coarse-mesh structure. Discontinuity factors were generated for both Coarse Mesh Finite Difference (CMFD) and quadratic approximations to the current. Discontinuity factors for the large mesh problem were generated independently of the method used to solve the fine mesh problem. Both large node methods were shown to match very

closely the results of fine mesh calculations. The CMFD results were generally closer than the quadratic results to the fine mesh calculation.

- The QUARTZ code was corrected to allow the adjoint flux to be correctly determined for cases in which the discontinuity factor ratios were not unity.
- A subroutine was added to implement the Aragoes and Ahnert scheme of guaranteeing convergence of the inner iterations in a CMFD-like solution scheme. This is accomplished by assuring that all discontinuity factor ratios are positive by changing the diffusion coefficients. The quadratic solution uses the CMFD-like equations through the non-linear iteration method. The convergence scheme did not, however, assure convergence of the quadratic solution. There does not yet exist a mathematical condition that assure convergence of the non-linear iteration scheme.
- Flux measurements were taken from the MITR-II core using fission chambers placed in water vent holes at the periphery of the core. The measurements were made during various static and transient conditions in two different cores.
- A model of the MITR-II core was developed using the QUARTZ code. The flux was seen to be generally in agreement flux predictions derived from a MCNP model of the core. However, near the bottom of the core in the C-ring, and in the A-ring near the top of the core, there are significant differences.
- A possible revised fuel management scheme for the MITR was presented.
- The flux shapes were combined with measurements taken from the core to synthesize a flux according to the instrumented flux synthesis method. The detectors responses were determined by normalizing them to predictions of the flux taken from the

QUARTZ model. This restricts the evaluation to only being able to determine whether the synthesis method can account for changes in the flux shape and amplitude from some initial condition.

- The flux synthesis method was shown to accurately reflect changes in the core condition, as well as determine power and reactivity in the core. Errors in the power were often attributable to inconsistent reproduction of transients used to provide flux measurements. The method was shown to be superior to point kinetics in terms of accounting for changes in flux shapes in its determination of reactivity.
- The experimental data were compared to the synthesis results as well as QUARTZ transient calculation results. The synthesis results were in good agreement with experimental data, while the QUARTZ results were not. Despite incorrect transient predictions by the QUARTZ model, the synthesis method was able to correctly combine static flux shapes taken from the model to reflect the transient conditions.

7.2 CONCLUSIONS

The instrumented flux synthesis method has been shown to be an effective tool in accurately determining changes in reactor conditions. Despite the fact that the flux shapes used in the method did not precisely predict conditions in the core, linear combinations of them were shown to, at the very least, accurately reflect changes in core conditions. Examination of the residuals showed them to be low and steady, even when the transient was not precisely replicated from one measurement to the next.

These accurate combinations of flux shapes enable reactivity to be predicted more accurately than using a single, unchanging flux shape. The lower residuals found with using the synthesis method show that the flux shape did indeed change during the several transients, and that the shape change was reflected in the synthesized flux. This leads to a more accurate reactivity calculation. This calculation would be improved with the accurate determination of the time behavior of the photoneutron source.

The modifications of the QUARTZ code were also seen to work well. A consistent issue with the quadratic approximation of the current has been the influence of the boundary conditions on the current determination. This seems to have affected the supernodal analyses as well. When a zero current boundary condition is used, the quadratic results match the fine mesh results as well as the CMFD calculations. When there is a current at the boundary, however, the CMFD calculation usually seems to match the reference more closely. However, the general conclusion is that the new routines are working properly and consistently.

The convergence subroutine, although not helpful in the particular case of analyzing the MITR, should allow problems not previously solvable to be analyzed. The corrected adjoint also allows the quadratic method to be used in transient analyses with the adjoint flux as a weighting function.

The differences between the QUARTZ transient predictions and the actual results come from the model, not the QUARTZ code itself. With improvements in the model, the code should be able to accurately predict MITR conditions.

7.3 RECOMMENDATIONS FOR FUTURE RESEARCH

The intention of the instrumented flux synthesis method has been to serve as the backbone of an automated control system. Such a system could determine power level and reactivity in an accurate manner in real time by incorporating changes in flux shape. With the numerical and experimental evaluations completed, the next step would be work on an actual controller. Such a controller could be tested in the MITR provided sufficient instrumentation was added. It is strongly recommended that work in this direction be pursued.

For application as a controller, more accurate flux shapes should be synthesized. The QUARTZ model can be improved to eliminate differences between it and the MCNP model by re-examining some of the material specifications in the input. It would also be advisable to reduce the dependence of the model on the boundary conditions by expanding the heavy water reflector and performing the analyses on a computer with larger run-time memory. Such computers, though more expensive than PCs, are currently available and can be used on a desktop.

There is currently renewed work by Redmond on generating cross sections using MCNP [R3]. Since an accurate model of the MITR already exists using the MCNP code, such a capability would provide an excellent source of cross section data for use in the QUARTZ code. Transient analyses, possibly incorporating McGuire's thermal-hydraulic model of the MITR core [M1], could be easily and accurately performed.

With an improved QUARTZ model, the code could be used as part of the MITR fuel management program. An outline for such a modified program is given at the end of Chapter 5.

The convergence of the non-linear iteration method employed in the quadratic solution in QUARTZ continues to be somewhat of a mystery. The QUARTZ code was modified for this project to include convergence “guarantees” for the CMFD-like equations used in the quadratic solution. Though these should improve the convergence for most situations, they did not prevent the MITR model from eventually diverging, albeit after a larger number of iterations. A thorough investigation of the convergence properties is strongly recommended.

REFERENCES

- [A-1] J.M. Aragones, C. Ahnert "A Linear Discontinuous Finite Difference Formulation for Synthetic Coarse-Mesh Few-Group Diffusion Calculations," *Nuclear Science and Engineering*, **94**, 309-322 (1986)
- [B-1] A. Ben-Israel, *Generalized Inverses: Theory and Applications*, Krieger, Huntington, NY (1980)
- [B-2] J.F. Briefmeister, Ed., "MCNP - A General Monte Carlo N-Particle Transport Code, Version 4A," LA-12625-M (1993)
- [B-3] M.E. Byers "A Transient Nodal Method for Reactor Models in R-Z Geometry," Ph.D. Thesis, Department of Nuclear Engineering, Massachusetts Institute of Technology (August, 1992)
- [B-4] J.A. Bernard, "MITR-II Fuel Management, Core Depletion, and Analysis: Codes Developed for the Diffusion Theory Program CITATION," Nuclear Engineer's Thesis, Department of Nuclear Engineering, Massachusetts Institute of Technology (June, 1979)
- [B-5] J.A. Bernard, D.D. Lanning "Considerations in the Design and Implementation of Control Laws for the Digital Operation of Research Reactors," *Nuclear Science and Engineering*, **110**, 425-444 (1992)
- [D-1] DeLorey, Thomas "A Transient, Quadratic Nodal Method for Triangular-Z Geometry," Ph.D. Thesis, Department of Nuclear Engineering, Massachusetts Institute of Technology (June, 1993)
- [D-2] J.J. Duderstadt, L.J. Hamilton, *Nuclear Reactor Analysis*, John Wiley and Sons, New York, NY (1976)
- [F-1] T.B. Fowler, D.R. Vondy, G.W. Cunningham, "Nuclear Reactor Core Analysis Code: CITATION," ORNL-TM-2496, Rev. 2 (1971)
- [G-1] G.H. Golub, C.F. Van Loan, *Matrix Computations*, Johns-Hopkins University Press, Baltimore, MD (1989)
- [G-2] J.C. Gehin "A Nodal Method for the Solution of the Static, Few Group Diffusion Equations in Hexagonal Geometry," Ph.D. Thesis, Department of Nuclear Engineering, Massachusetts Institute of Technology (September, 1992)
- [G-3] J. Gherchanoc "Supernodal Procedures for Transient Analysis," Final Project Report, Department of Nuclear Engineering, Massachusetts Institute of Technology (December, 1994)

- [H-1] A.F. Henry *Nuclear-Reactor Analysis* MIT Press, Cambridge, MA (1975)
- [J-1] R.P. Jacqmin “A Semi-Experimental Nodal Synthesis Method for the On-Line Reconstruction of Three Dimensional Neutron Flux-Shapes and Reactivity,” Ph.D. Thesis, Department of Nuclear Engineering, Massachusetts Institute of Technology (September, 1991)
- [K-1] K. Koebke, “Advances in Homogenization and Dehomogenization,” *Proc. Int. Topl. Mtg. Advances in Mathematical Methods for the Solution of Nuclear Engineering Problems*, Munich, Germany, **2**, 59 (1981)
- [K-2] W.S. Kuo “The General Evaluation of the Nodal Synthesis Method in Nuclear Reactor Transient Analysis,” Ph.D. Thesis, Department of Nuclear Engineering, Massachusetts Institute of Technology (December, 1993)
- [K-3] W.S. Kiger Master’s Thesis, work in progress, Department of Nuclear Engineering, Massachusetts Institute of Technology
- [M-1] M.J. McGuire “An Analysis of the Proposed MITR-III Core to Establish Thermal-Hydraulic Limits at 10 MW” Ph.D. Thesis, Department of Nuclear Engineering, Massachusetts Institute of Technology (June, 1995)
- [N-1] S. Nakamura *Computational Methods in Engineering and Science*
- [R-1] E.L. Redmond, J.C. Yanch, and O.K. Harling “Monte Carlo Simulation of the Massachusetts Institute of Technology Research Reactor” *Nuclear Technology*, **106**, (1994)
- [R-2] E.L. Redmond “The MCNP Model of the MITR-II: A User’s Guide” (September, 1991)
- [R-3] E.L. Redmond Ph.D. thesis, work in progress, Department of Nuclear Engineering, Massachusetts Institute of Technology
- [S-1] G.Strang *Introduction to Applied Mathematics* Wellesley-Cambridge Press, Wellesley, MA (1986)
- [S-2] Smith, K.S. “An Analytic Nodal Method for Solving the Two Group, Multidimensional, Static and Transient Neutron Diffusion Equations,” Nuclear Engineer’s Thesis, Department of Nuclear Engineering, Massachusetts Institute of Technology (March, 1979)
- [S-3] K.S. Smith “Nodal Method Storage Reduction by Non-linear Iteration,” *Trans. Am. Nucl. Soc.* **44**, 265 (1983)

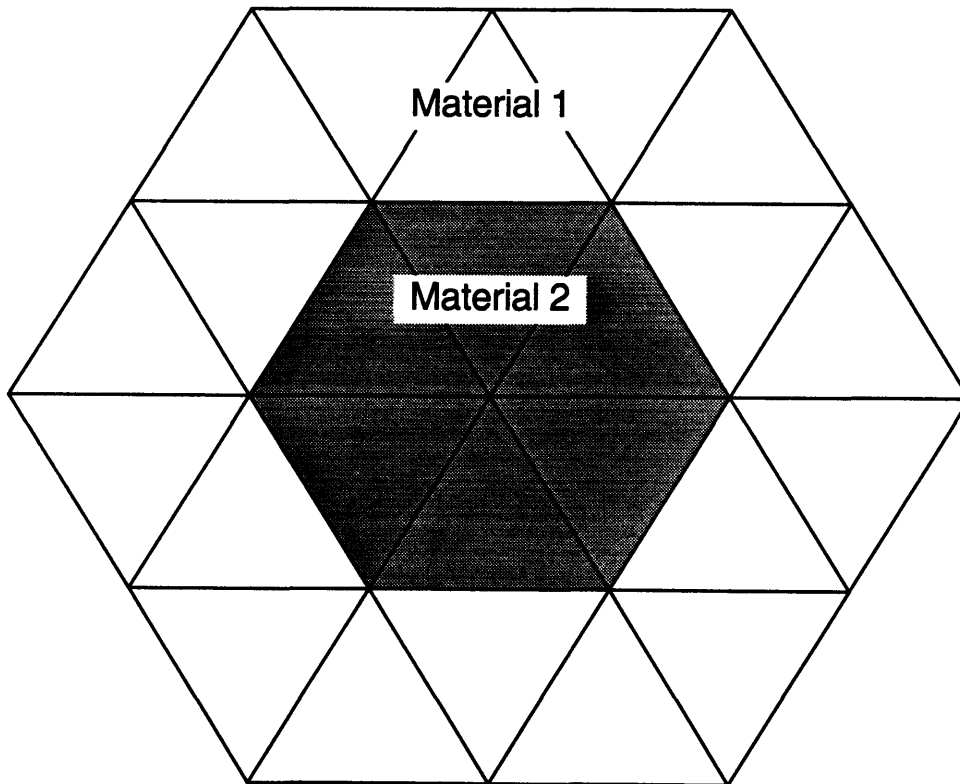
[S-4] L.C. Selby “Experimental Evaluation of an Instrumented Synthesis Method for the Real-Time Estimation of Reactivity” Nuclear Engineer’s Thesis, Department of Nuclear Engineering, Massachusetts Institute of Technology (June, 1993)

[V-1] R.S. Varga, *Matrix Iterative Analysis*, Prentice-Hall, Englewoods Cliffs, NJ (1962)

APPENDIX 1

SUPERNODAL TEST MODEL [Ref. D1]

The following test model is taken from the quadratic test case used by DeLorey. The nodes are subdivided, then recollapsed to test the supernodal case. Although the cross sections developed by the supernodal process are flux weighted, there is no mixture of material #1 and material #2 in any of the larger nodes. Thus the supernodal cross sections will be the same as the fine mesh cross sections. For the homogeneous cases, both regions are given the specifications of Material 1.



MATERIAL 1

D_g	χ_g	$\Sigma_{f,g}$	$\nu\Sigma_{f,g}$	Σ_g	$\Sigma_{gg'}$
1.49750×10^0	1.00000×10^0	1.38519×10^{-4}	3.46297×10^{-4}	3.32021×10^{-3}	$\Sigma_{21} 2.37634 \times 10^{-3}$
1.15689×10^0	0.00000×10^0	2.35888×10^{-3}	5.89720×10^{-3}	3.37634×10^{-3}	$\Sigma_{12} 0.00000 \times 10^0$

MATERIAL 2

D_g	χ_g	$\Sigma_{f,g}$	$\nu\Sigma_{f,g}$	Σ_g	$\Sigma_{gg'}$
1.27288×10^0	1.00000×10^0	1.24667×10^{-4}	3.11667×10^{-4}	4.15026×10^{-3}	$\Sigma_{21} 2.47634 \times 10^{-3}$
9.83360×10^{-1}	0.00000×10^0	2.12299×10^{-3}	5.30748×10^{-3}	4.22043×10^{-3}	$\Sigma_{12} 0.00000 \times 10^0$

OTHER DATA

- Length of Node Side:

Reference: 4.2363 cm
 Supernodal: 67.7805 cm

- Boundary Conditions

Case I Albedo (No Net Returning Current)
 Case II Zero Flux
 Case III Zero Current

APPENDIX 2

NUMBER DENSITIES

This appendix lists the number densities used in the QUARTZ model of the reactor. The specifications are taken from the `core106.inp` file. Each material uses microscopic cross section data from the CITATION model of the reactor. Listed below are the number densities for the structural materials used in the model. Each of the 33 materials consists of a title card, a card stating the number of materials used to make up the composition, and the material number followed by its number density (in #/barn-cm). The number densities are changed from the nominal number densities to account for changes in the geometry of the reactor model.

```
[Composition 1] Heavy Water
1
21 3.33200E-02
[Composition 2] Beam Port A
2
38 6.26500E-03 21 5.85800E-03
[Composition 3] Core Tank + H2O + Beam Port
3
38 1.21300E-02 23 9.43400E-03 21 4.29900E-03
[Composition 4] Beam Port B
2
38 4.60200E-03 21 1.78900E-02
[Composition 5] Core Tank+D2O+H2O
3
34 7.53000E-03 23 9.43400E-03 21 1.97300E-02
[Composition 6] Core Tank Edge+D2O
2
43 6.43400E-03 21 1.76326E-02
[Composition 7] Core Tank Edge+Beam Port
2
34 1.10400E-02 21 4.29900E-03
[Composition 8] Core Tank Edge
1
43 1.57800E-02
[Composition 9] Hex Material
1
```

36 4.26600E-02
[Composition 10] Hex Material + H2O
2
36 3.46600E-02 14 6.25100E-03
[Composition 11] Light Water Coolant in Inlet
1
47 2.96000E-02
[Composition 12] Fuel End Caps + H2O
2
32 2.70500E-02 33 1.13600E-02
[Composition 13] Fuel End Caps + Al + D2O
3
32 2.08000E-02 33 1.88900E-02 21 2.80300E-03
[Composition 14] Control Blades Inserted, nominal Boron
1
40 2.79956E-04
[Composition 15] Control Blades Withdrawn
2
47 1.69400E-02 36 2.04100E-02
[Composition 16] Control Blades 20% inserted
3
40 5.59912E-05 36 1.63280E-02 47 1.35520E-02
[Composition 17] Spider Material, arms, top
1
36 1.53700E-02
[Composition 18] Flow Holes with Water
2
47 1.16400E-02 43 1.17500E-02
[Composition 19] Flow holes with Reg Rod
3
32 7.10100E-03 45 1.64588E-03 35 2.31026E-02
[Composition 20] Flow Holes with Al Tubes
2
47 8.73100E-03 43 1.82800E-02
[Composition 21] Stainless Steel Spider Inserts
1
52 2.21400E-02
[Composition 22] Spider Material + Grid Plate
2
32 3.12700E-02 33 1.95600E-02
[Composition 23] Spider Inserts + Grid Plate
2
32 9.89100E-03 35 1.60800E-02
[Composition 24] H2O + Al
2
48 2.70900E-02 36 1.13000E-02
[Composition 25] Fuel End Caps + Grid
2
32 2.39300E-02 33 1.70100E-02
[Composition 26] Outside Shroud
2
48 1.45800E-02 36 3.38900E-02
[Composition 27] Inside Shroud
2


```

48 2.39600E-02  36 1.69500E-02
[Composition 28] Aluminum Dummy Element
1
11 5.45100E-02
[Composition 29] Control Blades 85% inserted
3
40 2.37963E-04  36 3.06150E-03  47 2.54100E-03
[Composition 30] Control Blades 70.9% inserted
3
40 1.98489E-04  36 5.93931E-03  47 4.92954E-03
[Composition 31] Spider, Arms & Hex, Bottom
1
38 1.64900E-02
[Composition 32] Water & Al Spider Inserts
2
36 1.01300E-02  14 3.37100E-02
[Composition 33] Control Blades 5.03% inserted
3
40 1.40818E-05  36 1.93834E-02  47 1.60879E-02

```

The fuel number densities are embedded in the DECK code itself, with the exception of U^{235} , which is read from kwandens .XXX, where XXX is the core designation. To change these number densities, the source listing of DECK must be changed. Two options are given in the code. The explanation of the fuel number densities, given below, is taken directly from the DECK source code listing.

```

c.fudge accounts for the difference in volumes between a
c real fuel element (2402 cm3) and the quartz model
c (2655 cm3)
c
      fudge = 2402.41383/2655.182
c
c MCNP (ELRedmond) values for number densities
c The 1.030382 factor is used to account for the difference
c in the MCNP definition of the fuel element, which
c is 6.9921 cm to a side, and the QUARTZ definition of a
c fuel element location which is 7.091847 cm. The
c difference between the two is taken
c up by water. This is consistent with drawings.
c
c
      c238=3.93773E-05
      ncool=1.60743E-02*1.030382
      nal=2.85546E-02

```

```

C
C     CITATION values for number densities
C
C     c238=3.35900E-05
C     ncool=1.54500E-02
C     nal=3.18300E-02
C
C     c238=c238*fudge
C     ncool=ncool*fudge
C     nal=nal*fudge
C
C fudge multiplied by 60.96/56.8325 to convert DEPCODE 24"
C core to actual 22.375" core.  The 2402/2655 ratio then
C converts this actual element to the QUARTZ model of the
C element
C
C further adjust the fudge factor to match CITATION U235
C mass results
C core 106: A-ring fudge: 1.007, B-,C-ring fudge: 1.009
C core 110: A-ring fudge: 0.9965 B-,C-ring fudge: 1.004
C
C     fudge = fudge*(60.96/56.8325)
C
C     if (fe(i).le.3) then
C         fudge=fudge*1.007
C     else
C         fudge=fudge*1.009
C     endif

```

It is recommended that the MCNP number densities be used instead of the CITATION densities. The MCNP number densities are taken directly from design data, and appear to have more of a physical basis.

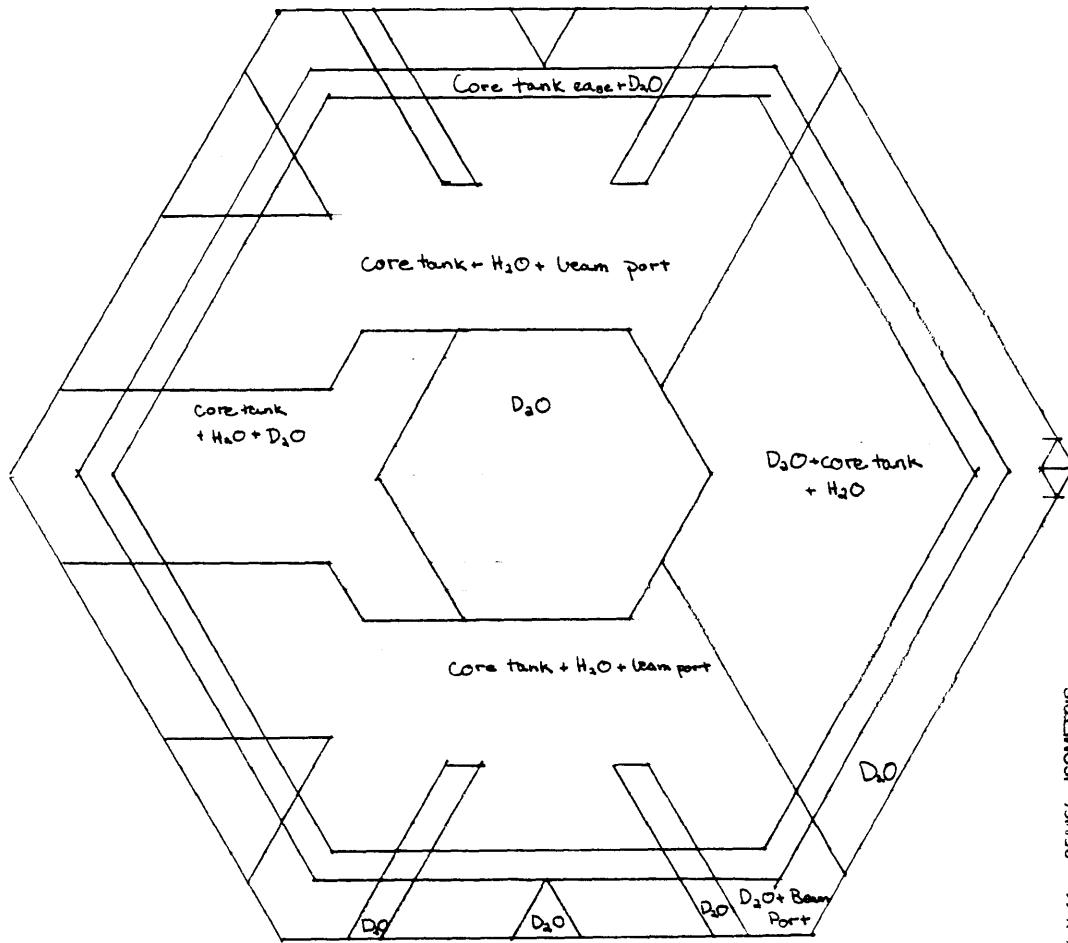
APPENDIX 3

QUARTZ MODEL OF MITR

The layout of the QUARTZ model of the MITR is given on the following pages. The model is drawn on a triangular mesh to enable users to see the location of all the materials in the triangular scheme.

The final graph is an example of the coarse mesh scheme. It is laid over the fine mesh model to illustrate which materials are homogenized into a given large node.

Plane 1

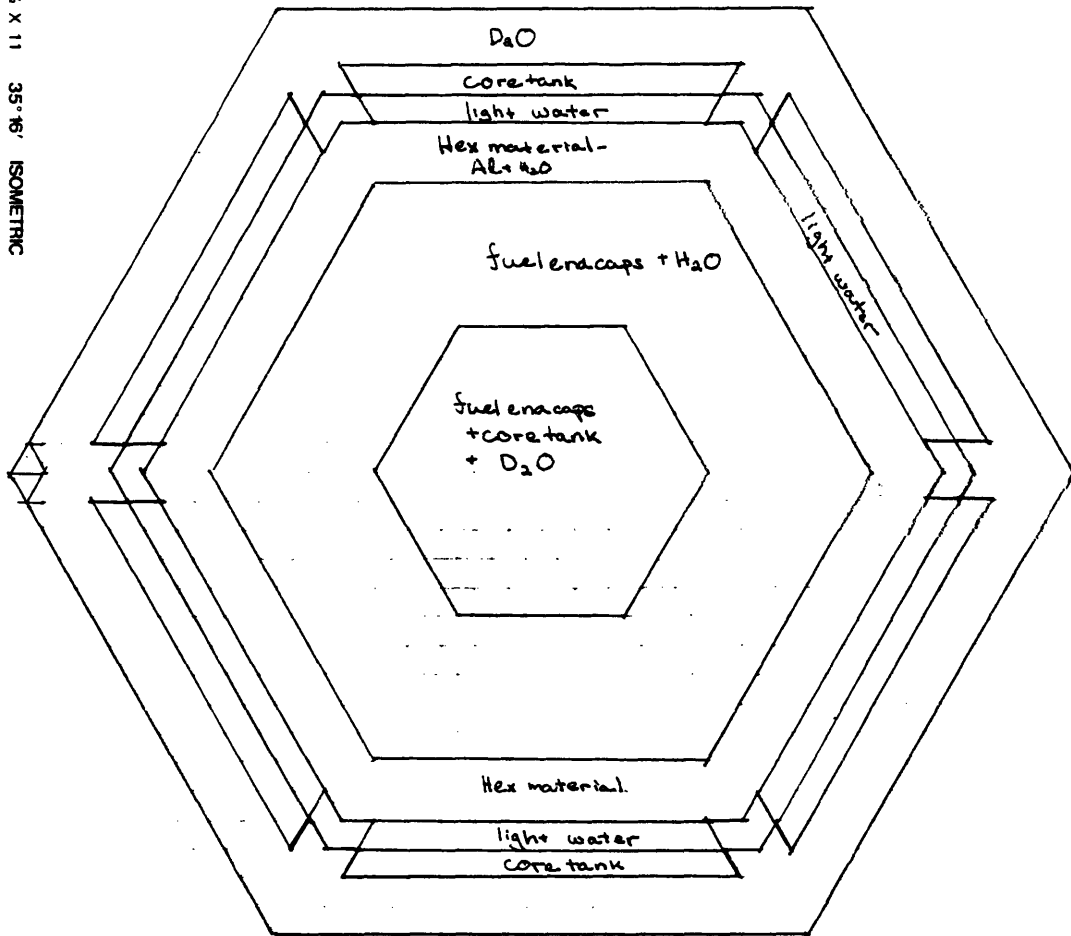


ALVIN
NO. 1242 - 8 1/2 X 11 35° 16' ISOMETRIC

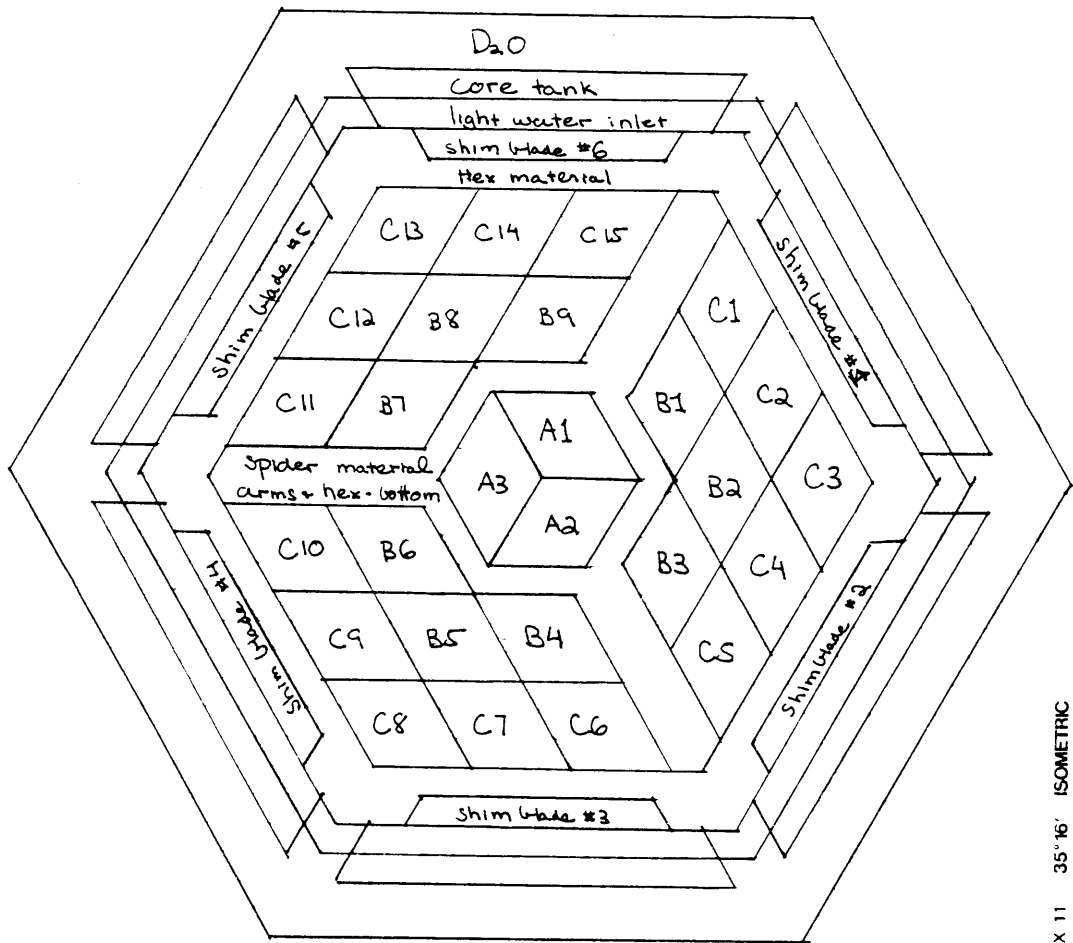


NO. 1242 - 8 1/2 X 11 35° 45' ISOMETRIC

Plane 2



Planes 3, 4, 5



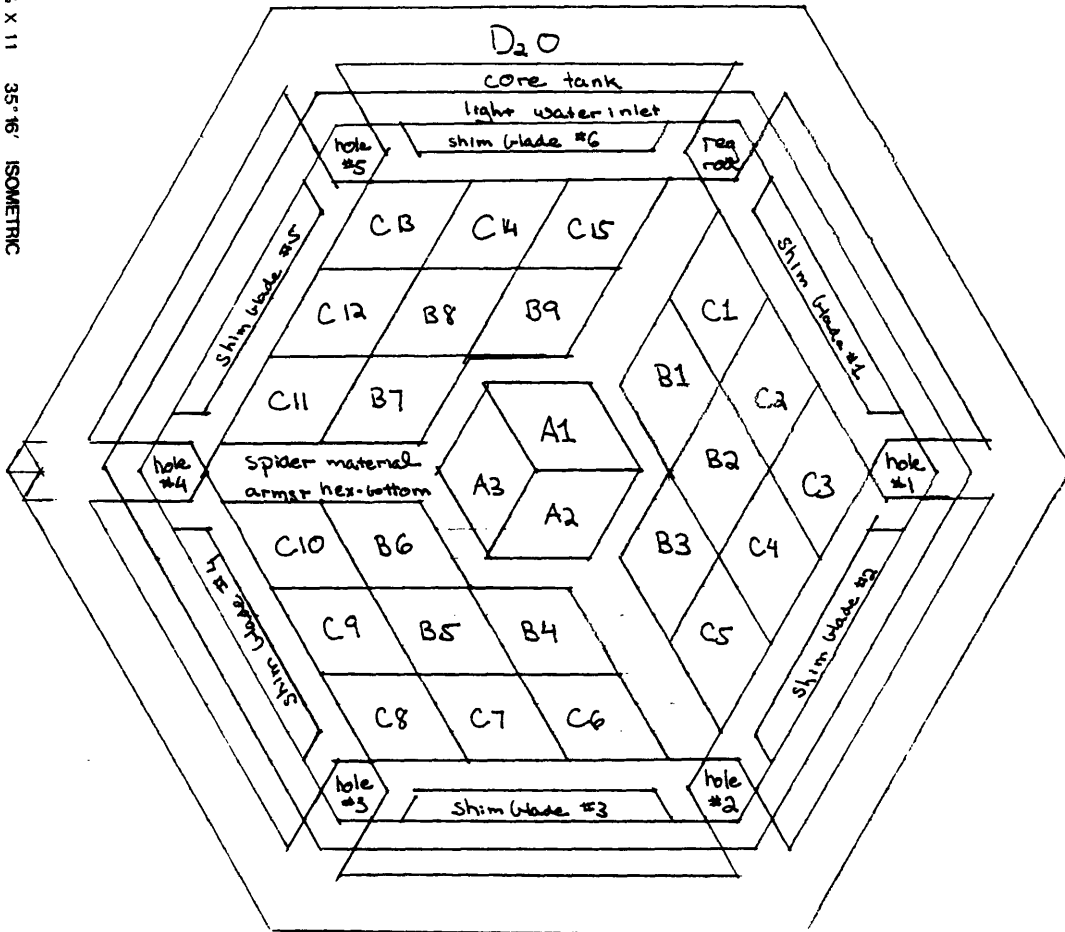
NO. 1242 - 8 1/2" X 11" 35° 16' ISOMETRIC



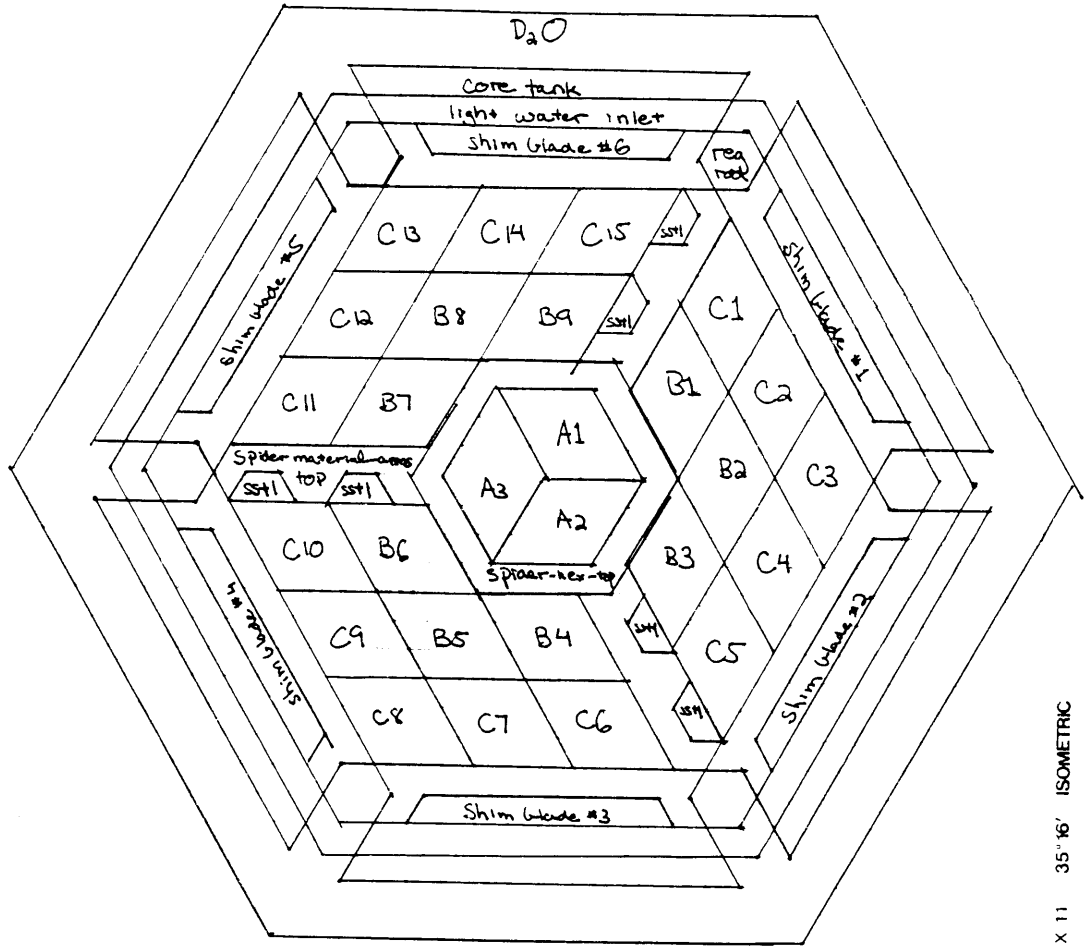


NO 1242 ... 8 1/2 X 11 35-65' ISOMETRIC

Plane 6,7



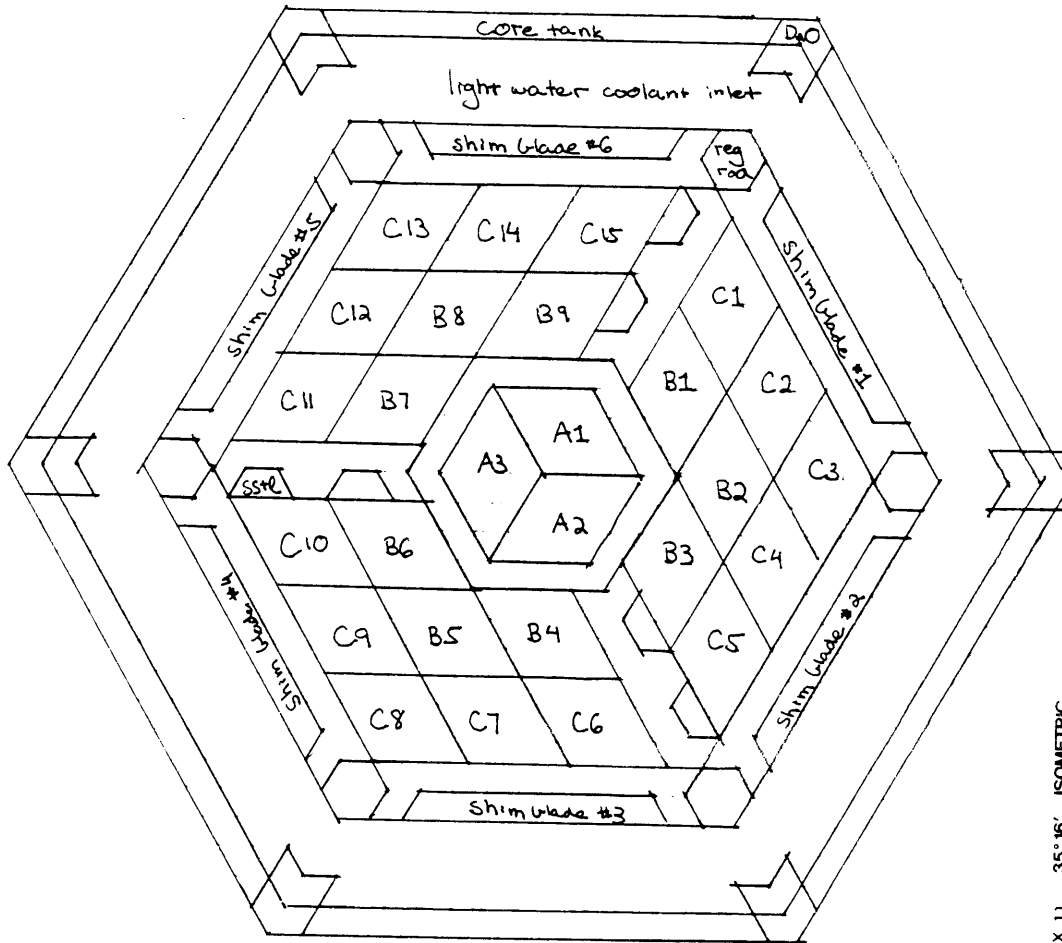
Planes 8, 9, 10



NO. 1242 -- 8 1/2 X 11 35" 16' ISOMETRIC

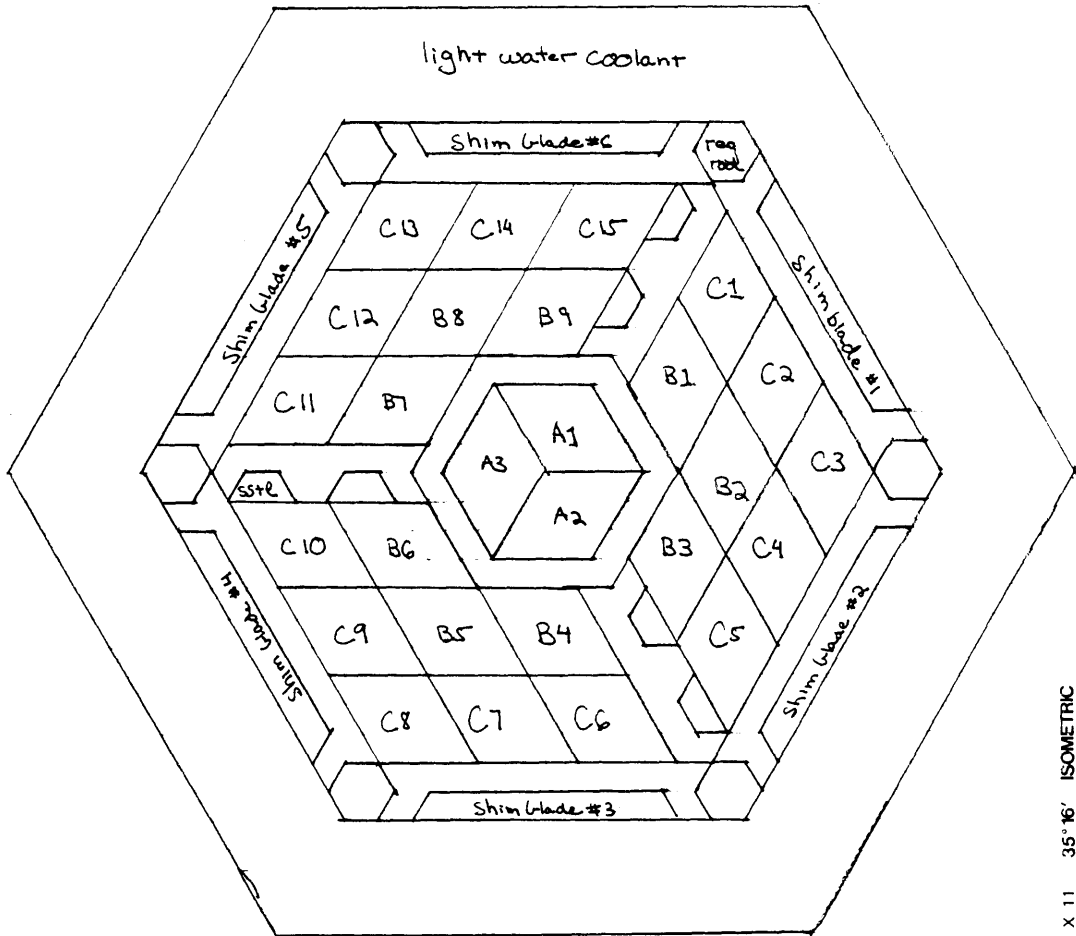


Plane 11



ALVIN
NO. 1242 - 8 1/2 X 11 35° 16' ISOMETRIC

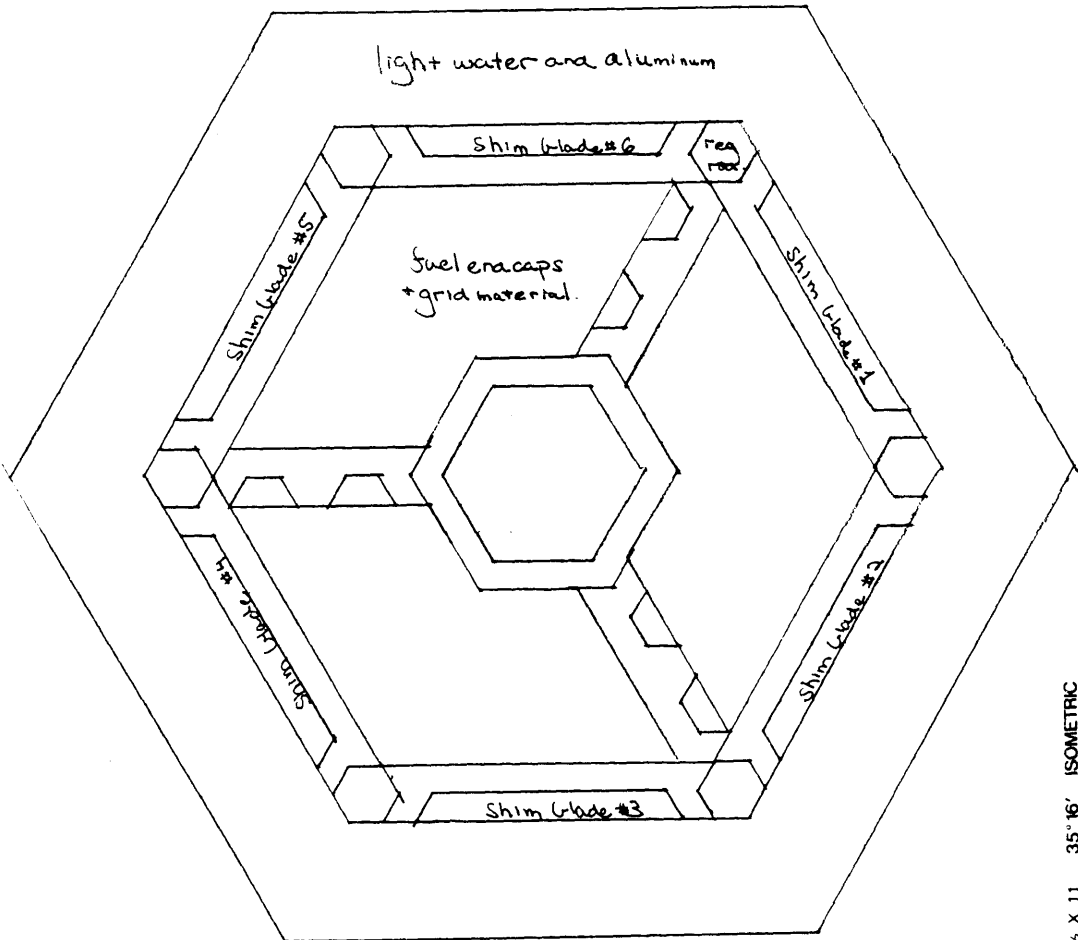
Planes 12, 13, 14



NO. 1242 - 8 1/2 X 11 35° 16' ISOMETRIC

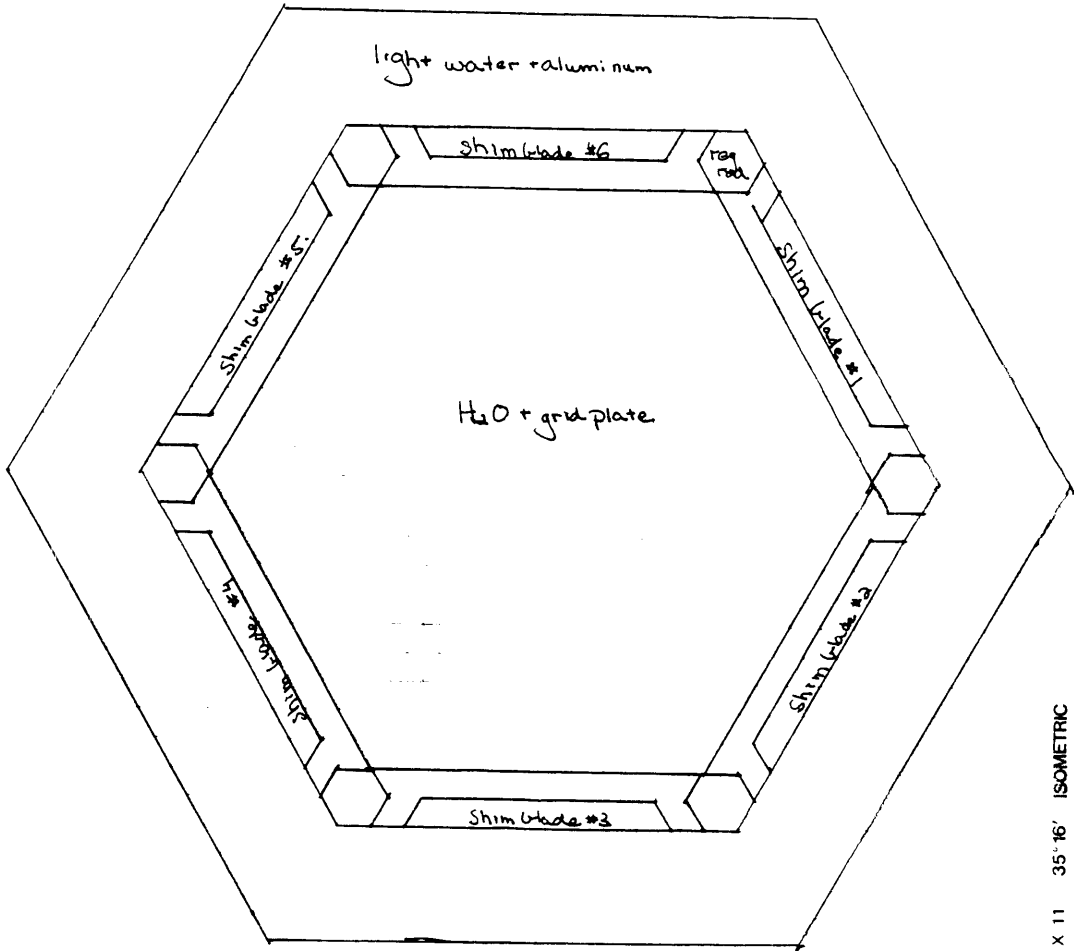


Plane 15



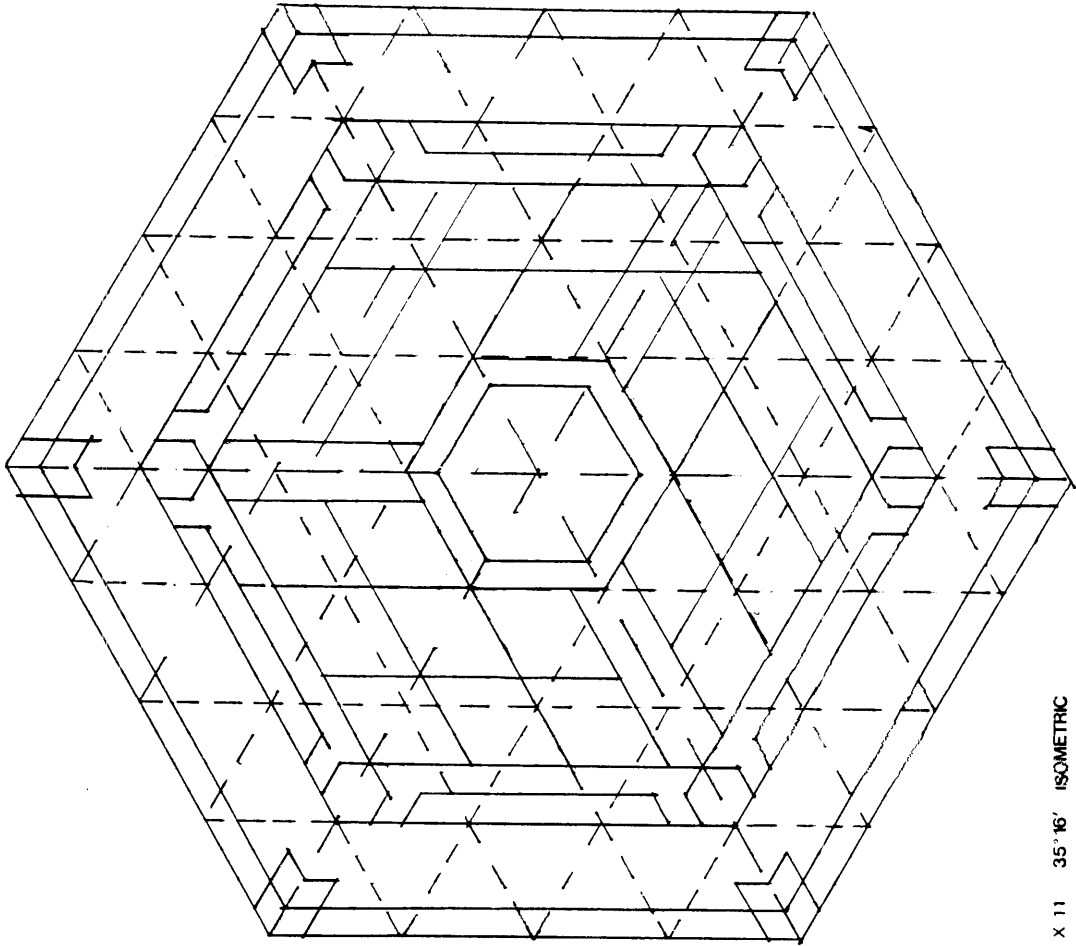
ALVIN NO. 1242 - 8 1/2 X 11 35° 16' ISOMETRIC


Plane 16



ALVIN
NO. 1242 - 8 1/2 X 11 35° 16' ISOMETRIC

Plane II - Coarse Mesh Overlay



 NO. 1242 - 8 1/2 X 11 35° 16' ISOMETRIC

APPENDIX 4

DECK AND PLOT CODE DESCRIPTIONS

There are two auxiliary codes developed as a part of this thesis that may be useful for those wishing to continue working with the QUARTZ code. They are DECK and PLOT. Both are written in standard FORTRAN-77. The use of each one will be briefly described here.

The DECK code is used to create input decks for the QUARTZ code. It was created for use with the MITR model because of the complexity of the system. The input to DECK is complicated to set up, but once done small changes to the model can be made more easily than in the QUARTZ input itself. It is also much easier to visualize the input to the DECK code than the QUARTZ code for large models.

The input to the DECK code begins with a title card. The title is not printed in the resulting QUARTZ input deck, but is used simply to identify the DECK input. It is followed by a card with four numbers: the number of planes, the number of rows, the minimum number of nodes per row and the maximum number of nodes per row.

```
**** core 106 my # densities,tilt2 50kw, 16 planes***  
16 32 33 63
```

The numbers are entered in 4I4 format.

This is followed by the another comment card and the shim blade positions.

```
***Shim Blade Heights***  
901 6 15 7 16 8 14  
902 6 15 7 16 8 14  
903 7 15 8 29 9 14  
904 6 15 7 16 8 14  
905 6 15 7 16 8 14  
906 6 15 7 16 8 14
```

In the composition numbers described later, materials #901-906 represent shim blades.

There are three groups of numbers given in each shim blade specification. Take, for example, material #901 - shim blade #1. As the compositions are read in for each plane, the nodes representing shim blade #1 will be reached. If those nodes are in plane 6 or below, the composition #15 is assigned to material #901. Composition #15 is a mixture of aluminum and water (see Appendix II) and represents the region below the shim blade. If the nodes are in plane #7, composition #16 is assigned. This represents a blade partially inserted into the node. Finally, if the nodes are in plane #8 or above, composition #14 is assigned. This is the borated stainless steel used by CITATION to represent the control blades. By using these cards, the positions of the control blades may be more easily changed.

The compositions assigned to each node are given next. While the layout is simple, keeping track of the compositions is somewhat complicated. It is, however, easier than the strings of numbers created for the QUARTZ input.

An example will be given for the midplane of the reactor so the use of the control blade compositions can be illustrated. Each plane begins with a title card. It is followed by a value showing the number of different groups of nodes in each row with the same composition. This is followed by groups of numbers, between vertical lines, showing the

number of nodes with the same composition, then the composition number. For example, the composition assignments for plane eight are given below. The first row has only one group of nodes with the same composition. There are 33 nodes in the row, all assigned composition #1. In the second row, there is again only one group of nodes, all assigned composition #1. In the third row, there are three groups of nodes. The first seven nodes are assigned composition #1, the second 23 are composition #8, and the final seven are composition #1. A maximum number of nine groups of nodes can be written on one line of input. The format statement is `format (9 (1x, i3, 1x, i3))`. If more than nine groups of nodes exist in a row in the model, the next line can be used to continue the row. For example, 13 groups of nodes exist in row #5. Input for this row occupies two lines. The number of rows in a plane (32 for the current MITR model) must match the value given at the beginning of the input deck. Only the first five rows of plane #8 are given below.

```

Plane 8
 1
| 33  1 |
 1
| 35  1 |
 3
| 7  1 | 23  8 | 7  1 |
 9
| 4  1 | 1  8 | 1  1 | 3  8 | 21 11 | 3  8 | 1  1 | 1  8 | 4  1 |
13
| 4  1 | 2  8 | 1 11 | 1  8 | 3 20 | 2  9 | 15 906 | 2  9 | 3 18 |
| 1  8 | 1 11 | 2  8 | 4  1 |

```

The nodes assigned compositions are counted by the DECK code. The results for each plane are printed to a file called junkout.

Note the 15 nodes that are assigned composition #906 in row #5. This composition number corresponds to shim blade #6. A look at the shim blade specifications shows that, in plane #8, composition #906 is equated to composition #14:

the control blade material. In plane #7, the composition would be #16, and in #3-#6, the composition would be #15. The use of the previous section to define control blade compositions now becomes clearer. The numbers 901-906 are used to define the control blades in the node assignments. But to change the position, the compositions need only to be replaced in one area, not in each plane. This simplifies the process of changing blade positions.

Compositions #16, #29, #30, #33, and #34 have been left open to define new materials. If different shim blades are in different positions, these compositions may be used for differing amounts of boron, aluminum, and water to represent the different insertion distances into a plane.

Compositions beginning with #35 are assigned to fuel material. Each of the 27 fuel elements are assigned 12 compositions, one for each plane. The water, aluminum, and U^{238} densities are the same for each element and are determined in the source code (see Appendix 2). The U^{235} number densities are read from the punched output file from DEPCOD2. That file is renamed `kwandens .XXX` for use with the DECK code. (XXX is the core number.) If that output is not available, another code called PREDEP is used to write the densities in the same form as the punched output. It requires as input all the U^{235} number densities, percentage of burnup limit, and fission product number densities, which can be typed in by hand using the fuel element history sheets also printed by DEPCOD2.

The specifications for one of the fuel elements from the `kwandens .106` file is given below. The first fourteen entries are U^{235} number densities, in #/barn-cm, for the inner portion of fuel element M212 in position A2. Each number corresponds to a plane,

going from top to bottom. The order is reversed when printing the QUARTZ input. The second fourteen numbers are the percentage of burnup limit at each location, and the third fourteen numbers are the lumped fission product number densities. These values are also given for the middle and outer portion of the fuel elements. The inner, middle, and outer portions are averaged together for use in the QUARTZ model. This is not required, but limits the number of compositions used. Also, the first two and last two planes are averaged together, creating 12 instead of 14 planes.

```
M212 A2
3.71000E-04 3.88000E-04 4.27000E-04 4.13000E-04 3.93000E-04 3.80000E-04
3.79000E-04 3.72000E-04 3.77000E-04 3.86000E-04 3.94000E-04 4.01000E-04
3.91000E-04 3.21000E-04
4.56500E+01 3.99100E+01 2.62500E+01 3.10800E+01 3.76500E+01 4.20900E+01
4.23500E+01 4.44700E+01 4.27200E+01 3.96800E+01 3.72300E+01 3.48200E+01
3.87600E+01 6.19600E+01
1.05908E-04 9.25912E-05 6.09000E-05 7.21056E-05 8.73480E-05 9.76488E-05
9.82520E-05 1.03170E-04 9.91104E-05 9.20576E-05 8.63736E-05 8.07824E-05
8.99232E-05 1.43747E-04
3.99000E-04 4.12000E-04 4.40000E-04 4.26000E-04 4.07000E-04 3.94000E-04
3.92000E-04 3.84000E-04 3.88000E-04 3.97000E-04 4.05000E-04 4.16000E-04
4.17000E-04 3.57000E-04
3.63400E+01 3.14500E+01 2.17000E+01 2.65100E+01 3.26400E+01 3.70200E+01
3.78100E+01 4.03200E+01 3.90100E+01 3.61200E+01 3.32700E+01 2.96000E+01
2.95800E+01 5.03000E+01
8.43088E-05 7.29640E-05 5.03440E-05 6.15032E-05 7.57248E-05 8.58864E-05
8.77192E-05 9.35424E-05 9.05032E-05 8.37984E-05 7.71864E-05 6.86720E-05
6.86256E-05 1.16696E-04
4.04000E-04 4.18000E-04 4.43000E-04 4.29000E-04 4.11000E-04 3.98000E-04
3.95000E-04 3.92000E-04 3.96000E-04 4.03000E-04 4.11000E-04 4.18000E-04
4.11000E-04 3.44000E-04
3.44100E+01 2.96800E+01 2.04900E+01 2.53900E+01 3.15100E+01 3.59200E+01
3.67600E+01 3.76900E+01 3.64300E+01 3.38300E+01 3.14600E+01 2.88600E+01
3.18100E+01 5.45100E+01
7.98312E-05 6.88576E-05 4.75368E-05 5.89048E-05 7.31032E-05 8.33344E-05
8.52832E-05 8.74408E-05 8.45176E-05 7.84856E-05 7.29872E-05 6.69552E-05
7.37992E-05 1.26463E-04
```

The composition numbers assigned to nodes containing fuel elements will be required in the DECK input. The current scheme is to use 35-47 for the first element, 48-60 for the second, etc. The lowest number is for the plane at the bottom of the element, the highest for the top. When running the code, the name of the punched output file (kwandens.106 here) will be requested. A file called `felms` will be required,

denoting the positions (1-27) where active fuel elements are located. The remaining positions will be aluminum dummy elements. Those locations must be assigned in the DECK input just as fuel locations.

The mass of the U^{235} , depleted U^{235} , and fission products are printed to a file called `massout2`. These values should closely match the values in the fuel element history sheets. The number of nodes in each plane, as given in the composition assignment portion, is also printed to a file called `junkout`.

The portion of the QUARTZ input deck created by DECK is contained in `deckout`. This file has the region assignments, composition assignments and all macroscopic cross sections used in the model printed in proper format. The cards above and below these regions required by QUARTZ are contained in `core106.top` and `core106.bot` for the MITR model. They can be easily pasted into the `deckout` file using a text editor, and a complete input deck is created. For the MITR model, the `deckout` file is quite large. A text editor able to edit large files should be used. EMACS was used for this project. A summary of the files required by DECK and generated by DECK is given in Table IV.1

The PLOT code is an interactive code to generate data tables from QUARTZ output to be used by plotting programs, specifically TECPLOT on Athena. All information is requested at run time. To use PLOT, take the `FORFLUX.OUT` file and eliminate the first line of text. The remaining data manipulation is handled by PLOT.

PLOT offers four options. The ones of most interest to future users will be the planar plots and the axial plots. For the planar plots, simply enter the number of the plane

to be plotted. For the axial plots, enter the node number of the first plane. A third option is to determine average flux in a fuel element. Three numbers must be entered. They are the numbers of the first node in the bottom plane in each of the three rows making up a fuel element locations¹. This means that fuel elements oriented such that the vertices lie along vertical and horizontal axes cannot be analyzed. They consist of five rows of nodes. This option is useful when comparing QUARTZ predictions to MCNP or other results.

Filename	Purpose
<input file name>	Requested by DECK. Contains information about control blade position and assigns composition numbers to each node.
kwandens .XXX	Requested by DECK. Contains all the U235 number densities, percentages of burnup limit, and fission product number densities for each element as predicted by DEPCOD2. Can be generated by the PREDEP code if not available.
felms	Contains the locations of all the active fuel elements
deckout	Produced by DECK. Contains region assignments, composition assignments, and macroscopic cross sections in proper QUARTZ format
massout2	Produced by DECK. Contains the masses of all U235 and fission products in a particular element. Should match DEPCOD2 results.
junkout	Produced by DECK. Contains the number of nodes in each plane contained in the composition assignments in the DECK input file. Serves as a check whether all nodes have been assigned a composition number.

Table IV.1. Files Required and Generated by DECK

¹ Even though the fuel elements do not extend to the bottom of the model, the values on the first plane are used. The top two and bottom two planes should be eliminated when making comparisons to other fuel element results.

APPENDIX 5

EXPERIMENTAL PROCEDURES

The procedures for the experimental evaluation of the instrumented flux synthesis method are detailed on the following pages. Detector measurements from the static cases along with control blade positions are included with the procedures. The data from the April 26, 1994, and March 25, 1995, experiments were used for the experimental evaluation.

Procedure for Experimental Evaluation of the Instrumented Flux Synthesis Method

Experimenter:
Jeff Hughes, x3-4218
NW12-306b

Experiment Date: 12/06/93

Supervisors: D.D. Lanning, A.F. Henry, J.A. Bernard, Ed Lau

I. PREREQUISITES

1. The Reactor Radiation Protection Office will be notified of the experimental procedure and the potential for high radiation from exposed fission chambers and aluminum guide tubes. Specifically, special arrangements may need to be made at the end of the experiment to allow for decay of the activated fission chambers and aluminum guide tubes.
2. Reactor is shutdown and reactor coolant temperature less than 25 °C.
3. Reactor top shield is off.
4. Reactor is ready for startup or startup checklist is near completion.
5. When the reactor is critical during the experiment, the reactor coolant temperature must be maintained below 50 °C. Since coolant flow degrades the accuracy of the results, the reactor coolant pumps will be secured for the experiment. If at any time during the experiment the coolant temperature reaches 50 °C, testing will be halted and primary coolant flow will be established to reduce coolant temperature. **CAUTION:** The reactor must be shutdown prior to restoring flow.
6. Calculate the reactivity worth of the fission chambers prior to inserting them in the core.

II. PROCEDURE

A. Prepare Experiment

- A1. Ops Verify the prerequisites are met.
- A2. Ops Verify experiment is ready and all necessary materials are on hand in the reactor top.
- A3. Ops Verify proper operation of the reactor top hand-held spotlight.
- A4. Ops Prepare and clean all three aluminum instrument guide tubes to be inserted into the reactor.
- A5. Ops Establish communications between the reactor top and the control room.
- A6. Ops A licensed Senior Reactor Operator (SRO) and an experimenter present on the reactor top. One licensed Reactor Operator (RO) present in the control room. Supervisor and RRPO notified of start of the experiment.
- A7. Ops Align the grid latch with water vent holes if necessary.
- A8. Ops Notify the control room that the aluminum guide tubes are to be inserted into the core.

CAUTION: When lowering the aluminum guide tubes into the core, care must be taken to keep the tubes close to the outer walls of the core tank to prevent the rod from being held above the fuel elements. For this reason it is important to stand directly above the targeted water vent hole.

- A9. Ops SRO carefully inserts the aluminum tubes fully into each of the three designated water vent holes. **DO NOT FORCE THE ALUMINUM TUBES INTO THE WATER VENT HOLES.**
- A10. Ops Notify the control room when the above step has been completed.
- A11. JCH Insert the three fission chamber strings into the aluminum instrument guide tubes. One string of three detectors is inserted into each guide tube. Insert the strings such that the bottom detector is at the bottom of the guide tube.
- A12. JCH Experimenter performs preliminary check of the electronics and completes final setup of the equipment on top of the reactor top front platform. Once this has been completed, experimenter performs a full set of background readings, taking readings from all nine detectors. Record the core tank temperature at the time these readings are taken.

Core Tank Temperature: ___ °C

Table A1. Background Measurements

Detector	Current (µA)	Detector	Current (µA)	Detector	Current (µA)
#1	0.068	#2	0.059	#3	0.072
#1b	0.043	#2b	0.035	#3b	0.039
#1c	0.013	#2c	0.010	#3c	0.012

B. Steady State “Flat” Measurements at 1 kW

- B1. JCH Notify control room that experimenter is ready to begin and requests the control room to conduct a reactor startup. Raise reactor power to 1 kW.

Note startup time: 1055
 Shutdown time prior to startup: N/A hrs.

- B2. JCH With reactor power at 1 kW experimenter conducts flux mapping with the nine fission chamber detectors. Note the position of all control blades and the regulating rod below. Also note the core tank temperature.

Shim Bank Height (SBH): 0891
 Regulating Rod Height (RRH): 0080
 Core tank temperature: 36.5°C D2O Temperature: 27.5°C

Table B1. “Flat” Flux Measurements, 1 kW

Detector	Current (µA)	Detector	Current (µA)	Detector	Current (µA)
#1	0.1543	#2	0.1522	#3	0.1837
#1b	0.1025	#2b	0.1000	#3b	0.1005
#1c	0.0341	#2c	0.0232	#3c	0.0337

- B3. JCH Upon completion of the above step, the SRO will notify the control room.

C. Steady State Tilted Measurements at 1 kW, #1

C1. Ops After the above data are taken, establish a flux tilt by moving the control blades in the following manner (RO maintains criticality at 1 kW by compensating with the regulating rod):

- Control Blade #1: SBH + 6"
- Control Blade #2: SBH + 2"
- Control Blade #3: SBH - 2"
- Control Blade #4: SBH - 6"
- Control Blade #5: SBH - 2"
- Control Blade #6: SBH + 2"

C2. Ops Note the positions of all control blades and the regulating rod below:

- Control Blade #1 Position: 1491
- Control Blade #2 Position: 1091
- Control Blade #3 Position: 0691
- Control Blade #4 Position: 0291
- Control Blade #5 Position: 0691
- Control Blade #6 Position: 1091
- RRH: 0844

C3. Ops The control room notifies the experimenter once this flux tilt is achieved.

C4. JCH When the experimenter has recorded data from all nine fission chamber detectors, the SRO notifies the control room.

Table C1. Tilted Flux Measurements #1, 1 kW

Detector	Current (μA)	Detector	Current (μA)	Detector	Current (μA)
#1	0.1919	#2	0.1484	#3	0.1955
#1b	0.1190	#2b	0.0980	#3b	0.1069
#1c	0.0377	#2c	0.0239	#3c	0.0353

D. Steady State Tilted Measurements at 1 kW, #2

D1. Ops When ready, the experimenter requests the control room to shift the flux tilt to the other side of the core by positioning the control blades as follows (RO maintains criticality at 1 kW by compensating with the regulating rod):

- Control Blade #1: SBH - 6"
- Control Blade #2: SBH - 2"
- Control Blade #3: SBH + 2"
- Control Blade #4: SBH + 6"
- Control Blade #5: SBH + 2"
- Control Blade #6: SBH - 2"

D2. Ops Note the position of all control blades and the regulating rod below:

- Control Blade #1 Position: 0291
- Control Blade #2 Position: 0738
- Control Blade #3 Position: 1091
- Control Blade #4 Position: 1491

Control Blade #5 Position: 1091
 Control Blade #6 Position: 0691
 RRH: 1167

- D3. Ops The control room notifies the experimenter once the flux tilt is achieved.
- D4. JCH When the experimenter has recorded data from all nine fission chamber detectors, the SRO notifies the control room.

Table D1. Tilted Flux Measurements #2, 1 kW

Detector	Current (μ A)	Detector	Current (μ A)	Detector	Current (μ A)
#1	0.1446	#2	0.1824	#3	0.1880
#1b	0.1002	#2b	0.1087	#3b	0.1032
#1c	0.0337	#2c	0.0250	#3c	0.0342

E. Steady State "Flat" Measurements at 10 kW

- E1. Ops When ready, experimenter requests the control room to raise reactor power to 10 kW and reshim.
- E2. JCH With reactor power at 10 kW, experimenter conducts flux mapping with the nine fission chamber detectors. Note the new shim bank and regulating rod positions below once power is leveled at 10 kW. Also note the core tank temperature.

SBH: 0891
 RRH: 0172
 Core tank temp: 36.7°

Table E1. "Flat" Flux Measurements, 10 kW

Detector	Current (μ A)	Detector	Current (μ A)	Detector	Current (μ A)
#1	0.968	#2	1.014	#3	1.238
#1b	0.670	#2b	0.696	#3b	0.690
#1c	0.226	#2c	0.151	#3c	0.237

- E3. JCH Upon completion of the above step, the SRO will notify the control room.

F. Steady State Tilted Measurements at 10 kW, #1

- F1. Ops After the above data are taken, establish a flux tilt by moving the control blades in the following manner (RO maintains criticality at 10 kW by compensating with the regulating rod):

Control Blade #1: SBH + 6"
 Control Blade #2: SBH + 2"
 Control Blade #3: SBH - 2"
 Control Blade #4: SBH - 6"
 Control Blade #5: SBH - 2"
 Control Blade #6: SBH + 2"

- F2. JCH Note the positions of all control blades and the regulating rod below. Also note the core tank temperature.

Control Blade #1 Position: 1091
 Control Blade #2 Position: 0991
 Control Blade #3 Position: 0791
 Control Blade #4 Position: 0691
 Control Blade #5 Position: 0791
 Control Blade #6 Position: 0991
 RRH: 0257
 Core tank temp: 37.3°C

- F3. Ops The control room notifies the experimenter once the flux tilt is achieved.
- F4. JCH When the experimenter has recorded data with all nine fission chamber detectors , the SRO notifies the control room.

Table F1. Tilted Flux Measurements #1, 10 kW

Detector	Current (μA)	Detector	Current (μA)	Detector	Current (μA)
#1	1.061	#2	0.999	#3	1.269
#1b	0.714	#2b	0.683	#3b	0.700
#1c	0.235	#2c	0.151	#3c	0.241

G. Steady State Tilted Measurements at 10 kW, #2

- G1. Ops When ready, the experimenter requests the control room to shift the flux tilt to the other side of the core as follows (RO maintains criticality at 10 kW by compensating with the regulating rod).

Control Blade #1: SBH - 6"
 Control Blade #2: SBH - 2"
 Control Blade #3: SBH + 2"
 Control Blade #4: SBH + 6"
 Control Blade #5: SBH + 2"
 Control Blade #6: SBH - 2"

- G2. JCH Note the positions of all control blades and the regulating rod below. Also note the core tank temperature.

Control Blade #1 Position: 0691
 Control Blade #2 Position: 0791
 Control Blade #3 Position: 0991
 Control Blade #4 Position: 1091
 Control Blade #5 Position: 0991
 Control Blade #6 Position: 0791
 RRH: 0299
 Core tank temp: 37.6°C

- G3. Ops The control room notifies the experimenter once the flux tilt is achieved.
- G4. JCH When the experimenter has recorded data with all nine fission chamber detectors, the SRO notifies the control room.

Table G1. Tilted Flux Measurements #2, 10 kW

Detector	Current (μA)	Detector	Current (μA)	Detector	Current (μA)
#1	0.915	#2	1.108	#3	1.236
#1b	0.651	#2b	0.725	#3b	0.691
#1c	0.224	#2c	0.156	#3c	0.240

H-M. Experiment stopped.

O. Shutdown

- O1. Ops When ready, experimenter requests the control room to conduct a reactor shutdown.
- O2. Once reactor shutdown has been completed, experimenter conducts a full set of background readings.

Table O1. Background Measurements

Detector	Current (μA)	Detector	Current (μA)	Detector	Current (μA)
#1		#2		#3	
#1b		#2b		#3b	
#1c		#2c		#3c	

- O3. JCH Once all testing is completed, carefully remove the nine fission chamber detectors from the aluminum instrument guide tubes. Care must be taken in handling the detectors since they will be activated from the neutron flux.
- O4. JCH Carefully remove the three aluminum instrument guide tubes from the reactor core tank. Dry the aluminum tubes with absorbent rags. (**CAUTION:** High beta exposure on contact with aluminum tubes.)
- O5. Ops A licensed SRO inspects the core tank for any foreign objects left behind from the experiment.
- O6. Ops If no additional experiments are to be performed within the core tank, replace the reactor top shield lid.
- O7. JCH Remove and store all tools used in this procedure. Notify the control room, the Reactor Supervisor, and RRPO that the experiment has been completed.

Supervisor: Frank Warmsley Date: 12/07/93

Procedure for Experimental Evaluation of the Instrumented Flux Synthesis Method

Experimenter:
Jeff Hughes, x3-4218
NW12-306b

Experiment Date: 04/26/94

Supervisors: D.D. Lanning, A.F. Henry, J.A. Bernard, Ed Lau

I. PREREQUISITES

1. The Reactor Radiation Protection Office will be notified of the experimental procedure and the potential for high radiation from exposed fission chambers and aluminum guide tubes. Specifically, special arrangements may need to be made at the end of the experiment to allow for decay of the activated fission chambers and aluminum guide tubes.
2. Reactor is shutdown and reactor coolant temperature less than 25 °C.
3. Reactor top shield is off.
4. Reactor is ready for startup or startup checklist is near completion.
5. When the reactor is critical during the experiment, the reactor coolant temperature must be maintained below 50 °C. Since coolant flow degrades the accuracy of the results, the reactor coolant pumps will be secured for the experiment. If at any time during the experiment the coolant temperature reaches 50 °C, testing will be halted and primary coolant flow will be established to reduce coolant temperature. **CAUTION:** The reactor must be shutdown prior to restoring flow.
6. Calculate the reactivity worth of the fission chambers prior to inserting them in the core.

II. PROCEDURE

A. Prepare Experiment

- A1. ops Verify the prerequisites are met.
- A2. ops Verify experiment is ready and all necessary materials are on hand in the reactor top.
- A3. ops Verify proper operation of the reactor top hand-held spotlight.
- A4. ops Prepare and clean all three aluminum instrument guide tubes to be inserted into the reactor.
- A5. ops Establish communications between the reactor top and the control room.
- A6. ops A licensed Senior Reactor Operator (SRO) and an experimenter present on the reactor top. One licensed Reactor Operator (RO) present in the control room. Supervisor and RRPO notified of start of the experiment.
- A7. ops Align the grid latch with water vent holes if necessary.
- A8. ops Notify the control room that the aluminum guide tubes are to be inserted into the core.

CAUTION: When lowering the aluminum guide tubes into the core, care must be taken to keep the tubes close to the outer walls of the core tank to prevent the rod from being held above the fuel elements. For this reason it is important to stand directly above the targeted water vent hole.

- A9. ops Experimenter carefully inserts the aluminum tubes fully into each of the three designated water vent holes. **DO NOT FORCE THE ALUMINUM TUBES INTO THE WATER VENT HOLES.**
- A10. ops Notify the control room when the above step has been completed.
- A11. JCH Insert the three fission chamber strings into the aluminum instrument guide tubes. One string of three detectors is inserted into each guide tube. Insert the strings such that the bottom detector is at the bottom of the guide tube.
- A12. JCH Experimenter performs preliminary check of the electronics and completes final setup of the equipment on top of the reactor top front platform. Once this has been completed, experimenter performs a full set of background readings, taking readings from all nine detectors. Record the core tank temperature at the time these readings are taken.

Core Tank Temperature: ___ °C

Table A1. Background Measurements

Detector	Current (µA)	Detector	Current (µA)	Detector	Current (µA)
#1		#2		#3	
#1b		#2b		#3b	
#1c		#2c		#3c	

B. Steady State “Flat” Measurements at 1 kW

- B1. JCH Notify control room that experimenter is ready to begin and requests the control room to conduct a reactor startup. Raise reactor power to 1 kW.

Note startup time: 0930
 Shutdown time prior to startup: -48 hrs.

- B2. JCH With reactor power at 1 kW experimenter conducts flux mapping with the nine fission chamber detectors. Note the position of all control blades and the regulating rod below. Also note the core tank temperature.

Shim Bank Height (SBH): 0780
 Regulating Rod Height (RRH): 0155
 Core tank temperature: 29.1°C inlet, 31.8° outlet D2O Temperature: 21.2°C

Table B1. “Flat” Flux Measurements, 1 kW

Detector	Current (µA)	Detector	Current (µA)	Detector	Current (µA)
#1	0.1251	#2	0.1609	#3	0.1622
#1b	0.0861	#2b	0.1104	#3b	0.0827
#1c	0.0268	#2c	0.0343	#3c	0.0273

- B3. JCH Upon completion of the above step, the experimenter will notify the control room.

C. Steady State Tilted Measurements at 1 kW, #1

C1. ops After the above data are taken, establish a flux tilt by moving the control blades in the following manner (RO maintains criticality at 1 kW by compensating with the regulating rod):

- Control Blade #1: SBH + 6"
- Control Blade #2: SBH + 2"
- Control Blade #3: SBH - 2"
- Control Blade #4: SBH - 6"
- Control Blade #5: SBH - 2"
- Control Blade #6: SBH + 2"

C2. ops Note the positions of all control blades and the regulating rod below:

- Control Blade #1 Position: 1380
- Control Blade #2 Position: 0900
- Control Blade #3 Position: 0700
- Control Blade #4 Position: 0180
- Control Blade #5 Position: 0700
- Control Blade #6 Position: 0900
- RRH: 0752

C3. ops The control room notifies the experimenter once this flux tilt is achieved.

C4. JCH When the experimenter has recorded data from all nine fission chamber detectors, he notifies the control room.

Table C1. Tilted Flux Measurements #1, 1 kW

Detector	Current (μA)	Detector	Current (μA)	Detector	Current (μA)
#1	0.1504	#2	0.1563	#3	0.1692
#1b	0.0971	#2b	0.1098	#3b	0.0863
#1c	0.0291	#2c	0.0347	#3c	0.0285

D. Steady State Tilted Measurements at 1 kW, #2

D1. ops When ready, the experimenter requests the control room to shift the flux tilt to the other side of the core by positioning the control blades as follows (RO maintains criticality at 1 kW by compensating with the regulating rod):

- Control Blade #1: SBH - 6"
- Control Blade #2: SBH - 2"
- Control Blade #3: SBH + 2"
- Control Blade #4: SBH + 6"
- Control Blade #5: SBH + 2"
- Control Blade #6: SBH - 2"

D2. ops Note the position of all control blades and the regulating rod below:

- Control Blade #1 Position: 0180
- Control Blade #2 Position: 0700
- Control Blade #3 Position: 0860
- Control Blade #4 Position: 1380
- Control Blade #5 Position: 0860

Control Blade #6 Position: 0700
 RRH: 0155

- D3. ops The control room notifies the experimenter once the flux tilt is achieved.
- D4. JCH When the experimenter has recorded data from all nine fission chamber detectors, he notifies the control room.

Table D1. Tilted Flux Measurements #2, 1 kW

Detector	Current (μA)	Detector	Current (μA)	Detector	Current (μA)
#1	0.1195	#2	0.1869	#3	0.1629
#1b	0.0843	#2b	0.1223	#3b	0.0837
#1c	0.0270	#2c	0.0361	#3c	0.0278

E. Steady State "Flat" Measurements at 10 kW

- E1. ops When ready, experimenter requests the control room to raise reactor power to 10 kW and reshim.
- E2. JCH With reactor power at 10 kW, experimenter conducts flux mapping with the nine fission chamber detectors. Note the new shim bank and regulating rod positions below once power is leveled at 10 kW. Also note the core tank temperature.

SBH: 0780
 RRH: 0360
 Core tank temp: 32.0° inlet, 29.5° outlet

Table E1. "Flat" Flux Measurements, 10 kW

Detector	Current (μA)	Detector	Current (μA)	Detector	Current (μA)
#1	0.8854	#2	1.0941	#3	1.1935
#1b	0.6282	#2b	0.7775	#3b	0.6243
#1c	0.1894	#2c	0.2168	#3c	0.1992

- E3. JCH Upon completion of the above step, the experimenter will notify the control room.

F. Steady State Tilted Measurements at 10 kW, #1

- F1. ops After the above data are taken, establish a flux tilt by moving the control blades in the following manner (RO maintains criticality at 10 kW by compensating with the regulating rod):

Control Blade #1: SBH + 6"
 Control Blade #2: SBH + 2"
 Control Blade #3: SBH - 2"
 Control Blade #4: SBH - 6"
 Control Blade #5: SBH - 2"
 Control Blade #6: SBH + 2"

- F2. ops Note the positions of all control blades and the regulating rod below. Also note the core tank temperature.

Control Blade #1 Position: 1380

Control Blade #2 Position: 0910
 Control Blade #3 Position: 0700
 Control Blade #4 Position: 0180
 Control Blade #5 Position: 0700
 Control Blade #6 Position: 0910
 RRH: 0910
 Core tank temp: 32.8°C inlet, 29.7° outlet

- F3. ops The control room notifies the experimenter once the flux tilt is achieved.
- F4. JCH When the experimenter has recorded data with all nine fission chamber detectors , he notifies the control room.

Table F1. Tilted Flux Measurements #1, 10 kW

Detector	Current (µA)	Detector	Current (µA)	Detector	Current (µA)
#1	1.1308	#2	1.0272	#3	1.2551
#1b	0.7386	#2b	0.7702	#3b	0.6669
#1c	0.2098	#2c	0.2223	#3c	0.2107

G. Steady State Tilted Measurements at 10 kW, #2

- G1. ops When ready, the experimenter requests the control room to shift the flux tilt to the other side of the core as follows (RO maintains criticality at 10 kW by compensating with the regulating rod).

Control Blade #1: SBH - 6"
 Control Blade #2: SBH - 2"
 Control Blade #3: SBH + 2"
 Control Blade #4: SBH + 6"
 Control Blade #5: SBH + 2"
 Control Blade #6: SBH - 2"

- G2. ops Note the positions of all control blades and the regulating rod below. Also note the core tank temperature.

Control Blade #1 Position: 0180
 Control Blade #2 Position: 0680
 Control Blade #3 Position: 0880
 Control Blade #4 Position: 1380
 Control Blade #5 Position: 0880
 Control Blade #6 Position: 0680
 RRH: 0387
 Core tank temp: 33.5°C inlet, 29.9°C outlet

- G3. ops The control room notifies the experimenter once the flux tilt is achieved.
- G4. JCH When the experimenter has recorded data with all nine fission chamber detectors, he notifies the control room.

Table G1. Tilted Flux Measurements #2, 10 kW

Detector	Current (μA)	Detector	Current (μA)	Detector	Current (μA)
#1	0.8141	#2	1.3474	#3	1.1974
#1b	0.6043	#2b	0.8894	#3b	0.6356
#1c	0.1884	#2c	0.2351	#3c	0.2027

H. Steady State "Flat" Measurements at 50 kW

- H1. ops When ready, experimenter requests the control room to raise reactor power to 50 kW and reshim.
- H2. JCH With reactor power at 50 kW, experimenter conducts flux mapping with the nine fission chamber detectors. Note the new shim bank and regulating rod positions below once power is leveled at 50 kW. Also note the core tank temperature.

SBH: 0795
 RRH: 0175
 Core tank temp: 36.2°C

Table H1. "Flat" Flux Measurements, 50 kW

Detector	Current (μA)	Detector	Current (μA)	Detector	Current (μA)
#1	4.4202	#2	5.3959	#3	5.7086
#1b	3.0383	#2b	3.7977	#3b	3.1053
#1c	0.9579	#2c	1.0500	#3c	1.0100

- H3. JCH Upon completion of the above step, the experimenter will notify the control room.

I. Steady State Tilted Measurements at 50 kW, #1

- I1. ops After the above data are taken, establish a flux tilt by moving the control blades in the following manner (RO maintains criticality at 50 kW by compensating with the regulating rod):

Control Blade #1: SBH + 6"
 Control Blade #2: SBH + 2"
 Control Blade #3: SBH - 2"
 Control Blade #4: SBH - 6"
 Control Blade #5: SBH - 2"
 Control Blade #6: SBH + 2"

- I2. ops Note the positions of all control blades and the regulating rod below. Also note the core tank temperature.

Control Blade #1 Position: 1395
 Control Blade #2 Position: 0920
 Control Blade #3 Position: 0720
 Control Blade #4 Position: 0195
 Control Blade #5 Position: 0720
 Control Blade #6 Position: 0920
 RRH: 0895
 Core tank temp: 40.1°C

- I3. ops The control room notifies the experimenter once the flux tilt is achieved.

- I4. JCH When the experimenter has recorded data with all nine fission chamber detectors, he notifies the control room.

Table I1. Tilted Flux Measurements #1, 50 kW

Detector	Current (μ A)	Detector	Current (μ A)	Detector	Current (μ A)
#1	5.7937	#2	5.0125	#3	6.1496
#1b	3.4634	#2b	3.7309	#3b	3.2839
#1c	1.0803	#2c	1.0835	#3c	1.0690

J. Steady State Tilted Measurements at 50 kW, #2

- J1. ops When ready, the experimenter requests the control room to shift the flux tilt to the other side of the core as follows (RO maintains criticality at 50 kW by compensating with the regulating rod).

Control Blade #1: SBH - 6"
 Control Blade #2: SBH - 2"
 Control Blade #3: SBH + 2"
 Control Blade #4: SBH + 6"
 Control Blade #5: SBH + 2"
 Control Blade #6: SBH - 2"

- J2. ops Note the positions of all control blades and the regulating rod below. Also note the core tank temperature.

Control Blade #1 Position: 0195
 Control Blade #2 Position: 0735
 Control Blade #3 Position: 0895
 Control Blade #4 Position: 1395
 Control Blade #5 Position: 0895
 Control Blade #6 Position: 0735
 RRH: 0136
 Core tank temp: 47.4°C

- J3. ops The control room notifies the experimenter once the flux tilt is achieved.
- J4. JCH When the experimenter has recorded data with all nine fission chamber detectors, he notifies the control room.

Table J1. Tilted Flux Measurements #2, 50 kW

Detector	Current (μ A)	Detector	Current (μ A)	Detector	Current (μ A)
#1	3.9889	#2	6.6757	#3	5.7630
#1b	2.6956	#2b	4.2369	#3b	3.0545
#1c	0.9374	#2c	1.1417	#3c	1.0065

K. Transient Measurements, Shim Blade #6 Insertion

- K1. ops When ready, the experimenter requests the control room to reshim with power at 50 kW.

- K2. ops Note the new shim bank and regulating rod positions below after the reshim. Also note the core tank temperature.

SBH: 0795
RRH: 0380
Core tank temp: 41.3°C

- K3. ops With the power steady at 50 kW, drive in with shim blade #6 for ten seconds. Take readings from detectors #1, 2, and 3. These are at the bottom of the string. Note the position of shim blade #6 after this shim (hold the remainder of the shim bank and regulating rod positions constant during this ten second shim). At sixty seconds following the initiation of the step power decrease, restore power to 50 kW using shim blade #6 and the regulating rod. Note shim blade #6 position, the regulating rod position, and the core tank temperature once power is restored to 50 kW.

Reading fission chamber detectors #1,2,3:

Shim blade #6 position (after 10 second shim): 0725
Shim blade #6 position (power restored to 50 kW): 0795
New RRH (power restored to 50 kW): 0410
Core tank temperature: 42.3°C

- K4. JCH When ready, experimenter requests the control room to restore the control bank to the original position (as it was before the ten second shim). Use the regulating rod to compensate and keep power at 50 kW. Note the shim bank height and regulating rod position below.

SBH: 0795
RRH: 0410

- K5. ops With reactor power restored to 50 kW the SRO notifies the control room. The above step power decrease is repeated, and readings are taken from detectors #1b, 2b, and 3b in the middle of the string. This is repeated taking readings from detectors #1c, 2c, and 3c.

Reading fission chamber detectors #1b, 2b, and 3b:

SBH (before shim): 0795
RRH (before shim): 0410
Shim blade #6 position (after 10 second shim): 0724
Shim blade #6 position (power restored to 50 kW): 0795
New RRH (power restored to 50 kW): 0512
Core tank temperature: 43.6°C

Reading fission chamber detectors #1c, 2c, and 3c:

SBH (before shim): 0795
RRH (before shim): 0453
Shim blade #6 position (after 10 second shim): 0723
Shim blade #6 position (power restored to 50 kW): 0795
New RRH (power restored to 50 kW): 0512
Core tank temperature: 43.6°C

- K6. ops After completing the above step, maintain power at 50 kW and reshim. Note the position of the shim bank and the regulating rod below. Also note the core tank temperature.

SBH: 0795
RRH: 0485
Core tank temp: 43.7°C

L. Transient Measurements, Shim Blade #3 Insertion

- L1. ops With the power steady at 50 kW, drive in with shim blade #3 for ten seconds. Take readings from detectors #1, 2, and 3. These are at the bottom of the string. Note the position of shim blade #3 after this shim (hold the remainder of the shim bank and regulating rod positions constant during this ten second shim). At sixty seconds following the initiation of the step power decrease, restore power to 50 kW using shim blade #3 and the regulating rod. Note shim blade #3 position, the regulating rod position, and the core tank temperature once power is restored to 50 kW.

Reading fission chamber detectors #1,2,3:

Shim blade #3 position (after 10 second shim): 0689
Shim blade #3 position (power restored to 50 kW): 0795
New RRH (power restored to 50 kW): 0553
Core tank temperature: 44.3°C

- L2. ops When ready, experimenter requests the control room to restore the control bank to the original position (as it was before the ten second shim). Use the regulating rod to compensate and keep power at 50 kW. Note the shim bank height and regulating rod position below.

SBH: 0795
RRH: 0548

- L3. ops With reactor power restored to 50 kW the SRO notifies the control room. The above step power decrease is repeated, and readings are taken from detectors #1b, 2b, and 3b in the middle of the string. This is repeated taking readings from detectors #1c, 2c, and 3c.

Reading fission chamber detectors #1b, 2b, and 3b:

SBH (before shim): 0795
RRH (before shim): 0548
Shim blade #3 position (after 10 second shim): 0687
Shim blade #3 position (power restored to 50 kW): 0795
New RRH (power restored to 50 kW): 0622
Core tank temperature: 45.0°C

Reading fission chamber detectors #1c, 2c, and 3c:

SBH (before shim): 0795
RRH (before shim): 0561

Shim blade #3 position (after 10 second shim): 0691
Shim blade #3 position (power restored to 50 kW): 0795
New RRH (power restored to 50 kW): 0960
Core tank temperature: 45.4°C

M. Transient Measurements, Shim Blade #6 Withdrawal

- M1. ops After completing the above step, lower power at 5 kW and reshim. Note the position of the shim bank and the regulating rod below. Also note the core tank temperature.

SBH: 0795
RRH: 0060
Core tank temp: 45.4 °C

- M2. ops When ready, the experimenter requests the RO move control blade #6 out to establish a 50 second steady period. Once the 50 second period is attained, note control blade #6 position below and take readings from detectors #1, 2, and 3 at the bottom of the string. When reactor power reaches 50 kW, re-insert shim blade #6 and level power at 60 kW. Again note control blade #6 position when power is leveled at 60 kW. Also note the core tank temperature.

Reading fission chamber detectors #1, 2 and 3:

Control blade #6 position with 50 second period: 0908
Control blade #6 position with power leveled at 60 kW: 0795
RRH: 0710
Core tank temperature: 45.1°C

- M3. ops When experimenter is ready, lower power to 5 kW and restore shim blade #6 to the bank height.

- M4. ops With power leveled at 5 kW the SRO notifies the control room. Repeat the above reactor power increase transient, reading first fission chamber detectors #1b, 2b, and 3b, then #1c, #2c, and #3c. Be sure to note the control bank and regulating rod positions before the transient and note control blade #6 position during and after the transient as above. Also note the core tank temperature.

Reading fission chamber detectors #1b, 2b, and 3b:

SBH before withdrawal: 0795
RRH before withdrawal: 0060
Control blade #6 position with 50 second period: 0908
Control blade #6 position with power leveled at 60 kW: 0795
RRH: 0767
Core tank temperature: 45.5°C

Reading fission chamber detectors #1c, 2c, and 3c:

SBH before withdrawal: 0795
RRH before withdrawal: 0070

Control blade #6 position with 50 second period: ops
 Control blade #6 position with power leveled at 60 kW: ops
 Core tank temperature: ops

N. Transient Measurements, Shim Blade #1 Drop

N1. ops After completing the last transient above and when the experimenter is ready, lower reactor power to 50 kW and reshim.

N2. ops Note the control bank and regulating rod positions and core tank temperature below.

SBH: 0805
 RRH: 0226
 Core tank temp: 48.8 °C

N3. ops When ready, experimenter requests the control room to drop control blade #1. Readings are taken from chambers #1b, 2, and 3.

N4. ops When ready, experimenter requests the control room to restore reactor power to 50 kW. Note the new shim bank and regulating rod positions below. Also note the core tank temperature.

SBH: ops
 RRH: ops
 Core tank temp: ops °C

O. Shutdown

O1. ops When ready, experimenter requests the control room to conduct a reactor shutdown.

O2. ops Once reactor shutdown has been completed, experimenter conducts a full set of background readings.

Table O1. Background Measurements

Detector	Current (µA)	Detector	Current (µA)	Detector	Current (µA)
#1		#2		#3	
#1b		#2b		#3b	
#1c		#2c		#3c	

O3. ops Once all testing is completed, carefully remove the nine fission chamber detectors from the aluminum instrument guide tubes. Care must be taken in handling the detectors since they will be activated from the neutron flux.

O4. ops Carefully remove the three aluminum instrument guide tubes from the reactor core tank. Dry the aluminum tubes with absorbent rags. **(CAUTION: High beta exposure on contact with aluminum tubes.)**

O5. ops A licensed SRO inspects the core tank for any foreign objects left behind from the experiment.

O6. ops If no additional experiments are to be performed within the core tank, replace the reactor top shield lid.

- O7. ops Remove and store all tools used in this procedure. Notify the control room, the Reactor Supervisor, and RRPO that the experiment has been completed.

Supervisor: _____

Date: _____

Procedure for Experimental Evaluation of the Instrumented Flux Synthesis Method

Experimenter:
Jeff Hughes, x3-4218
NW12-306b

Experiment Date: 03/24/95

Supervisors: D.D. Lanning, A.F. Henry, J.A. Bernard, Ed Lau

I. PREREQUISITES

1. The Reactor Radiation Protection Office will be notified of the experimental procedure and the potential for high radiation from exposed fission chambers and aluminum guide tubes. Specifically, special arrangements may need to be made at the end of the experiment to allow for decay of the activated fission chambers and aluminum guide tubes.
2. Reactor is shutdown and reactor coolant temperature less than 25 °C.
3. Reactor top shield is off.
4. Reactor is ready for startup or startup checklist is near completion.
5. When the reactor is critical during the experiment, the reactor coolant temperature must be maintained below 50 °C. Since coolant flow degrades the accuracy of the results, the reactor coolant pumps will be secured for the experiment. If at any time during the experiment the coolant temperature reaches 50 °C, testing will be halted and primary coolant flow will be established to reduce coolant temperature. **CAUTION:** The reactor must be shutdown prior to restoring flow.
6. Calculate the reactivity worth of the fission chambers prior to inserting them in the core.

II. PROCEDURE

A. Prepare Experiment

- A1. ops Verify the prerequisites are met.
- A2. ops Verify experiment is ready and all necessary materials are on hand in the reactor top.
- A3. ops Verify proper operation of the reactor top hand-held spotlight.
- A4. ops Prepare and clean all three aluminum instrument guide tubes to be inserted into the reactor.
- A5. ops Establish communications between the reactor top and the control room.
- A6. ops A licensed Senior Reactor Operator (SRO) and an experimenter present on the reactor top. One licensed Reactor Operator (RO) present in the control room. Supervisor and RRPO notified of start of the experiment.
- A7. ops Align the grid latch with water vent holes if necessary.
- A8. ops Notify the control room that the aluminum guide tubes are to be inserted into the core.

CAUTION: When lowering the aluminum guide tubes into the core, care must be taken to keep the tubes close to the outer walls of the core tank to prevent the rod from being held above the fuel elements. For this reason it is important to stand directly above the targeted water vent hole.

- A9. ops Experimenter carefully inserts the aluminum tubes fully into each of the three designated water vent holes. **DO NOT FORCE THE ALUMINUM TUBES INTO THE WATER VENT HOLES.**
- A10. ops Notify the control room when the above step has been completed.
- A11. JCH Insert the three fission chamber strings into the aluminum instrument guide tubes. One string of three detectors is inserted into each guide tube. Insert the strings such that the bottom detector is at the bottom of the guide tube.
- A12. JCH Experimenter performs preliminary check of the electronics and completes final setup of the equipment on top of the reactor top front platform. Once this has been completed, experimenter performs a full set of background readings, taking readings from all nine detectors. Record the core tank temperature at the time these readings are taken.

Core Tank Temperature: 37.8 °C

Table A1. Background Measurements

Detector	Current (µA)	Detector	Current (µA)	Detector	Current (µA)
#1		#2		#3	
#1b		#2b		#3b	
#1c		#2c		#3c	

B. Steady State “Flat” Measurements at 1 kW

- B1. JCH Notify control room that experimenter is ready to begin and requests the control room to conduct a reactor startup. Raise reactor power to 1 kW.

Note startup time: 1222

Shutdown time prior to startup: ~67.5 hrs.

- B2. JCH With reactor power at 1 kW experimenter conducts flux mapping with the nine fission chamber detectors. Note the position of all control blades and the regulating rod below. Also note the core tank temperature.

Shim Bank Height (SBH): 0885

Regulating Rod Height (RRH): 0310

Core tank temperature: 37.8°C D₂O Temperature:

Table B1. “Flat” Flux Measurements, 1 kW

Detector	Current (µA)	Detector	Current (µA)	Detector	Current (µA)
#1	0.1630	#2	0.2291	#3	0.2083
#1b	0.0942	#2b	0.1476	#3b	0.0964
#1c	0.0334	#2c	n/a	#3c	0.0318

- B3. JCH Upon completion of the above step, the experimenter will notify the control room.

C. Steady State Tilted Measurements at 1 kW, #1

C1. ops After the above data are taken, establish a flux tilt by moving the control blades in the following manner (RO maintains criticality at 1 kW by compensating with the regulating rod):

- Control Blade #1: SBH + 6"
- Control Blade #2: SBH + 2"
- Control Blade #3: SBH - 2"
- Control Blade #4: SBH - 6"
- Control Blade #5: SBH - 2"
- Control Blade #6: SBH + 2"

C2. ops Note the positions of all control blades and the regulating rod below:

- Control Blade #1 Position: 1485
- Control Blade #2 Position: 1085
- Control Blade #3 Position: 0685
- Control Blade #4 Position: 0485
- Control Blade #5 Position: 0685
- Control Blade #6 Position: 1085
- RRH: 0480

C3. ops The control room notifies the experimenter once this flux tilt is achieved.

C4. JCH When the experimenter has recorded data from all nine fission chamber detectors, he notifies the control room.

Table C1. Tilted Flux Measurements #1, 1 kW

Detector	Current (μA)	Detector	Current (μA)	Detector	Current (μA)
#1	0.1922	#2	0.2168	#3	0.2159
#1b	0.1055	#2b	0.1442	#3b	0.0999
#1c	0.0362	#2c	n/a	#3c	0.0328

D. Steady State Tilted Measurements at 1 kW, #2

D1. ops When ready, the experimenter requests the control room to shift the flux tilt to the other side of the core by positioning the control blades as follows (RO maintains criticality at 1 kW by compensating with the regulating rod):

- Control Blade #1: SBH - 6"
- Control Blade #2: SBH - 2"
- Control Blade #3: SBH + 2"
- Control Blade #4: SBH + 6"
- Control Blade #5: SBH + 2"
- Control Blade #6: SBH - 2"

D2. ops Note the position of all control blades and the regulating rod below:

- Control Blade #1 Position: 0400
- Control Blade #2 Position: 0685
- Control Blade #3 Position: 1085

Control Blade #4 Position: 1485
 Control Blade #5 Position: 1085
 Control Blade #6 Position: 0685
 RRH: 0600

- D3. ops The control room notifies the experimenter once the flux tilt is achieved.
- D4. JCH When the experimenter has recorded data from all nine fission chamber detectors, he notifies the control room.

Table D1. Tilted Flux Measurements #2, 1 kW

Detector	Current (μA)	Detector	Current (μA)	Detector	Current (μA)
#1	0.1544	#2	0.2659	#3	0.2122
#1b	0.0924	#2b	0.1660	#3b	0.0984
#1c	0.0333	#2c	n/a	#3c	0.0324

E. Steady State “Flat” Measurements at 10 kW

- E1. ops When ready, experimenter requests the control room to raise reactor power to 10 kW and reshim.
- E2. JCH With reactor power at 10 kW, experimenter conducts flux mapping with the nine fission chamber detectors. Note the new shim bank and regulating rod positions below once power is leveled at 10 kW. Also note the core tank temperature.

SBH: 0890
 RRH: 0204
 Core tank temp: 38.4°C

Table E1. “Flat” Flux Measurements, 10 kW

Detector	Current (μA)	Detector	Current (μA)	Detector	Current (μA)
#1	0.8117	#2	1.1915	#3	1.1959
#1b	0.5112	#2b	0.8068	#3b	0.5828
#1c	0.1939	#2c	n/a	#3c	0.1889

- E3. JCH Upon completion of the above step, the experimenter will notify the control room.

F. Steady State Tilted Measurements at 10 kW, #1

- F1. ops After the above data are taken, establish a flux tilt by moving the control blades in the following manner (RO maintains criticality at 10 kW by compensating with the regulating rod):

Control Blade #1: SBH + 6”
 Control Blade #2: SBH + 2”
 Control Blade #3: SBH - 2”
 Control Blade #4: SBH - 6”
 Control Blade #5: SBH - 2”
 Control Blade #6: SBH + 2”

F2. ops Note the positions of all control blades and the regulating rod below. Also note the core tank temperature.

Control Blade #1 Position: 1490
 Control Blade #2 Position: 1090
 Control Blade #3 Position: 0690
 Control Blade #4 Position: 0460
 Control Blade #5 Position: 0690
 Control Blade #6 Position: 1090
 RRH: 0765
 Core tank temp: 40.7°C

F3. ops The control room notifies the experimenter once the flux tilt is achieved.

F4. JCH When the experimenter has recorded data with all nine fission chamber detectors , he notifies the control room.

Table F1. Tilted Flux Measurements #1, 10 kW

Detector	Current (μA)	Detector	Current (μA)	Detector	Current (μA)
#1	1.0708	#2	1.0651	#3	1.2380
#1b	0.5963	#2b	0.7463	#3b	0.6008
#1c	0.2187	#2c	n/a	#3c	0.1961

G. Steady State Tilted Measurements at 10 kW, #2

G1. ops When ready, the experimenter requests the control room to shift the flux tilt to the other side of the core as follows (RO maintains criticality at 10 kW by compensating with the regulating rod).

Control Blade #1: SBH - 6"
 Control Blade #2: SBH - 2"
 Control Blade #3: SBH + 2"
 Control Blade #4: SBH + 6"
 Control Blade #5: SBH + 2"
 Control Blade #6: SBH - 2"

G2. ops Note the positions of all control blades and the regulating rod below. Also note the core tank temperature.

Control Blade #1 Position: 0400
 Control Blade #2 Position: 0690
 Control Blade #3 Position: 1090
 Control Blade #4 Position: 1490
 Control Blade #5 Position: 1090
 Control Blade #6 Position: 0690
 RRH: 0603
 Core tank temp: 28.0°C

G3. ops The control room notifies the experimenter once the flux tilt is achieved.

- G4. JCH When the experimenter has recorded data with all nine fission chamber detectors, he notifies the control room.

Table G1. Tilted Flux Measurements #2, 10 kW

Detector	Current (μA)	Detector	Current (μA)	Detector	Current (μA)
#1	0.7191	#2	1.5605	#3	1.2169
#1b	0.4697	#2b	0.9810	#3b	0.5924
#1c	0.1904	#2c	n/a	#3c	0.1945

H. Steady State “Flat” Measurements at 50 kW

- H1. ops When ready, experimenter requests the control room to raise reactor power to 50 kW and reshim.
- H2. JCH With reactor power at 50 kW, experimenter conducts flux mapping with the nine fission chamber detectors. Note the new shim bank and regulating rod positions below once power is leveled at 50 kW. Also note the core tank temperature.

SBH: 0900
 RRH: 0375
 Core tank temp: 27.9°C

Table H1. “Flat” Flux Measurements, 50 kW

Detector	Current (μA)	Detector	Current (μA)	Detector	Current (μA)
#1	3.6774	#2	5.4363	#3	5.5041
#1b	2.3171	#2b	3.7157	#3b	3.7755
#1c	0.9240	#2c	n/a	#3c	0.9130

- H3. JCH Upon completion of the above step, the experimenter will notify the control room.

I. Steady State Tilted Measurements at 50 kW, #1

- I1. ops After the above data are taken, establish a flux tilt by moving the control blades in the following manner (RO maintains criticality at 50 kW by compensating with the regulating rod):

Control Blade #1: SBH + 6”
 Control Blade #2: SBH + 2”
 Control Blade #3: SBH - 2”
 Control Blade #4: SBH - 6”
 Control Blade #5: SBH - 2”
 Control Blade #6: SBH + 2”

- I2. ops Note the positions of all control blades and the regulating rod below. Also note the core tank temperature.

Control Blade #1 Position: 1500
 Control Blade #2 Position: 1100
 Control Blade #3 Position: 0700
 Control Blade #4 Position: 0500
 Control Blade #5 Position: 0700

Control Blade #6 Position: 1100
 RRH: 0737
 Core tank temp: 27.9°C

- I3. ops The control room notifies the experimenter once the flux tilt is achieved.
- I4. JCH When the experimenter has recorded data with all nine fission chamber detectors, he notifies the control room.

Table I1. Tilted Flux Measurements #1, 50 kW

Detector	Current (μ A)	Detector	Current (μ A)	Detector	Current (μ A)
#1	5.1532	#2	4.9163	#3	5.8081
#1b	2.7652	#2b	3.4103	#3b	2.8240
#1c	1.0765	#2c	n/a	#3c	0.9521

J. Steady State Tilted Measurements at 50 kW, #2

- J1. ops When ready, the experimenter requests the control room to shift the flux tilt to the other side of the core as follows (RO maintains criticality at 50 kW by compensating with the regulating rod).

Control Blade #1: SBH - 6"
 Control Blade #2: SBH - 2"
 Control Blade #3: SBH + 2"
 Control Blade #4: SBH + 6"
 Control Blade #5: SBH + 2"
 Control Blade #6: SBH - 2"

- J2. ops Note the positions of all control blades and the regulating rod below. Also note the core tank temperature.

Control Blade #1 Position: 0450
 Control Blade #2 Position: 0700
 Control Blade #3 Position: 1100
 Control Blade #4 Position: 1500
 Control Blade #5 Position: 1100
 Control Blade #6 Position: 0700
 RRH: 0568
 Core tank temp: 27.9°C

- J3. ops The control room notifies the experimenter once the flux tilt is achieved.
- J4. JCH When the experimenter has recorded data with all nine fission chamber detectors, he notifies the control room.

Table J1. Tilted Flux Measurements #2, 50 kW

Detector	Current (μA)	Detector	Current (μA)	Detector	Current (μA)
#1	3.3019	#2	7.4175	#3	5.7474
#1b	2.0804	#2b	4.5183	#3b	2.7534
#1c	0.8986	#2c	n/a	#3c	0.9147

K. Transient Measurements, Shim Blade #6 Insertion

- K1. ops When ready, the experimenter requests the control room to reshim with power at 50 kW.
- K2. ops Note the new shim bank and regulating rod positions below after the reshim. Also note the core tank temperature.

SBH: 0900
 RRH: 0208
 Core tank temp: 27.9°C

- K3. ops With the power steady at 50 kW, drive in with shim blade #6 for ten seconds. Take readings from detectors #1, 2, and 3. These are at the bottom of the string. Note the position of shim blade #6 after this shim (hold the remainder of the shim bank and regulating rod positions constant during this ten second shim). At sixty seconds following the initiation of the step power decrease, restore power to 50 kW using shim blade #6 and the regulating rod. Note shim blade #6 position, the regulating rod position, and the core tank temperature once power is restored to 50 kW.

Reading fission chamber detectors #1,2,3:

Shim blade #6 position (after 10 second shim): 0829
 Shim blade #6 position (power restored to 50 kW): 0900
 New RRH (power restored to 50 kW): 0235
 Core tank temperature: 27.9°C

- K4. JCH When ready, experimenter requests the control room to restore the control bank to the original position (as it was before the ten second shim). Use the regulating rod to compensate and keep power at 50 kW. Note the shim bank height and regulating rod position below.

SBH: 0900
 RRH: 0243

- K5. ops With reactor power restored to 50 kW the SRO notifies the control room. The above step power decrease is repeated, and readings are taken from detectors #1b, 2b, and 3b in the middle of the string. This is repeated taking readings from detectors #1c, 2c, and 3c.

Reading fission chamber detectors #1b, 2b, and 3b:

SBH (before shim): 0900
 RRH (before shim): 0243
 Shim blade #6 position (after 10 second shim): 0828
 Shim blade #6 position (power restored to 50 kW): 0893
 New RRH (power restored to 50 kW): 0279

Core tank temperature: 27.9°C

Reading fission chamber detectors #1c, 2c, and 3c:

SBH (before shim): 0900

RRH (before shim): 0235

Shim blade #6 position (after 10 second shim): 0827

Shim blade #6 position (power restored to 50 kW): 0900

New RRH (power restored to 50 kW): 0250

Core tank temperature: 27.9°C

- K6. ops After completing the above step, maintain power at 50 kW and reshim. Note the position of the shim bank and the regulating rod below. Also note the core tank temperature.

SBH: 0900

RRH: 0327

Core tank temp: 27.9°C

L. Transient Measurements, Shim Blade #3 Insertion

- L1. ops With the power steady at 50 kW, drive in with shim blade #3 for ten seconds. Take readings from detectors #1, 2, and 3. These are at the bottom of the string. Note the position of shim blade #3 after this shim (hold the remainder of the shim bank and regulating rod positions constant during this ten second shim). At sixty seconds following the initiation of the step power decrease, restore power to 50 kW using shim blade #3 and the regulating rod. Note shim blade #3 position, the regulating rod position, and the core tank temperature once power is restored to 50 kW.

Reading fission chamber detectors #1,2,3:

Shim blade #3 position (after 10 second shim): 0833

Shim blade #3 position (power restored to 50 kW): 0900

New RRH (power restored to 50 kW): 0416

Core tank temperature: 27.9°C

- L2. ops When ready, experimenter requests the control room to restore the control bank to the original position (as it was before the ten second shim). Use the regulating rod to compensate and keep power at 50 kW. Note the shim bank height and regulating rod position below.

SBH: 0900

RRH: 0310

- L3. ops With reactor power restored to 50 kW the SRO notifies the control room. The above step power decrease is repeated, and readings are taken from detectors #1b, 2b, and 3b in the middle of the string. This is repeated taking readings from detectors #1c, 2c, and 3c.

Reading fission chamber detectors #1b, 2b, and 3b:

SBH (before shim): 0900

RRH (before shim): 0310
Shim blade #3 position (after 10 second shim): 0832
Shim blade #3 position (power restored to 50 kW): 0900
New RRH (power restored to 50 kW): 0465
Core tank temperature: 27.9°C

Reading fission chamber detectors #1c, 2c, and 3c:

SBH (before shim): 0900
RRH (before shim): 0455
Shim blade #3 position (after 10 second shim): 0837
Shim blade #3 position (power restored to 50 kW): 0900
New RRH (power restored to 50 kW): 0511
Core tank temperature: 27.9°C

M. Transient Measurements, Shim Blade #6 Withdrawal

- M1. ops After completing the above step, lower power at 5 kW and reshim. Note the position of the shim bank and the regulating rod below. Also note the core tank temperature.

SBH: 0890
RRH: 0329
Core tank temp: 53.1 °C

- M2. ops When ready, the experimenter requests the RO move control blade #6 out to establish a 50 second steady period. Once the 50 second period is attained, note control blade #6 position below and take readings from detectors #1, 2, and 3 at the bottom of the string. When reactor power reaches 50 kW, re-insert shim blade #6 and level power at 60 kW. Again note control blade #6 position when power is leveled at 60 kW. Also note the core tank temperature.

Reading fission chamber detectors #1, 2 and 3:

Control blade #6 position with 50 second period: 1064
Control blade #6 position with power leveled at 60 kW: 0982
Core tank temperature: 52.9°C

- M3. ops When experimenter is ready, lower power to 5 kW and restore shim blade #6 to the bank height.

- M4. ops With power leveled at 5 kW the SRO notifies the control room. Repeat the above reactor power increase transient, reading first fission chamber detectors #1b, 2b, and 3b, then #1c, 2c, and 3c. Be sure to note the control bank and regulating rod positions before the transient and note control blade #6 position during and after the transient as above. Also note the core tank temperature.

Reading fission chamber detectors #1b, 2b, and 3b:

Control blade #6 position with 50 second period: 1062
Control blade #6 position with power leveled at 60 kW: 1011
Core tank temperature: 53.2°C

Reading fission chamber detectors #1c, 2c, and 3c:

Control blade #6 position with 50 second period: 1066
Control blade #6 position with power leveled at 60 kW: 1015
Core tank temperature: 53.2

N. Transient Measurements, Shim Blade #1 Drop

N1. ops After completing the last transient above and when the experimenter is ready, lower reactor power to 50 kW and reshim.

N2. ops Note the control bank and regulating rod positions and core tank temperature below.

SBH: 0905
RRH: 0307
Core tank temp: 53.4°C

N3. ops When ready, experimenter requests the control room to drop control blade #1. Readings are taken from chambers #1, 2b, and 3c.

N4. ops When ready, experimenter requests the control room to restore reactor power to 50 kW. Note the new shim bank and regulating rod positions below. Also note the core tank temperature.

SBH: ops
RRH: ops
Core tank temp: ops °C

O. Shutdown

O1. ops When ready, experimenter requests the control room to conduct a reactor shutdown.

O2. ops Once reactor shutdown has been completed, experimenter conducts a full set of background readings.

Table O1. Background Measurements

Detector	Current (μA)	Detector	Current (μA)	Detector	Current (μA)
#1		#2		#3	
#1b		#2b		#3b	
#1c		#2c		#3c	

O3. ops Once all testing is completed, carefully remove the nine fission chamber detectors from the aluminum instrument guide tubes. Care must be taken in handling the detectors since they will be activated from the neutron flux.

O4. ops Carefully remove the three aluminum instrument guide tubes from the reactor core tank. Dry the aluminum tubes with absorbent rags. (**CAUTION:** High beta exposure on contact with aluminum tubes.)

- O5. ops A licensed SRO inspects the core tank for any foreign objects left behind from the experiment.
- O6. ops If no additional experiments are to be performed within the core tank, replace the reactor top shield lid.
- O7. ops Remove and store all tools used in this procedure. Notify the control room, the Reactor Supervisor, and RRPO that the experiment has been completed.

Supervisor: _____

Date: _____